UNIVERSITÉ DE SHERBROOKE

Faculté de génie
Département de génie civil et de génie du bâtiment

PERFORMANCE OF PRECAST CONCRETE TUNNEL LINING SEGMENTS REINFORCED WITH GFRP BARS UNDER QUASI-STATIC CYCLIC FLEXURAL LOADING

PERFORMANCE DE VOUSSOIRS DE TUNNEL PRÉFABRIQUÉS EN BÉTON ARMÉ D'ARMATURES EN PRFV SOUS CHARGE DE FLEXION CYCLIQUE QUASI-STATIQUE

Thèse de doctorat

Spécialité : Génie civil

BASIL IBRAHIM

A Dissertation
Submitted to the Faculty if Graduate Studies
In partial fulfilment of the requirements for the degree of
Doctor of Philosophy
(Civil Engineering)

A dissertation submitted in partial fulfillment of the requirements for the degree of Ph.D in Civil Engineering

Thèse présentée au départent de génie civil et de génie du bâtiment en vue de l'obtention du grade de doctorat (Ph.D.) en génie civil

Sherbrooke (Québec) Canada December 2022

MEMBRES DU JURY

Prof. Brahim BENMOKRANE
Directeur de recherche

Prof. Charles-Philippe LAMARCHE
Rapporteur

Prof. Mark GREEN
Membre Externe

Prof. Amr ELRAGABY
Membre Externe

Dr. Hamdy MOHAMED
Membre Externe

ABSTRACT

Current design provisions are not applicable to designing precast concrete tunnel lining (PCTL) segments reinforced internally with fiber-reinforced polymer (FRP) bars. The strength and behavior of segments of precast concrete tunnel linings (PCTLs) reinforced internally with FRP bars under quasi-static cyclic flexural loading is one area in which no experimental research results are available. A total of twelve full-scale PCTL segments with a total length, width, and thickness of 3100 mm, 1500 mm, and 250 mm, respectively, were constructed and tested under quasi-static cyclic flexural loading. Two cycles of loading and unloading were applied at 1.25%, 2.5%, 5%, 10%, 25%, 50%, and 75% of the estimated maximum displacement, followed by a single cycle up to failure. The test parameters included reinforcement flexural stiffness (GFRP versus steel), GFRP longitudinal reinforcement ratio, the concrete compressive strength (high-strength concrete (HSC) versus normal-strength concrete (NSC)), the concrete type (fiber-reinforced concrete (FRC) versus NSC), and the transverse reinforcement configuration (closed versus double U-shaped ties). The hysteresis response, cracking pattern, residual deformation, dissipated energy, ductility index, deformability, and secant stiffness damage index of the tested specimens, under the quasi-static cyclic flexural loading, were defined, estimated, and evaluated. The experimental results of the study show the feasibility of using GFRP bars instead of steel bars for PCTL segments under quasi-static cyclic flexural loading. Moreover, the experimental results show the effectiveness of using HSC and FRC over the NSC for the GFRP-reinforced PCTL segment applications. A theoretical prediction according to the various current design provisions – including the flexural capacities, the shear capacities, the cracking moments, and the crack-width predictions of the PCTL segments – was carried out and compared to the experimental results. Furthermore, using the layer-by-layer iterative approach, an analytical model was presented for the hysteresis response of the GFRP-reinforced PCTL segments under quasi-static cyclic flexural loading. In addition, analytical models for the post-cracking loading tangent stiffness and the unloading stiffness for the GFRP reinforced PCTL segments were proposed. The analytically predicted models show accurate predictions with comparable loading stiffness, unloading stiffness and residual deformation at the end of each loading cycles.

Keywords: Precast concrete tunnel lining (PCTL) segments; glass fiber-reinforced polymer (GFRP) bars; quasi-static cyclic load.

RÉSUMÉ

Les dispositions de conception actuelles dans les normes ne sont pas applicables à la conception de voussoirs de revêtement de tunnels en béton préfabriqué (RTBP) armé d'armature en polymère renforcé de fibres de verre (PRFV). La résistance et le comportement des voussoirs de revêtements de tunnels en béton préfabriqué (RTBP) armé d'armature en PRFV sous des charges de flexion cyclique quasi-statique est un domaine dans lequel aucun résultat de recherche expérimentale n'est disponible. Un total de douze voussoirs de RTBP à pleine échelle ayant une longueur de 3100 mm, une largeur de 1500 mm et une épaisseur de 250 mm ont été construits et testés sous des charges de flexion cycliques quasi-statiques. Deux cycles de chargement et de déchargement ont été appliqués à 1,25%, 2,5%, 5%, 10%, 25%, 50% et 75% du déplacement maximal estimé, suivis d'un seul cycle de chargement jusqu'à la rupture. Les paramètres de l'essai comprenaient le type d'armature (armature en PRFV et d'acier), le taux d'armature longitudinal, la résistance à la compression du béton (béton à haute résistance (BHR) et béton à résistance normale (BRN)), le type de béton (béton renforcé de fibres (BRF) par rapport au BRN), et la configuration de l'armature transversale (cadres fermés par rapport aux cadres doubles en forme de U). La réponse d'hystérésis, le modèle de fissuration, la déformation résiduelle, l'énergie dissipée, l'indice de ductilité, la déformabilité et l'indice de dommage de la rigidité sécante des spécimens testés ont été définis et évalués. Les résultats expérimentaux de l'étude montrent la faisabilité de l'utilisation de barres en PRFV au lieu de barres d'acier pour les voussoirs de RTBP sous des charges de flexion cycliques quasi-statiques. De plus, les résultats expérimentaux montrent l'efficacité de l'utilisation de BHR et BRF par rapport au BRN pour les applications de voussoirs de RTBP armé d'armature en PRFV. Une prédiction théorique selon les diverses dispositions de conception actuelles - y compris la résistance en flexion, la résistance à l'effort tranchant, le moment de fissuration et la prédiction de largeur de fissure des voussoirs de RTBP - a été effectuée incluant une comparaison aux résultats expérimentaux. En outre, utilisant l'approche itérative couche par couche, un modèle analytique a été présenté pour la réponse d'hystérésis des voussoirs de RTBP armé d'armature de PRFV sous des charges de flexion cycliques quasi-statiques. De plus, des modèles analytiques pour la rigidité tangente de chargement après fissuration et la rigidité de déchargement pour les voussoirs en RTBP armé d'armature de PRFV ont été proposés. Les modèles analytiques montrent

des prédictions précises avec une rigidité de chargement, une rigidité de déchargement et une déformation résiduelle comparables à la fin de chaque cycle de chargement.

Mots clés: Voussoirs de revêtement de tunnel en béton préfabriqué (RTBP), barres d'armature en polymère renforcé de fibres de verre (PRFV), charge cyclique quasi-statique.

DEDICATION

To my father and my mother

To my brothers Kamel, Tariq and Ragheb

To my friends

I would not have succeeded in my journey without your support and motivation

To those who appreciate the value of knowledge

ACKNOWLEDGEMENT

"*My Lord (Almighty Allah), direct me to be thankful for your blessings that you bestowed upon me and upon my parents, and to work righteousness, pleasing you. And admit me, by your grace, into the company of your virtuous worships*."

All praise and glory to Almighty Allah, who gave me courage and patience to carry out this work. Peace and blessing of Allah be upon last prophet Muhammad (PBUH). "O Allah, benefit me by that which you have taught me, and teach me that which will benefit me, and increase me in knowledge".

It is a genuine pleasure to express my deep sense of thanks and gratitude to my supervisor and guide **Prof. Brahim Benmokrane**. I deeply appreciate how he has been continuously encouraging and guiding me in the past few years, and also how has always been so friendly and supportive of all of my efforts. Working under the supervision of Prof. Brahim, has been very enjoyable and I have learned and grown a lot.

I would also like to acknowledge and give my warmest thanks to both **Dr. Hamdy M. Mohamed** and **Dr. Salaheldin Mousa**, who helped me in making this work possible. Words would never be able to express my appreciation for their guidance and advice, which carried me through all the stages of my journey.

My appreciations are also extended to the jury members of this dissertation (**Prof. Charles-Philippe Lamarche**, **Prof. Mark Green**, and **Prof. Amr Elragaby**) for accepting to revise my work.

This research was conducted with funding from the Natural Sciences and Engineering Research Council of Canada (NSERC), Mathematics of Information Technology and Complex Systems (MITACS), the Fonds de recherche du Québec en nature et technologies (FRQ-NT), The Pole de Recherche et d'Innovation en Matériaux Avancés au Quebec (PRIMA Quebec) and the Tier-1 Canada Research Chair in Advanced Composite Materials for Civil Structures.

The authors are grateful to the precast company (Sym-Tech Béton Préfabriqué, Sainte-Hyacinthe, QC, Canada) and to the GFRP bar manufacturer (Pultrall Inc., Thetford Mines, QC, Canada) for its effective involvement in this project, and to the technical staff of the structural lab in the Department of Civil Engineering at the University of Sherbrooke.

Many thanks also go to my colleagues and friends at the Université de Sherbrooke for their invaluable help and support throughout my journey.

I would like also to give special thanks to my first teacher and supporter **Prof. Samer Barakat**, and to my friends **Dr. Ousmane Hisseine** and **Ahmed Shweiki** for their always support and motivation.

Last and most important, my love goes to my parents, my brothers, and my friends for their support throughout my journey.

TABLE OF CONTENTS

LIST OF FIGURES

CHAPTER 1

CHAPTER 2

CHAPTER 3

CHAPTER 4

CHAPTER 5

CHAPTER 6

CHAPTER 7

LIST OF TABLES

CHAPTER 2

CHAPTER 3

CHAPTER 4

CHAPTER 5

CHAPTER 6

CHAPTER 7

CHAPTER 1 INTRODUCTION

1.1 BACKGROUND

Tunnels are defined by the *American Association of State Highway and Transportation Officials*, t*echnical Committee for Tunnels (T-20)* [AASHTO, 2010], as "the covered passageways with vehicles or subways access that is limited to portals regardless of structure types and construction techniques". Tunnel structures protect and preserve surface landscapes, cultural heritages, and historical buildings, resulting in having green and sustainable civil infrastructures. Moreover, tunnel structures significantly reduce traffic congestions, resulting in improved environmental quality parameters such as noise and air pollution [Hung et al., 2009]. Tunnel linings act as defensive barriers against large overburden loads and complex geotechnical surrounding exposure conditions. The structural and durability performance of tunnels significantly depends on its lining system. Therefore, the tunnel lining systems is an important component of tunnel infrastructure. Precast concrete tunnel lining segments are applicable for both soft and hard ground conditions and can function both as preliminary and final support alongside large overburden loads [Hung et al., 2009]. The use of precast concrete tunnel lining (PCTL) systems in tunneling construction projects has been rising over the conventional in-site lining technique, because of its economic efficiency. PCTL speeds the construction process along with ensuring highest quality due to enhanced control during precast segment fabrication in precast plants [Cheong et al., 2005]. The structural performance of PCTL segments significantly depends on its durability performance. Tunnel structures constructed from steel reinforced concrete are designed for service life in excess of 100 years. The ingress of chloride ions into PCTL segments can induce reinforcement corrosion, which has been the primary cause that threaten the structural safety of PCTL and reducing the designed service life. Corrosion of the embedded reinforcement bars is considered the most prevalent mode of deterioration affecting serviceability, safety, and structural integrity of the tunnel structure [Gulikers, 2003]. In fact, many reinforced concrete tunnels around the world are deteriorating as they age [Zhiqiange and Mansoor, 2013].

Steel reinforced PCTL often suffer premature degradation mainly due to corrosion of the reinforcement bars which requires expensive repair and maintenance. The groundwater surrounding the steel reinforced concrete tunnels in the roadways applications is rich in chlorine

from the deicing salts. Since concrete is not perfectly impermeable, the chlorine from this groundwater gradually saturates the concrete and ends up permeating through the cover and produces an electrolytic reaction with the steel which accelerates the corrosion of the reinforcement [Rancourt, 2016]. This corrosion can lead to the bursting of concrete and the loss of structural integrity. Corrosion of steel reinforcement is the most expensive and problematic deterioration mechanism in concrete structures [ACI 440.1R-15]. In Canada, the annual cost of repairing corrosion damage in reinforced concrete structures has been estimated at more than $10 billion per year [Davis, 2000]. In the United States, the problem of corrosion of reinforced concrete structures costs the economy about $100 billion each year, or nearly 1% of the country's gross domestic product [Whitmore and Ball, 2004].

The effective solution to this corrosion problem is to replace steel reinforcements with noncorrosive fiber reinforced polymer (FRP) reinforcing bars. These lightweight, high-strength FRP bars are characterized by high corrosion resistance, long service life and reduced maintenance costs [Mohamed and Benmokrane 2015; 2016; Benmokrane and Ali, 2018; Mousa el al. 2019; 2020; Manalo et al., 2020; Mohamed et al., 2017; 2019; 2020; Benmokrane et al., 2021]. Recently, valuable research has been conducted to evaluate the cyclic behavior of glass FRP (GFRP) reinforced concrete members [Vafaei et al., 2023; Hassanli et al., 2023]. The results from the experimental tests demonstrated that the GFRP reinforcement was a suitable substitute for the steel reinforcement under the quasi-static cyclic loading conditions [Vafaei et al., 2023]. Moreover, compared to the steel reinforced concrete slabs, the GFRP reinforced slabs demonstrated elastic hysteresis behavior with small residual deflections, while the steel reinforced concrete slabs exhibited an elastoplastic performance with large residual deformations [Hassanli et al., 2023]. In which unlike the steel reinforced concrete slabs, the rapid softening behavior and stiffness degradation of the GFRP reinforced concrete slabs was governed by the concrete crushing [Hassanli et al., 2023]. Moreover, due to the elastic properties of the GFRP reinforcement bars, the GFRP reinforced concrete slabs showed an exceptional self-centering mechanism under the quasi-static cyclic loading, characterized by small residual deflections upon unloading [Hassanli et al., 2023].

1.2 RESEARCH HYPOTHESIS

Recently, few studies investigated the possibility of using the glass FRP (GFRP) reinforcement in the PCTL segments [Caratelli et al., 2016; 2017; Spagnuolo et al., 2017, 2018; Hosseini et al., 2022]. All these studies proved the suitability of using GFRP bars as reinforcement for PCTL segments. The experimental evidence from these investigations illustrated that the GFRP-reinforced PCTL segments exhibited a better cracking control behavior compared to the traditional reinforced concrete segments, where the load related to the first crack formation was higher and the cracks openings were reduced. Moreover, these studies demonstrated that there is no significant difference in the flexural behavior of the GFRP reinforced PCTL segments compared to the steel reinforced ones. Substantively, the increasing of the strength of the GFRP bars compensates the lack of ductility compared to the steel reinforced PCTL segments. However, previous studies mainly focused on the static flexural resistance of PCTL in order to evaluate its structural properties. Accordingly, the performance of full-scale PCTL segments under quasi-static cyclic flexural loading needs to be investigated.

According to *the International Concrete Federation* [fib, Bulletin 83], during its service life, the tunnel structures can be subjected to different loads from the fabrication phase (demoulding loads, stacking loads, transportation loads, and handling loads); the construction phase (Thrust jack loads); or the service live phase (vehicular loads, live load surcharges, etc.). Moreover, according to [ACI 544.7R-16], the loads act on the PCTL, starting from the time of segment casting up to the time of the segment erection within the tunnel-boring machine (TBM) shield, are congregated in three stages. These stages are the production and transient stage, the construction stage, and the service stage. During the production and transient stage, the internal forces and stresses from stripping, storage, transportation, and handling are used for the design of the PCTL. Construction stage includes the TBM jacking thrust loads on the circumferential ring joints and the pressures during the grouting operation exerted against the exterior of the completed rings. PCTL segments are designed to resist significant bursting and spalling tensile stresses that develop along the circumferential joints due to advancement of the TBM. The final service stages are represented by the long-term loads imposed on the lining from the ground, groundwater, surcharges, and other loads from any circumstances such as earthquake, fire, explosion, and breakouts at cross passageways. Essence, the cyclic performance of GFRP reinforced PCTL segments is one area in

which no research results are available. The performance of full-scale PCTL segments under cyclic loads needs to be investigated.

1.3 RESEARCH SIGNIFICANCE

The design of the PCTL segments reinforced with FRP bars is not defined or discussed in the current design provisions such as in [CAN/CSA S806-12(R2017)], [CAN/CSA S6-19], [ACI 440.11-22], [ACI 544.7R-16], and [ACI PRC-533.5-20]. The strength and behavior of such members reinforced with FRP bars is one area in which limited research results are available for implementing this noncorroding composite reinforcement. So far, this research is the first experimental work aimed at providing experimental data involving the laboratory testing of the performance of PCTL segments reinforced with GFRP reinforcement under quasi-static cyclic flexural loading. As this work presents the first results of their kind on the applicability of using GFRP as internal reinforcement for PCTLs under quasi-static cyclic flexural loading, the results of this work represent a significant contribution to the relevant literature and provide end users, engineers, and code committees with much-needed data and recommendations to advance the use of GFRP reinforcement in PCTL segments.

1.4 RESEARCH DEFINITION AND CLASSIFICATION

The coupling and dynamics flow chart (**Fig. 1.1**) describes the flow of the research conducted between the four dynamics of *Research, Knowledge, Technology and Application*. Following the research justification described in the research hypothesis, this work is expected to be a step toward further research to assess the possibility of developing new applications for GFRP bars and ties, resulting in more durable, economic, and competitive PCTL segments for tunnel applications; and thus, this work is classified as applied research.

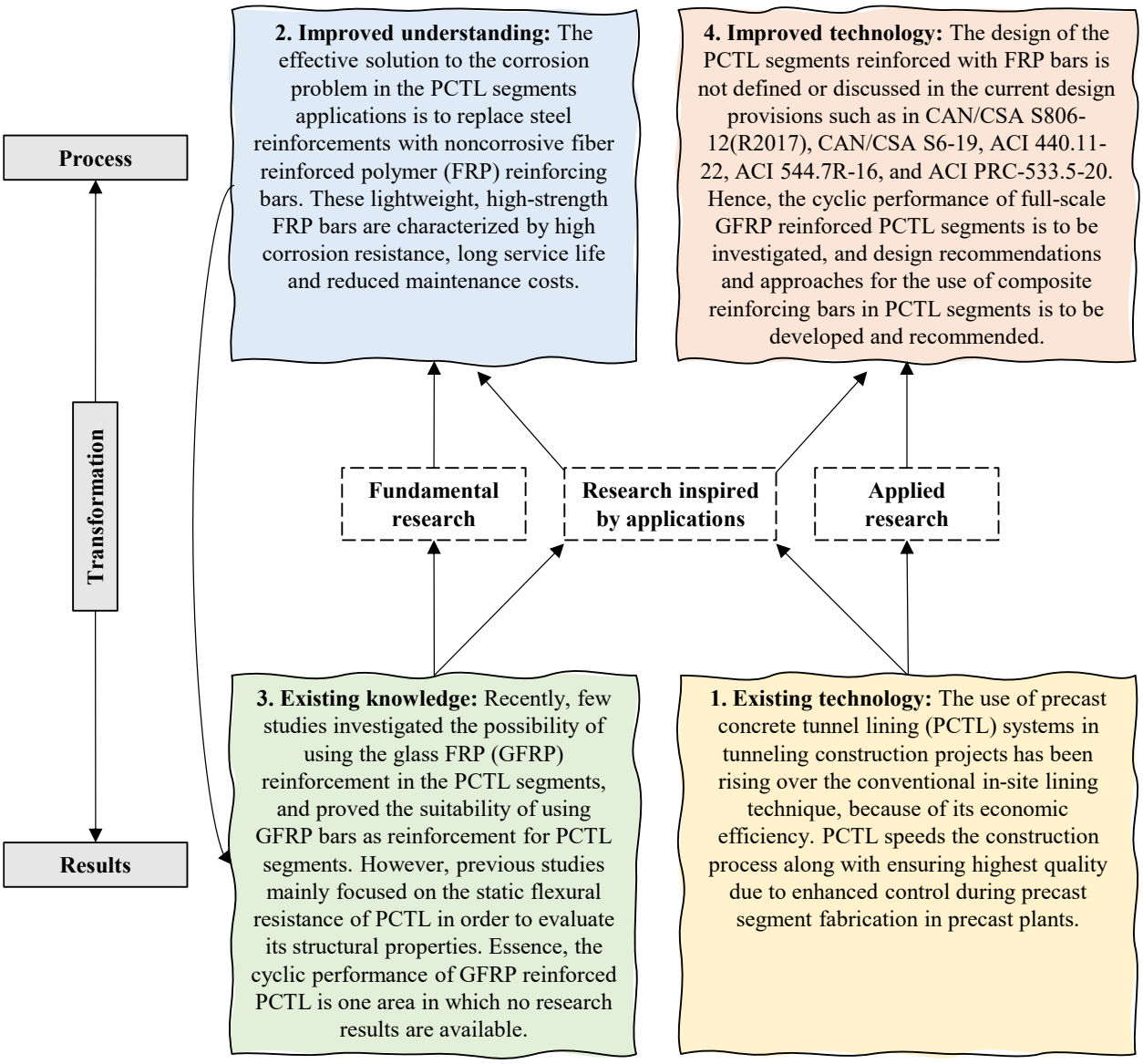

Fig. 1.1 Schematic for the research flow.

1.5 RESEARCH OBJECTIVES

The aim of this work is to assess the structural behavior of full-scale precast concrete tunnel lining (PCTL) segments reinforced internally with FRP bars at the structural laboratory. Tunnel lining segments behavior is evaluated under simulated cyclic loading. A total 12 precast concrete tunnel lining segments of different configuration are designed, fabricated, and tested under quasi-static cyclic flexural loading, considering different parameters concerning the tunnel applications. The main objective of this work is to assess the flexural behavior of full-scale precast concrete tunnel lining segments reinforced with longitudinal FRP bars and transverse FRP ties. Moreover, this work aims at investigating the effect of longitudinal and transverse FRP reinforcement parameters on the ultimate capacity, post-peak behavior, and failure mechanisms of the precast concrete tunnel lining segments.

The specific objectives can be summarized as follows:

1. To assess the structural performance of full-scale precast concrete tunnel lining segments reinforced with FRP bars under cyclic flexural loading conditions (compared to conventional members reinforced with steel reinforcement.
2. To evaluate the efficiency of using GFRP as internal reinforcement for the precast concrete tunnel lining segments under quasi-static cyclic flexural loading.
3. To investigate the advantages of using high-strength concrete (HSC) and fiber-reinforced concrete (FRC) for the GFRP reinforced precast concrete tunnel lining segments under quasi-static cyclic flexural loading.
4. To evaluate the validity of the current analytical and design approaches to FRP reinforced precast concrete tunnel lining segments.
5. To develop design recommendations and approaches for the different international standards for the use of composite reinforcing bars in precast concrete tunnel lining segments.

1.6 RESEARCH METHODOLOGY

To achieve the objectives of this research, extensive experimental, theoretical, and analytical programs were designed and conducted as schematized in **Fig. 1.2**. The experimental program was conducted to investigate the cyclic behavior of GFRP reinforced precast concrete tunnel lining (PCTL) segments. A total of twelve full-scale PCTL segments with a total length, width and thickness of 3100 mm, 1500 mm, and 250 mm, respectively, were constructed and tested under quasi-static cyclic flexural loading. In line with the practicality, segments are skewed at their ends rather than straight edges. Quasi-static compressive loading was applied in terms of percentage of maximum displacement achieved during the monotonic tests at the failure point. Two cycles of loading and unloading are conducted for 1.25%, 2.5%, 5%, 10%, 25%, 50%, and 75% of the maximum displacement. Subsequently, one cycle of loading up to failure is conducted. The test parameters included were the reinforcement flexural stiffness, GFRP longitudinal reinforcement ratio, concrete compressive strength and type, and transverse reinforcement configuration. The experimental research was conducted to investigate the efficiency of using GFRP as internal reinforcement for the PCTLs under quasi-static cyclic loading in terms of cyclic behavior stability of the GFRP reinforced PCTL segments, and its strength degradation under the cyclic loading. Moreover, the experimental outcomes and conclusions was directed towards investing the suitability of using high-strength concrete (HSC) and fiber-reinforced concrete (FRC) for the applications involving GFRP-reinforced PCTL segments. The experimental results were reported in terms of hysteresis response, cracking pattern, unloading stiffness degradation and residual deformation, dissipate energy, ductility index, deformability, and secant stiffness damage index. In addition, a theoretical prediction according to the various current design provisions – including the flexural and shear capacities, cracking moment, and crack width of the GFRP reinforced PCTL segments – was carried out and compared to the experimental results. Using a layer-by-layer iterative approach, an analytical model was prepared and presented in this work could predict the hysteresis response of the GFRP reinforced PCTL segments under quasi-static cyclic flexural loading. Furthermore, an analytical prediction for the load carrying capacity, deflection, loading and unloading stiffness of the GFRP reinforced PCTL segments was carried out and validated with the experimental results. The GFRP reinforced PCTL segments' analytically predicted models for the pos-cracking loading tangent stiffness and the unloading stiffness was proposed.

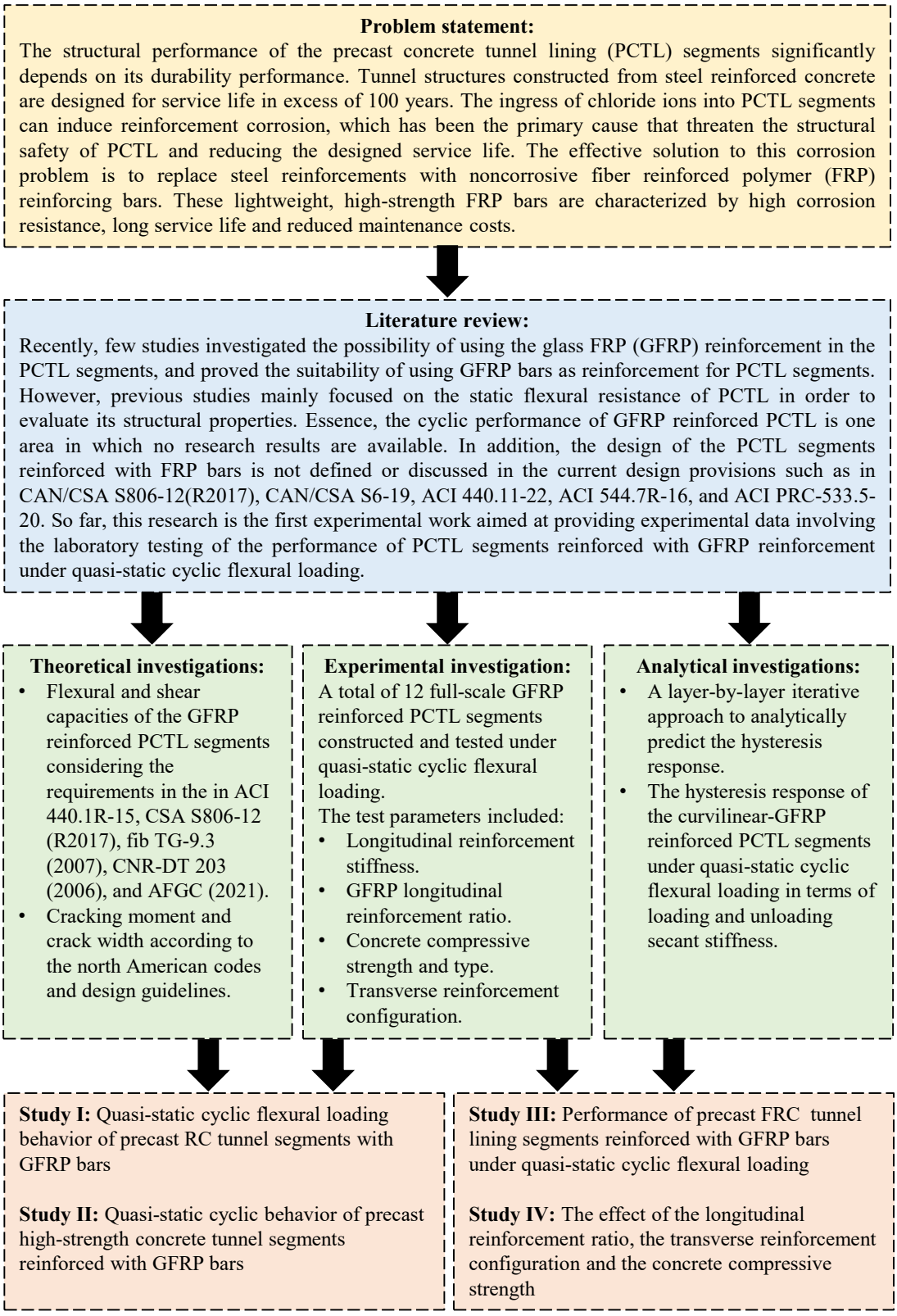

Fig. 1.2 Schematic for the research methodology.

1.7 DISSERTATION LAYOUT

The dissertation consists of six chapters (schematized in **Fig. 1.3**). The contents of each chapter can be summarized as follow:

Chapter 1. Introduction

In the introduction chapter, the problem statement has been introduced by a brief background. Then the research justification is defined in the research significance section. Followed by the objectives of the research and the methodology employed in order to achieve the objectives of the research.

Chapter 2. Literature review

The literature review chapter starts with introducing the fiber reinforced polymers (FRP), in terms of history of use, physical and mechanical properties. The literature review chapter provides, thereafter, a brief summary of the tunneling constructions, and discusses the main studies investigated the possibility of replacing the steel reinforcement with the noncorrosive GFRP reinforcement for the PCLT segments application. Current design provisions and design guidelines that related to the flexural behavior of the GFRP reinforced concrete structures are moreover summarised and presented in this chapter.

Chapter 3. Experimental research program

The experimental research program chapter presents the details of the experimental program undertaken on the present study. Detailed information is provided on the segments' design and details, test setup and instrumentation, properties of the materials used, and the simulated quasi-static cyclic flexural loading.

Chapter 4. Quasi-static cyclic flexural loading behavior of precast RC tunnel segments with GFRP bars

Chapter 4 investigated the cyclic behavior of GFRP-reinforced PCTL segments, both experimentally and theoretically, compared to the conventionally steel reinforced PCTL segments. This chapter investigates the feasibility of replacing the conventional steel reinforcement with the

non-corrodible GFRP reinforcement for the PCTL segments application under quasi-static cyclic flexural loading conditions.

[**Paper I**: Ibrahim, B., Mousa, S., Mohamed, H., and Benmokrane, B., (2022) " Quasi-static Cyclic Flexural Loading Behavior of Precast RC Tunnel Segments with GFRP bars." ACI Structural Journal, Accepted June 2022]

Chapter 5. Quasi-static cyclic behavior of precast high-strength concrete tunnel segments reinforced with GFRP bars

Chapter 5 investigated the cyclic behavior of precast high-strength concrete (HSC) tunnel lining segments reinforced with glass-FRP (GFRP). Both the experimental and theoretical investigations carried out in this chapter assess the advantages of using HSC for the applications involving GFRP reinforced PCTL segments. The outcomes of this chapter demonstrate the effectiveness of using HSC for the GFRP reinforced PCTL segments under the quasi-static cyclic flexural loading conditions.

[**Paper II**: Ibrahim, B., Mousa, S., Mohamed, H., and Benmokrane, B., (2022) " Quasi-static Cyclic Behavior of Precast High-Strength Concrete Tunnel Segments Reinforced with GFRP bars." Engineering Structures, Submitted March 2022.]

Chapter 6. Performance of precast FRC tunnel lining segments reinforced with GFRP bars under quasi-static cyclic flexural loading

Chapter 6 reports on an investigation of the cyclic behavior of GFRP-reinforced precast FRC tunnel lining segments. Both the experimental and analytical investigations carried out in this chapter assess the suitability of using FRC for the GFRP reinforced PCTL segments applications. The outcomes of this chapter highlights advantages of using FRC for the GFRP reinforced PCTL segments under the quasi-static cyclic flexural loading conditions.

[**Paper III**: Ibrahim, B., Mousa, S., Mohamed, H., and Benmokrane, B., (2022) " Performance of Precast FRC Tunnel Lining Segments Reinforced with GFRP Bars under Quasi-Static Cyclic Flexural Loading." Composite Structures, Submitted July 2022.].

Chapter 7. Hysteresis response of curvilinear-GFRP reinforced precast concrete tunnel lining segments under quasi-static cyclic flexural loading

Chapter 7 investigates the hysteresis behavior of PCTL segments reinforced internally with glass-FRP (GFRP) bars. Full-scale curvilinear-GFRP reinforced PCTL segments were designed, fabricated and tested under quasi-static cyclic flexural loading. In addition, an analytical prediction for the load carrying capacity, deflection, loading and unloading stiffness of the test segments was carried out in this chapter. The segments' analytically predicted responses were validated and compared to the experimental results. The segments' analytically predicted models for the post-cracking loading tangent stiffness and the unloading stiffness for the curvilinear-GFRP reinforced PCTL segments was proposed in this chapter.

[**Paper IV**: Ibrahim, B., Mousa, S., Mohamed, H., and Benmokrane, B., (2022) "Stiffness and Hysteresis Response Prediction of Curvilinear GFRP-Reinforced Precast Concrete Tunnel Segments under Quasi-Static Cyclic Loading." ACI Structural Journal, Submitted January 2023.].

Chapter 8. Summary, conclusions, and recommendations

Chapter 8 summarizes the outcomes of the current research and presents conclusions and recommendations for further studies.

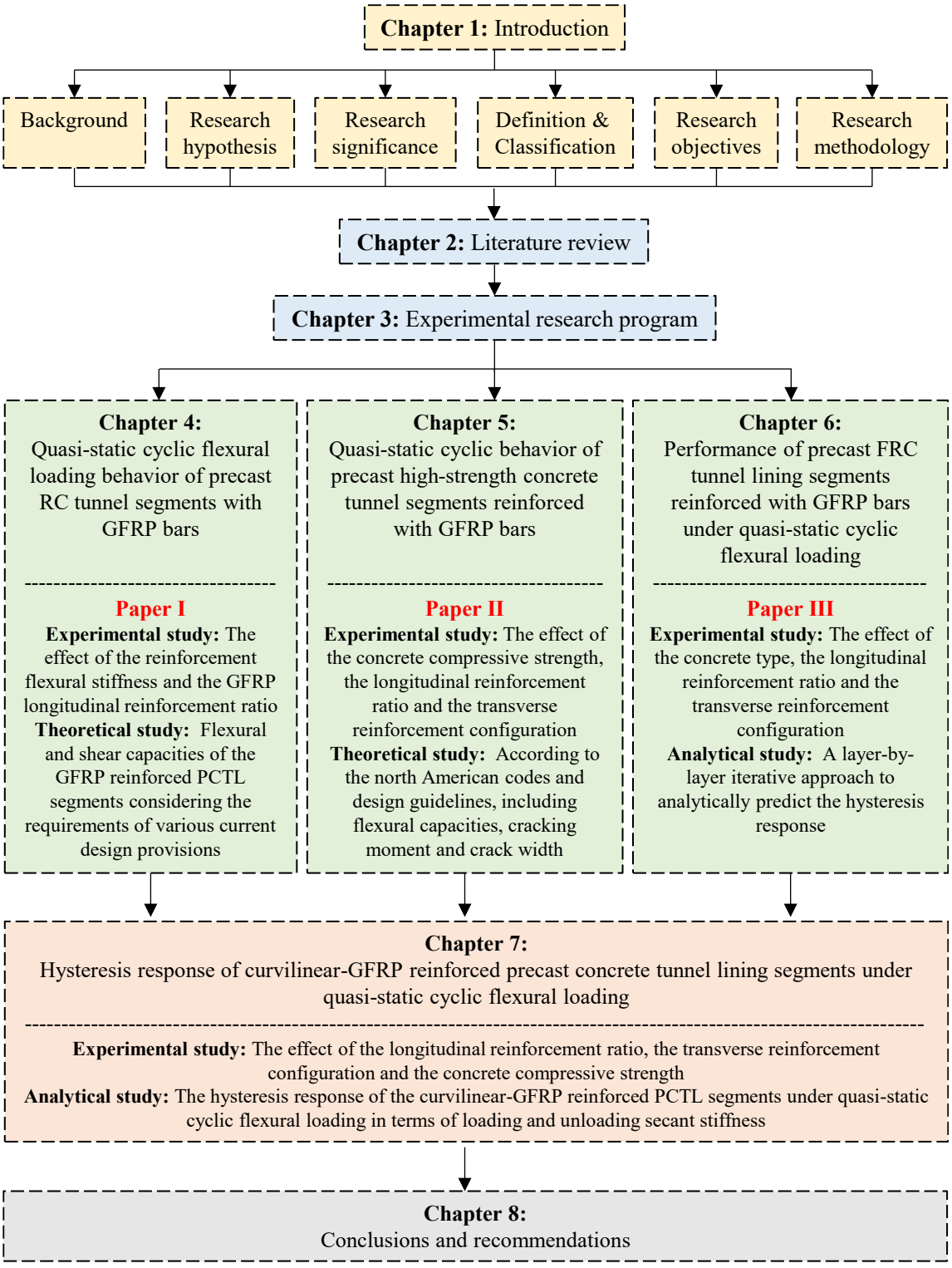

Fig. 1.3 Schematic for the dissertation layout.

CHAPTER 2 LITERATURE REVIEW

2.1 INTRODUCTION

For durable and serviceable construction solution, the steel reinforcement in the conventional concrete structure is initially coated and protected against corrosion by the concrete alkalinity. However, for structures subjected to aggressive environmental conditions, such as marine structure, bridges and parking garages exposed to de-icing salts, combinations of moisture, temperature and chlorides reduce the concrete alkalinity, and result in the steel reinforcing corrosion. Fiber reinforced polymers (FRP), which is a composite material made of fiber embedded in a polymer resins, can be used as an alternative for the steel in the reinforced concrete structures, to avoid the structures' deterioration and loss of serviceability due to corrosion [ACI 440.1R-15]. Where the problem of the electromagnetic interference and steel corrosion can be avoided, as the FRP are nonmagnetic and noncorrosive materials. Moreover, FRP materials exhibit several advantages, such as high tensile strength, that make them suitable for the use as concrete structural reinforcement [Benmokrane and Ali, 2018; Manalo et al., 2020; Mohamed et al., 2020; Benmokrane et al., 2021].

2.2 FIBER REINFORCED POLYMER (FRP)

2.2.1 General

After the World War II in the 1940s, and during the Cold War, advancements in the aerospace and defense industry cause an increase in the fiber reinforced polymer use, where these industries had long recognised the advantages of the high strength and the light weight of these composite materials. Moreover, the need to provide year-round maintenance has increased in 1950s, due to the expansion of the highway systems. As also it became common to apply de-icing salts on highway bridges. Therefore, reinforcing steel in these structures becoming a major concern and requiring a high maintenance cost. Various solutions were investigated such as electrostatic-spray fusion-bonded coating, epoxy coating, galvanized coating, alloy steel bars, polymer-impregnated concrete, and glass-FRP (GFRP) reinforcing bars [ACI 544.7R-16].

Of these investigated solutions, epoxy-coated steel reinforcement showed to be the best alternative and was therefore implemented for the aggressive environmental conditions. FRP reinforcing bars

was not considered a viable option and not commercially used until the late 1970s. In the 1980s, the advantages of FRP reinforcement became better known and desired, specifically in seawall construction, substation reactor bases, airport runways and electronics laboratories [Brown and Bartholomew, 1996]. Furthermore, the detection of corrosion in the commonly used epoxy-coated reinforcing bars increased interest in alternative method of avoiding corrosion, and therefore FRP reinforcement began to be considered as a general solution to address corrosion problems in bridge decks and other structures [Benmokrane and Masmoudi, 1996].

2.2.2 History of use

Up to the mid-1990s, Japan had the most FRP reinforcement applications, with more than 100 demonstration and commercial projects. Fiber-reinforced polymer design provisions were included in the design and construction recommendations of the *Japanese Society of Civil Engineering* [Uomoto, 1997]. And according to [Ye et al., 2003], China became the largest user of composite reinforcement, in the 2000s, in construction applications that is span from bridge decks to underground works. In 1986, Germany was the first to use the FRP reinforcement application in Europe, with construction of prestressed FRP highway bridge [Meier, 1992]. And since the construction of this bridge in Europe, programmes have been implemented to increase investigating of using FRP reinforcement in Europe [Taerwe, 1997].

According to [Rizkalla, 1997], the Headingley Bridge in Canada was one of several projects included both CFRP and GFRP reinforcement, after Canadian civil engineers have developed provision for FRP reinforcement in the *Canadian Highway Bridge Design Code* [CAN/CSA S6-19]. The Floodway Bridge over the Red River in Winnipeg, MB, Canada, was completed in 2006, with all concrete elements above the girders reinforced with GFRP bars. The project consumed 310,000 Ib of GFRP reinforcing bar, making it the largest non-metallic-reinforced concrete bridge in the world. Moreover, several bridges have been built in Quebec using GFRP reinforcing bars in the decks, such as the Magog Bridge on Highway 55 North, the Cookshire-Eaton Bridge on Route 108, Wotton Bridge in Wotton and the Val-Alain Bridge on Highway 20 East [El-Salakawy and Benmokrane, 2003; El-Salakawy et al., 2003; El-Salakawy et al., 2005; Benmokrane et al., 2004; Benmokrane et al., 2007]. And according to [Mufti et al., 2007; 2011], these bridges have been in service for more than ten years, without any signs of deterioration of the GFRP reinforcement.

According to [Drouin et al., 2011], more than 200 bridges structures have been successfully constructed using GFRP reinforcing bars in Canada, which shows the remarkable increase in the use of GFRP. Moreover, GFRP bars have been used in other concrete structures applications in Canada, such as highway concrete pavement [Benmokrane et al., 2007], parking such as parking garages [Benmokrane et al., 2012], incinerators [Michaud et al., 2013], and water tanks [Benmokrane and Mohamed, 2014]. Moreover, [ACI 544.7R-16] has reported typical uses of FRP reinforcement in the United States. **Fig. 2.1** shows bridge deck construction applications using FRP reinforcement bars.

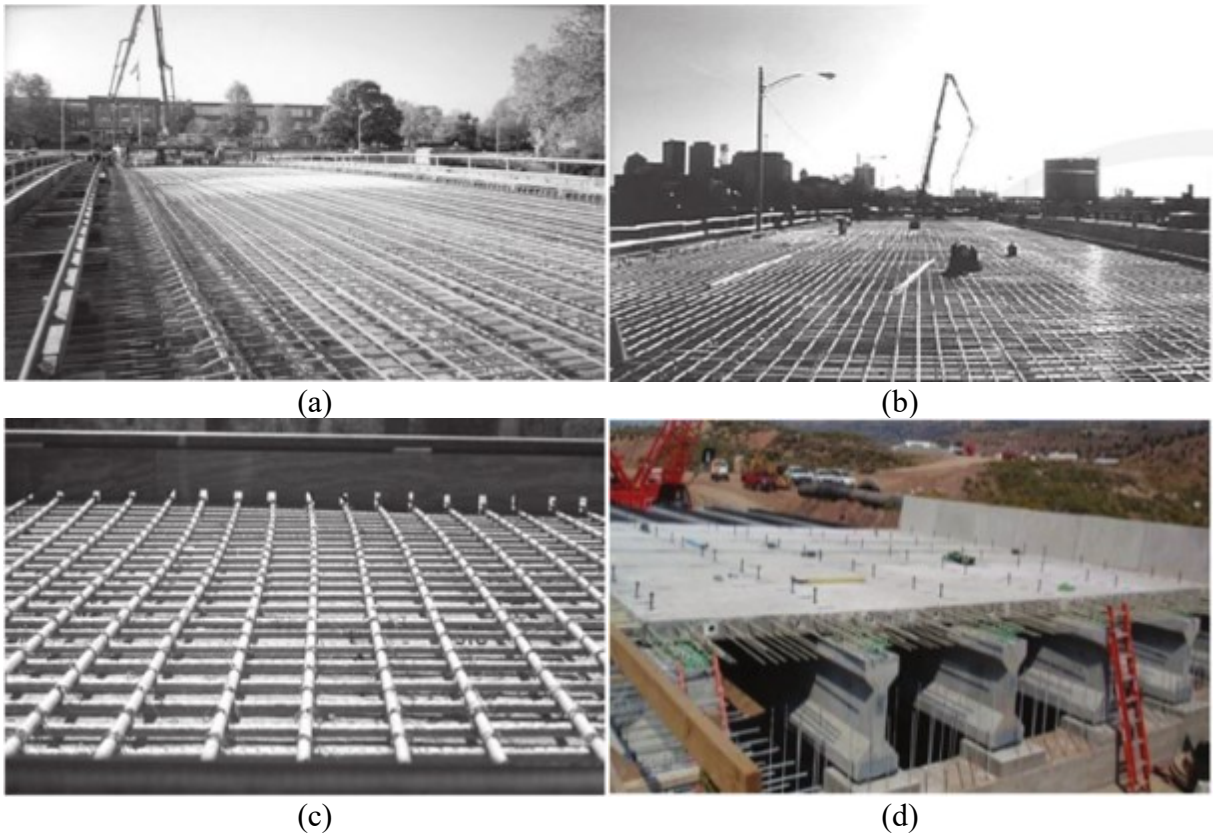

Fig. 2.1 Bridge deck construction using FRP reinforcement bars in (a) Lima, OH - Pierce Street Bridge; (b) Dayton, OH, Salem Avenue Bridge; (c) Sierrita de la Cruz Creek Bridge deck near Amarillo, TX; and (d) Emma Park Bridge deck panel [ACI 544.7R-16].

GFRP bar were used in the rail plinths for Airport Link, which connects the existing Earlington Heights Station to the new Miami Intermodal Center (MIC) in 2011 in Miami, FL, as shown in **Fig. 2.2(a)**. GFRP reinforcing bars is also found on larger and high-volume traffic bridges. In 2013, the I-635 bridge deck over State Avenue in Kansas City, KS was replaced with cast-in-place

GFRP reinforcing bar, shown in **Fig. 2.2(b)**. Moreover, tunnel construction, where GFRP reinforcement is used in the portion of the concrete wall to be excavated by the tunnel-boring machine, has become common in many major metropolitan areas of the world [ACI 544.7R-16].

(a) (b)

Fig. 2.2 GFRP bars used in (a) rail plinths for Airport Link in Miami Intermodal Center (MIC); and (b) I-635 Bridge over State Ave, Kansas City, KS [ACI 544.7R-16].

2.2.3 Materials characteristics

According to [ACI 544.7R-16], factors such as fiber volume, fiber type, resin type, fiber orientation, dimensional effects, and quality control during manufacturing all play a major role in defining the characteristics of an FRP bar. In the equipment sensitive to the electromagnetic fields, the nanomagnetic properties of FRP reinforcement are of principle importance, such as structures supporting magnetic resonance imaging (MRI) units. In addition, the FRP reinforcement corrosion resistance is a significant benefit for structures in the hard-condition environments, such as seawalls and marine structures or pavements and superstructures exposed to de-icing salts.

FRP reinforcement as a light weigh material, has a high tensile strength, significant elongation and exhibits linear stress-strain behavior of failure. Due to lack of experience in the FRP use, it is not recommended for moment frames or zones where moment redistribution is required. Moreover, the FRP reinforcement should be limited to structures that will significantly benefit from other properties such as the noncorrosive or nonconductive behavior of its materials [ACI 544.7R-16]. With all the advantages of the FRP over the steel reinforcement regarding sustainability, steel has a higher carbon footprint in the high temperatures required for production with compared to the

FRP reinforcement [Pearson et al., 2011]. Moreover, [Pearson et al., 2011] stated that recycling of FRP reinforcement is not easy or commonplace as recycling steel reinforcement. However, life cycle costs associated with FRP reinforcement structures where corrosion is a concern, are likely to be lower than those for steel reinforced structures, where FRP does not corrode. FRP reinforcement has a smaller environmental impact than steel reinforcement. According to [Bank, 1993; Bakis, 1993], FRP bars are anisotropic in nature and can be manufactured using different techniques such as pultrusion, braiding and weaving.

2.2.3.1 Physical properties

According to [ACI 544.7R-16], fiber reinforced polymer bars have a one-sixth to one-fourth the steel density, ranging from 1.25 to 1.60 g/cm^3. Where reduced weight lowers transportation costs and eases handling of the bars on site. **Table 2.1** lists the average density of different FRP bar types, with compared to the steel reinforcement bars.

Table 2.1 The average density of different FRP bar types, compared to the steel reinforcement bars [ACI 440.1R-15]

Type	Steel	Glass fiber reinforce polymers (GFRP)	Carbon fiber reinforced polymers (CFRP)	Aramid fiber reinforced polymers (AFRP)
Density (g/cm^3)	7.9	1.25 to 2.10	1.50 to 1.60	1.25 to 1.40

The coefficients of thermal expansion of FRP bars vary in the longitudinal and transverse directions, depending on the types of fiber, resin, and volume fraction of fiber. According to [Bank, 1993], the thermal expansion longitudinal coefficient of the FRP depend on the properties of the fibers whereas the transverse coefficient depends on the resin. **Table 2.2** lists the longitudinal and transverse coefficients of thermal expansion for typical FRP reinforcement, compared to the steel reinforcement bars. Under temperature increase, the splitting cracks within the concrete can be caused due to the difference between the FRP and the concrete thermal coefficients in the transverse direction, causing a failure of the concrete cover if the confining action of concrete is insufficient [Gentry and Husain, 1999; Bellakehal et al., 2013; Zaidi et al., 2013]. Experimental results show that a ratio of concrete cover thickness to bar diameter, c/d_b, greater than 1.6 is required to avoid cracking of concrete under high temperature up to 80° C [Masmoudi et al., 2005; Zaidi et al., 2013].

Table 2.2 Longitudinal and transverse coefficient of thermal expansion for typical FRP reinforcement, compared to the steel [ACI 440.1R-15]

Direction	CTE, $\times 10^{-6}$ / ° C				
	Steel	GFRP	CFRP	AFRP	Concrete
Longitudinal, αL	11.7	6.0 to 10.0	-9.0 to 0.0	-6 to -2	7.2 to 10.8
Transverse, αT	11.7	21.0 to 23.0	74.0 to 104.0	60.0 to 80.0	7.2 to 10.8

2.2.3.2 Mechanical properties

The tensile behavior of FRP bars characterized by a linearly elastic stress-strain relationship until failure. Where FRP bars exhibit no plastic behavior before rapture when loaded in tension. The FRP bars tensile strength and stiffness depend on several factors. According to [Wu, 1990], even in bars with the same diameter, appearance and constituents, the strength and stiffness vary in the FRP bars with the different fiber-volume fractions. Moreover, the rate of curing, the manufacturing process, and the manufacturing quality control also affect the mechanical characteristics of the FRP bars. **Table 2.3** lists the tensile properties for typical FRP reinforcement types, compared to the steel reinforcement. According to a study carried by [Faza and GangaRao, 1993], GFRP bars from three different manufacturers show tensile strength reduction of up to 40 percent as the diameter increases proportionally from 9.5 to 22.2 mm. Therefore, unlike steel reinforcement, the FRP bars unit tensile strength varies with the bar diameter. Test methods for determining the tensile strength and stiffness of FRP bars are available in [ASTM D7205/D7205M-21].

Table 2.3 Tensile properties for typical FRP reinforcement types, compared to the steel reinforcement [ACI 440.1R-15]

	Steel	GFRP	CFRP	AFRP
Nominal yield stress (MPa)	276 to 517	NA	NA	NA
Tensile strength (MPa)	483 to 1600	483 to 690	600 to 3690	1720 to 2540
Elastic modulus (GPa)	200	35 to 51	120 to 580	41 to 125
Yield strain (%)	0.14 to 0.25	NA	NA	NA
Rupture strain (%)	6 to 12	1.2 to 3.1	0.5 to 1.7	1.9 to 4.4

According to the [ACI 440.1R-15], standard test methods are not yet fully established to characterize the FRP bars compressive behavior. Compressive strengths of 55, 78, and 20 percent of the tensile strength have been reported for GFRP, CFRP, and AFRP, respectively [Mallick, 2007; Wu, 1990]. In general, compressive strengths are higher for bars with higher tensile

strengths, except in the case of AFRP, where the fibers exhibit nonlinear behavior in compression at a relatively low level of stress. The mode of failure for FRP bars subjected to longitudinal compression depends on the type of fiber, the fiber-volume fraction, and the type of resin. According to the [ACI 544.7R-16], the mode of failure for FRP bars subjected to longitudinal compression can include transverse tensile failure, fiber microbuckling, or shear failure. The compressive modulus of elasticity of FRP reinforcing bars performs to be smaller than its tensile modulus of elasticity. The compressive modulus of elasticity is approximately 80 percent, 85 percent and 100 percent of the tensile modulus of elasticity for GFRP, CFRP and CFRP, respectively [Mallick, 1988; Ehsani, 1993]. The most accepted explanation for the slightly lower values of modulus of elasticity in compression is the premature failure in the test resulting from end brooming and internal fiber microbuckling under compressive loading [ACI 544.7R-16].

According to [ACI 544.7R-16], the interlaminar shear strength in the FRP bar composites is governed by the relatively weak polymer matrix, and there is usually no reinforcement across layers. Therefore, FRP bar composites are relatively weak in interlaminar shear. The FRP shear resistance can be increased by orienting the fibers in and off-axis direction across the layers. For FRP bars, this can be accomplished by braiding or winding fibers transverse to the main fibers. Off-axis fibers can also be placed in the pultrusion process by introducing a continuous strand mat in the roving/mat creel.

2.3 TUNNELING

Tunnels are defined by the *American Association of State Highway and Transportation Officials*, t*echnical Committee for Tunnels (T-20)* [AASHTO, 2010], as “the covered passageways with vehicles or subways access that is limited to portals regardless of structure types and construction techniques”. Tunnel structures protect and preserve surface landscapes, cultural heritages, and historical buildings, resulting in having green and sustainable civil infrastructures. Moreover, tunnel structures significantly reduce traffic congestions, resulting in improved environmental quality parameters such as noise and air pollution [Hung et al., 2009].

2.3.1 General

For thousands of years, there have been many advancements in technology improving the safety, efficiency, and overall productivity of tunneling systems. Tunneling operations involve soil/rock

excavation, which therefore results in increasing the loosed native soil stress. Therefore, additional reinforcement using rock bolts, wire mesh or concrete lining, is required in the areas where cover is inadequate, or in low strength areas. Depending on the tunnel depth, length and location characteristics, different methods of tunneling are used. The commonly used form of tunneling is the drilling and blasting (D&B) revolutionised tunneling technology. The D&B process involves drilling several holes at the tunnel faces and filling them with explosives causing the rock to collapse. Then the exposed surface to be reinforced appropriately. Moreover, in shallow tunnels, such as in subway, railway and metro systems applications, cut-and cover tunneling method is the commonly used. The cut-and-cover process consists of excavating, constructing the tunnel, backfilling the excavated trench, and then reinstating the surface. Furthermore, the tunnel boring machine is an increasingly common method of tunneling.

2.3.2 Tunnel boring

A Tunnel Boring Machine (TBM), shown in the **Fig. 2.3**, also known as (mole), is a circular cross section machine used to excavate tunnels trough a anything from soft sand to hard rock strata. In unstable ground conditions, as the TBM advances, concrete tunnel segments in a from of lining system are placed for the purpose of increasing the ultimate strength capacity of the excavated area, during and after construction [Mashimo et al., 2002]. The most important advantage of TBM over drilling and blasting techniques, is limiting the disturbance to the surrounding ground for soft unstable ground conditions, as well as the disturbance for the local populations in the residential areas' applications. Although the overhead costs of the machineries used for the TBM machine is relatively high, TBM proved to be more economical solution for the modern long tunnels' applications compared to the D&B method, due to its ability to reduce the construction project time frame with high efficiency. Currently, the commonly used TBM machine for highly sophisticated operations is the double-shield machine, as this machine suitable in variety geological conditions. The double-shield machine runs efficiently in stable ground conditions, where the gripper pads provide forward thrust capability to allow for tunnel segment installation simultaneously during excavation. As well as in the fractured ground conditions, where the thrust is shifted to thrust cylinders to push off the concrete tunnel segments behind the machine. Unlike in the stable ground conditions, in the fractured ground conditions process, the excavation and the installation of the concrete segments are preformed independently.

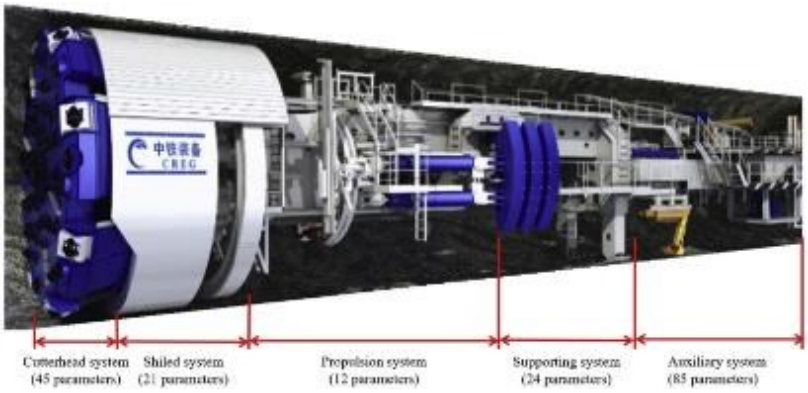

Fig. 2.3 Tunnel boring machine [Li et al., 2021].

2.3.3 Precast segmental tunnel linings

To reduce the formwork/unit cost of the tunnel linings construction, precast concrete tunnel lining (PCTL) segments can be produced in reusable molds, cured, then assembled inside the shield of the TBM to form full tunnel segmental rings. Where the cast beds are used in the precast operations can be reused with small maintenance if needed. According to [El Naggar and Hinchberger, 2008], using precast segments results in lowering the overall structure's stiffness compared to the cast in place liner or shotcrete, by having the benefit of being jointed. As the precast tunnel absorbs external forces by deforming, and hence is subjected to lower moments. Preparing and installing precast tunnel segments require very high level of quality control, due to the minimal allowable tolerance. Where the joint alignment may be compromised if a tunnel segment is out of line by only less than one inch, causing difficulty in assembling the segments. Therefore, to ensure high production quality, mock-up tests involve assembling a small section of couple rings usually performed in a controlled environment.

2.3.4 Tunnel lining segments full scale testing

Full-scale bending and point load tests on typical fiber-reinforced concrete projects such as Monte Lirio Tunnel [Caratelli et al., 2012; de Rivaz et al., 2012], Brenner Base Tunnel [Moccichino et al., 2010], and El Alto Tunnel [Barwart et al., 2013] were part of the design procedure and verification.

2.3.4.1 Bending testing

To verify the design and performance of the PCTL segments during the stripping, storage, transportation, and handling stages, and to verify the performance of the unsymmetrical earth pressure on the PCTL segments at the service stage, [Hilar and Beno, 2012] performed tunnel segments bending test, as shown in **Fig. 2.4**.

Fig. 2.4 Full-scale PCTL segments bending test [Hilar and Beno, 2012].

2.3.4.2 Point load testing

[Caratelli et al., 2012] simulated the tunnel boring machine (TBM) thrust jack forces on the segments during the excavation process by a full-scale point load test as shown in **Fig. 2.5**. Moreover, the full-scale point load test was performed to simulate the force transfer through a reduced cross section in longitudinal joints.

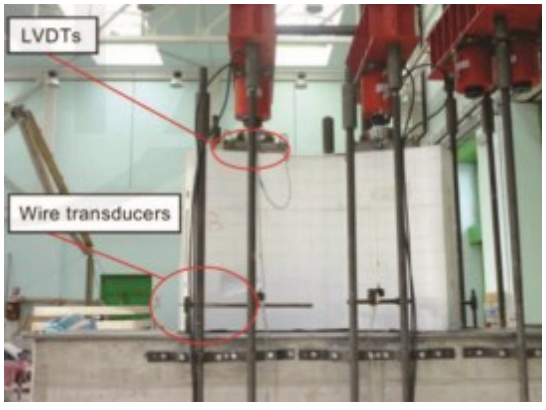

Fig. 2.5 Full-scale PCTL segments point loading test [Caratelli et al., 2012].

2.3.4.3 Cantilever load testing

The cantilever loading test is another full-scale test used to investigate the circumferential joint strength under misaligned jacking loads, as shown in **Fig. 2.6** [Poh et al., 2009].

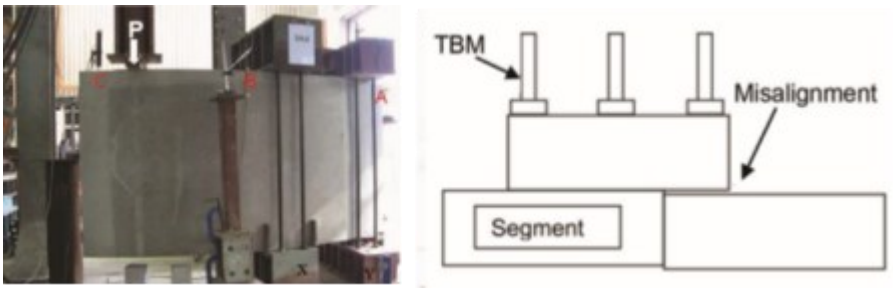

Fig. 2.6 Full-scale PCTL segments cantilever loading test [Poh et al., 2009].

2.3.4.4 Axial load testing

[Mashimo et al., 2002] tested concrete tunnel lining axial forces, bending moment, and combined action of axial loads and bending moments to simulate dominant effects, as shown in **Fig. 2.7**.

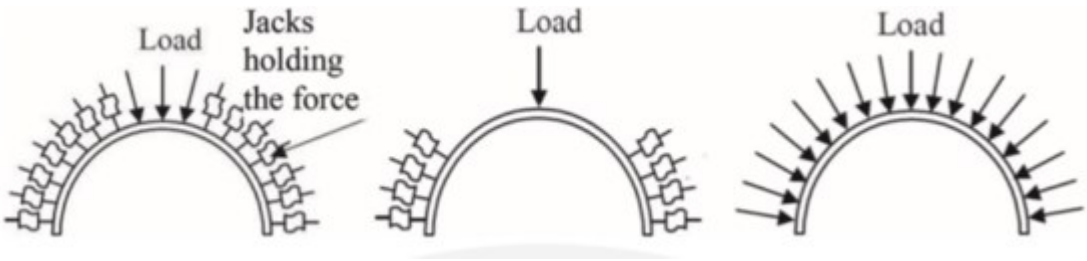

Fig. 2.7 Full-scale PCTL segments axial loading test [Mashimo et al., 2002].

2.3.5 Tunnel lining segments cyclic testing

[Abbas, 2014] studied the structural and durability performance of full-scale conventional reinforced concrete (RC) tunnel lining segments in comparison to steel fibre-reinforced concrete (SFRC). To evaluate the flexural behavior of the precast tunnel lining segments, the author applied Quasi-static compressive loading, shown in **Fig. 2.8**, in terms of percentage of maximum displacement achieved during the monotonic tests at the failure point. Two cycles of loading and unloading were conducted for 1.25%, 2.5%, 5%, and 10% of the maximum displacement. Subsequently, three cycles were applied for 20%, 40%, 60%, 80%, 100% of the maximum

displacement. The elasto-plastic behaviour of both the RC and the SFRC segments under cyclic load has been illustrated through the load-mid span displacement hysteresis curves.

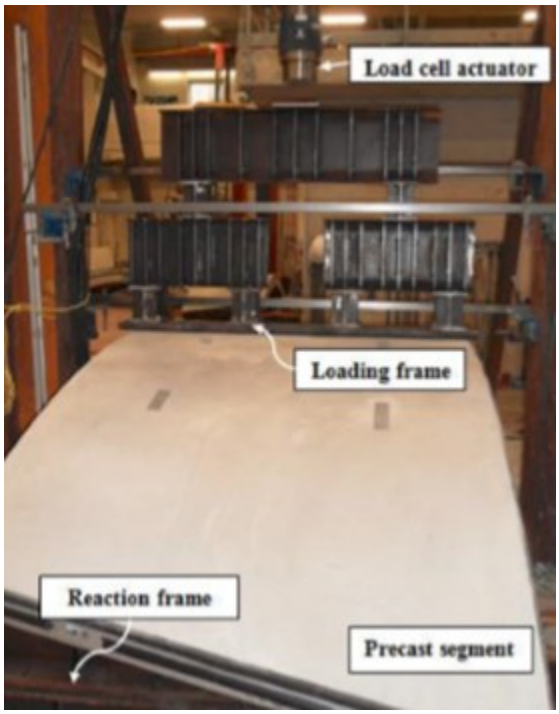

Fig. 2.8 Quasi-static cyclic flexural loading test of PCTL segments [Abbas, 2014].

Initially, a linear relationship between load and displacement was found before concrete cracking. At this stage, there was no evidence of stiffness degradation and residual deformations were very small, indicating that the segments were in the elastic range. As cracking initiated, the slope of the hysteresis curves changed as the load and displacement increased. Consistent with previous study [Kesner et al., 2003], due to the permanent deformations occurred in RC and SFRC segments, a parabolic unloading response was noticed after the linear elastic portion of unloading. It was also observed that the deformations in both segment types were larger during the initial cycling and then decreased to a constant growth at intermediate cycling. These deformations increased again more rapidly nearing failure point. Which also agrees with the results of [Karssan and Jirsa, 1969]. [Abbas, 2014] reported that for each loading amplitude and for both the RC and SFRC segments, little reduction in maximum load was observed in the subsequent cycles compared to that of the first cycle. Similar observation was reported by [Xue et al., 2008] in their cyclic experiments on fibre-reinforced concrete beams. [Abbas, 2014] also reported in his study that the slope of the hysteresis of RC segment changed rather abruptly compared to that of SFRC segments due to more

internal material damage in RC segments. The spalling of the concrete cover was observed in RC segments subjected to cyclic loads. On the other hand, SFRC segments did not exhibit severe spalling compared to that of the RC segments. Which can be attributed to better holding of the concrete matrix through the bridging action of steel fibres until pull-out or fracture of fibres. This reduction of concrete spalling in SFRC segments under cyclic loads could lead to lower rehabilitation costs after earthquake events [Hameed et al., 2009].

Moreover, [Abbas, 2014] reported that the bridging action of steel fibres tends to reduce the crack width in SFRC segments compared to that of cracks in RC segments. Similar finding was reported by other study [Moccichino et al., 2010]. The RC segment showed a sudden drop in its load carrying capacity after the peak/ultimate loading cycle and the segment failed into two pieces. Prior to cracking of the SFRC segment, the results showed that its compressive stresses are in the elastic range, leading to elastic unloading behaviour. After cracking, the loading and unloading cycles were no longer linear. At that point stresses were transferred to the steel fibres and the crack opening initiated. These cracks further opened along with the formation of new cracks as the tensile strain increased beyond the previous loading cycle. After reaching the peak load, a softening cyclic response is initiated. As damage progressed in the segment, the load carrying capacity dropped during each additional cyclic amplitude. This damage is a function of the interaction between the matrix and the steel fibres [Kesner et al., 2003]. The incorporation of steel fibres in SFRC segments reduces the strain magnitude thus restricting the propagation of micro and macro-cracks and leading to lower internal damage compared to that of the RC segment [Daniel and Loukili, 2002; Holschemacher and Muller, 2007]. Therefore, as fibre pull-out and de-bonding increased, the stresses carried by steel fibres increased with higher number of loading cycles until failure of the segment [Li and Leung, 1992].

2.4 ALTERNATIVE REINFORCEMENT FOR THE PCTL SEGMENTS

2.4.1 General

At the back of the tunnel-boring machine, in soft ground and weak rock tunnels constructions, precast concrete segments are used to support the tunnel bone. Combined tunnel segments, as part of a one-pass liner system, provide the ground support against the tunnel-boring machine. These tunnel segments are designed to resist both the ground/groundwater permanent loads, and the

production and construction temporary loads. With conventional reinforcing bar, a significant expanse of labor is needed to place the reinforcing bar and build the reinforcement cages. Therefore, to improve operating and placement of precast concrete segments practically, fiber-reinforced concrete (FRC) can be benefitted with the added value of decreasing job-site labor requirements [ACI 544.7R-16].

According to [di Prisco et al., 2009], the post-cracking behavior and the toughness can be considerably improved using the fiber reinforced concrete. Moreover, according to [Minelli et al., 2011; Tiberti et al., 2014], FRC has better crack distribution characteristics compared to the concrete reinforced with the conventional steel. Generally, FRC improves the durability over the structure's life, as it results in smaller crack widths compared to the conventional steel reinforced concrete.

[de Waal, 1999; Schnütgen, 2003] have stated in their studies, the beneficial effect of FRC in the presence of concentrated loads. During the tunnel-boring machine jacking process, the fiber reinforcement effectively resists the bursting and spalling stress. As the fibers disperse uniformly throughout the segment, including the area around the segment face. Furthermore, [di Prisco and Felicetti, 2004] showed that during segment handling and tunnel construction operations, the fiber in the concrete helps to mitigate against unintentional impact loads, by increasing the fatigue and impact resistance of the segments. During production, reinforcing bar is efficient for resisting localized stress in the concrete segment. However, the distributed stresses such as earth pressure loads and groundwater loads at final service stages, are better dealt with by fiber reinforcement. Therefore, tunnel segments can be manufactured using a hybrid system, which is a combination of conventional reinforcing bar and fiber reinforcement, to resist both the localized and the distributed stresses present in the tunnel linings [ACI 544.7R-16].

2.4.2 FRC tunnel segments design

FRC has been widely used as concrete reinforcement and can be used for PCTL segments using fundamental approaches recommended in the various international design guidelines, codes, and standards [ACI 544.7R-16]. The various international design guidelines, codes, and standard propose stress crack width or stress-strain constitutive laws of FRC as a linear post-cracking behavior (hardening or softening) or as a rigid perfectly plastic behavior based on bending test

results. Alternatively, an approach using nonlinear fracture mechanics can be adapted to analyze cracking phenomena [Hillerborg et al., 1976]. In [ACI 544.8R-15], there are models that can be adopted to obtain required constitutive laws for the calculation of axial force/bending moment interaction diagrams for use with FRC precast tunnel segments. Moreover, [ACI 544.8R-15] provides method that uses results of standard beam tests such as [ASTM C1609/C1609M-19a; BS EN 14651:2005] to determine post-crack residual tensile strength as one of the key design parameters for FRC tunnel segments. In addition to beam tests, panel or plate tests including square panels such as [*European Federation of Producers and Applicators of Specialist Products for Structures*, 1999] panel test and round panels such as [ASTM C1550-20] can be used as alternatives to evaluate tensile properties of FRC materials.

An experimental study on the possibility of replacing the traditional steel reinforced concrete precast tunnel segments with the FRC has been carried by [Caratelli et al., 2011], for the several advantages in terms of quality and cost reduction. Full-scale tunnel segments were tested under both flexural and tunnel boring machine thrust loading, in order to check the feasibility and the effectiveness of using FRC for the precast tunnel segments. Two types of tunnel segments were tested in this study. The first one was tunnel segments reinforced with ordinary concrete, with an average cubic compressive strength of 50MPa. The other type of segments tested was FRC segments without any traditional reinforcement, with an average cubic compressive strength of 75 MPa. The concrete matrix of the fiber reinforced material was opportunely designed for enhancing the performance of the adopted steel fibers, characterised by a diameter of 0.35 mm and a length of 30 mm and whose dosage was equal to about 40 kg/m3. The elements geometry considered in the research are shown in **Fig. 2.9**.

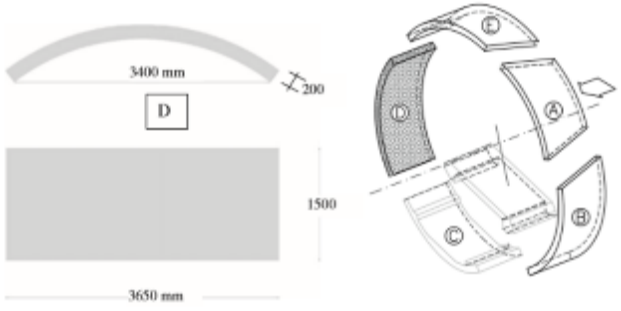

Fig. 2.9 Specimens geometry [Caratelli et al., 2011].

A reacting frame having a maximum bearing capacity equal to 4000 kN has been adopted for both the flexural and point load tests. For the flexural load testing, the tunnel segment is placed on hinge supports with a span of 2040 mm, as show in **Fig. 2.10**. The load was applied by means of a 1000 kN electromechanical jacket with a PID control. The tests were conducted up to the failure by using the jacked displacement as control signal.

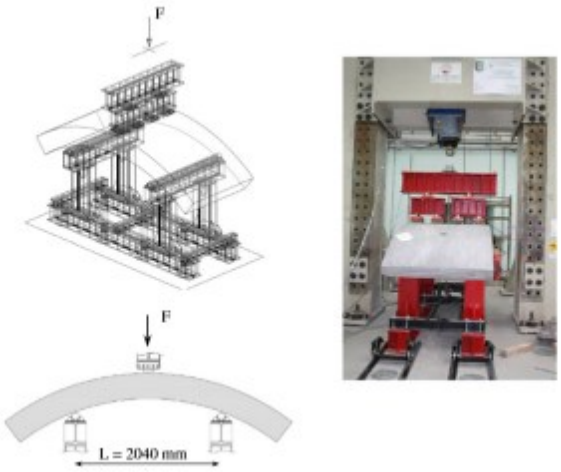

Fig. 2.10 Flexural loading test setup [Caratelli et al., 2011].

For the point load testing, a rigid plate with the same geometry of the actual shoe, was placed between jacked and segment, operating the same TBM loading of the situation on site, as shown in **Fig. 2.11**. Two LVDTs were placed in order to measure the splitting crack while three potentiometric wire traducers were adopted for measuring the displacement of the loading plate. The load was measured by means of a pressure sensor.

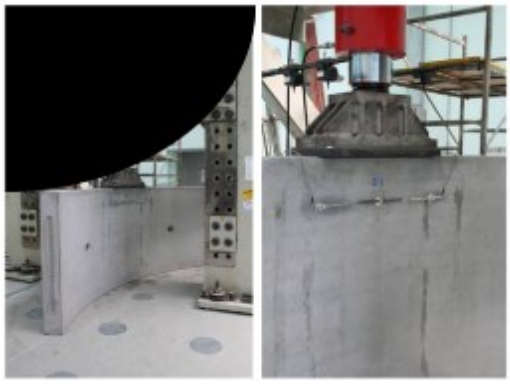

Fig. 2.11 Point loading test setup [Caratelli et al., 2011].

The experimental results of [Caratelli et al., 2011] showed that FRC tunnel segments exhibited a better cracking control behavior compared to the traditional reinforced concrete segments, where the load related to the first crack formation was higher and the cracks openings were reduced. Therefore, for this kind of structures, where the cracking limitations in the primary concern, the FRC tunnel segments can be successfully adopted.

2.4.3 GFRP reinforced PCTL segments

The flexural behavior of PCTL segments reinforced with the noncorrosive GFRP reinforcement bars as an alternative for the conventional steel reinforcement has been narrowly investigated in the literature [Caratelli et al., 2016; Spagnuolo et al., 2017; 2018; Hosseini et al., 2022]. Compared to the flexural behavior of the streel reinforced PCTL segments, it has been demonstrated that the GFRP reinforcement can be an effective alternative to the conventional steel reinforcement [Hosseini et al., 2022]. Moreover, it has been illustrated that the flexural behavior of both GFRP reinforced and conventionally steel reinforced PCTL segments are comparable. Despite the brittleness of the curvilinear-GFRP reinforcement, it has been moreover demonstrated that the GFRP reinforced PCTL segments exhibited adequate ductility compared to the conventionally steel reinforced PCTL segments [Caratelli et al., 2016]. In addition, the failure warning in the GFRP reinforced PCTL segments is ensured by the wide cracking generated by the high strain that the curvilinear-GFRP bars exhibited before failure [Spagnuolo et al., 2017].

Moreover, [Caratelli et al., 2017] suggested optimization for the GFRP reinforcement topologies for tunnel segments cages, in terms of cost-benefit analysis. Four full-scale types of GFRP cages typologies (ring reinforcement for both longitudinal and transverse, a combination of curvilinear bars interlined by means of lattice structures, wire net in extrados and intrados with “C” shaped stirrups reinforcement, and sand coated ring reinforcement for both longitudinal and transverse) have been tested under both bending and TBM thrust loading. For every reinforcement typology of the three typologies, one segment was subjected to bending and another specimen tested simulating the TBM thrust. The analysed metro tunnel in this study has an internal diameter and lining thickness of 5800 mm 300 mm, respectively. The lining precast segments have a width of 1420 mm as shown in **Fig. 2.12**.

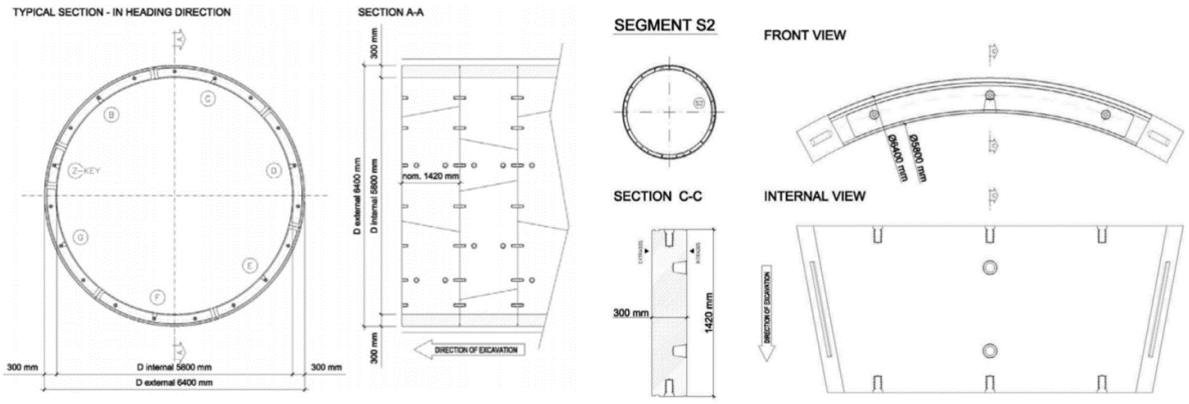

Fig. 2.12 Specimen geometry [Caratelli et al., 2017].

In this study, two testing setups were carried out, the bending test setup to represent the transient load conditions, and the point load setup to simulate the TBM thrust. The bending test setup, shown in the **Fig. 2.13**, aimed to verify the segment performance under prevalent bending moment action, it also representative of the provisional loading stages as demoulding, storing, and handing. The segment in this setup was placed on roller support with a span of 2 m. Moreover, **Fig. 2.14** shows the point load setup. The point loads, simulating the TBM thrust, have been applied on the segment, adopting the actual pad configuration and geometry used by the TBM machine.

Fig. 2.13 Flexural loading test setup [Caratelli et al., 2017].

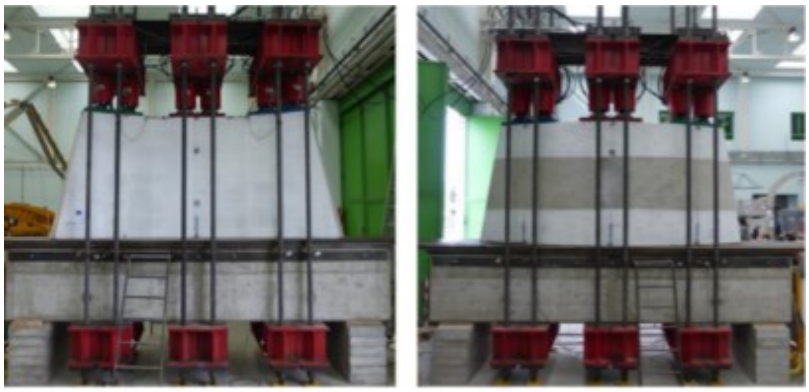

Fig. 2.14 Point loading test setup [Caratelli et al., 2017].

Compared to the structural behavior of a traditional steel reinforcement segments, the results of [Caratelli et al., 2017] showed the effectiveness of the proposed GFRP reinforcement. [Caratelli et al., 2017] have also concluded that with reference to the structural performance under both flexural and TBM thrust loading, the closed ring reinforcement was the best cost-benefit solution.

2.4.3.1 GFRP reinforced concrete flexural strength

The flexural design of FRP-reinforced concrete members is analogous to the design of steel-reinforced concrete members. Experimental data on concrete members reinforced with FRP bars show that the flexural capacity can be calculated based on assumptions similar to those made for members reinforced with steel bars [Ruan et al., 2020]. The flexural strength of the FRP reinforced cross section is calculated based on the following assumptions:

- Strain in the concrete and the FRP reinforcement is proportional to the distance from the neutral axis (a plane section before loading remains plane after loading).
- The tensile strength of the concrete is ignored.
- The tensile behavior of the FRP reinforcement is linearly elastic until failure.
- A perfect bond exists between the concrete and FRP reinforcement.
- The maximum usable compressive strain in the concrete is assumed to be 0.003 in [ACI 440.R-15] and 0.0035 in [CAN/CSA S806-12(R2017)], *fib* [TG-9.3, 2007], [CNR-DT 203, 2006] and [AFGC, 2021].

The FRP reinforcement ratio is computed according to [ACI 440.1R-15] with **Equation 2.1**, and the balanced FRP reinforcement ratio can be computed with **Equation 2.2**.

$$\rho_f = A_f / bd \tag{2.1}$$

Where, A_f, is the area of the fiber-reinforced polymer (FRP) reinforcement; b is the width of the rectangular cross section; and d is the distance from the extreme compression fiber to the centroid of the tension reinforcement

$$\rho_{fb} = 0.85\beta_1 \frac{f_c^{'}}{f_{fu}} \frac{E_f \varepsilon_{cu}}{E_f \varepsilon_{cu} + f_{fu}} \tag{2.2}$$

where $f_c^{'}$ is the specified compressive strength of the concrete; f_{fu} is the design tensile strength of the FRP, defined as the guaranteed tensile strength multiplied by the environmental reduction factor; E_f is the design or guaranteed modulus of elasticity of FRP, defined as the mean modulus of a sample from the test specimens; and ε_{cu} is the ultimate strain in the concrete.

According to [ACI 440.1R-15], when $\rho_f > \rho_{fb}$, the controlling limit state is crushing of the concrete, and the stress distribution in the concrete can be approximated with the ACI rectangular stress block. Based on the equilibrium of forces and strain compatibility, the following can be derived.

$$M_n = A_f f_f \left(d - \left(a/2\right)\right) \tag{2.3}$$

$$a = \frac{A_f f_f}{0.85 f_c^{'} b} \tag{2.4}$$

$$f_f = E_f \varepsilon_{cu} \frac{\beta_1 d - a}{a} \tag{2.5}$$

In [ACI 440.1R-15], the nominal flexural strength is determined from **Equations 2.3 – 2.5**. The FRP reinforcement is linearly elastic at the concrete crushing limit state, so the stress level in the FRP can be found from **Equation 2.5**, as it is less than f_{fu}. Alternatively, the nominal flexural strength at a section can be expressed, according to [ACI 440.1R-15], in terms of the FRP reinforcement ratio, as given in **Equation 2.6**.

$$M_n = \rho_f f_f \left(1 - 0.59 \frac{\rho_f f_f}{f_c'}\right) bd^2 \qquad (2.6)$$

According to [CAN/CSA S806-12 (R2017)], the concrete crushing mode of failure occurs in the FRP-reinforced section when the extreme compressive strain in the concrete reaches its ultimate strain provided that

$$(c/d) \geq 7/(7 + 2000\varepsilon_{Fu}) \qquad (2.7)$$

where c is the distance from the extreme compression fiber to the neutral axis; d is the distance from the extreme compression fiber to the centroid of the longitudinal tension force; and ε_{Fu} is the ultimate strain in the FRP reinforcement.

When c/d satisfies the requirements of **Equation 2.7**, the nominal flexural strength in a section can be determined, similar to as in [ACI 440.1R-15], based on the equilibrium of forces and strain compatibility.

According to *fib* [TG-9.3, 2007], the ultimate flexural moment resistance of an FRP RC section can be evaluated by adopting the framework of *Eurocode-2* [CEN, 2004]. Similar to as in [ACI 440.1R-15], when $\rho_f > \rho_{fb}$, flexural failure is expected to occur due to concrete crushing, and the ultimate moment resistance can be calculated based on the equilibrium of forces and strain compatibility with **Equation 2.8**.

$$M_u = \eta f_{cd} bd^2 (\lambda\zeta)(1 - (\lambda\zeta/2)) \qquad (2.8)$$

where η is a factor defining the effective strength of the concrete; f_{cd} is the design value of the concrete compressive strength; b is the width of the rectangular cross section; d is the effective depth of a cross section; λ is a factor defining the effective height of the compression zone; and ζ is a reduction factor coefficient.

As in *fib* [TG-9.3, 2007], the ultimate flexural moment resistance of FRP RC section can be evaluated according to [AFGC, 2021] by adopting the framework of *Eurocode-2* [CEN, 2004]. According to [AFGC, 2021], the FRP reinforcement ratio can be computed with **Equation 2.9**, and the balanced FRP reinforcement ratio can be computed with **Equation 2.10**.

$$\rho_{PRF} = A_{PRF} / A_{c,red} \tag{2.9}$$

where A_{PRF} is the area of the longitudinal reinforcement composite bars; and $A_{c,red}$ is the reduced area of the concrete section.

$$\rho_{PRF,b} = \frac{\eta.f_{cd}.\lambda.x_u}{\varepsilon_{PRF,u,d}.E_{PRF}.d} = \frac{\eta.f_{cd}.\lambda}{f_{PRF.d}} = \frac{\varepsilon_{cu2}}{\varepsilon_{PRF,u,d} + \varepsilon_{cu2}} \tag{2.10}$$

where η is a factor defining the effective strength of the concrete; f_{cd} is the design value of the concrete compressive strength; λ is a factor defining the effective height of the compression zone; x_u is the position of the neutral axis corresponding to the concrete balanced section; $\varepsilon_{PRF,u,d}$ is the limit strain of the FRP reinforcement; E_{PRF} is the FRP modulus of elasticity; d is the effective depth of a cross section; $f_{PRF.d}$ is the design FRP stress; and ε_{cu2} is the ultimate concrete strain.

Similar to as in *fib* [TG-9.3, 2007], when $\rho_f > \rho_{fb}$, flexural failure is expected to occur due to concrete crushing, and the ultimate moment resistance, M_{Rd}, in [AFGC, 2021], can be calculated, based on the equilibrium of forces and strain compatibility, with **Equation 2.11**.

$$M_{Rd} = A_{PRF}.E_{PRF}.\varepsilon_{PRF}.\left(d - \frac{\lambda x}{2}\right) = \lambda.x.\eta.f_{cd}.b.\left(d - \frac{\lambda x}{2}\right) \tag{2.11}$$

where A_{PRF} is the area of the longitudinal reinforcement composite bars; E_{PRF} is the FRP modulus of elasticity; ε_{PRF} is the strain in the FRP reinforcement; d is the effective depth of a cross section; λ is a factor defining the effective height of the compression zone; x is the position of the neutral axis; and f_{cd} is the design value of the concrete compressive strength.

[CNR-DT 203, 2006] assumes that flexural failure takes place when one of the following conditions is met:

- The maximum concrete compressive strain, as defined by the current building code, is reached.

- The maximum FRP tensile strain ε_{fd} is reached. This value is computed from the characteristic tensile strength ε_{fk} with **Equation 2.12**.

$$\varepsilon_{fd} = 0.9\eta_a \left(\varepsilon_{fk} / \gamma_f \right) \tag{2.12}$$

where η_a is an environmental conversion factor and γ_f is a material partial factor.

For both failure modes, the nominal flexural strength in a section can be determined based on the equilibrium of forces and strain compatibility.

2.4.3.2 GFRP reinforced concrete shear strength

The shear design of FRP-reinforced concrete is similar to that of steel-reinforced concrete members. The different mechanical properties of FRP bars, however, affect shear strength and should be considered. GFRP bars have a relatively low modulus of elasticity compared to steel, low transverse shear resistance, and high tensile strength with no yielding point. In addition, the tensile strength of the bent portion of an FRP bar is significantly lower than that of the straight portion.

The concrete shear capacity V_c of flexural members using FRP as the main reinforcement can be evaluated according to [ACI 440.1R-15] based on **Equation 2.13**.

$$V_c = \frac{2}{5}\sqrt{f_c'} b_w (kd) \tag{2.13}$$

where b_w is the width of the web; k is the ratio of the neutral-axis depth to the reinforcement depth; and d is the distance from the extreme compression fiber to the centroid of the tension reinforcement.

In the [CAN/CSA S806-12 (R2017)], the concrete shear capacity V_c for sections having an effective depth not exceeding 300 mm and with no axial load action on them, can be calculated using **Equation 2.14**.

$$V_c = 0.05\lambda\phi_c k_m k_r \left(f_c' \right)^{\frac{1}{3}} b_w d_v \tag{2.14}$$

where λ is a factor to account the concrete density; ϕ_c is the resistance factor for concrete; k_m is a coefficient taking into account the effect of moment in the section on the shear strength; k_r is coefficient taking into account the effect of reinforcement rigidity on its shear strength; $f_c^{'}$ is the specified concrete compressive strength; b_w is the minimum effective web width; and d_v is the effective shear depth.

According to [CAN/CSA S806-12 (R2017)], however, V_c shall not be taken as greater than $0.22\phi_c\sqrt{f_c^{'}}b_w d_v$ or less than $0.11\phi_c\sqrt{f_c^{'}}b_w d_v$.

fib [TG-9.3, 2007] presents and discusses various shear design recommendations to allow for the use of FRP reinforcement for the various design specifications available. Moreover, the modification, in **Equation 2.15**, has been proposed for the ACI shear equation to compensate for the unnecessary conservative shear prediction.

$$V_{c,proposed} = V_{c,ACI}\left(\frac{E_{FRP}}{E_s}\phi_s\right)^{1/3} \tag{2.15}$$

where $\phi_s = \varepsilon_f / \varepsilon_y$ represents the ratio between the maximum strain allowed in the FRP reinforcement ε_f and the yield strain of the steel ε_y.

In the [AFGC, 2021], the concrete shear capacity $V_{Rd,c}$ of flexural members with FRP as the main reinforcement is determined according to the *Eurocode-2* [CEN, 2004] equation, as shown in **Equation 2.16**.

$$V_{Rd,PFR} = C_{Rd,c}.k.\left(100\frac{E_{PRF}}{E_S}.\frac{A_{PFR}}{b_w d}f_{ck}\right)^{1/3} b_w d \tag{2.16}$$

where $C_{Rd,c} = 0.18/\gamma_c$; $k = \min\left\{2.0; 1+\sqrt{\frac{200}{d}}\right\}$; E_{PRF} is the FRP modulus of elasticity; E_S is the steel modulus of elasticity; A_{PRF} is the area of the longitudinal reinforcement composite bars; b_w is the width of the web; d is the distance from the extreme compression fiber to the centroid of the tension reinforcement; and f_{ck} is the concrete compressive strength.

In [CNR-TD 203, 2006], the concrete shear capacity $V_{Rd,ct}$ of flexural members with FRP as the main reinforcement can be evaluated with **Equation 2.17**.

$$V_{Rd,ct} = 1.3\left(\frac{E_f}{E_s}\right)^{1/2}.\tau_{Rd}.k.\left(1.2+40\rho_1\right).b.d \qquad (2.17)$$

where E_f and E_s are the Young's modulus of elasticity of the FRP and steel bars; τ_{Rd} is the design shear stress; k is a coefficient to be set as equal to 1 for members if more than 50% of the bottom reinforcement is interrupted and $\left(1.6-d\right)\geq 1$ if that is not the case; ρ_1 is the FRP reinforcement ratio; b is the width of rectangular cross section; and d is the effective depth of a cross section.

CHAPTER 3 EXPERIMENTAL RESEARCH PROGRAM

3.1 GENERAL

The design of the precast concrete tunnel lining (PCTL) segments reinforced with FRP bars is not defined or discussed in the current design provisions. The strength and behavior of such members reinforced with FRP bars is one area in which limited research results are available for implementing this noncorroding composite reinforcement. Therefore, a comprehensive research program was carried out in the Department of Civil Engineering at the University of Sherbrooke to improve current practices and develop more efficient design and construction approaches for using curvilinear GFRP bars and stirrups in precast concrete tunnel lining segments. Full-scale GFRP-reinforced PCTL segments are tested under different loading conditions—static flexural loading [Hosseini et al., 2022]; quasi-static cyclic flexural loading **(Current work)**; and punching shear and settlement—to investigate different variables and design parameters. This research program presents the structural behavior of full-scale GFRP-reinforced PCTL segments under quasi-static cyclic flexural loading, according to [ACI 374.2R-13]. This chapter presents the details of the experimental research program carried out in this research work. The segments' details are discussed in section 3.2. Material properties and details of construction process are highlighted in sections 3.3 and 3.4. The test setup and the instrumentation are discussed in sections 3.5 and 3.6. Finally, the simulated quasi-static cyclic flexural loading application and the investigated quasi-static cyclic flexural indexes are defined in sections 3.7 and 3.8.

3.2 TEST SEGMENTS

Given the lack of experimental and analytical research on the cyclic behavior of the GFRP reinforced PCTL segments, it was decided to conduct a series of experiments to investigate the behavior of the GFRP reinforced PCTL segments under quasi-static cyclic flexural loading. A total of twelve full-scale reinforced PCTL segments, including one conventional steel reinforced precast normal-strength concrete tunnel segment, five GFRP reinforced precast normal-strength concrete tunnel segments, three GFRP reinforced precast high-strength concrete tunnel segments, and three GFRP reinforced precast fiber-reinforced concrete tunnel segments, were designed, fabricated, and tested under quasi-static cyclic flexural loading. The segments were designed with total length of 3100 mm and a width of 1500 mm. The segments were designed with a thickness of 250 mm. The

clear cover was kept constant at 40 mm for all the test segments. The inner and outer radii of the nine PCTL segments were designed to be 3250 mm and 3500 mm, respectively. In line with the practicality, the edges of the segments were skewed an both edges. According to [ACI 533.5R-20], the PCTL segments with the skewed edges in the rhomboidal or parallelogrammical-trapezoidal systems is the most common used system because of preventing crucifix joints and improved sealing performance, continuous ring build from bottom to top, and compatibility with dowel connection system. Moreover, the skewed edges of the PCTL segments provide major advantages in avoiding early rubbing of the gaskets during segment insertion in the ring assembly phase and facilitating the use of fast connecting dowels in circumferential joints [ACI 533.5R-20].

Table 3.1 Test matrix and segment details

Specimen ID	Reinforcement type	Concrete type	Longitudinal reinforcement	Transverse reinforcement	Transverse reinforcement configuration
7S15	Steel	NSC	7 15M bars	10M bars spaced at 200 mm	Closed ties
7G15	GFRP	NSC	7 No. 5 bars	No. 4 bars spaced at 200 mm	Closed ties
13G15	GFRP	NSC	13 No. 5 bars	No. 4 bars spaced at 200 mm	Closed ties
7G20	GFRP	NSC	7 No. 6 bars	No. 4 bars spaced at 200 mm	Closed ties
13G20	GFRP	NSC	13 No. 6 bars	No. 4 bars spaced at 200 mm	Closed ties
7G15-U	GFRP	NSC	7 No. 5 bars	No. 4 bars spaced at 200 mm	Double U-shaped ties
7G15-H	GFRP	HSC	7 No. 5 bars	No. 4 bars spaced at 200 mm	Closed ties
13G15-H	GFRP	HSC	13 No. 5 bars	No. 4 bars spaced at 200 mm	Closed ties
7G15-U-H	GFRP	HSC	7 No. 5 bars	No. 4 bars spaced at 200 mm	Double U-shaped ties
7G15-FRC	GFRP	FRC	7 No. 5 bars	No. 4 bars spaced at 200 mm	Closed ties
13G15-FRC	GFRP	FRC	13 No. 5 bars	No. 4 bars spaced at 200 mm	Closed ties
13G15-U-FRC	GFRP	FRC	7 No. 5 bars	No. 4 bars spaced at 200 mm	Double U-shaped ties

Table 3.1 lists the test matrix and reinforcement details of the tested segments. The test parameters investigated in this experimental work were the reinforcement type (conventional steel and GFRP), the concrete type (normal-strength concrete (NSC), high-strength concrete (HSC), and fiber-reinforced concrete (FRC)), the longitudinal reinforcement ratio, and the configuration of the transverse GFRP ties. The segments were designed in accordance with [ACI 440.1R-15] and

[CAN/CSA S806-12 (R2017)]. The longitudinal reinforcement ratios of 0.5%, 0.9% and 1.2% were chosen as the minimum reinforcement ratio for concrete crushing controlled by flexural failure, an intermediate reinforcement ratio, and the maximum reinforcement ratio practically possible. **Fig. 3.1** shows the reinforcement details of the tested segments.

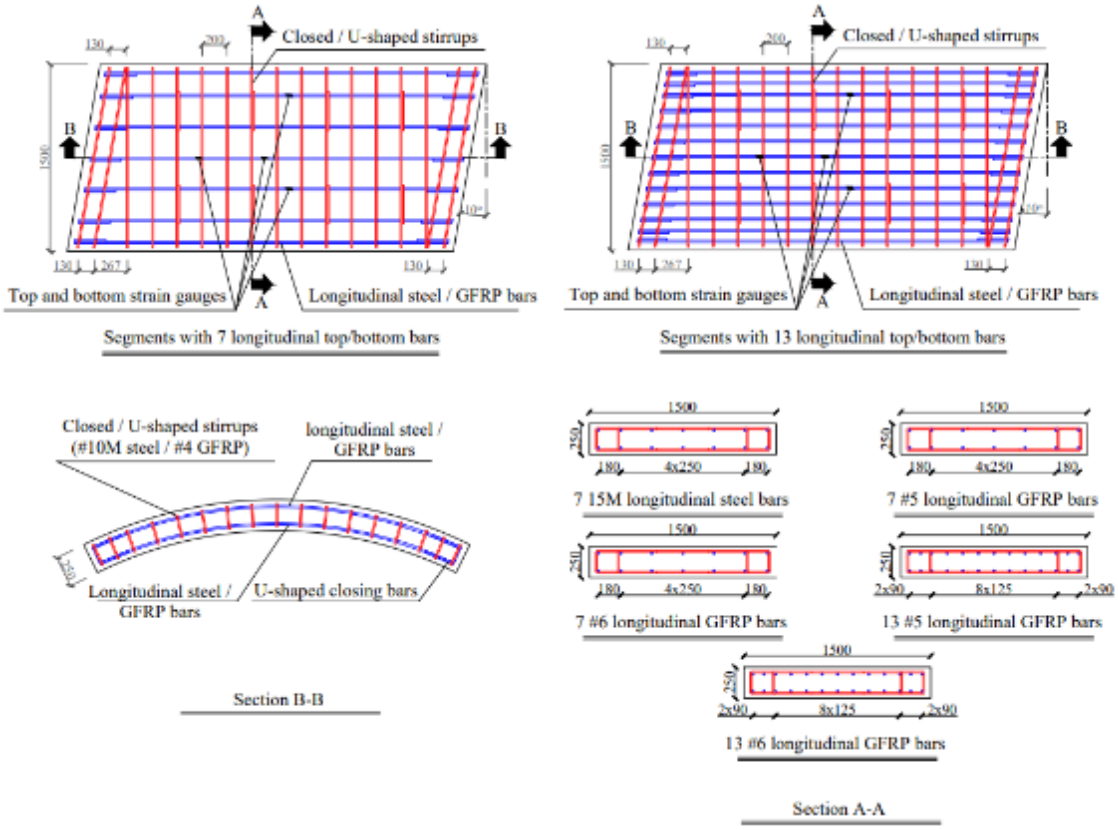

Fig. 3.1 Reinforcement details for the test specimens. (Note: all dimensions in mm)

3.3 MATERIAL PROPERTIES

3.3.1 Concrete

For the test segments, the targeted compressive strength was 40 MPa for the normal-strength concrete (NSC) and the fiber-reinforced concrete and 80 MPa for the high-strength concrete (HSC) segments. Half-inch (13 mm) micro-synthetic polypropylene fibers were added to the concrete mix for the FRC segments. **Table 3.2** gives the concrete mix designs used for test segments. **Table 3.3** presents the actual concrete strength based on the average test results of 100 x 200 mm concrete cylinders tested on the first day of segment testing.

Table 3.2 Concrete mix design

Concrete type	Cement (kg/m^3)	Sand (kg/m^3)	Limestone (kg/m^3)	Superplasticizer (mL/m^3)	Air entrainment (mL/m^3)	Water (L/m^3)	Fiber (kg/m^3)
NSC	450	615	1015	4500	140	170	-
HSC	475	778	800	7000	170	170	-
FRC	450	615	1015	4500	140	170	3.51

Moreover, the average tested results of the 100 x 100 x 500 mm concrete prism samples, taken from each precast FRC tunnel lining segment, were used to determine the tension behavior of the FRC. The prism samples were tested under four-point bending load in accordance with [ASTM C1609/C1609M-19a]. **Table 3.3** lists the peak load $\left(P_P\right)$, the residual load at the net deflection of L/600 $\left(P_{600}^D\right)$, and the residual load at the net deflection of L/150 $\left(P_{150}^D\right)$, for the precast FRC tunnel lining segments. The peak strength $\left(f_P\right)$, the residual strength at the net deflection of L/600$\left(f_{600}^D\right)$ and the residual strength at the net deflection of L/150 $\left(f_{150}^D\right)$ were determined with **Equation 3.1**, as shown in **Table 3.3**.

$$f = \frac{PL}{bd^2} \tag{3.1}$$

where L is length of the test span of the FRC prism samples; b is the average width of the prism sample; and d is the average depth of the prism sample.

Table 3.3 Concrete properties from the concrete cylinders and concrete prisms testing results

Specimen ID	Concrete type	Concrete compressive strength (MPa)	P_P (kN)	P_{600}^D (kN)	P_{150}^D (kN)	f_P (MPa)	f_{600}^D (MPa)	f_{150}^D (MPa)
7S15	NSC	53	-	-	-	-	-	-
7G15	NSC	52	-	-	-	-	-	-
13G15	NSC	52	-	-	-	-	-	-
7G20	NSC	47	-	-	-	-	-	-
13G20	NSC	50	-	-	-	-	-	-
7G15-U	NSC	50	-	-	-	-	-	-
7G15-H	HSC	83	-	-	-	-	-	-
13G15-H	HSC	80	-	-	-	-	-	-
7G15-U-H	HSC	81	-	-	-	-	-	-
7G15-FRC	FRC	37	12.3	5.4	4.4	3.69	1.62	1.32
13G15-FRC	FRC	37	12.1	5.0	3.9	3.63	1.50	1.17
7G15-U-FRC	FRC	37	12.1	5.2	4.1	3.63	1.56	1.23

3.3.2 Reinforcement bars

Table 3.4 provides the mechanical properties of the GFRP and steel bars used to reinforce the PCTL segments in this study. The GFRP bars were manufactured by pultruding boron-free glass fibers impregnated in a thermosetting vinyl-ester resin. The ultimate tensile strength f_{fu} and modulus of elasticity E_f of the GFRP bars were determined according to [ASTM D7205/D7205M-21]. The GFRP bars had a sand-coated surface to enhance bonding and force transfer between the bars and concrete. Number 6 (20 mm), #5 (15 mm), and #4 (13 mm) GFRP bars were used for both longitudinal and transverse reinforcement in the segments. Moreover, #6 (20 mm) and #5 (15 mm) closed U-shaped GFRP bars were used as anchorage for the longitudinal reinforcement bars. For the control steel reinforced segment, deformed 15M (16 mm) steel bars were used as longitudinal reinforcement and deformed 10M (11 mm) steel bars as transverse reinforcement. Deformed 15M (16 mm) U-shaped steel bars were used to anchor the longitudinal reinforcement bars.

Table 3.4 Mechanical properties of the reinforcement bars

Reinforcement type	Bar size	Bar diameter (mm)	Nominal cross-sectional area (mm^2)	Modulus of elasticity (GPa)	Tensile strength (MPa)	Tensile strain (%)
Curvilinear-GFRP bars	#5	15.0	199	55.1	1115	2.0
	#6	20.0	284	52.9	1068	2.0
U-shaped GFRP bars	#5	15.0	199	53.5	1283	2.4
	#6	20.0	284	53.2	1131	2.1
GFRP ties (Closed / double U-shaped)	#4	13.0	129	55.6	1248	2.2
Steel bars	10 M	11.3	100	200.0	480[a]	0.24[b]
	15 M	16.0	200	200.0	460[a]	0.23[b]

[a] The yield strength of the steel bars.
[b] The yield strain of the steel bars.

3.4 SEGMENTS FABRICATION

All the PCTL segments were cast at the SYM-TECH precast concrete facility in Saint-Hyacinthe, Quebec, Canada. The GFRP reinforcement cages, for the various details and configurations, were assembled in the University of Sherbrooke laboratory, as shown in **Figs. 3.2(a) and (b)**, and transported to the SYM-TECH precast concrete for casting. The specimens were cast in very stiff wooden forms prepared at the precast plant, as shown in **Fig. 3.2(c)**. **Figs. 3.2(d), (e), and (f)** show

the PCTL segments cast in the precast plant, segment storage, and segment transportation from the precast plant to the laboratory, respectively.

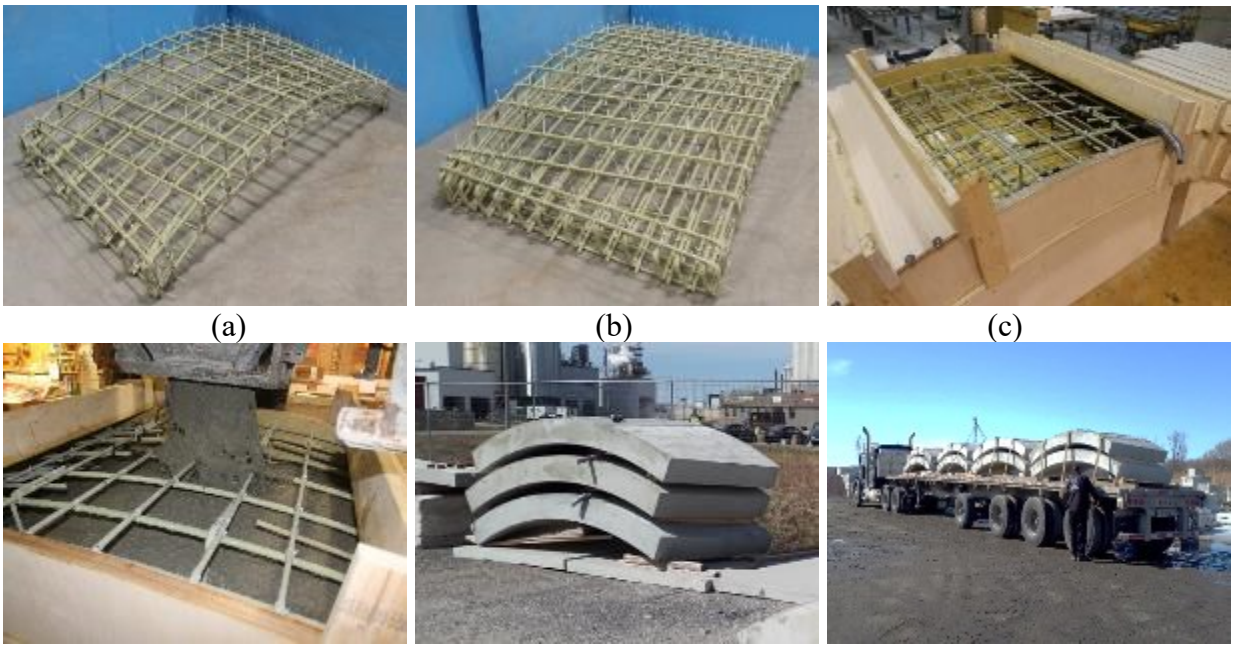

(a) (b) (c)

(d) (e) (f)

Fig. 3.2 Overview: (a) assembled GFRP cages for segments with 7 top/bottom GFRP bars; (b) assembled GFRP cages for segments with 13 top/bottom GFRP bars; (c) wooden formwork; (d) concrete casting; (e) segment storage; and (f) transportation from SYM-TECH to the laboratory.

3.5 TEST SETUP AND INSTRUMENTATION

The segments were loaded under three-point bending at a displacement-controlled rate of 0.8 mm/min in the University of Sherbrooke's CFI structural laboratory using an 11,000 kN capacity MTS universal testing machine attached to a spreader beam, as shown in **Fig. 3.3.** The span for the test segments was 2400 mm. While the skewed edges system was a key parameter to investigate in other phases of the project, such as the thrust jacking forces from the TBM machine on the PCTL segments, it is worth mentioning that under the quasi-static cyclic flexural loading, the skewed edges effect of the segments was avoided, in which the segments were supported over straight and parallel support lines **(Fig. 3.3).** Furthermore, to measure segment deflection at the mid- and quarter-span, five different linear potentiometers (LPOTs) were placed **(Fig. 3.3)**. Moreover, to measure the strain at mid- and quarter-span of the PCTL segments, 10 mm and

60 mm electrical resistance strain gauges were installed on the reinforcing bars and attached to the concrete surface, respectively **(Fig. 3.1)**.

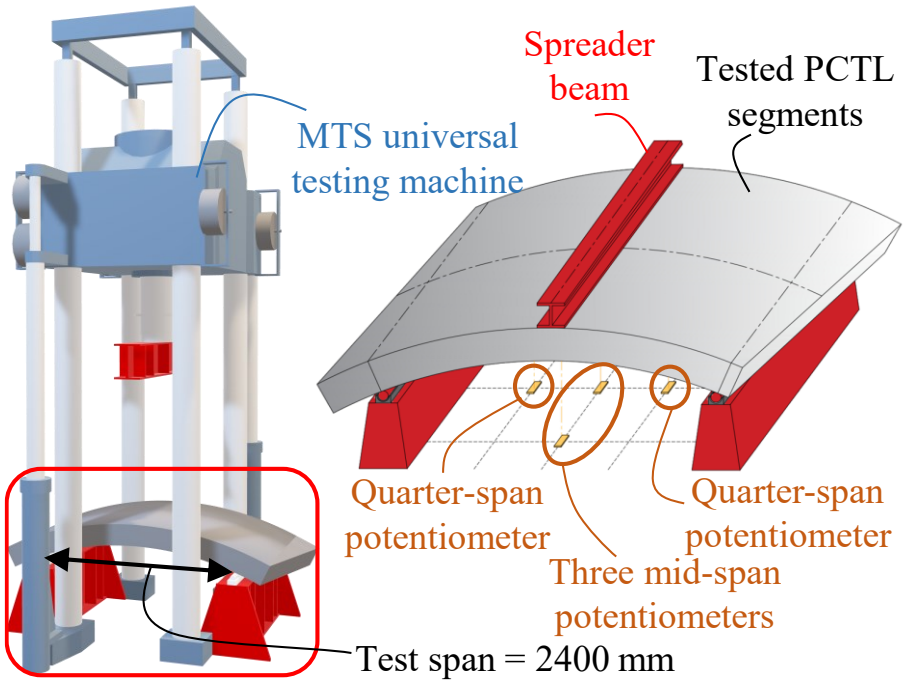

Fig. 3.3 Test setup.

3.6 SUPPORTING SYSTEM AND STRUCTRUAL ANALYSIS FOR THE MOMENT

As one of the recommended test setups in the [ACI 544.7R-16], the supporting system for the test setup was designed in accordance with the most commonly used supporting system for the flexural testing of the PCLT segments [Caratelli et al., 2016; 2017; Spagnuolo et al., 2017, 2018; Hosseini et al., 2022]. To minimize the tensile forces on the segments' sections, the segments were placed on cylindrical 150-mm-dimatere steel pinned supports at both ends, as shown in **Fig. 3.4**. A thin Teflon layer was placed between the supports and the segments to further reduce the friction between the two surfaces. The lateral displacements of the test segments were recorded during testing using four different linear potentiometers (LPOTs) placed at each edge of the segments to record the exact boundary conditions of the tested **(Fig. 3.4)**.

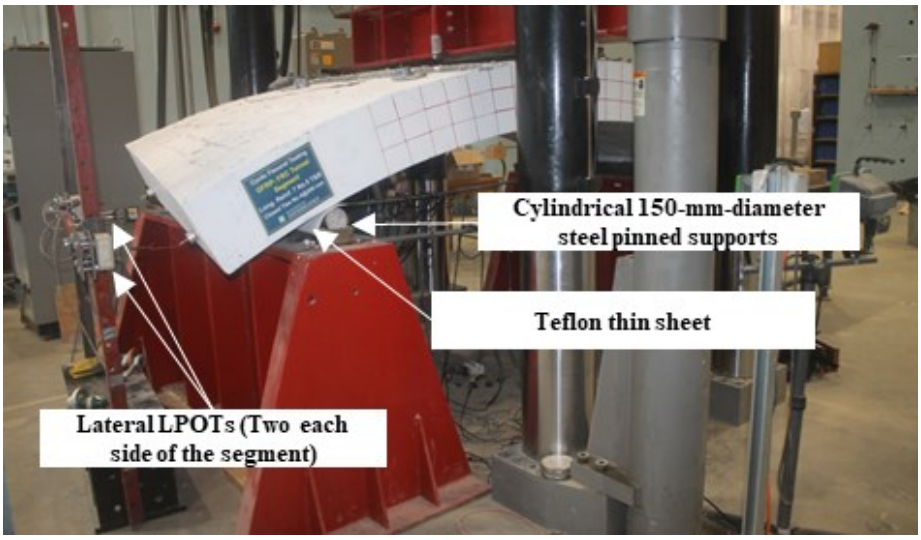

Fig. 3.4 Supporting system.

For the experimental moment calculations and the theoretical and analytical moment predictions, however, taking into account for the 23° of inclination between the supports from the vertical axis **(Fig. 3.5)**, the inclination effect was taken in consideration as expressed in **Equations 3.2 – 3.5**.

$$R = P/2\cos\theta \tag{3.2}$$

$$X = \left(P\tan\theta\right)/2 \tag{3.3}$$

$$Y = P/2 \tag{3.4}$$

$$\text{Moment} = \frac{PL}{4} + \frac{P\Delta\tan\theta}{2} \tag{3.5}$$

where θ is the angle of inclination of the segment's supports from the vertical axis, and Δ is the vertical distance between the segment's centerline at mid-span and the supports' resistance forces, as illustrated in **Fig. 3.5**.

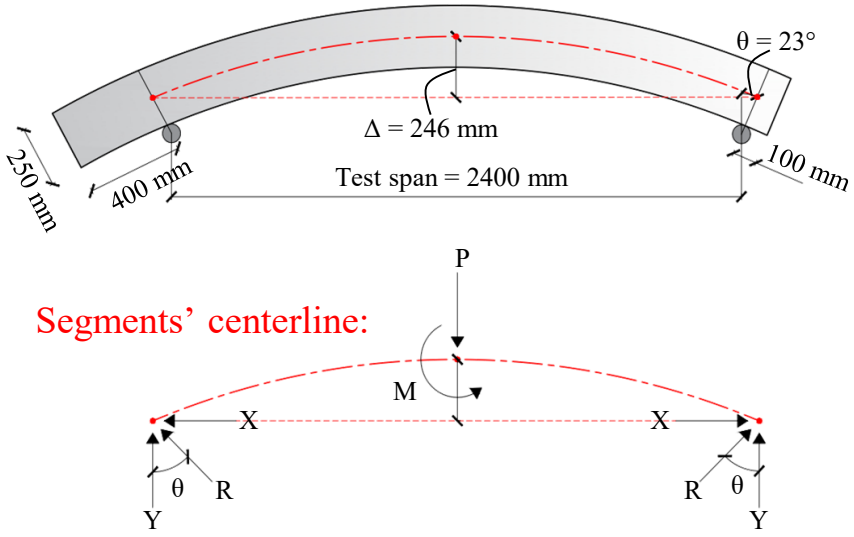

Fig. 3.5 Schematic for the section's moment calculations

3.7 QUASI-STATIC CYCLIC FLEXURAL LOADING

For the design of the PCTL segments, the internal forces and stresses imposed on the PCTL segments from the form stripping, storage, transportation, and handling stages have to be considered. The long-term loads acting on the PCTL segments are characterized by the service loads. According to [ACI 544.7R-16], loads act on PCTL segments from the time of casting up to installation of segments within the tunnel-boring machine (TBM) shield are grouped in three stages: production and transient, construction, and service. The service stage is represented by the enduring loads acting on the PCTL from the groundwater, surcharges, and other loads from any circumstances such as earthquake, fire, explosion, and breakouts at cross passageways. In this research work, the cyclic loads on the PCTL segments were simulated in accordance with the tests of structural components under slowly applied quasi-static loading in [ACI 374.2R-13]. Quasi-static cyclic flexural loading was applied in terms of percentage of the maximum displacement (Δ_{max}) obtained from the static testing results [Hosseini et al., 2022]. Two cycles of loading and unloading were conducted for 1.25%, 2.5%, 5%, 10%, 25%, 50%, and 75% of Δ_{max}, followed by one cycle up to failure, as shown in **Fig. 3.6**. In all cycles, the unloading phase ended at a minimum load of 5 kN in order to keep the test machine engaged.

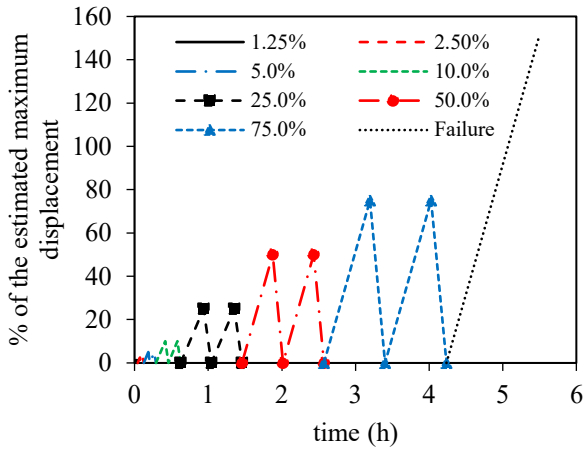

Fig. 3.6 Quasi-static cyclic flexural loading scheme for the tested segments.

3.8 IVESTIGATED QUASI-STATIC CYCLIC INDEXES

To evaluate the effect of the test parameters on the quasi-static cyclic flexural behavior of the test segments, different cyclic indexes – including the cumulative dissipated energy, the energy-based ductility index, the deformability, and the secant stiffness damage index – for the tested segments were defined, estimated, and evaluated. This section presents the details of the investigated quasi-static cyclic indexes.

3.8.1 The cumulative dissipated energy

The cyclic loading transfers energy into structures that must then be dissipated for safety reasons. The measurement of dissipated energy could thus become a good efficiency index independently of structural ductility considerations. During cyclic tests on structures, dissipative mechanisms are frequently encountered and must be distinguished to determine the action of reinforcement on the dissipated energy (**Equation 3.6**). In fact, a principal energy E_T is transferred to the structure and supports. One component of this energy is redistributed into the soil Es, while the other is used by the structure over the elastic E_e and inelastic E_a domains. The first component E_e represents the energy necessary both for specimen displacement (kinematic energy E_c) and for elastic strain E_{es} (**Equation 3.7**). The component E_a includes the damping energy E_d and hysteretic energy E_h E_{es} (**Equation 3.8**) [Daniel and Loukili, 2002].

$$E_T - E_S = E_e + E_a \tag{3.6}$$

$$E_e = E_c + E_{es} \tag{3.7}$$

$$E_a = E_d + E_h \tag{3.8}$$

To avoid structural collapse from occurring, it is important to increase the energy storage capability in the elastic domain and energy dissipation in the inelastic domain. For the former, increasing the longitudinal reinforcement ratio increases structural stiffness. Therefore, having higher reinforcement ratio prevents increasing energy storage in the inelastic domain. The energy dissipated during a loading cycle was determined by computing the hysteretic area of the loop.

3.8.2 The energy-based ductility index

The structural member's capability of resisting inelastic deformation without lessening in the carrying capacity is an essential requirement in the varied design codes and provisions, which is defined as the structural ductility. Unlike conventionally steel-reinforced concrete members, the ductility of FRP-reinforced concrete members can be indirectly computed in terms of energy absorption or deformability [Grace et al., 1998].

The ductility index, μ_e, for all tested segments was computed using the energy absorption approach proposed by [Naaman and Jeong, 1995], as expressed in **Equation 3.9**.

$$\mu_e = \frac{1}{2}\left(\frac{E_{tot}}{E_{el}} + 1\right) \tag{3.9}$$

where E_{tot} is the total energy computed as the area under the segment's load-deflection curve; and E_{el} is the elastic energy released upon failure, computed as the are of the triangle formed at failure load of the segment by the line having the weighted average slope of the two initial straight lines of the segment's load-deflection curve.

3.8.3 The deformability

[ACI 440.1R-15] defines the deformability factor as the ratio of the energy absorption at ultimate strength of the section to the energy absorption at the service level. The *Canadian Highway Bridge*

Design Code [CAN/CSA S6-19] adopted the [Jaeger et al., 1997] (J-factor) approach to evaluate the deformability index of FRP-RC members. The J-factor takes into account the strength effect as well as the curvature effect at service and ultimate conditions. **Equation 3.10** can be used to calculate the deformability J-factor.

$$J = \frac{M_{ultimate}}{M_s} \times \frac{\psi_{ultimate}}{\psi_s} = \frac{M_{ultimate}.\psi_{ultimate}}{M_s.\psi_s} \tag{3.10}$$

where ψ_s is the curvature at service condition (concrete strain equal to 0.001); ψ_u is the curvature at ultimate; M_s is the moment at service condition; and M_u is the ultimate moment.

[CAN/CSA S6-19] requires a J-factor greater than 4 for rectangular sections: the higher the J-factor values, the more sufficient warning given by the FRP-RC specimen before failure. In other words, the J-factor indicates the amount of cracking and deflection that the FRP-RC member will exhibit throughout the load history from service to ultimate condition.

3.8.4 The secant stiffness damage index

Several proposals currently ascertain the damage index based on a wide range of parameters, such as deformation [Cosenza et al., 1993], stiffness [Meyer et al., 1983; Ghobarah et al., 1999; Kim et al., 2005], and energy absorption [Fardis et al., 1993]. Based on the damage index proposed by [Meyer et al., 1983], which computes the damage index as the ratio of the initial stiffness to the reduced secant stiffness at the maximum displacement of each cycle, the effect of the test parameters on the secant stiffness index (KI) in loading and unloading was determined for the test segments. The value of this parameter and its changes is the index of damage in the segments. This stiffness index is described as the cycle's secant stiffness K_{sec} to the after-cracking stiffness ratio of the specimens. For each loading cycle, the cycle's secant stiffness damage index K_{sec} was computed using **Equation 3.11**.

$$K_{\text{sec}i} = \frac{P_{peak.i} - P_{o.i}}{\delta_{peak.i} - \delta_{o.i}} \tag{3.11}$$

CHAPTER 4 QUASI-STATIC CYCLIC FLEXURAL LOADING BEHAVIOR OF PRECAST RC TUNNEL SEGMENTS WITH GFRP BARS

FOREWORD

Authors and Affiliation:

- **Basil Ibrahim,** Ph.D. candidate, Department of Civil Engineering, Université de Sherbrooke, Sherbrooke, Quebec, Canada, J1K 2R1.
- **Salaheldin Mousa,** Postdoctoral fellow, Department of Civil Engineering, Université de Sherbrooke, Sherbrooke, Quebec, Canada, J1K 2R1.
- **Hamdy M. Mohamed,** Research Associate/Lecturer, Department of Civil Engineering, Université de Sherbrooke, Sherbrooke, Quebec, Canada, J1K 2R1.
- **Brahim Benmokrane,** Professor, Department of Civil Engineering, Université de Sherbrooke, Sherbrooke, Quebec, Canada, J1K 2R1.

Journal Title:

ACI Structural Journal

Paper Status:

Accepted on June 16, 2022.

Contribution:

The paper's outcomes are the first of their kind on the applicability of using GFRP as internal reinforcement for PCTLs under quasi-static cyclic flexural loading. These experimental results can be considered in the forthcoming provisions of ACI codes for the use of GFRP as internal reinforcement for PCTL applications.

ABSTRACT

The strength and behavior of segments of precast concrete tunnel linings (PCTLs) reinforced internally with fiber-reinforced polymer (FRP) bars under quasi-static cyclic flexural loading is one area in which no experimental research results are available. This research investigated the cyclic behavior of GFRP-reinforced PCTL segments, both experimentally and theoretically. Full-scale specimens with a total length, width, and thickness of 3100 mm (122 in.), 1500 mm (59 in.), and 250 mm (9.8 in.), respectively, were constructed and tested under quasi-static cyclic flexural loading. Two cycles of loading and unloading were applied at 1.25%, 2.5%, 5%, 10%, 25%, 50%, and 75% of the estimated maximum displacement, followed by a single cycle up to failure. The test parameters included reinforcement flexural stiffness (GFRP versus steel) and GFRP longitudinal reinforcement ratio. The hysteresis response, cracking pattern, residual deformation, dissipated energy, deformability, and secant stiffness damage index of the tested specimens were defined, estimated, and evaluated. The experimental results of this study show that the hysteresis cycles of the GFRP-reinforced specimens reflected stable cyclic behavior with no or limited strength degradation. Moreover, the test results show that the GFRP-reinforced specimens demonstrated adequate ductility index and deformability limits. A theoretical prediction according to the various current design provisions—including the flexural and shear capacities of the PCTL segments—was carried out and compared to the experimental results. The results of this study show the feasibility and efficiency of using GFRP bars instead of steel bars for PCTL segments under quasi-static cyclic flexural loading.

Keywords: Precast concrete tunnel lining (PCTL) segments; glass fiber-reinforced polymer (GFRP) bars; quasi-static cyclic load; hysteretic behavior; flexural and shear strength; design codes; deformability; energy dissipation.

4.1 INTRODUCTION

The use of precast concrete tunnel lining (PCTL) systems in tunneling construction projects has been gaining ground over the conventional on-site lining technique, because of its economic efficiency. PCTL speeds the construction process and ensures the highest quality due to enhanced control during fabrication of precast segments in precast plants [Cheong et al., 2005]. The structural performance of PCTL segments significantly depends on their durability performance. Tunnel structures built with steel-reinforced concrete are designed for service lives exceeding 100 years. The ingress of chloride ions into PCTL segments can induce reinforcement corrosion, which has been the primary cause threatening the structural safety of PCTLs and shortening their designed service lives. Corrosion of embedded reinforcement bars is considered the most prevalent mode of deterioration affecting the serviceability, safety, and structural integrity of tunnel structures [Gulikers, 2003]. In fact, many reinforced-concrete tunnels around the world are deteriorating as they age [Zhiqiang and Mansoor, 2013]. Steel-reinforced PCTLs often experience premature degradation mainly due to corrosion of the reinforcement bars requiring expensive repairs and maintenance. Since concrete is not perfectly impermeable, groundwater—often high in chlorine—gradually saturates the concrete, ultimately permeating the cover and producing an electrolytic reaction with the steel, which accelerates corrosion of the reinforcement [Rancourt, 2016]. This corrosion can lead to oxide jacking (also known as rust burst) and loss of structural integrity. Corrosion of steel reinforcement is the most expensive and problematic deterioration mechanism in concrete structures [ACI 440.1R-15]. In Canada, the annual cost of repairing corrosion damage in reinforced concrete structures has been estimated at more than $10 billion per year [Davis, 2000]. In the United States, the problem of corrosion of reinforced concrete structures costs the economy about $100 billion each year or nearly 1% of the country's gross domestic product [Whitmore and Ball, 2004]. One effective solution to this corrosion problem is to replace steel reinforcement with noncorroding fiber-reinforced polymer (FRP) reinforcing bars. These lightweight, high-strength FRP bars are characterized by high corrosion resistance, long service life, and reduced maintenance costs [Manalo et al., 2020].

Recently, a few studies have investigated the possibility of using glass-FRP (GFRP) reinforcement in PCTL segments [Caratelli et al., 2017; Spagnuolo et al., 2017; Meda et al., 2019; Hosseini et al., 2022]. All these studies have proved the suitability of using GFRP bars as reinforcement for

PCTL segments. The experimental evidence from these investigations showed that the GFRP-reinforced PCTL segments exhibited better cracking control behavior compared to traditional reinforced concrete segments. The load related to the first crack was higher and the crack openings were narrower. Moreover, these studies revealed no significant difference in the flexural behavior of the GFRP-reinforced PCTL segments compared to the steel-reinforced ones. Substantively, increasing of the strength of the GFRP bars compensated for the lack of ductility compared to the steel reinforced PCTL segments. Past studies, however, have focused mainly on the static flexural resistance of PCTLs in order to evaluate their structural properties. During its service life, a tunnel structure can be subjected to permanent loads (dead loads, earth pressure, surcharge loads,), live loads (vehicular loads, live-load surcharges, etc.), or transient loads (water loads, earthquake, superimposed deformations, blasts, fire, construction loads). According to [ACI 544.7R-16], the loads acting on PCTLs from the time of segment casting up to the time of segment erection within the tunnel-boring machine (TBM) shield fall into three stages. They are termed the production and transient stage, the construction stage, and the service stage. The internal forces and stresses in the production and transient stages are included in the design of PCTL segments. The construction stage includes the TBM jacking thrust loads on the circumferential ring joints and the pressures during the grouting operation exerted against the exterior of the completed rings. PCTL segments are designed to resist significant bursting and spalling tensile stresses that develop along the circumferential joints due to advancement of the TBM. The final service stages are represented by the long-term loads imposed on the lining from the ground, groundwater, surcharges, and other loads from any circumstances such as earthquake, fire, explosion, and breakouts at cross passageways. The flexural behavior of steel-fiber reinforced concrete and conventionally steel reinforced PCTL segments under quasi-static cyclic flexural loading has been experimentally studied by [Abbas, 2014]. It was revealed that both steel-fiber reinforced concrete and conventionally steel reinforced PCTL segments exhibited reasonable levels of ductility and energy dissipation capacities and satisfied the flexural requirement under quasi-static cyclic flexural loading. Basically, there are no research results in the literature on the cyclic behavior of GFRP-reinforced PCTLs. Accordingly, the performance of full-scale PCTL segments under quasi-static cyclic flexural loading needs to be investigated.

This study is part of an ongoing comprehensive research program carried out in the Department of Civil Engineering at the University of Sherbrooke to improve current practices and develop more

efficient design and construction approaches for using curvilinear GFRP bars and stirrups in precast concrete tunnel lining segments. Full-scale GFRP-reinforced PCTL segments are tested under different loading conditions—static flexural loading [Hosseini et al., 2022]; quasi-static cyclic flexural loading; and punching shear and settlement—to investigate different variables and design parameters. This paper presents the structural behavior of full-scale GFRP-reinforced PCTL segments under quasi-static cyclic flexural loading, according to [ACI 374.2R-13]. The effect of reinforcement type and ratio on the behavior of GFRP-reinforced precast concrete tunnel lining segments under quasi-static cyclic flexural loading was investigated. This paper is the first study to investigate the cyclic behavior of PCTL segments reinforced with GFRP bars. It also aimed at determining the feasibility and efficiency of using GFRP instead of steel reinforcement.

4.2 RESEARCH SIGNIFICANCE

The design of the PCTL segments reinforced with FRP bars is not defined or discussed in the current design provisions such as in [ACI 440.1R-15; ACI 544.7R-16; ACI PRC-533.5-20]. The strength and behavior of such members reinforced with FRP bars is one area in which limited research results are available for implementing this noncorroding composite reinforcement. So far, this research is the first experimental work aimed at providing experimental data involving the laboratory testing of the performance of PCTL segments reinforced with GFRP reinforcement under quasi-static cyclic flexural loading. Full-scale PCTL specimens were tested to determine the effects of reinforcement flexural stiffness (GFRP versus steel) and GFRP longitudinal reinforcement ratio. A theoretical study was also conducted to calculate the flexural and shear capacities of PCTL segments reinforced with GFRP bars according to the various current design provisions [ACI 440.1R-15; CAN/CSA S806-12 (R2017); fib TG-9.3, 2007; CNR-DT 203, 2006; AFGC, 2021]. As this study presents the first results of their kind on the applicability of using GFRP as internal reinforcement for PCTLs under quasi-static cyclic flexural loading, the results reported in this manuscript represent a significant contribution to the relevant literature and provide end users, engineers, and code committees with much-needed data and recommendations to advance the use of GFRP reinforcement in PCTL segments. The study also is expected to be a step toward further research to assess the possibility of developing new applications for GFRP bars and ties, resulting in more durable, economic, and competitive PCTL segments for tunnel applications.

4.3 EXPERIMENTS

4.3.1 Materials

Table 4.1 provides the mechanical properties of the GFRP and steel bars used to reinforce the PCTL segments in this study. The GFRP bars were manufactured by pultruding boron-free glass fibers impregnated in a thermosetting vinyl-ester resin. The ultimate tensile strength f_{fu} and modulus of elasticity E_f of the GFRP bars were determined according to [ASTM D7205/D7205M-21]. The GFRP bars had a sand-coated surface to enhance bonding and force transfer between the bars and concrete. Number 6 (20 mm), #5 (15 mm), and #4 (13 mm) GFRP bars were used for both longitudinal and transverse reinforcement in the segments, as shown in **Fig. 4.1(a)**. Moreover, #6 (20 mm) and #5 (15 mm) closed U-shaped GFRP bars were used as anchorage for the longitudinal reinforcement bars. For the control specimen, deformed 15M (16 mm) steel bars were used as longitudinal reinforcement and deformed 10M (11 mm) steel bars as transverse reinforcement. Deformed 15M (16 mm) U-shaped steel bars were used to anchor the longitudinal reinforcement bars. All the PCTL segments were cast with normal-weight concrete by the SYM-TECH precast company (Saint-Hyacinthe, QC). The average actual compressive strength based on the average test results of 100 × 200 mm (3.94 × 7.89 in) concrete cylinders tested on the first day of the start of testing of the specimens was 52.2 MPa (7.6 ksi).

Table 4.1 Mechanical properties of the reinforcement bars

Reinforcement type	Bar size	Bar diameter (mm)	Nominal cross-sectional area (mm^2)	Modulus of elasticity (GPa)	Tensile strength (MPa)	Tensile strain (%)
Curvilinear-GFRP bars	#5	15.0	199	55.1	1115	2.0
	#6	20.0	284	52.9	1068	2.0
U-shaped GFRP bars	#5	15.0	199	53.5	1283	2.4
	#6	20.0	284	53.2	1131	2.1
Closed GFRP ties	#4	13.0	129	55.6	1248	2.2
Steel bars	10 M	11.3	100	200.0	480[a]	0.24[b]
	15 M	16.0	200	200.0	460[a]	0.23[b]

[a] The yield strength of the steel bars.
[b] The yield strain of the steel bars.
Note: 1 mm = 0.0394 in; 1 MPa = 145.04 psi; 1 GPa = 145.04 ksi.

4.3.2 Specimen details

The experimental program was designed to provide data on the cyclic behavior of PCTL segments reinforced with GFRP bars. Four full-scale PCTL segments (three reinforced with GFRP bars and one with conventional steel reinforcement) were tested under quasi-static cyclic flexural loading. The inner and outer radii of the four PCTL segments were designed to be 3250 mm (128 in) and 3500 mm (138 in), respectively. The test specimens measured 3100 mm (122 in.) in length, 1500 mm (59 in.) in width, and 250 mm (9.8 in.) in thickness. The segments were skewed at their ends rather than straight. **Figs. 4.1(b) and (c)** show assembled GFRP cages for the test specimens.

(a) (b) (c)

Fig. 4.1 Overview of (a) GFRP bars and ties; (b) assembled GFRP cage for specimens with 7 top and bottom longitudinal bars and (c) assembled GFRP cage for the specimens with 13 top and bottom longitudinal bars.

The test matrix was arranged to assess the influence of the flexural reinforcement type (GFRP versus steel) and the GFRP flexural reinforcement ratio. The longitudinal reinforcement ratios of 0.5%, 0.9% and 1.2% were chosen as the minimum reinforcement ratio for concrete crushing controlled by flexural failure, an intermediate reinforcement ratio, and the maximum reinforcement ratio practically possible. **Table 4.2** provides the test matrix and reinforcement details of the test specimens. The test specimens are identified as follows. The first number indicates the number of longitudinal bars. The letters G and S stand for GFRP and steel reinforcement, respectively. The second number indicates the nominal diameter of the longitudinal bars. Specimen 7G15 had top and bottom longitudinal reinforcement consisting of 7 #5 GFRP bars with a longitudinal reinforcement ratio of 0.5%. Seven #5 U-shaped GFRP anchorage bars were installed on each side of the specimen. Specimens 13G15 and 13G20 had top and bottom longitudinal reinforcement consisting of 13 #5 GFRP bars and 13 #6 GFRP bars with longitudinal reinforcement ratios of 0.9% and 1.25%, respectively. Thirteen #5 U-shaped GFRP anchorage bars

and 13 #6 U-shaped GFRP anchorage bars were installed on each side of specimens 13G15 and 13G20, respectively. All the GFRP specimens were reinforced transversally with #4 GFRP ties at a spacing of 200 mm (7.87 in.). The control steel specimen (7S15) had top and bottom longitudinal reinforcement consisting of 7 M15 deformed steel bars with a reinforcement ratio of 0.5% and transverse reinforcement consisting of M10 ties at a spacing of 200 mm (7.87 in.). Seven deformed 15M U-shaped anchorage steel bars were installed on each side of the specimen. **Fig. 4.2** shows the reinforcement details for all the test specimens. The clear cover was kept constant at 40 mm for all specimens.

Table 4.2 Test matrix

Specimen ID	Reinforcement type	Concrete compressive strength (MPa)	Longitudinal reinforcement		Transverse reinforcement
			ρ_f (%)	Number of bars	
7S15	Steel	53	0.5	7 15M bars	10M bars @200 mm
7G15	GFRP	52	0.5	7 No. 5 bars	No. 4 bars @200 mm
13G15	GFRP	52	0.9	13 No. 5 bars	No. 4 bars @200 mm
13G20	GFRP	50	1.2	13 No. 6 bars	No. 4 bars @200 mm

Note: 1 mm = 0.0394 in; 1 MPa = 145.04 psi.

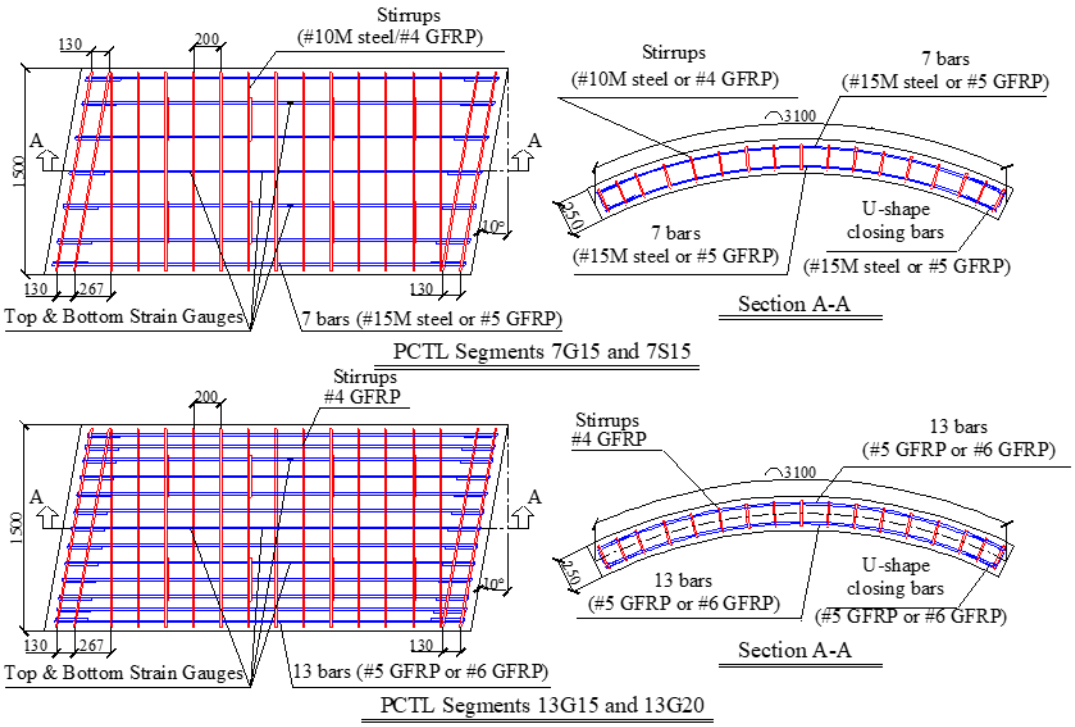

Fig. 4.2 Reinforcement details for the test specimens. (Note: all dimensions in mm; 1 mm = 0.0394 in)

4.3.3 Instrumentation and test setup

Strains in the longitudinal and transverse reinforcing bars were measured with electrical resistance strain gauges with a gauge length of 10 mm (0.39 in.) (**Fig. 4.2**). In addition, five strain gauges with a gauge length of 60 mm (2.36 in.) were mounted on the concrete surface at the mid- and quarter-span to measure the concrete compressive strain. Specimen deflections were measured with five linear potentiometers (LPOTs) placed at the mid- and quarter-span. The test setup was designed and fabricated at the University of Sherbrooke's CFI structural laboratory.

The specimens were loaded under three-point bending load, as shown in **Fig. 4.3(a)**, using an 11,000 kN (247.3 kips) capacity MTS universal testing machine attached to a spreader beam. The span for the test specimens was 2400 mm (94.5 in.). The load was applied at a displacement-controlled rate of 0.8 mm/min. An automatic data-acquisition system monitored by a computer was used to record the readings of the LPOTs, load cells, and strain gauges.

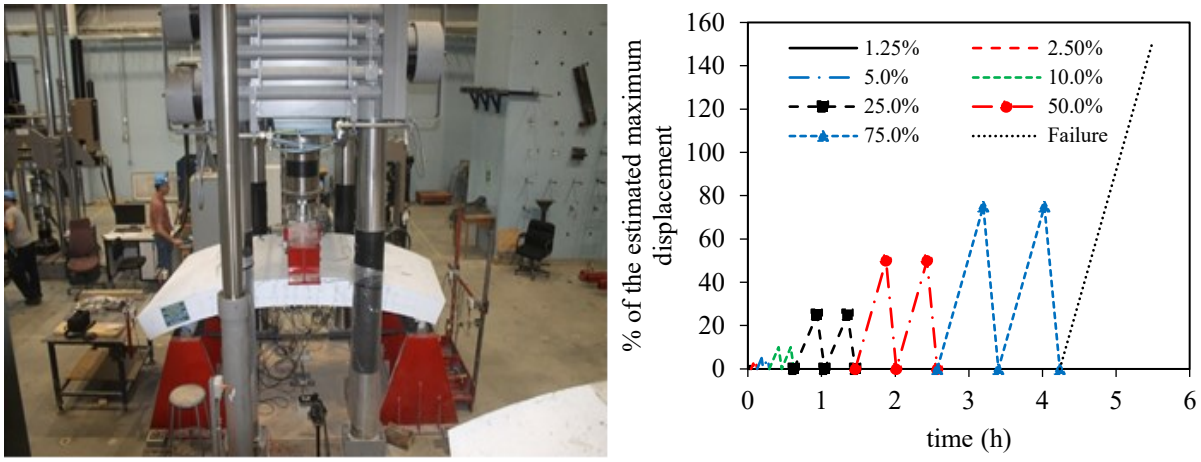

(a) (b)

Fig. 4.3 (a) Test setup (b) loading scheme for the tested specimens.

4.3.4 Quasi-static cyclic loading procedure

The test protocol followed is that in [ACI 374.2R-13], tests of structural components under slowly applied quasi-static loading, either as monotonically increasing or reversed cyclic loading. Quasi-static cyclic flexural loading was applied in terms of the percentage of the maximum displacement (Δ_{max}) obtained from the static testing results in the literature [Hosseini et al., 2022]. Two cycles of loading and unloading were conducted for 1.25%, 2.5%, 5%, 10%, 25%, 50%, and 75% of Δ_{max}, followed by one cycle up to failure. In all the cycles, the unloading phase was finished with a

minimum load of 5 kN (1.12 kips) in order to keep the test jack engaged. **Fig. 4.3(b)** shows the loading scheme for the tested specimens.

4.4 TEST REULTS AND DISCUSSION

This section summarizes the experimental results, including the general behavior of the test specimens in terms of hysteresis response, crack patterns and failure modes, strain in reinforcement and concrete, neutral-axis depth, deformability, dissipated energy, and ductility and secant-stiffness damage index. **Table 4.3** summarizes the flexural moment and shear load-carrying capacities of the test specimens.

Table 4.3 Summary of the experimental and the theoretical results

Specimen ID	Cracking moment (kN.m)	Service moment[a] (kN.m)	Failure moment (kN.m)	Type of failure	Deflection at failure (mm)	Ductility Index	Deformability J-factor
7G15	48	62	206	Concrete crushing	56.5	1.5	5.9
13G15	49	73	243[b]	Shear compression	41.3	1.3	6.1
13G20	55	71	238[c]	Diagonal shear	30.3	1.3	4.1

Specimen ID	M_{exp}/M_{pred}				
	ACI 440.1R-15	CSA S806-12 (R2017)	fib TG-9.3 (2007)	AFGC (2021)	CNR-DT-203 (2006)
7G15	0.97	0.86	0.96	0.96	1.29
13G15	0.87	0.78	0.81	0.87	0.88
13G20	0.76	0.68	0.68	0.77	0.67

Specimen ID	V_{exp}/V_{pred}				
	ACI 440.1R-15	CSA S806-12 (R2017)	fib TG-9.3 (2007)	AFGC (2021)	CNR-DT-203 (2006)
7G15	1.63	1.11	1.26	1.19	0.81
13G15	1.44	1.09	1.11	1.14	0.85
13G20	1.28	0.97	0.99	1.01	0.76

[a] The service moment of the test specimens is estimated at 0.3 of M_n.
[b] The shear load failure = 178 kN.
[c] The shear load failure = 174 kN.
Note: 1 mm = 0.0394 in; 1 kN.m = 0.738 kip.ft.

4.4.1 Hysteresis response

The hysteresis behavior is shown in the form of the moment versus mid-span deflection of specimens, as presented in **Fig. 4.4**. Initially, all the specimens exhibited identical linear load–deflection behavior. After cracking, the stiffness of the GFRP specimens reduced with almost linear load–deflection behavior. The steel-reinforced specimen also had initial linear load–deflection behavior corresponding to the uncracked condition of the specimen. Its stiffness decreased due to yielding of the longitudinal reinforcement in the tension zone, followed by a gradual decrease in overall stiffness. **Fig. 4.5** shows the cracking pattern in the test specimens. The first vertical flexural crack initiated in the tension zone under the loading point. The corresponding cracking moment was recorded during testing and verified from the moment–strain and moment–deflection relationships. The cracking moment M_{cr} ranged from 48 kN·m (35.40 kip·ft) to 55 kN·m (40.57 kip·ft), occurring in the first cycle at 5% of the maximum displacement. At this stage, there were no significant strain-gauge readings for the GFRP or steel reinforcing bars before initiation of the first flexural crack. In addition, the concrete strains were insignificant in all specimens, ranging from -60 to -130 με at the top location of the mid-span, as shown in **Fig. 4.6(a)**. Beyond the first cracking load, additional flexural cracks developed within the shear span of the 7G15 specimen, in the 10% and 25% of maximum displacement cycles. With further loading, in the first 75% of the maximum displacement cycle, the flexural cracks became wider and propagated upward towards the loading point, while some new cracks started to develop in the shear span (**Fig. 4.5**). Before failure occurred, the cracks along the shear span started to incline towards the loading points. The concrete crushing moment M_n for the 7G15 specimen was 206 kN·m (151.9 kip·ft), with a maximum recorded mid-span concrete compressive strain of -3840 με on concrete crushing, as shown in **Fig. 4.6(a)**. Specimens 13G15 and 13G20 behaved similarly before the 75% of the maximum displacement cycle. Beyond this stage, a main shear crack started to develop and propagated until shear failure occurred at a shear load V_n of 178 kN (40.02 kips) and 174 kN (39.12 kips), respectively. The failure of specimens 13G15 and 13G20 occurred by shear compression failure and diagonal tension failure, respectively. The maximum recorded mid-span concrete compressive strain in specimen 13G15 was -3285 με, indicating shear compression failure. In contrast, the diagonal tension failure in specimen 13G20 resulted in a maximum mid-span concrete compressive strain of -2051 με, as shown in **Fig. 4.6(a)**.

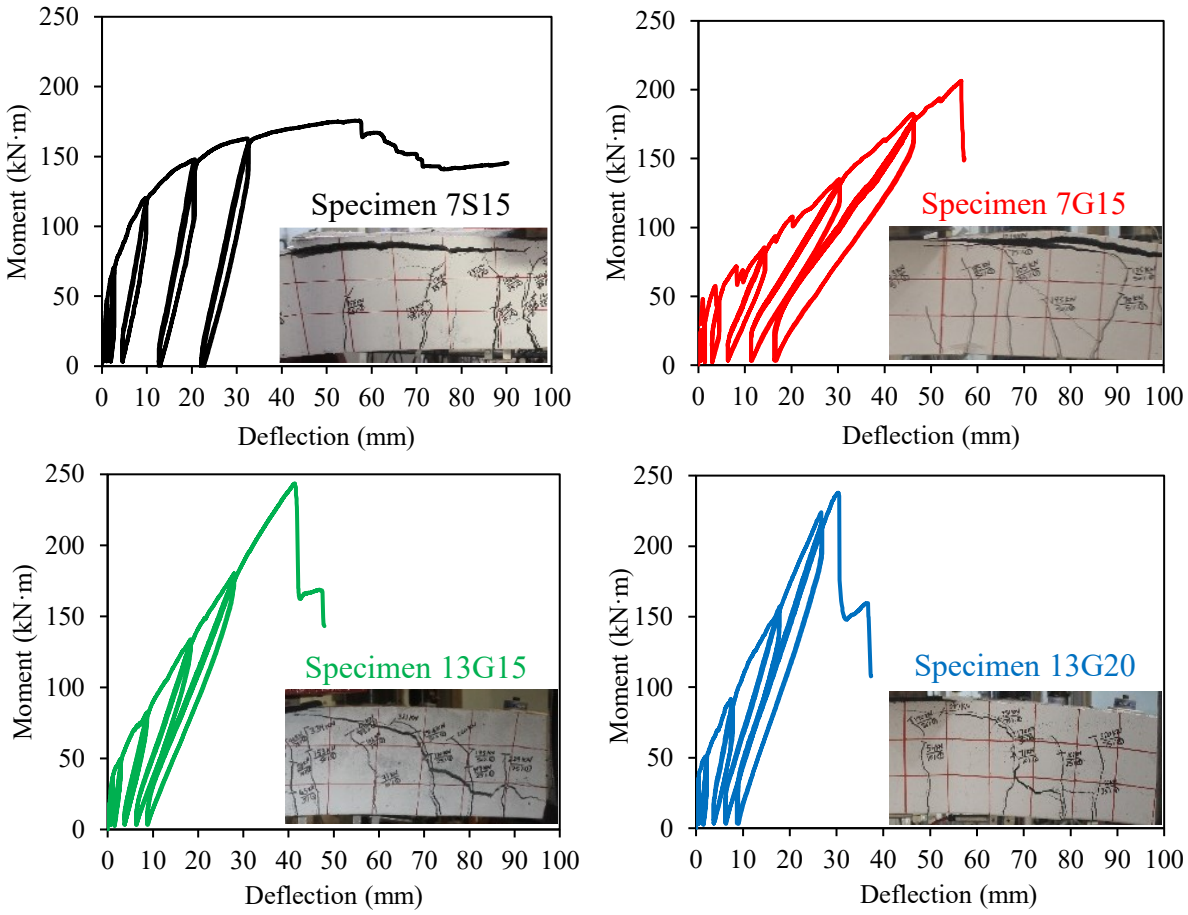

Fig. 4.4 Hysteresis response and failure mode of the test specimens.

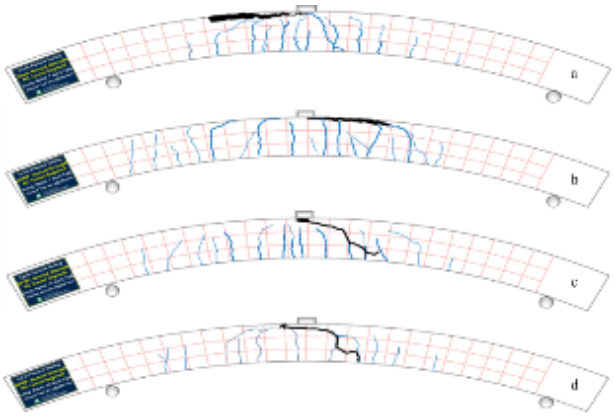

Fig. 4.5 Cracking pattern in (a) specimens 7S15; (b) specimens 7G15; (c) specimens 13G15; and (d) specimen 13G20.

The hysteretic response for the GFRP-reinforced specimens, in all second excursion loading cycles, reflected stable cyclic behavior with no or limited strength degradation until failure. In

contrast, the early yielding of the steel bars in specimen 7S15 resulted in wider concentrated cracks compared to the GFRP-reinforced specimens. Specimen 7S15 yielded (at a corresponding strain of approximately 2,300 με) in the first 25% of the maximum displacement cycle at an applied moment of 114 kN·m (84.1 kip·ft) (approximately at 64% of the specimen's peak moment). The gradual yielding of 7S15 specimen was attributed to the yielding of the bottom steel reinforcement bars in the specimen before the yielding of the top reinforcement bars, in which the strain-gauge readings show that the top reinforcement bars in the 7S15 specimen were under tension, which contributed in carrying tensile stresses and resulted in the gradual yielding of the specimen **(Fig 4.6(c))**. The mid-span concrete compressive strain reading in specimen 7S15 when the steel yielded was -795 με, as shown in **Fig. 4.6(a)**. The concrete strain gauge continued recording after this point until the ultimate applied moment of 176 kN·m (129.8 kip·ft) (concrete crushing) at 3336 με. The strain in the GFRP bars on the tension side gradually increased up to specimen failure at 17695, 8508, and 7023 με (88%, 43%, and 35% of the ultimate tensile strain of the GFRP bars) for specimens 7G15, 13G15 and 13G20, respectively, as shown in **Fig. 4.6(b)**. In addition, the strain-gauge readings show that the top reinforcement bars in all the specimens were under tension, which enhanced specimen strength. The recorded strains in specimens 7S15, 7G15, 13G15, and 13G20 in the top reinforcement (GFRP or steel bars) at failure were 3761, 2163, 1164, and 3603 με, respectively, as shown in **Fig. 4.6(c)**. The test results indicate that the recorded strains at the quarter-span for both the reinforcement bars and the concrete surface were less than that at mid-span.

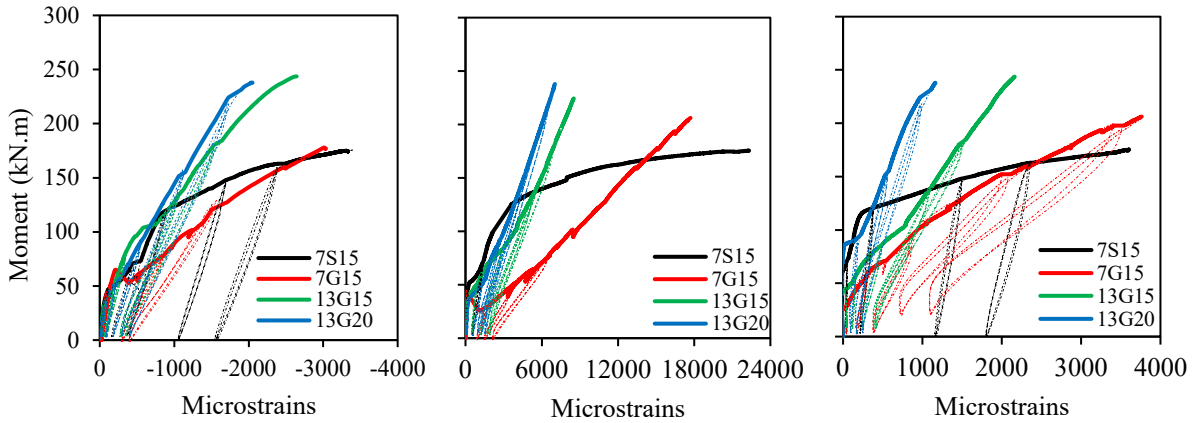

(a) (b) (c)

Fig. 4.6 Moment – strain relationship at mid-span at (a) concrete surface; (b) bottom reinforcement bars; and (c) top reinforcement bars.

4.4.2 Unloading stiffness and residual deformation

Unloading stiffness is an important parameter because it determines the value of the residual deformation thus determining the recoverability of the structure [Fahmy et al., 2009]. As shown in **Fig. 4.4**, the unloading stiffness for the GFRP-reinforced specimens in all cycles was nearly equal to the reloading stiffness. In contrast, the yielding of the steel bars in specimen 7S15 at 25% of the maximum displacement cycle resulted in higher residual deformation compared to the GFRP reinforced specimen 7G15. The average unloading stiffness of specimen 7S15 at 25%, 50%, and 75% of the estimated maximum displacement cycles was 95%, 85%, and 89%, respectively, of the reloading stiffness. Residual deformation is often used as a key measure of the required recoverability of RC structures [Dong et al., 2016]. **Fig. 4.7** compares the cumulative residual deformation of specimens 7G15 and 7S15. The residual deformation of the GFRP-reinforced specimen during the unloading at 50% and 75% of the maximum displacement cycles was less than that of the steel-reinforced specimen due to the yielding of the steel bars in the tension zone. In general, the GFRP specimens recovered most of their deflection during the unloading at 50% and 75% of the maximum displacement cycles. When 50% of the maximum displacement cycles in specimen 7S15 was exceeded, a permanent deflection occurred in the unloading cycles due to the yielding of the steel bars.

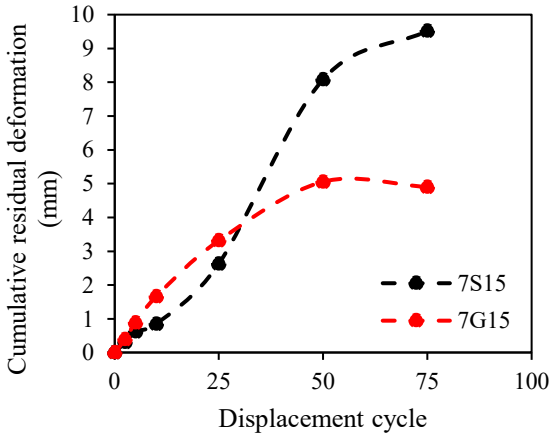

Fig. 4.7 Cumulative residual deformation for the GFRP-reifnroced (7G15) versus steel-reifnroced (7S15) specimens with similar reinfocement ratios.

4.4.3 Effect of parameters

This section presents the envelope moment–deflection curves at mid-span of the test specimens in two groups to show the effect of test parameters on specimen behavior, as depicted in **Fig. 4.8**. Before cracking occurred, identical linear moment–deflection behavior was observed in all the test specimens, regardless of reinforcement ratio and type, representing the uncracked condition governed by the properties of the concrete section. After cracking occurred, the response of the GFRP-reinforced specimens was almost linear up to failure. The moment–deflection curve of the steel-reinforced specimen shows a typical yielding plateau, followed by concrete crushing in the compression zone. Afterward, a sudden load drop occurred, followed by total loss of flexural stiffness.

4.4.3.1 Effect of the axial stiffness of the longitudinal reinforcement

Specimens 7G15 and 7S15 were designed to have the same flexural longitudinal reinforcement ratio. Before specimen 7G15 cracked, its stiffness was similar to that of 7S15, as shown in **Fig. 4.8(a)**. Specimen 7G15 had lower post-cracking flexural stiffness—calculated as the average slope of the curve—than its steel-reinforced counterpart (specimen 7S15). The ratio between the post-cracking flexural stiffness of specimen 7S15 to 7G15 was approximately 4.28. This ratio is approximately the same as the 4.35 ratio of the axial stiffness (EA) of the steel to that of the GFRP bars. This is in good agreement with the results of [Mousa et al., 2018]. It can be seen, however, that the GFRP-reinforced specimen had a longer ascending branch with higher stiffness compared to the post-yielding flexural stiffness of the steel-reinforced specimen. This is mainly due to the fact that, after the steel bars yielded, their tangent modulus was lower than that of the GFRP bars, which maintained their modulus of elasticity throughout the entire duration of loading. In addition, the test results indicate that specimen 7G15 had 1.5 times the flexural strength of specimen 7S15 at yielding, as shown in **Table 4.3**. The higher strength gain of the GFRP specimen provided sufficient deformability according to the [CAN/CSA S6-19] code limit of 4 for rectangular sections, so that warning of failure in the form of excessive deflection and cracking would be expected before reaching the GFRP bars reached their rupture tensile strain.

4.4.3.2 Effect of the longitudinal reinforcement ratio

The three GFRP-reinforced specimens (7G15, 13G15, and 13G20) were designed to have reinforcement ratios of 0.50%, 0.90%, and 1.20%, respectively. **Fig. 4.8(b)** provides a comparison

of the envelope moment–deflection curves for the three specimens, indicating that specimen 13G15 had ultimate strength 18% higher than specimen 7G15, as in **Table 4.3**. Moreover, **Table 4.3** shows that the percentage was lower when comparing specimen 13G20 to 13G15. This could be attributed to the fact that the failure of specimens 13G15 and 13G20 were shear compression failure and diagonal tension failure, respectively. The post-cracking flexural stiffness of specimen 13G15 (reinforcement ratio of 0.90%) was 72% higher than that of specimen 7G15 (reinforcement ratio of 0.50%). Similarly, the post-cracking flexural stiffness of specimen 13G20 (reinforcement ratio of 1.20%) was 140% higher than that of specimen 7G15 (reinforcement ratio of 0.50%) and 39% higher than that of specimen 13G15 (reinforcement ratio of 0.90%). These percentages were approximately similar to the percentage increases in the reinforcement ratios (80% from 0.50% to 0.90%, 33% from 0.90% to 1.2%, and 140% from 0.50% to 1.2%).

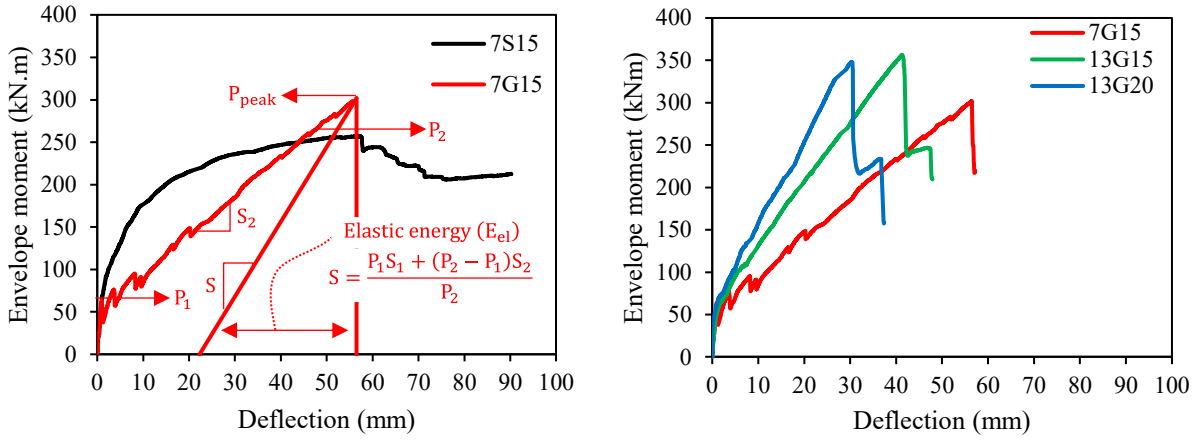

Fig. 4.8 Effect of test parameters on the envelope moment-deflection relationship: (a) the stiffness longitudinal reinforcement ratio; and (b) the longitudinal reinforcement ratio.

4.4.4 Strain distribution over the cross section

An analysis of strains along the cross section was carried out using the results from the concrete and bar strain gauges at the mid-span of the specimens; the experimental neutral-axis depth was deduced. **Fig. 4.9** presents the strain profile along the depth of the section at different moment levels. The figure shows a linear strain profile with some deviation. It is worth mentioning, however, that the strain gauges in specimen 13G15 were damaged before failure because several cracks occurred in the instrumented region. The Bernoulli hypothesis (a plane section remains plane after deformation up to failure), however, could be considered an acceptable simplification

of this behavior. **Fig. 4.10** illustrates the relation between neutral-axis depth at mid-span with the applied moment for the test specimens. In all of the test specimens, the position of the neutral axis in a section prior to cracking remained unchanged at the geometrical centroid of the specimen cross section. After cracking occurred, the neutral-axis depth decreased rapidly at first and then tended to stabilize. In the GFRP-reinforced specimens, the stabilizing behavior continued up to concrete crushing. In contrast, the yielding of tensile steel in the reinforced-steel specimen resulted in a rapid decrease in the neutral-axis depth. **Fig. 4.10** also shows that the neutral-axis depth for specimen 7G15 was less than that of specimen 7S15 despite them having similar reinforcement ratios. This could be attributed to the difference in the modulus of elasticity of the GFRP and steel bars.

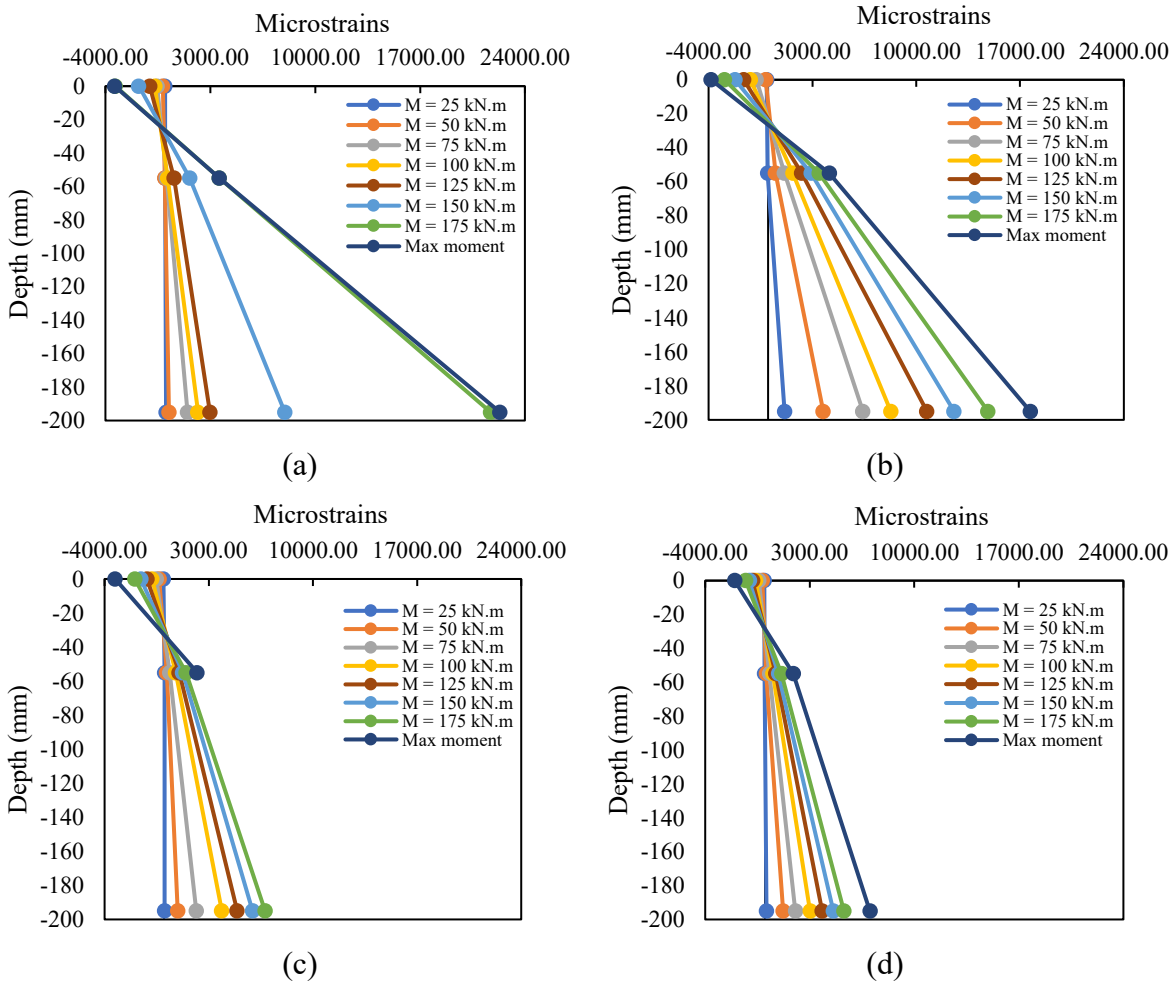

Fig. 4.9 Strain along the mid-span section for specimens (a) 7S15; (b) 7G15; (c) 13G15; and (d) 13G20.

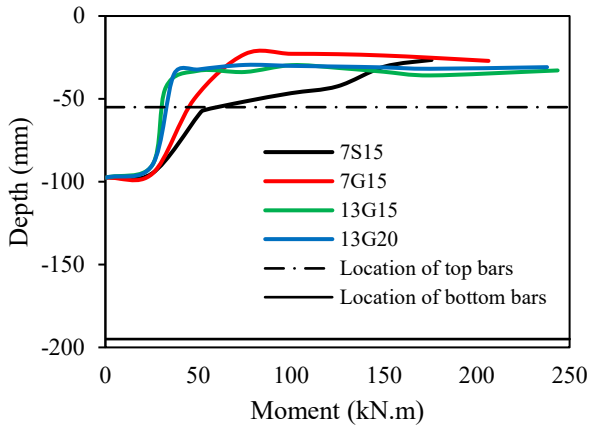

Fig. 4.10 Neutral-axis depth.

4.4.5 Cumulative dissipated energy

The cyclic loading transfers energy into structures that must then be dissipated for safety reasons. The measurement of dissipated energy could thus become a good efficiency index independently of structural ductility considerations. During cyclic tests on structures, dissipative mechanisms are frequently encountered and must be distinguished to determine the action of reinforcement on the dissipated energy (**Equation 4.1**). In fact, a principal energy E_T is transferred to the structure and supports. One component of this energy is redistributed into the soil Es, while the other is used by the structure over the elastic E_e and inelastic E_a domains. The first component E_e represents the energy necessary both for specimen displacement (kinematic energy E_c) and for elastic strain E_{es}. The component E_a includes the damping energy E_d and hysteretic energy E_h [Daniel and Loukili, 2002].

$$E_T - E_S = E_e + E_a \tag{4.1}$$

$$E_e = E_c + E_{es} \tag{4.2}$$

$$E_a = E_d + E_h \tag{4.3}$$

To avoid structural collapse from occurring, it is important to increase the energy storage capability in the elastic domain and energy dissipation in the inelastic domain. For the former, increasing the longitudinal reinforcement ratio increases structural stiffness. Therefore, having higher

reinforcement ratio prevents increasing energy storage in the inelastic domain, as shown in **Fig. 4.11(a)**. The computation of primary dissipated energy was carried out up until concrete crushing. The energy dissipated during a loading cycle was determined by computing the hysteretic area of the loop. The overall dissipated energy of specimen 7G15 was 16% and 63% higher than that of specimens 13G15 and 13G20, respectively. Similarly, the overall dissipated energy of specimen 13G15 was 40% higher than that of specimen 13G20. Considering the type of reinforcement, **Fig. 4.11(b)** shows that the steel specimen's cumulative dissipated energy was about twice the cumulative dissipated energy of GFRP-reinforced specimen 7G15 at concrete crushing.

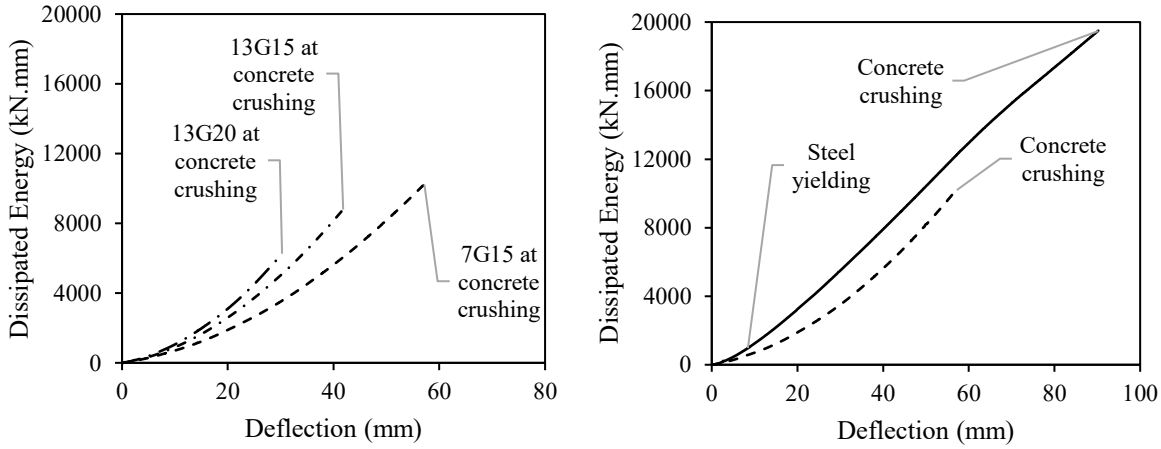

Fig. 4.11 Dissipated energy versus normalized deflection for (a) specimens with different longitudinal reinforcement ratio; and (b) specimens with different reinforcement type.

4.4.6 Energy-based ductility index

Ductility is a structural-design requirement in most design codes. The traditional definition of ductility for steel-reinforced concrete members, which considers the yielding of steel bars as a reference point, cannot be directly applied to members reinforced with FRP reinforcement due to the linear elastic behavior of FRP bars up to failure. Several methods have been proposed to calculate the ductility of FRP-RC structures. [Naaman and Jeong, 1995] defined ductility as the ratio of the total energy to the elastic energy and proposed **Equation 4.4** to compute the ductility index μ_e, which can be applied to steel- and FRP-reinforced concrete members.

$$\mu_e = 0.5\left(\left(E_{tot}/E_{el}\right)+1\right) \tag{4.4}$$

where E_{tot} is the total energy computed as the area under the load–deflection curve; and E_{el} is the elastic energy released upon failure, computed as the area of the triangle formed at failure load by the line having the weighted average slope of the two initial straight lines of the load–deflection curve, as illustrated in **Fig. 4.8(a)**. The computed energy-based ductility index μ_e for specimens 7G15, 13G15, 13G20, and 7S15 were 1.5, 1.3, 1.3 and 1.9, respectively. Considering the type of reinforcement, specimen 7G15 had a ductility index equal to 78% of the ductility of specimen 7S15, its steel-reinforced counterpart. This difference in ductility was compensated for by the high strength reserve of specimen 7G15, which had flexural strength 150% higher than specimen 7S15 at yielding. Moreover, the computed μ_e was slightly lower when the reinforcement ratio was increased. In the case specimen 13G15, increasing its reinforcement ratio resulted in a computed μ_e slightly lower than that of specimen 7G15 (from 1.5 to 1.3). Further increasing the reinforcement ratio did not lower the computed μ_e for specimen 13G20 further.

4.4.7 Deformability factor

[ACI 440.1R-15] defines the deformability factor as the ratio of the energy absorption at ultimate strength of the section to the energy absorption at the service level. The *Canadian Highway Bridge Design Code* [CAN/CSA S6-19] adopted the [Jaeger et al., 1997] (J-factor) approach to evaluate the deformability index of FRP-RC members. The J-factor takes into account the strength effect as well as the curvature effect at service and ultimate conditions. **Equation 4.5** can be used to calculate the deformability J-factor.

$$J = \frac{M_{ultimate}}{M_s} \times \frac{\psi_{ultimate}}{\psi_s} = \frac{M_{ultimate} \cdot \psi_{ultimate}}{M_s \cdot \psi_s} \tag{4.5}$$

where ψ_s is the curvature at service condition (concrete strain equal to 0.001); ψ_u is the curvature at ultimate; M_s is the moment at service condition; and M_u is the ultimate moment.

[CAN/CSA S6-19] requires a J-factor greater than 4 for rectangular sections: the higher the J-factor values, the more sufficient warning given by the FRP-RC specimen before failure. In other words, the J-factor indicates the amount of cracking and deflection that the FRP-RC member will exhibit throughout the load history from service to ultimate condition. The computed deformability J-factor shows that all the GFRP-reinforced specimens demonstrated adequate deformability when

compared to the [CAN/CSA S6-19] code limit of 4 for rectangular sections. The deformability J-factors for specimens 7G15, 13G15, and 13G20 were 5.9, 6.1, and 4.1, respectively.

4.4.8 Secant-stiffness damage index

Several researchers have established a set of damage indexes to ascertain the residual capacity of structures [Daniel and Loukili, 2002; Ranjbaran et al., 2018]. A wide array of parameters may be used, such as number of cycles, stiffness, and ductility. This section discusses the effect of the longitudinal reinforcement ratio on the secant stiffness index (KI) in loading and unloading. The parameter's values and changes are the index of damage in the specimens. This stiffness index is described as the cycle's secant stiffness K_{sec} to the after-cracking stiffness ratio of the specimens. For each loading cycle, the cycle's secant stiffness damage index K_{sec} was computed using **Equation 4.6**, as illustrated in **Fig. 4.12(a)**.

$$K_{\text{sec}i} = \frac{P_{peak.i} - P_{o.i}}{\delta_{peak.i} - \delta_{o.i}} \tag{4.6}$$

Fig. 4.12(b) illustrates the effect of the GFRP longitudinal reinforcement ratio on the secant stiffness damage index (KI). As shown, GFRP-reinforced PCLT specimen 7G15 had a decrease in stiffness comparable to that of its counterpart specimen 7S15. Moreover, increasing the longitudinal reinforcement ratio did not significantly affect the rate of decrease in stiffness. The residual stiffness at ultimate deflection of specimen 13G15 (reinforcement ratio of 0.90%) was 18.8% lower than that of specimen 7G15 (reinforcement ratio of 0.50%). Similarly, the residual stiffness at ultimate deflection of specimen 13G20 (reinforcement ratio of 1.20%) was 34.9% lower than that of specimen 13G15 (reinforcement ratio of 0.90%).

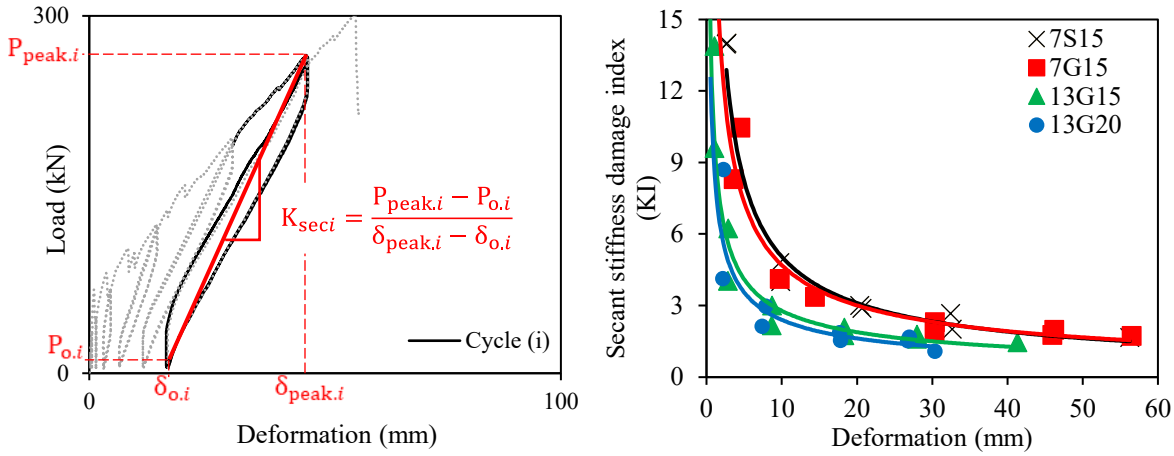

Fig. 4.12 (a) Secant stiffness; and (b) secant stiffness damage index versus deflection.

4.5 THEORETICAL STUDY

This section presents a theoretical study to calculate the flexural and shear capacities of PCTL segments reinforced with GFRP bars. It provides the calculations of the flexural and shear capacities of the PCTL tunnel segments reinforced with GFRP bars considering the requirements in the [ACI 440.1R-15], [CAN/CSA S806-12 (R2017)], *fib* [TG-9.3, 2007], [CNR-DT 203, 2006] and [AFGC, 2021].

4.5.1 Flexural capacity

The flexural design of FRP-reinforced concrete members is analogous to the design of steel-reinforced concrete members. Experimental data on concrete members reinforced with FRP bars show that the flexural capacity can be calculated based on assumptions similar to those made for members reinforced with steel bars [Ruan et al., 2020]. The flexural strength of the FRP reinforced cross section is calculated based on the following assumptions:

- Strain in the concrete and the FRP reinforcement is proportional to the distance from the neutral axis (a plane section before loading remains plane after loading).
- The tensile strength of the concrete is ignored.
- The tensile behavior of the FRP reinforcement is linearly elastic until failure.
- A perfect bond exists between the concrete and FRP reinforcement.

- The maximum usable compressive strain in the concrete is assumed to be 0.003 in [ACI 440.15] and 0.0035 in [CAN/CSA S806-12 (R2017)], *fib* [TG-9.3, 2007], [CNR-DT, 203 2006] and [AFGC, 2021].

4.5.1.1 ACI 440.1R (2015)

The FRP reinforcement ratio is computed according to the [ACI 440.1R-15] with **Equation 4.7**, and the balanced FRP reinforcement ratio can be computed with **Equation 4.8**.

$$\rho_f = A_f / bd \tag{4.7}$$

where A_f is the area of the fiber-reinforced polymer (FRP) reinforcement; b is the width of the rectangular cross section; and d is the distance from the extreme compression fiber to the centroid of the tension reinforcement.

$$\rho_{fb} = 0.85\beta_1 \frac{f_c^{'}}{f_{fu}} \frac{E_f \varepsilon_{cu}}{E_f \varepsilon_{cu} + f_{fu}} \tag{4.8}$$

where $f_c^{'}$ is the specified compressive strength of the concrete; f_{fu} is the design tensile strength of the FRP, defined as the guaranteed tensile strength multiplied by the environmental reduction factor; E_f is the design or guaranteed modulus of elasticity of FRP, defined as the mean modulus of a sample from the test specimens; and ε_{cu} is the ultimate strain in the concrete.

According to [ACI 440.1R-15], when $\rho_f > \rho_{fb}$, the controlling limit state is crushing of the concrete, and the stress distribution in the concrete can be approximated with the ACI rectangular stress block. Based on the equilibrium of forces and strain compatibility, the following can be derived. In [ACI 440.1R-15], the nominal flexural strength is determined from **Equations 4.9 – 4.11**.

$$M_n = A_f f_f \left(d - \left(a/2\right)\right) \tag{4.9}$$

$$a = \frac{A_f f_f}{0.85 f_c^{'} b} \tag{4.10}$$

$$f_f = E_f \varepsilon_{cu} \frac{\beta_1 d - a}{a} \tag{4.11}$$

The FRP reinforcement is linearly elastic at the concrete crushing limit state, so the stress level in the FRP can be found from **Equation 4.11**, as it is less than f_{fu}.

Alternatively, the nominal flexural strength at a section can be expressed, according to [ACI 440.1R-15], in terms of the FRP reinforcement ratio, as given in **Equation 4.12**.

$$M_n = \rho_f f_f \left(1 - 0.59 \frac{\rho_f f_f}{f_c'}\right) b d^2 \tag{4.12}$$

4.5.1.2 CAN/CSA S806 (2012) – Reapproved in 2017

According to the [CAN/CSA S806-12 (R2017)], the concrete crushing mode of failure occurs in the FRP-reinforced section when the extreme compressive strain in the concrete reaches its ultimate strain provided that

$$\left(c / d\right) \geq 7 / \left(7 + 2000 \varepsilon_{Fu}\right) \tag{4.13}$$

where c is the distance from the extreme compression fiber to the neutral axis; d is the distance from the extreme compression fiber to the centroid of the longitudinal tension force; and ε_{Fu} is the ultimate strain in the FRP reinforcement.

When c / d satisfies the requirements of **Equation 4.13**, the nominal flexural strength in a section can be determined, similar to as in [ACI 440.1R-15], based on the equilibrium of forces and strain compatibility.

4.5.1.3 fib TG-9.3 (2007)

According to *fib* [TG-9.3, 2007], the ultimate flexural moment resistance of an FRP RC section can be evaluated by adopting the framework of *Eurocode-2* [CEN, 2004]. Similar to as in [ACI 440.1R-15], when $\rho_f > \rho_{fb}$, flexural failure is expected to occur due to concrete crushing, and the ultimate moment resistance can be calculated based on the equilibrium of forces and strain compatibility with **Equation 4.14**.

$$M_u = \eta f_{cd} b d^2 (\lambda\zeta)\left(1-(\lambda\zeta/2)\right) \quad (4.14)$$

where η is a factor defining the effective strength of the concrete; f_{cd} is the design value of the concrete compressive strength; b is the width of the rectangular cross section; d is the effective depth of a cross section; λ is a factor defining the effective height of the compression zone; and ζ is a reduction factor coefficient.

4.5.1.4 AFGC (2021)

As in *fib* [TG-9.3, 2007], the ultimate flexural moment resistance of FRP RC section can be evaluated according to [AFGC, 2021] by adopting the framework of *Eurocode-2* [CEN, 2004]. According to [AFGC, 2021], the FRP reinforcement ratio can be computed with **Equation 4.15**, and the balanced FRP reinforcement ratio can be computed with **Equation 4.16**.

$$\rho_{PRF} = A_{PRF} / A_{c,red} \quad (4.15)$$

where A_{PRF} is the area of the longitudinal reinforcement composite bars; and $A_{c,red}$ is the reduced area of the concrete section.

$$\rho_{PRF,b} = \frac{\eta . f_{cd} . \lambda . x_u}{\varepsilon_{PRF,u,d} . E_{PRF} . d} = \frac{\eta . f_{cd} . \lambda}{f_{PRF.d}} = \frac{\varepsilon_{cu2}}{\varepsilon_{PRF,u,d} + \varepsilon_{cu2}} \quad (4.16)$$

where η is a factor defining the effective strength of the concrete; f_{cd} is the design value of the concrete compressive strength; λ is a factor defining the effective height of the compression zone; x_u is the position of the neutral axis corresponding to the concrete balanced section; $\varepsilon_{PRF,u,d}$ is the limit strain of the FRP reinforcement; E_{PRF} is the FRP modulus of elasticity; d is the effective depth of a cross section; $f_{PRF.d}$ is the design FRP stress; and ε_{cu2} is the ultimate concrete strain.

Similar to as in *fib* [TG-9.3, 2007], when $\rho_f > \rho_{fb}$, flexural failure is expected to occur due to concrete crushing, and the ultimate moment resistance, M_{Rd}, in [AFGC, 2021], can be calculated, based on the equilibrium of forces and strain compatibility, with **Equation 4.17**.

$$M_{Rd} = A_{PRF}.E_{PRF}.\varepsilon_{PRF}.\left(d - \frac{\lambda x}{2}\right) = \lambda.x.\eta.f_{cd}.b.\left(d - \frac{\lambda x}{2}\right) \qquad (4.17)$$

where A_{PRF} is the area of the longitudinal reinforcement composite bars; E_{PRF} is the FRP modulus of elasticity; ε_{PRF} is the strain in the FRP reinforcement; d is the effective depth of a cross section; λ is a factor defining the effective height of the compression zone; x is the position of the neutral axis; and f_{cd} is the design value of the concrete compressive strength.

4.5.1.5 CNR-DT 203 (2006)

[CNR-DT 203, 2006] assumes that flexural failure takes place when one of the following conditions is met:

- The maximum concrete compressive strain, as defined by the current building code, is reached.
- The maximum FRP tensile strain ε_{fd} is reached. This value is computed from the characteristic tensile strength ε_{fk} with **Equation 4.18**.

$$\varepsilon_{fd} = 0.9\eta_a\left(\varepsilon_{fk}/\gamma_f\right) \qquad (4.18)$$

where η_a is an environmental conversion factor and γ_f is a material partial factor.

For both failure modes, the nominal flexural strength in a section can be determined based on the equilibrium of forces and strain compatibility.

4.5.2 Shear capacity

The shear design of FRP-reinforced concrete is similar to that of steel-reinforced concrete members. The different mechanical properties of FRP bars, however, affect shear strength and should be considered. GFRP bars have a relatively low modulus of elasticity compared to steel, low transverse shear resistance, and high tensile strength with no yielding point. In addition, the tensile strength of the bent portion of an FRP bar is significantly lower than that of the straight portion.

4.5.2.1 ACI 440.1R (2015)

The concrete shear capacity V_c of flexural members using FRP as the main reinforcement can be evaluated according to [ACI 440.1R-15] based on **Equation 4.19**.

$$V_c = \frac{2}{5}\sqrt{f_c'}b_w(kd) \tag{4.19}$$

where b_w is the width of the web; k is the ratio of the neutral-axis depth to the reinforcement depth; and d is the distance from the extreme compression fiber to the centroid of the tension reinforcement.

4.5.2.2 CAN/CSA S806 (2012) – Reapproved in 2017

In [CAN/CSA S806-12 (R2017)], the concrete shear capacity V_c for sections having an effective depth not exceeding 300 mm and with no axial load action on them, can be calculated using **Equation 4.20**.

$$V_c = 0.05\lambda\phi_c k_m k_r \left(f_c'\right)^{\frac{1}{3}} b_w d_v \tag{4.20}$$

where λ is a factor to account the concrete density; ϕ_c is the resistance factor for concrete; k_m is a coefficient taking into account the effect of moment in the section on the shear strength; k_r is coefficient taking into account the effect of reinforcement rigidity on its shear strength; f_c' is the specified concrete compressive strength; b_w is the minimum effective web width; and d_v is the effective shear depth.

According to [CAN/CSA S806-12 (R2017)], however, V_c shall not be taken as greater than $0.22\phi_c\sqrt{f_c'}b_w d_v$ or less than $0.11\phi_c\sqrt{f_c'}b_w d_v$.

4.5.2.3 fib TG-9.3 (2007)

fib [TG-9.3, 2007] presents and discusses various shear design recommendations to allow for the use of FRP reinforcement for the various design specifications available. Moreover, the modification in **Equation 4.21** has been proposed for the ACI shear equation to compensate for the unnecessary conservative shear prediction.

$$V_{c,proposed} = V_{c,ACI}\left(\frac{E_{FRP}}{E_s}\phi_s\right)^{1/3} \quad (.21)$$

where $\phi_s = \varepsilon_f / \varepsilon_y$ represents the ratio between the maximum strain allowed in the FRP reinforcement ε_f and the yield strain of the steel ε_y.

4.5.2.4 AFGC (2021)

The concrete shear capacity $V_{Rd,c}$ of flexural members with FRP as the main reinforcement is determined according to the *Eurocode-2* [CEN, 2004] equation, as shown in **Equation 4.22**.

$$V_{Rd,PFR} = C_{Rd,c}.k.\left(100\frac{E_{PRF}}{E_S}.\frac{A_{PFR}}{b_w d}f_{ck}\right)^{1/3} b_w d \quad (4.22)$$

where $C_{Rd,c} = 0.18/\gamma_c$; $k = \min\left\{2.0; 1+\sqrt{\frac{200}{d}}\right\}$; E_{PRF} is the FRP modulus of elasticity; E_S is the steel modulus of elasticity; A_{PRF} is the area of the longitudinal reinforcement composite bars; b_w is the width of the web; d is the distance from the extreme compression fiber to the centroid of the tension reinforcement; and f_{ck} is the concrete compressive strength.

4.5.2.5 CNR-DT 203 (2006)

In [CNR-TD 203, 2006], the concrete shear capacity $V_{Rd,ct}$ of flexural members with FRP as the main reinforcement can be evaluated with **Equation 4.23**.

$$V_{Rd,ct} = 1.3\left(\frac{E_f}{E_s}\right)^{1/2}.\tau_{Rd}.k.(1.2+40\rho_1).b.d \qquad (4.23)$$

where E_f and E_s are the Young's modulus of elasticity of the FRP and steel bars; τ_{Rd} is the design shear stress; k is a coefficient to be set as equal to 1 for members if more than 50% of the bottom reinforcement is interrupted and $(1.6-d)\geq 1$ if that is not the case; ρ_1 is the FRP reinforcement ratio; b is the width of rectangular cross section; and d is the effective depth of a cross section.

4.5.3 Comparison of the theoretical to experimental results

The nominal flexural-moment and shear-load capacities of the test segments were compared to the theoretical predictions according to [ACI 440.1R-15], [CAN/CSA S806-12 (R2017)], *fib* [TG-9.3, 2007], [AFGC, 2021] and [CNR-DT 203, 2006]. In all the theoretical analyses, the concrete density factor, material resistance factor, and member safety factor were taken as equal to unity. **Table 4.3** illustrates that all the design codes properly predicted the shear failure over the flexural failure for segments 13G15 and 13G20 with experimental-to-predicted flexural moment capacities less than one and experimental-to-predicted shear load capacities greater than one. In contrast, all the design codes, except [CNR-DT 203, 2006], failed to correctly predict the flexural failure of segment 7G15. While, by considering the maximum FRP strain limit ε_{fd}, the [CNR-DT 203, 2006] correctly predicted that the concrete flexural crushing failure would occur before the shear failure at an experimental-to-predicted flexural moment and shear load ratios of 1.29 and 0.81, respectively.

Moreover, **Table 4.3** shows that [ACI 440.1R-15] yielded accurate predictions for the segments' moment carrying capacity, where the experimental-to-predicted ratio for the moment capacity of segment 7G15 was 0.97. The [ACI 440.1R-15] shear predictions were, however, conservative with experimental-to-predicted ratios of 1.44 and 1.28 for 13G15 and 13G20, respectively. The ACI shear modification model proposed in *fib* [TG-9.3, 2007] compensated for the unnecessary

conservativism in the ACI shear predictions. The *fib* [TG-9.3, 2007] shear predictions were in good agreement with the experimental shear results with the experimental-to-predicted ratios of 1.11 and 0.99 for 13G15 and 13G20, respectively. Moreover, both *fib* [TG-9.3, 2007] and [AFGC, 2021] produced accurate predictions for the segments' moment carrying capacity, where the experimental-to-predicted ratio for the moment capacity of segment 7G15 was 0.96 according to both *fib* [TG-9.3, 2007] and [AFGC, 2021]. Moreover, the [AFGC, 2021] shear predictions were in good agreement with the experimental shear results with experimental-to-predicted ratios of 1.14 and 1.01 for 13G15 and 13G20, respectively.

Furthermore, **Table 4.3** illustrates that [CAN/CSA S806-12 (R2017)] accurately predicted the shear capacity of the test segments with experimental-to-predicted ratios of 1.09 and 0.97 for 13G15 and 13G20, respectively. [CAN/CSA S806-12 (R2017)], however, overestimated the moment carrying capacity of 7G15, with an experimental-to-predicted ratio of 0.86. On the other hand, considering the maximum FRP strain limit ε_{fd} in [CNR-DT, 203 2006] resulted in conservative predictions of the moment capacities of the test segments. [CNR-DT, 203 2006] underestimated the moment carrying capacity of 7G15 with an experimental-to-predicted ratio of 1.29. Conversely, [CNR-DT 203, 2006] overestimated the shear capacity of the test segments with experimental-to-predicted ratios of 0.85 and 0.76 for 13G15 and 13G20, respectively.

4.6 CONCLUSIONS

This paper reports on an experimental and theoretical investigation of the behavior of PCTL segments reinforced with GFRP bars under quasi-static cyclic flexural loading. Based on the experimental results and the theoretical study presented in this paper, the following conclusions can be drawn:

- The failure of specimen 7G15 occurred by concrete crushing, while specimens 13G15 and 13G20 failed due to shear compression and diagonal shear, respectively. Specimen 7S15, which was reinforced with steel, failed due to steel yielding, followed by concrete crushing.
- The hysteresis cycles of the GFRP-reinforced specimens reflected stable cyclic behavior with no or limited strength degradation that was less than that experienced by the steel-reinforced specimen.

- The unloading stiffness for the GFRP-reinforced specimens in all cycles was nearly equal to the reloading stiffness. The yielding of the steel bars in the steel-reinforced specimen resulted in degradation of the specimen's unloading stiffness.
- The residual deformation of the GFRP-reinforced specimens during unloading at 50% and 75% of the maximum displacement cycles was less than in the steel-reinforced specimen due to the steel bars yielding.
- The GFRP-reinforced specimens' ductility index was 78% of the steel-reinforced specimen's ductility at a similar reinforcement ratio. This difference in ductility was compensated for by the high strength reserve of specimen 7G15. Specimen 7G15 achieved a flexural strength 1.5 times that of specimen 7S15 specimen at yielding.
- The test results show that all the GFRP-reinforced specimens demonstrated adequate deformability when compared to the [CAN/CSA S6-19] code limit of 4 for rectangular sections.
- The experimental results indicate that the hysteresis cycles of the GFRP-reinforced specimens had stable cyclic behavior with no or limited strength degradation. In addition, these specimens demonstrated adequate strength, ductility index, and deformability limits.
- The experimental-to-predicted ratio of the flexural-moment capacity of specimen 7G15 indicates good predictions for [ACI 440.1R-15], *fib* [TG-9.3, 2007], and [AFGC, 2021], while [CAN/CSA S806-12 (R2017)] overestimated its flexural-moment capacity. On the other hand, [CNR-DT 203, 2006] yielded conservative predictions of its flexural-moment capacity.
- [ACI 440.1R-15] produced conservative shear-load predictions for the test specimens. Conversely, [CNR-DT 203, 2006] overestimated the shear–load capacities for the test segments. The ACI shear modification model proposed in *fib* [TG-9.3, 2007], [AFGC, 2021], and [CAN/CSA S806-12 (R2017)] yielded accurate predictions of the shear–load capacities for the test specimens.
- The experimental results were the first of their kind on the applicability of using GFRP as internal reinforcement for PCTLs under quasi-static cyclic flexural loading. These experimental results can be considered in the forthcoming provisions of ACI codes for the use of GFRP as internal reinforcement for PCTL applications.

CHAPTER 5 QUASI-STATIC CYCLIC BEHAVIOR OF PRECAST HIGH-STRENGTH CONCRETE TUNNEL SEGMENTS REINFORCED WITH GFRP BARS

FOREWORD

Authors and Affiliation:

- **Basil Ibrahim,** Ph.D. candidate, Department of Civil Engineering, Université de Sherbrooke, Sherbrooke, Quebec, Canada, J1K 2R1.
- **Salaheldin Mousa,** Postdoctoral fellow, Department of Civil Engineering, Université de Sherbrooke, Sherbrooke, Quebec, Canada, J1K 2R1.
- **Hamdy M. Mohamed,** Research Associate/Lecturer, Department of Civil Engineering, Université de Sherbrooke, Sherbrooke, Quebec, Canada, J1K 2R1.
- **Brahim Benmokrane,** Professor, Department of Civil Engineering, Université de Sherbrooke, Sherbrooke, Quebec, Canada, J1K 2R1.

Journal Title:

Engineering Structures

Paper Status:

Submitted on March 07, 2022.

Contribution:

The paper's outcomes are the first of their kind for GFRP-reinforced precast HSC tunnel lining segments under quasi-static cyclic flexural loading. The results of this work could be considered in the forthcoming provisions of codes related to the efficacy of using HSC for GFRP-reinforced PCTL segments under cyclic conditions.

ABSTRACT

Currently, there are no experimental results for the cyclic behavior of precast concrete tunnel lining (PCTL) segments reinforced internally with fiber-reinforced polymer (FRP) bars. This study investigated the cyclic behavior of precast high-strength concrete (HSC) tunnel lining segments reinforced with glass-FRP (GFRP). Full-scale segments measuring 3100 × 1500 × 250 mm were tested under quasi-static cyclic flexural loading. The test parameters included concrete compressive strength, longitudinal reinforcement ratio and transverse reinforcement configuration (closed ties versus double U-shaped ties). A theoretical prediction according to the North American codes and design guidelines, including flexural capacities, cracking moment, and crack width, was made and the results compared to the experimental results. The hysteresis response, cracking pattern, deformability, ductility index, dissipated energy, and secant stiffness damage index of the tested segments were defined, estimated, and evaluated. The experimental results of this study revealed that the hysteretic response of the precast HSC tunnel lining segments with GFRP reinforcement reveal stable cyclic behavior with no or limited strength degradation until failure. Moreover, the test results show that the GFRP-reinforced precast HSC tunnel lining segments achieved an adequate ductility index and deformability limits. Moreover, they show the effectiveness of using HSC for the GFRP-reinforced PCTL segment applications under quasi-static cyclic flexural conditions.

Keywords: Precast concrete tunnel lining (PCTL) segments; high-strength concrete (HSC); glass fiber-reinforced polymer (GFRP) bars; quasi-static cyclic flexural loading; hysteretic behavior; deformability; energy dissipated.

5.1 INTRODUCTION

Precast concrete tunnel lining (PCTL) segments are an essential element in tunneling applications because they ensure tunnel stability and user safety [ACI 544.7R-16]. The corrosion of the reinforcement bars in conventional steel-reinforced PCTL segments often causes premature strength degradation, requiring periodic maintenance and expensive repair of segments. Steel reinforcement corrosion can lead to bursting of the concrete and the loss of structural integrity. This corrosion is the most expensive and problematic weakening mechanism in conventional steel-reinforced concrete structures [ACI 440.1R-15]. The global cost of the corrosion-related maintenance strategies in the industry is valued to be about US$2.5 trillion [Koch et al., 2016]. Worldwide, the repair and maintenance cost of conventional steel-reinforced concrete infrastructure alone has been estimated at over US$100 billion annually [Chen, 2004]. As a durable and serviceable solution, noncorroding fiber-reinforced polymer (FRP) reinforcing bars can be used as an alternative to conventional steel reinforcement bars. Indeed, FRP materials exhibit several advantages over conventional steel reinforcement, such as light weight, high tensile strength, long service life, and high corrosion resistance [Wang et al., 2017; Solyom and Balázs, 2020; Pan and Yan, 2021; Benmokrane et al., 2021].

A few recent studies have investigated the feasibility of using GFRP reinforcement in PCTL segments [Caratelli et al., 2017; Spagnuolo et al., 2017,2018; Meda et al., 2019; Hosseini et al., 2022]. All of them have proven the suitability of GFRP bars as reinforcement for PCTL segments. Nevertheless, these studies focused on examining the static flexural behavior of PCTL segments. According to [ACI 544.7R-16], loads act on PCTL segments from the time of casting up to installation of segments within the tunnel-boring machine (TBM) shield. This time can be broken down into three stages: production and transient, construction, and service. The service-stage loads are embodied by the enduring loads acting on the PCTL from the groundwater, surcharges, and other loads from any circumstances such as earthquake, fire, explosion, and breakouts at cross passageways [ACI 544.7R-16]. Basically, the literature contains no information about the cyclic behavior of GFRP-reinforced PCTL segments. [Abbas, 2014] conducted an experimental study of the flexural behavior of steel-fiber reinforced concrete and conventional steel-reinforced PCTL segments under quasi-static cyclic flexural loading. In a recent experimental study on the flexural behaviour of steel-fiber reinforced concrete and conventionally steel-reinforced PCTL segments

under quasi-static cyclic flexural loading, [Abbas, 2014] illustrated that, compared to conventionally steel-reinforced PCTL segments, steel fiber-reinforced concrete segments exhibited adequate levels of ductility and energy dissipation capacities. [Abbas, 2014] demonstrated, moreover, that the steel fiber-reinforced concrete segments tested satisfied the flexural requirement under quasi-static cyclic flexural loading. Correspondingly, the performance of full-scale PCLT segments under quasi-static cyclic flexural loading needs to be investigated.

Taking advantage of the high tensile strength of FRP reinforcement bars by using high-strength concrete (HSC) is fundamental [Yost and Gross, 2002]. The compressive strength of the concrete significantly affects the strength and behavior of FRP-reinforced concrete structures. In some studies, using HSC for GFRP-reinforced concrete beams increased the overall strength and enhanced the specimens' mid-span deflections [Yost and Gross, 2002; Nanni, 1993; Kalpana and Subramanian, 2011; Goldston et al., 2017]. In contrast, [Thériault and Benmokrane, 1998] reported that high longitudinal FRP reinforcement ratios are essential in order to enhance the FRP-reinforced concrete members' behavior. With low reinforcement ratios, using HSC might soften the load–deflection behavior of FRP-reinforced HSC members and neutralize the increase in stiffness due to increased crack width and the sharp dropping of the load–deflection curve. Therefore, this study investigated the behavior of GFRP-reinforced precast HSC tunnel lining segments under quasi-static cyclic flexural loading.

This experimental study is part of an ongoing comprehensive research program carried out in the Department of Civil Engineering at the University of Sherbrooke. This works aims at improving current practices and developing more efficient design and construction approaches for the use of curvilinear GFRP bars and stirrups in precast concrete tunnel lining segments. This ongoing research investigates the behavior of full-scale GFRP reinforced PCTL segments under different loading conditions: static flexural loading [Hosseini et al., 2022]; quasi-static cyclic flexural loading; punching shear and settlement. So far, this research is the first experimental work providing experimental data using laboratory testing on the performance of GFRP-reinforced precast HSC tunnel lining segments under quasi-static cyclic flexural loading according to [ACI 374.2R-13]. The findings could be considered in forthcoming code provisions related to the effectiveness of using HSC for GFRP-reinforced PCTL segments under quasi-static cyclic flexural conditions.

5.2 RESEARCH OBJECTIVES

No experimental research results are available for the flexural cyclic behavior of GFRP-reinforced precast HSC tunnel lining segments. This study was carried out to provide experimental data on the hysteresis response of GFRP-reinforced precast HSC tunnel lining segments under quasi-static cyclic flexural loading. All the experimental and theoretical outcomes of this work are implemented to explore the feasibility of using GFRP bars as internal reinforcement for PCTL segments under quasi-static cyclic flexural loading. In addition, this work aims at assessing the suitability of using HSC for applications involving GFRP-reinforced PCTL segments.

5.3 EXPERIMENTS

5.3.1 Test segments

The experimental program was designed to provide data on the behavior of GFRP-reinforced precast HSC tunnel lining segments under quasi-static cyclic flexural loading. Three GFRP-reinforced precast HSC tunnel lining segments and one GFRP-reinforced precast NSC tunnel lining segment (as a control) were tested under quasi-static cyclic flexural loading. The test segments measured 3100 × 1500 × 250 mm. For issues of practicality, the test segments were designed with skewed ends. The test parameters in this experimental program were concrete strength (NSC versus HSC), the GFRP flexural reinforcement ratio, and the transverse reinforcement configuration (closed ties versus double U-shaped ties). **Table 5.1** gives the text matrix and reinforcement details of the test segments.

Table 5.1 Test matrix and segment details

Specimen ID	Reinforcement type	Concrete type	Concrete compressive strength (MPa)	Transverse reinforcement configuration	Longitudinal reinforcement	Transverse reinforcement
13G15	GFRP	Normal-strength concrete	52	Closed ties	13 bars No. 5	No. 4 bars @200 mm
7G15-H	GFRP	High-strength concrete	83	Closed ties	7 bars No. 5	No. 4 bars @200 mm
13G15-H	GFRP	High-strength concrete	80	Closed ties	13 bars No. 5	No. 4 bars @200 mm
7G15-U-H	GFRP	High-strength concrete	81	U-shaped ties	7 bars No. 5	No. 4 bars @200 mm

The first number in the segment label designates the number of top/bottom longitudinal reinforcement bars. The letter G stands for GFRP reinforcement. The second number indicates the nominal diameter of the longitudinal reinforcement bars. To differentiate between the segments with different transverse reinforcement configurations (closed versus double U-shaped ties), the letter U indicates segments reinforced transversely with double U-shaped ties. Lastly, the letter H identifies segments cast with HSC. Segments 7G15-H and 13G15-H are HSC segments with top/bottom longitudinal reinforcement consisting of 7 #5 GFRP bars and 13 #5 GFRP bars, respectively. Both segments (7G15-H and 13G15-H) were reinforced transversely with #4 closed GFRP ties spaced at 200 mm. Segment 7G15-U-H is an HSC segment reinforced longitudinally (top and bottom) with 7 #5 GFRP bars and transversely with #4 double U-shaped GFRP ties spaced at 200 mm. Control segment 13G15 was made with NSC and reinforced longitudinally (top and bottom) with 13 #5 GFRP bars and transversely with #4 closed GFRP ties spaced at 200 mm. All of the test segments had #5 GFRP U-shaped anchorage bars installed at each end. **Fig. 5.1** shows the dimensions and reinforcement details of the test segments. The clear cover was kept constant at 40 mm for all segments.

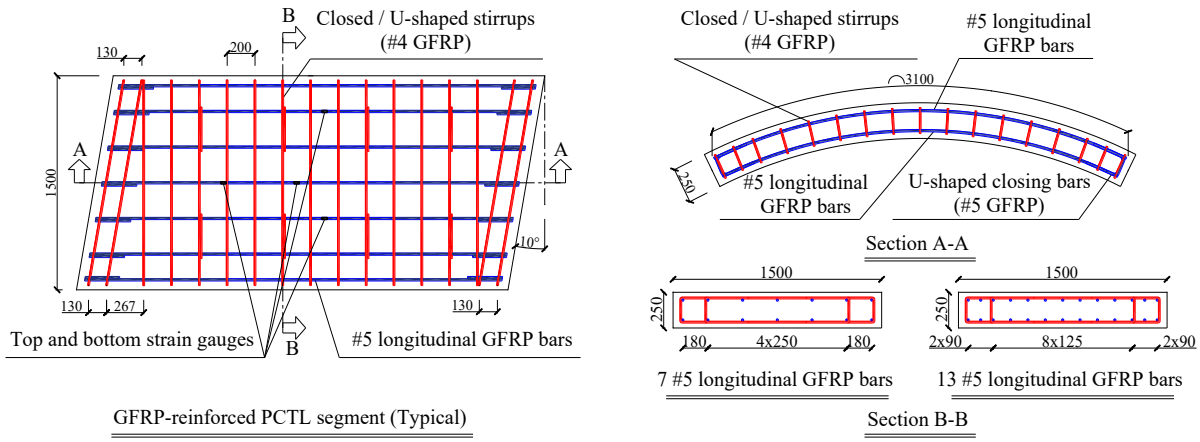

Fig. 5.1 Dimensions and reinforcement details of the test segments. (Note: all dimensions in mm)

The segments were designed in accordance with [ACI 440.1R-15] and [CAN/CSA S806-12 (R2017)]. The arch effect was taken in consideration as expressed in **Equations 5.1 – 5.4**.

$$R = P/2\cos\theta \tag{5.1}$$

$$X = \left(P\tan\theta\right)/2 \tag{5.2}$$

$$Y = P/2 \tag{5.3}$$

$$\text{Moment} = \frac{PL}{4} + \frac{P\Delta \tan\theta}{2} \tag{5.4}$$

where θ is the angle of inclination of the segment's supports from the vertical axis, and Δ is the vertical distance between the segment's centerline at mid-span and the supports' resistance forces, as illustrated in **Fig. 5.2**.

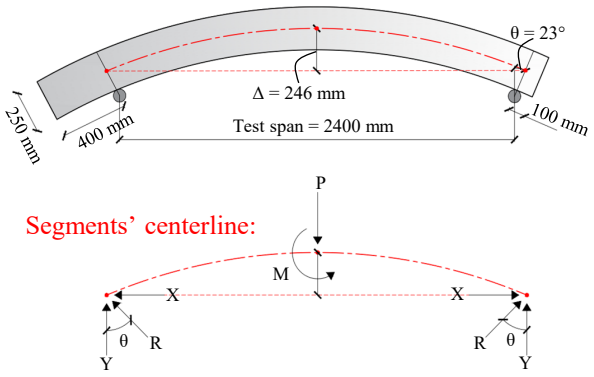

Fig. 5.2 Shcematic of the arch effect on the moment carrying capacity.

5.3.2 Materials

Table 5.2 provides the mechanical properties of the different sand-coated GFRP bars used in this study as internal reinforcement for the PCTL segments as determined according to [ASTM D7205/D7205M-21]. Number 5 (15 mm), and #4 (13 mm) GFRP bars were used for the longitudinal and transverse reinforcement, respectively, as shown in **Fig. 5.3.** Number 5 (15 mm) GFRP U-shaped closing bars were used as anchorage for the longitudinal reinforcement bars. **Fig. 5.4** schematizes the assembled GFRP cages for the test segments.

Table 5.2 Mechanical properties of the GFRP reinforcement

Reinforcement type	Bar size	Bar diameter (mm)	Nominal cross-sectional area (mm^2)	Modulus of elasticity (GPa)	Tensile strength (MPa)	Tensile strain (%)
Curvilinear-GFRP bars	#5	15.0	199	55.1	1115	2.0
U-shaped GFRP bars	#5	15.0	199	53.5	1283	2.4
GFRP ties (closed / U-shaped)	#4	13.0	129	55.6	1248	2.2

All the PCTL segments were cast at the SYM-TECH precast concrete facility in Saint-Hyacinthe, Quebec, Canada. The targeted compressive strength was 40 MPa and 80 MPa for the normal-strength concrete (NSC) and the high-strength concrete (HSC) segments, respectively. The average actual compressive strength based on the average test results of 100×200 mm concrete cylinders tested on the first day of the start of testing of the segments are listed in **Table 5.1**.

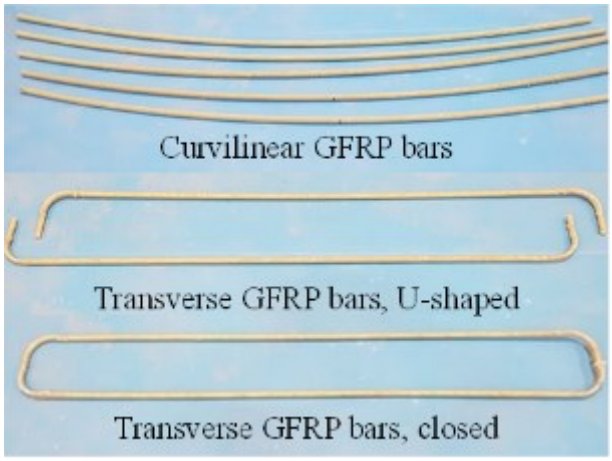

Fig. 5.3 GFRP longitudinal and transverse bars.

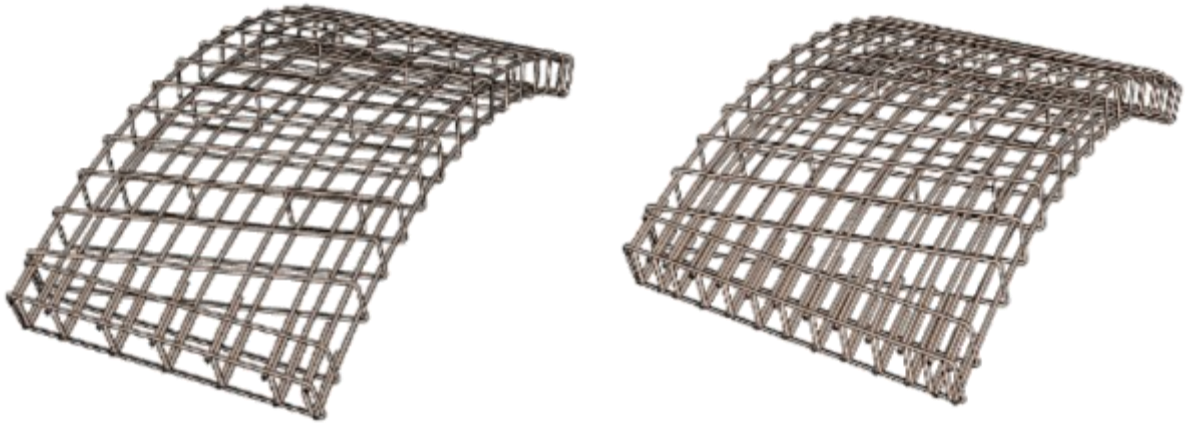

(a) (b)

Fig. 5.4 Schematic for the FRP reinforcement: (a) assembled GFRP cages with 7 top and bottom longitudinal bar segments; and (b) assembled GFRP cages with 13 top and bottom longitudinal bar segments.

5.3.3 Test setup and instrumentation

The segments were loaded under three-point bending at a displacement-controlled rate of 0.8 mm/min in the University of Sherbrooke's CFI structural laboratory using an 11,000 kN capacity MTS universal testing machine attached to a spreader beam, as shown in **Fig. 5.5(a)**. The span for the test segments was 2400 mm. Five different linear potentiometers (LPOTs) were placed to measure segment deflection at the mid- and quarter-span. Moreover, to measure the strain at mid- and quarter-span of the PCTL segments, 10 mm and 60 mm electrical resistance strain gauges were installed on the reinforcing bars and attached to the concrete surface, respectively.

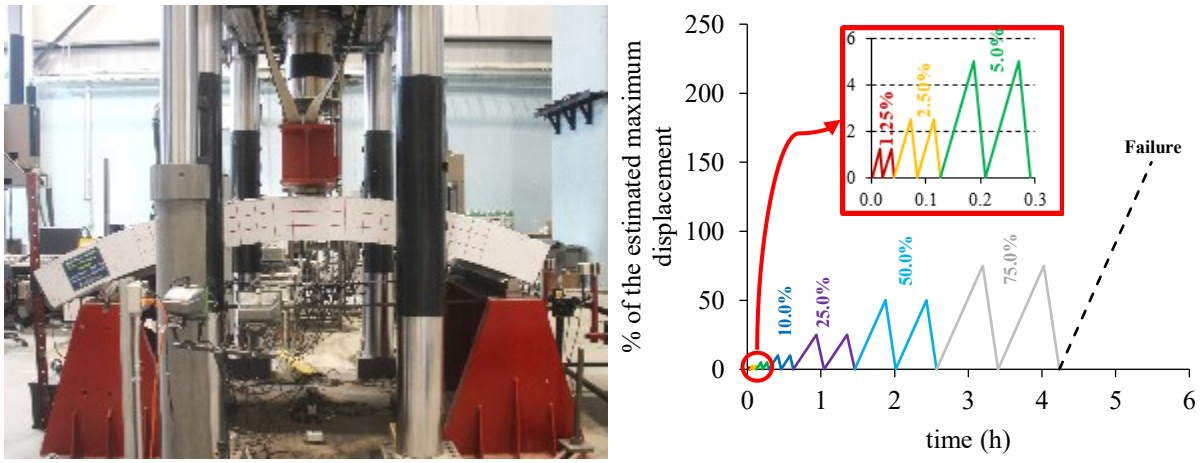

(a) (b)

Fig. 5.5 (a) Test setup; and (b) quasi-static cyclic loading scheme for the tested segments.

5.3.4 Testing protocol

For the design of the PCTL segments, the internal forces and stresses imposed on the PCTL segments from the form stripping, storage, transportation, and handling stages have to be considered. The long-term loads acting on the PCTL segments are characterized by the service loads. According to [ACI 544.7R-16], loads act on PCTL segments from the time of casting up to installation of segments within the tunnel-boring machine (TBM) shield are grouped in three stages: production and transient, construction, and service. The service stage is represented by the enduring loads acting on the PCTL from the groundwater, surcharges, and other loads from any circumstances such as earthquake, fire, explosion, and breakouts at cross passageways. In this study, the cyclic loads on the PCTL segments were simulated in accordance with the tests of structural components under slowly applied quasi-static loading in [ACI 374.2R-13]. Quasi-static

cyclic flexural loading was applied in terms of percentage of the maximum displacement (Δ_{max}) obtained from the static testing results [Hosseini et al., 2022]. Two cycles of loading and unloading were conducted for 1.25%, 2.5%, 5%, 10%, 25%, 50%, and 75% of Δ_{max}, followed by one cycle up to failure, as shown in **Fig. 5.5(b)**. In all cycles, the unloading phase ended at a minimum load of 5 kN in order to keep the test machine engaged.

5.4 ANALYSIS AND DISCUSSION OF TEST RESULTS

This section summarizes the experimental results, including the general behavior and failure mode of the test segments, as well as the segments' hysteresis response. In addition, the segments' strain distribution, crack width, ductility index and deformability are defined and discussed in this section.

5.4.1 General behavior and failure mode

Table 5.3 summarizes the failure mode and the moment-carrying capacities of all tested segments. At 1.25% and 2.5% of the maximum displacement cycles, all the test segments exhibited the same linear moment – deflection behavior, corresponding to the condition of the uncracked section, as shown in **Fig. 5.6**. After cracking occurred, the stiffness of all the tested segments decreased with almost linear moment–deflection behavior. The initial flexural cracks in the tension zone of all tested segments appeared under the loading point in the first 5% of the maximum displacement cycle. The cracking moment M_{cr} was 39 kN·m for the NSC segment (13G15) and ranged between 41 kN·m and 46 kN·m for the HSC segments (13G15-H, 7G15-H, and 7G15-U-H). In agreement with what [El-Nemr et al., 2013] reported, increasing the concrete compressive strength in the test segments resulted in higher cracking moments. The ratio of the square root of the compressive strength of segment 13G15-H (79.8 MPa) and that of segment 13G15 (52.5 MPa) was 1.23. In comparison, segment 13G15-H cracked at a moment 1.18 times higher than its counterpart segment 13G15 **(Table 5.3)**.

At 10% and 25% of the maximum displacement cycles, further flexural cracks grew within the shear span of segments 7G15-H and 7G15-U-H. Thereafter, at the first 75% of the maximum displacement cycle, the main flexural cracks in both segments (7G15-H and 7G15-U-H) widened and propagated towards the loading point. Furthermore, the cracks along the shear span in the last cycle of segments 7G15-H and 7G15-U-H started to incline towards the point of loading up until

failure occurred. The failure of segments 7G15-H and 7G15-U-H was concrete crushing controlled with a failure moment, M_n, of 202.4 kN·m and 213.4 kN·m, respectively.

Table 5.3 Experimental test results

Specimen ID	Cracking moment (kN.m)	$M_{cr.exp}/M_{cr.pred}$		Service moment[1] (kN.m)	Failure moment (kN.m)	Type of failure	Deflection at failure (mm)	Ductility Index	J-factor
		ACI 440.1R-15	CSA S806-12 (R2017)						
13G15	39	1.13	1.20	73	243[2]	Shear compression	41.3	1.31	6.1
7G15-H	41	0.80	0.83	61	202	Concrete crushing	54.0	1.59	4.1
13G15-H	46	0.90	0.95	86	288[3]	Shear compression	45.0	1.58	4.0
7G15-U-H	41	0.79	0.84	64	213	Concrete crushing	59.5	1.78	4.2

[1] The service moment of the test specimens is estimated at 0.3 of M_n.
[2] The shear load failure = 178 kN.
[3] The shear load failure = 211 kN.

Segments 13G15-H and 13G15 behaved similarly before 75% of the maximum displacement cycle. Beyond this stage, both segments started to develop a main shear crack that propagated until shear–compression failure occurred. The shear load failure V_n for segment 13G15-H and its counterpart segment 13G15 was 211 kN and 178 kN, respectively. Indeed, increasing the concrete compressive strength of segment 13G15-H increased its ultimate carrying capacity by 18.4% compared to its counterpart segment 13G15, as shown in **Table 5.3**.

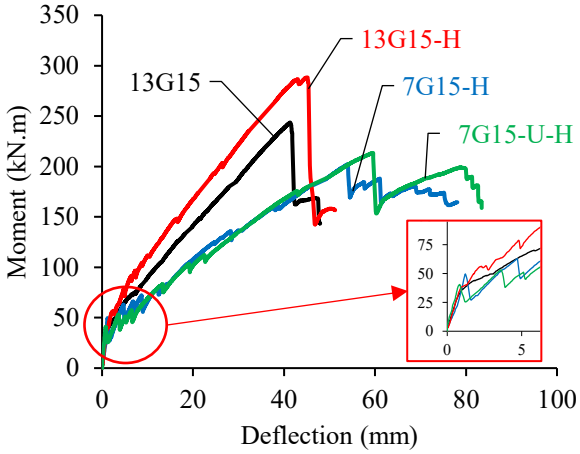

Fig. 5.6 Envelope moment – deflection relationship for all tested segments.

According to [Thériault and Benmokrane, 1998], using a low longitudinal reinforcement ratio in FRP-reinforced HSC members might soften the load–deflection behavior and neutralize the increased stiffness due to increased crack width and the load–deflection curve sharply dropping. Therefore, increasing the longitudinal reinforcement ratio in the HSC segments was important in enhancing segment behavior. The two HSC segments (7G15-H and 13G15-H) had longitudinal reinforcement ratios of 0.50% and 0.90%, respectively. Segment 13G15-H had an ultimate strength 42.5% higher than segment 7G15-H. Furthermore, increasing the concrete strength yielded efficient use of the GFRP reinforcement. The increase in the post-cracking flexural stiffness (77%) of segment 13G15-H compared to 7G15-H was approximately similar to the percentage increase in the segment's longitudinal reinforcement ratio (80%), as shown in **Fig. 5.6**.

5.4.2 Hysteresis response

The hysteresis behavior, for all tested segments, is shown in the form of the moment versus mid-span deflection, as depicted in **Fig. 5.7**. The hysteresis response for the HSC segments, in all second excursion loading cycles, reflected stable cyclic behavior with no or limited strength degradation until failure. Moreover, the primary dissipated energy computations for the test segments, under quasi-static cyclic loading, were carried out by determining the hysteretic area of each cycle up to failure. **Fig. 5.8** shows that increasing segment 13G15-H's concrete compressive strength yielded an overall dissipated energy 36.3% higher than its counterpart (13G15). Moreover, increasing the reinforcement ratio from 0.50% (7G15-H) to 0.90% (13G15-H) increased the overall dissipated energy by 22.5%. Therefore, a higher reinforcement ratio in the HSC segments subjected to quasi-static cyclic flexural loading did not prevent the possibility of increasing energy storage in the inelastic domain.

Under the quasi-static cyclic flexural loading, the damage caused to the test segments was established using the damage index. Several proposals currently ascertain the damage index based on a wide range of parameters, such as deformation [Cosenza et al., 1993], stiffness [Meyer et al., 1983; Ghobarah et al., 1999; Kim et al., 2005], and energy absorption [Fardis et al., 1993]. Based on the damage index proposed by [Meyer et al., 1983], which computes the damage index as the ratio of the initial stiffness to the reduced secant stiffness at the maximum displacement of each cycle, the effect of the test parameters on the secant stiffness index (KI) in loading and unloading was determined for the test segments. The value of this parameter and its changes is the index of

damage in the segments. This stiffness index is described as the cycle's secant stiffness $K_{sec.i}$ to the after-cracking stiffness ratio of the segments.

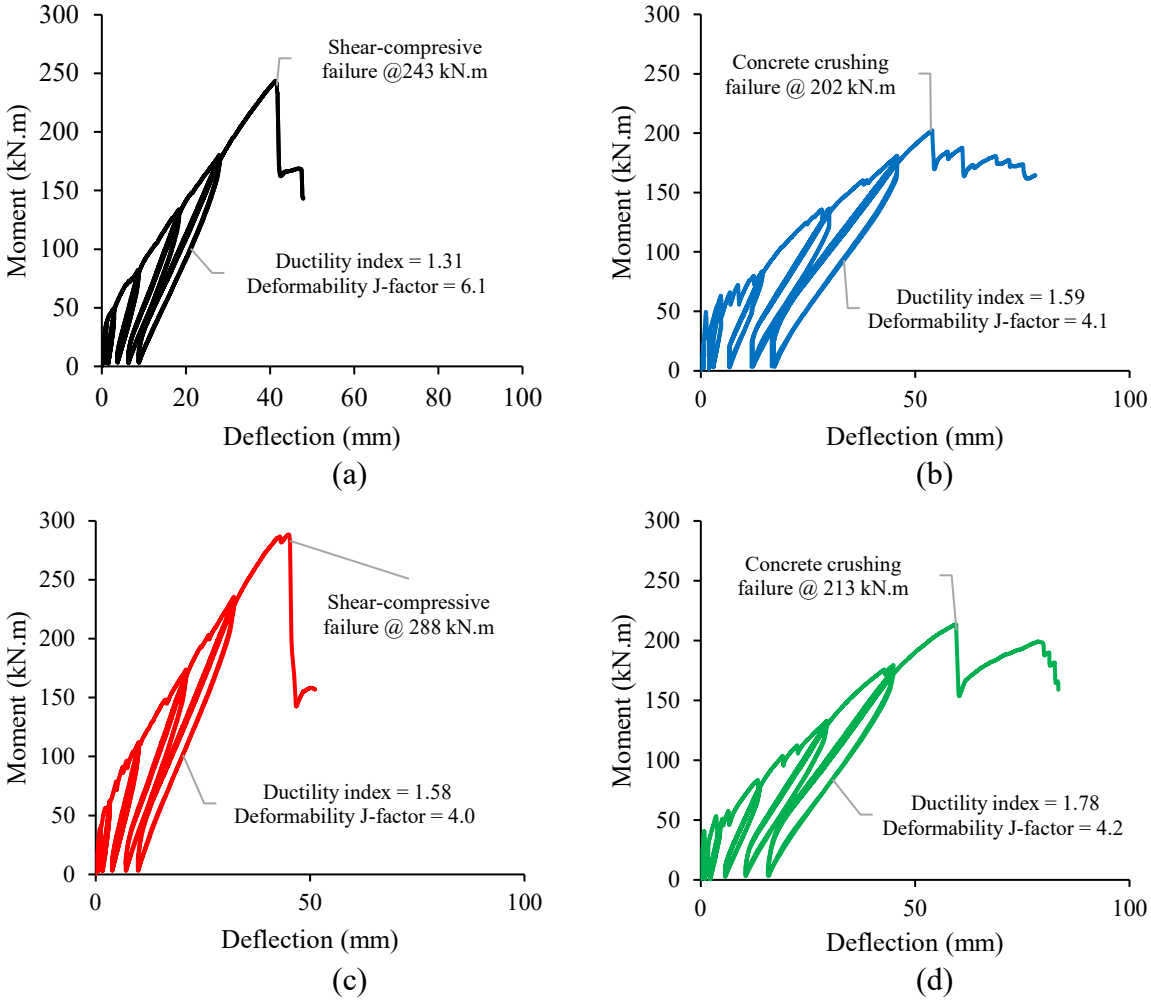

Fig. 5.7 Hysteresis response for (a) segment 13G15; (b) segment 7G15-H; (c) segment 13G15-H; and (d) segment 7G15-U-H.

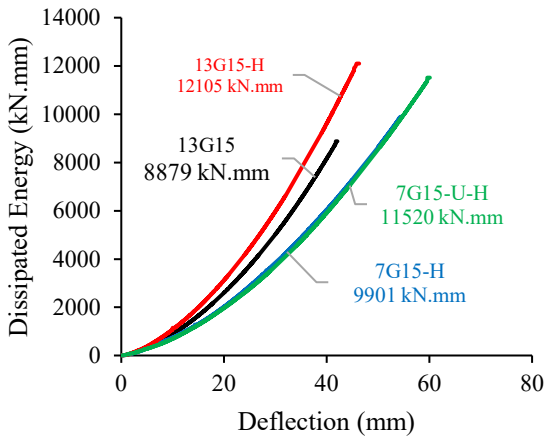

Fig. 5.8 Dissipated energy versus normalized deflection for all the test segments.

Fig. 5.9 shows that increasing the concrete compressive strength did not significantly affect the rate of decrease of stiffness. By increasing the concrete compressive strength in 13G15-H segment, its residual stiffness at ultimate deflection was similar to that of segment 13G15. Moreover, increasing the longitudinal reinforcement ratio of the HSC segments (13G15-H and 7G15-H) increased their residual stiffness at ultimate deflections. The residual stiffness at ultimate deflection for 13G15-H (reinforcement ratio of 0.90%) was 50% higher than that of 7G15-H (reinforcement ratio of 0.50%).

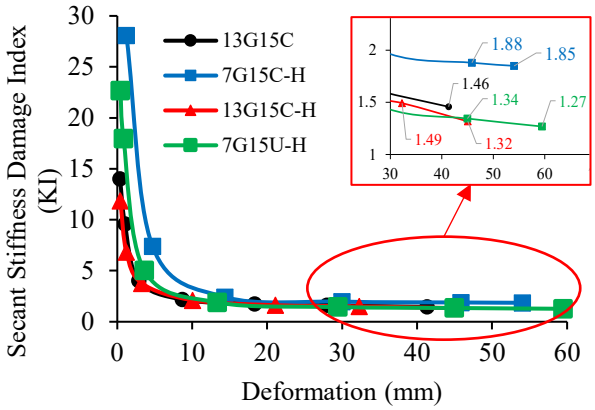

Fig. 5.9 Secant stiffness damage index versus normalized deflection for all the test segments.

5.4.3 Strain development and distribution

Fig. 5.10 presents the moment versus the recorded mid-span strains for all tested segments. Up to 5% of the maximum displacement cycle, the concrete strains in the location of the top concrete fibers of the mid-span were insignificant (-75 to -90 με) in all tested segments, as shown in **Fig. 5.10(a)**. The maximum recorded mid-span concrete compressive strain in segments 13G15-H, 7G15-H, 7G15-U-H, and 13G15 were -2450 με, -2350 με, -2950 με, and -3285 με, respectively. The test results indicate that the strains in the top concrete fibers at the quarter-span were less than that at the mid-span. The maximum recorded concrete compressive strains at the quarter-span in segments 13G15-H, 7G15-H, 7G15-U-H, and 13G15 were -1089 με, -476 με, -617 με, and -1074 με, respectively.

Likewise, there were no significant strain-gauge readings up to 5% of the maximum displacement cycle, in either the top or bottom longitudinal GFRP bars. The bottom longitudinal GFRP bars in all tested segments exhibited a gradual strain increase until failure with mid-span strain-gauge readings of 11350 με, 14020 με, 17890 με, and 9235 με (57%, 70%, 89%, and 46% of the GFRP bars' ultimate tensile strain) for 13G15-H, 7G15-H, 7G15-U-H, and 13G15, respectively, as shown in **Fig. 5.10(b)**. The maximum recorded quarter-span strains in the bottom longitudinal GFRP bars in segments 13G15-H, 7G15-H, 7G15-U-H, and 13G15 were 5791 με, 7527 με, 7380 με, and 5661 με, respectively. Moreover, the strain-gauge readings show that the top longitudinal GFRP bars in all tested segments were under tension, which enhanced segment flexural strength. The recorded mid-span strains in the top longitudinal GFRP bars of 13G15-H, 7G15-H, 7G15-U-H, and 13G15 at failure were 4120 με, 4560 με, 5275 με and 2570 με, respectively. The maximum recorded quarter-span strains in the top longitudinal GFRP bars in segments 13G15-H, 7G15-H, 7G15-U-H, and 13G15 were 1092 με, 2332 με, 2105 με, and 930 με, respectively.

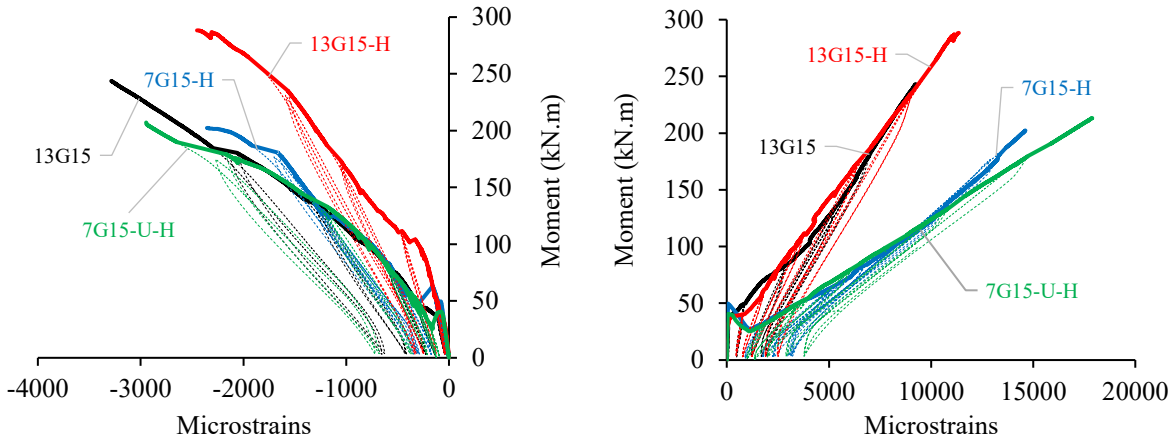

Fig. 5.10 Moment – strain relationship at mid-span at (a) concrete surface; and (b) bottom reinforcement bars.

Based on the strain-gauge readings for the concrete and both the top and bottom GFRP bars at segment mid-span, a cross-sectional analysis and an experimental neutral-axis depth of the segments were carried out and are discussed below. The strain profile along the cross section in all tested segments was linear with some deviation, as shown in **Fig. 5.11(a)**. Bernoulli's hypothesis (plane sections perpendicular to the neutral axis before deformation stay plane and perpendicular to the neutral axis after deformation and up to failure) has been considered as an appropriate simplification for this behavior. Before 5% of the maximum displacement cycles was reached and prior to cracking, the position of the neutral axis, in all tested segments, was located at the geometrical centroid of the segments' cross section. Immediately after cracking occurred, the neutral-axis depth decreased rapidly and then stabilized until failure occurred, as shown in **Fig. 5.11(b)**. Moreover, **Fig. 5.11(b)** illustrates that the neutral-axis depth in the HSC segments was less than that of the control NSC segment 13G15. This behavior can be explained by exploiting the higher tensile strength of the GFRP reinforcing bars with HSC. Although both segments 13G15 and 13G15-H had the same reinforcement ratio and the same reinforcement tensile strength, the maximum recorded strains in the bottom GFRP reinforcement at mid-span for these segments was 9235 με and 11350 με (46% and 57% of the GFRP bars' ultimate tensile strain), respectively. We concur with [Faza and GangaRao, 1993] that the use of high-strength concrete was fundamental to exploiting the high tensile strength of the GFRP bars. Increasing the concrete compressive strength in segment 13G15-H resulted in the GFRP reinforcement bars achieving more tensile

strain. Thus, the neutral-axis depth in HSC segment 13G15-H was less than that of the control NSC segment 13G15.

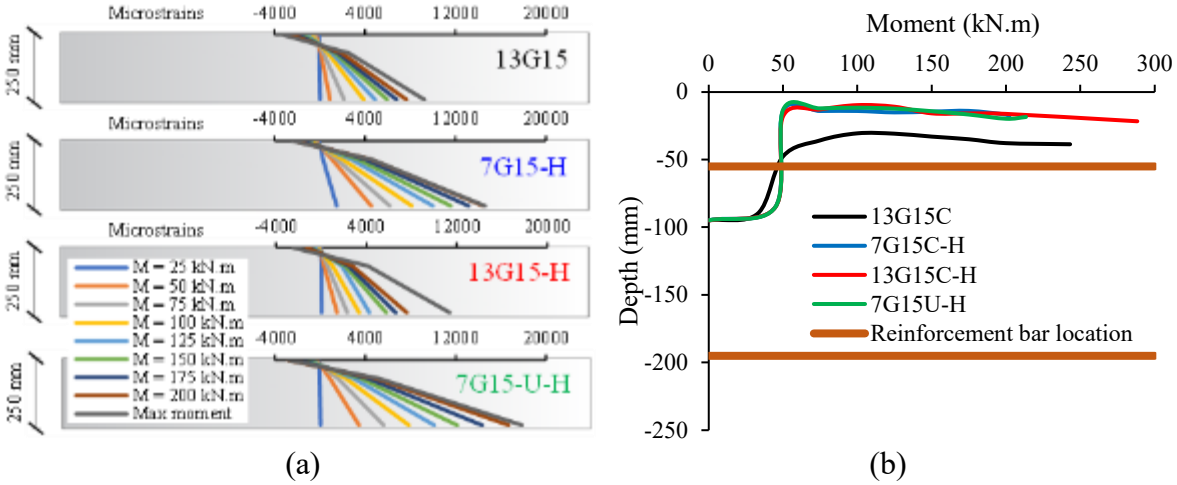

(a) (b)

Fig. 5.11 (a) Strain along the mid-span cross section; and (b) neutral-axis depth for all the test segments.

5.4.4 Crack-width

Although concrete fractures under cyclic loading are characterized by larger cracks and strains than concrete fractures under static loading, the linear behavior of the GFRP-reinforced PCTL segments reduced the cyclic effects on crack width and eliminated the residual cracks at the end of each unloading cycle. The LVDTs readings at the end of each unloading cycle, for all tested segments, indicated that the crack widths were insignificant (nearly equal to zero).

Fig. 5.12 shows the effect of concrete strength on the cracking behavior of all tested segments under quasi-static cyclic flexural loading. Segment 13G15-H produced higher cracking moments compared to its counterpart segment 13G15. The higher concrete strength, under quasi-static cyclic flexural loading resulted in narrower cracks with closer crack spacing in all loading cycles. **Fig. 5.13** shows the moment crack-width relationship for all the test segments. At both service and ultimate load levels, segment 13G15 evidenced wider cracks compared to 13G15-H. The crack width in 13G15 was about 130% greater than that of 13G15-H at 2000 με. Moreover, increasing the reinforcement ratio from 0.50% (7G15-H) to 0.90% (13G15-H) generally enhanced the cracking behavior at both service and ultimate load levels. The crack width in 7G15-H was about 5% greater than that of 13G15-H at 2000 με **(Fig. 5.13)**.

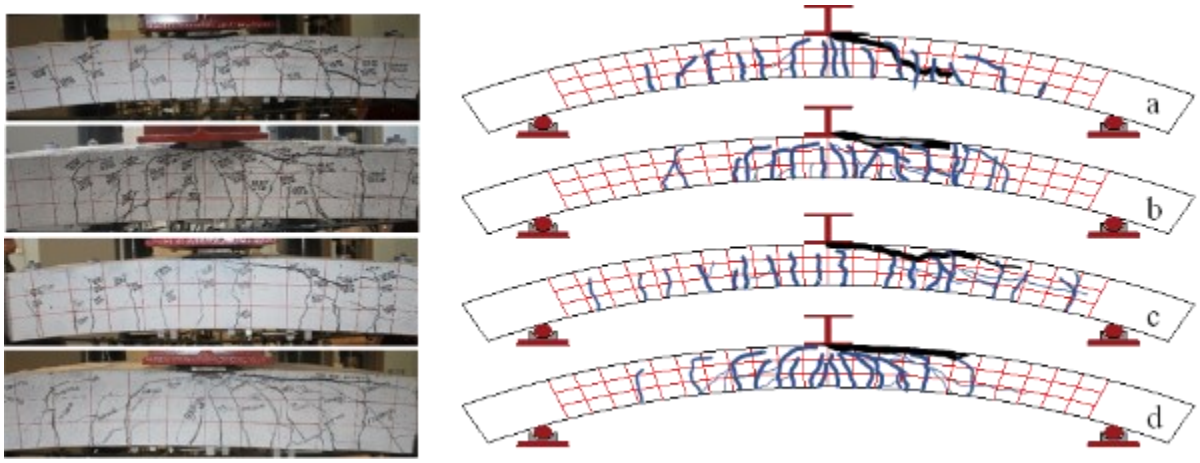

Fig. 5.12 Cracking pattern at failure in (a) segment 13G15; (b) segment 7G15-H; (c) segment 13G15-H; and (d) segment 7G15-U-H.

Although segments 7G15-H and 7G15-U-H had the same hysteresis response, segment 7G15-H produced higher cracking moments under the quasi-static cyclic flexural loading than segment 7G15-U-H. **Fig. 5.13** reveals that the closed tie configurations enhanced the crack distribution within the section. Both segments (7G15-H and 7G15-U-H) evidenced similar crack widths at service load levels. Nevertheless, the cracks at M_n in 7G15-U-H were wider than those with to the closed tie configuration in segment 7G15-H. The crack width in 7G15-U-H was about 25% greater than that of 7G15-H at M_n **(Fig. 5.13)**.

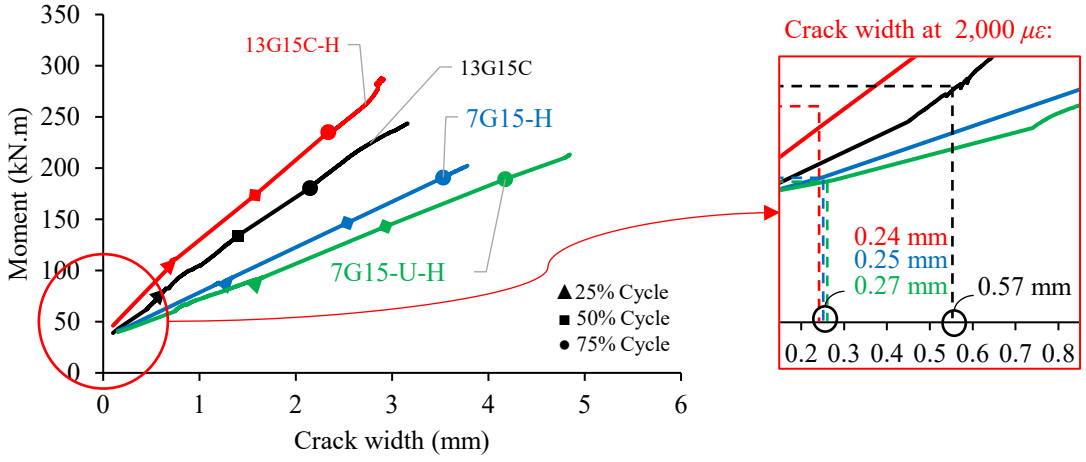

Fig. 5.13 Moment – crack-width relationship for all test segments.

5.4.5 Energy-based ductility index

The structural member's capability of resisting inelastic deformation without lessening in the carrying capacity is an essential requirement in the varied design codes and provisions, which is defined as the structural ductility. Unlike conventionally steel-reinforced concrete members, the ductility of FRP-reinforced concrete members can be indirectly computed in terms of energy absorption or deformability [Grace et al., 1998].

The ductility index, μ_e, for all tested segments was computed using the energy absorption approach proposed by [Naaman and Jeong, 1995], as expressed in **Equation 5.5**.

$$\mu_e = \frac{1}{2}\left(\frac{E_{tot}}{E_{el}} + 1\right) \tag{5.5}$$

where E_{tot} is the total energy computed as the area under the segment's load-deflection curve; and E_{el} is the elastic energy released upon failure, computed as the are of the triangle formed at failure load of the segment by the line having the weighted average slope of the two initial straight lines of the segment's load-deflection curve.

Table 5.3 lists the computed μ_e for the test segments. Considering the concrete compressive strength under quasi-static cyclic flexural loading, segment 13G15-H had a ductility index 21.2% higher than that its NSC counterpart segment (13G15). Moreover, the computed μ_e was not affected for the HSC segments by increasing the reinforcement ratio. Indeed, both 13G15-H (reinforcement ratio of 0.90%) and 7G15-H (reinforcement ratio of 0.50%) had a computed μ_e of 1.58 and 1.59, respectively. The U-shaped ties of the 7G15-U-H segment hardly allowed any more deflection of the longitudinal reinforcement than that of the 7G15-H specimen, which tended to straighten. Therefore, using the U-shaped ties in 7G15-U-H resulted in a higher ductility index for the segment, given that the computed microstrains for 7G15-U-H was 11.5% higher than that for 7G15-H.

5.4.6 Deformability

The deformability of the tested segments was determined using the J-factor approach of [Jaeger et al., 1997], which has been adopted in the *Canadian Highway Bridge Design Code* [CAN/CSA S6-19]. The approach considers the moment-carrying capacity and the curvature at both the service and ultimate conditions of FRP-reinforced concrete members, as shown in **Equation 5.6**. Throughout the loading history from the service loading state to the ultimate state, the J-factor illustrates the deflection and cracking of FRP-reinforced concrete members. As shown by **Fig. .7**, a higher J-factor provides more appropriate warning of impending failure of the FRP-reinforced member.

$$J = \frac{M_{ultimate}}{M_s} \times \frac{\psi_{ultimate}}{\psi_s} \tag{5.6}$$

where ψ_s is the curvature at the service condition (strain at top concrete surface = 1000 με); ψ_u is the curvature at ultimate; M_s is the moment at the service condition; and M_u is the ultimate moment. **Table 5.3** shows that all tested segments demonstrated adequate deformability under quasi-static cyclic flexural loading when compared to the [CAN/CSA S6-19] limit of 4 for rectangular sections. The deformability J-factors for segments 13G15-H, 7G15-H, 7G15-U-H and 13G15 were 4.03, 4.05, 4.22, and 6.08, respectively.

5.5 THEORETICAL STUDY

5.5.1 Flexural capacity

The flexural capacities of GFRP-reinforced concrete members can be computed based on assumptions similar to those applied to concrete members reinforced with steel [Mousa et al., 2019; Ruan et al., 2020]. According to both [ACI 440.1R-15] and [CAN/CSA S806-12 (R2017)], compression-controlled flexural behavior is the preferable mode of failure for FRP-reinforced concrete members. The ultimate usable compressive strain in the concrete ε_{cu}, in which the concrete crushing failure occurs, is assumed to be 0.003 in [ACI 440.1R-15] and 0.0035 in [CAN/CSA S806-12 (R2017)].

[ACI 440.1R-15] allows the use of the rectangular stress block model to replace the more detailed approximation of the concrete stress distribution.

Based on the work of [Nedderman, 1973] on steel-reinforced HSC structures, the rectangular stress block model in [ACI 440.1R-15] has an average stress of $0.85f_c^{'}$ ($\alpha_1 = 0.85$), with a lower β_1 limit of 0.65 for concrete strengths greater than 55 MPa. The rectangular stress block model parameter β_1 could be expressed by **Equation 5.7**.

$$\beta_1 = 0.85 - 0.05\left(f_c^{'} - 27.6\right)/6.9, \text{ where } 0.65 \le \beta_1 \le 0.85 \qquad (5.7)$$

Canadian standards [CAN/CSA S806-12 (R2017)] and [CAN/CSA S6-19] also replace the more detailed approximation of the concrete stress distribution over the cross section with the rectangular stress block model. The rectangular stress block model parameters in [CAN/CSA S806-12 (R2017)] and [CAN/CSA S6-19], for concrete strengths not greater than 80 MPa can be expressed with **Equations 5.8 and 5.9**.

$$\alpha_1 = 0.85 - 0.0015\left(f_c^{'}\right) \ge 0.67 \qquad (5.8)$$

$$\beta_1 = 0.97 - 0.0025\left(f_c^{'}\right) \ge 0.67 \qquad (5.9)$$

For the segments that failed in flexure (7G15-H and 7G15-U-H), the ultimate moment capacity predictions for both [ACI 440.1R-15] and [CAN/CSA S806-12 (R2017)] codes were evaluated

against their experimental ultimate moment-carrying capacities. **Table 5.4** shows the experimental-to-predicted ultimate moment capacity ($M_{\exp}/M_{pred}$) for the segments 7G15-H and 7G15-U-H, revealing that both [ACI 440.1R-15] and [CAN/CSA S806-12 (R2017)] were unconservative for the HSC segments. The $M_{\exp}/M_{pred}$ for the HSC segments 7G15-H and 7G15-U-H was 0.72 and 0.77, respectively, according to [ACI 440.1R-15]. According to [CAN/CSA S806-12 (R2017)], the $M_{\exp}/M_{pred}$ for the HSC segments 7G15-H and 7G15-U-H was 0.68 and 0.72, respectively **(Table 5.4)**.

[Ozbakkaloglu and Saatcioglu, 2004] proposed a modification for the rectangular stress block model for high-strength concrete in which α_1 should be reduced continuously from 0.85 at a rate of 0.014 for each 10 MPa of strength in excess of 30 MPa **(Equation 5.10)**, and β_1 should be reduced continuously from 0.85 at a rate of 0.02 for each 10 MPa of strength in excess of 30 MPa **(Equation 5.11)**.

$$\alpha_1 = 0.85 - 0.0014\left(f_c^{'} - 30\right), \text{ where } 0.72 \le \alpha_1 \le 0.85 \qquad (5.10)$$

$$\beta_1 = 0.85 - 0.002\left(f_c^{'} - 30\right), \text{ where } 0.67 \le \beta_1 \le 0.85 \qquad (5.11)$$

To examine the approach of [Ozbakkaloglu and Saatcioglu, 2004], the moment capacity for HSC segments 7G15-H and 7G15-U-H was calculated with **Equations 5.10 and 5.11** and compared to the measured values. Their approach showed the [ACI 440.1R-15] and [CAN/CSA S806-12 (R2017)] predictions **(Table 5.4)** were enhanced. The $M_{\exp}/M_{pred}$ of these segments with the proposed model was 0.76 and 0.81, respectively, according to [ACI 440.1R-15]. According to [CAN/CSA S806-12 (R2017)], the $M_{\exp}/M_{pred}$ for these segments using the approach of [Ozbakkaloglu and Saatcioglu, 2004] was 0.71 and 0.76, respectively **(Table 5.4)**.

[Hadhood et al., 2018] proposed a modification of the ACI model, in which α_1 should be reduced continuously from 0.85 at a rate of 0.02 for each 7 MPa of strength in excess of 28 MPa **(Equation 5.12)**, and β_1 should be reduced continuously from 0.85 at a rate of 0.05 for each 7 MPa of strength in excess of 28 MPa **(Equation 5.13)**, with a maximum concrete strain of 0.003, as proposed in [ACI 440.1R-15].

$$\alpha_1 = 0.85 - 0.02\left(f_c^{'} - 28\right)/7, \text{ where } 0.65 \le \alpha_1 \le 0.85 \qquad (5.12)$$

$$\beta_1 = 0.85 - 0.05\left(f_c^{'} - 28\right)/7, \text{ where } 0.65 \le \beta_1 \le 0.85 \qquad (5.13)$$

Moreover, [Hadhood et al., 2018] proposed a modification for the *CSA* model, in which α_1 should be reduced continuously from 0.85 at a rate of 0.02 foreach 10 MPa of strength in excess of 28 MPa **(Equation 5.14)**, and β_1 should be reduced continuously from 0.97 at a rate of 0.035 for each 10 MPa of strength in excess of 28 MPa **(Equation 5.15)** with a maximum concrete strain of 0.0035, as proposed in [CAN/CSA S806-12 (R2017)].

$$\alpha_1 = 0.85 - 0.002\left(f_c^{'}\right), \text{ where } 0.67 \le \alpha_1 \le 0.80 \qquad (5.14)$$

$$\beta_1 = 0.97 - 0.0035\left(f_c^{'}\right), \text{ where } 0.67 \le \beta_1 \le 0.90 \qquad (5.15)$$

The approach of [Hadhood et al., 2018], showed further enhancement in the [ACI 440.1R-15] and [CAN/CSA S806-12 (R2017)] predictions for HSC segments 7G15-H and 7G15-U-H **(Table 5.4)**. The $M_{\exp}/M_{pred}$ for these segments using the approach of [Hadhood et al., 2018] was 0.81 and 0.79, respectively, according to [ACI 440.1R-15]. According to [CAN/CSA S806-12 (R2017)], the $M_{\exp}/M_{pred}$ for these segments using the approach of [Hadhood et al., 2018] was 0.74 and 0.79, respectively **(Table 5.4)**.

Table 5.4 Experimental-to-predicted moment capacities and crack-widths

Segment ID	M_n (kN.m)	M_{exp}/M_{pred} at M_n					
		ACI 440.1R-15	CSA S806-12 (R2017)	ACI – approach I[1]	CSA – approach I[1]	ACI – approach II[2]	CSA – approach II[2]
7G15-H	202	0.72	0.68	0.76	0.71	0.81	0.74
7G15-U-H	213	0.77	0.72	0.81	0.76	0.79	0.79
Segment ID	W_{exp} (mm) at 2,000 με	W_{exp}/W_{pred} at 2,000 με					
		ACI 440.1R-15		CAN/CSA S6-19		AASHTO 2018	
13G15	0.57	0.93		1.23		1.09	
7G15-H	0.25	0.92		1.21		1.08	
13G15-H	0.24	0.91		1.26		1.09	
7G15-U-H	0.27	0.92		1.21		1.08	
Average		0.92		1.23		1.08	
COV (%)		0.9		1.9		0.7	

[1] [Ozbakkaloglu and Saatcioglu, 2004].
[2] [Hadhood et al., 2018].

5.5.2 Cracking moment

The cracking moments for the test segments were predicted with **Equation 5.16**, where f_r is calculated from **Equation 5.17** for [ACI 440.1R-15] and from **Equation 5.18** for [CAN/CSA S806-12 (R2017)].

$$M_{cr} = \frac{f_r I_g}{y_t} \tag{5.16}$$

$$f_r = 0.62\lambda\sqrt{f_c'} \tag{5.17}$$

$$f_r = 0.6\lambda\sqrt{f_c'} \tag{5.18}$$

where f_r is the concrete modulus of rupture; I_g is the concrete cross-sectional moment of inertia about the centroid axis; f_c' is the concrete compressive strength; and λ is a concrete density factor. The cracking moment predictions for both the [ACI 440.1R-15] and [CAN/CSA S806-12 (R2017)] equations were evaluated against the experimental cracking moments of the test segments, as shown in **Table 5.3**. It is worth mentioning that, to take into consideration the segments' self-weight, the segments' self-weight was deducted from the segments' predicted cracking moment. For the HSC segments, [CAN/CSA S806-12 (R2017)] produced slightly better predictions for cracking moments than [ACI 440.1R-15], due to the smaller modulus of rupture considered in the former. According to the equation in [CAN/CSA S806-12 (R2017)] the HSC segments (13G15-H, 7G15-H, 7G15-U-H) had $M_{cr.\exp}/M_{cr.pred}$ ranging between 0.83 and 0.95 with an average and coefficient of variance (CoV) of 0.87 and 7.6%, respectively. In contrast, using the equation in [ACI 440.1R-15], the HSC segments (13G15-H, 7G15-H, 7G15-U-H) had $M_{cr.\exp}/M_{cr.pred}$ ranging between 0.79 and 0.90 with an average and COV of 0.83 and 7.3%, respectively. Moreover, both [ACI 440.1R-15] and [CAN/CSA S806-12 (R2017)] underestimated the cracking moment for the NSC segment (13G15). The $M_{cr.\exp}/M_{cr.pred}$ for the NSC segment (13G15) was 1.13 and 1.20 using the [ACI 440.1R-15] and [CAN/CSA S806-12 (R2017)] equations, respectively.

5.5.3 Crack-width

Unlike steel, FRP resists corrosion. Consequently, the design codes provisions for FRP-reinforced concrete structures allow for a larger crack width than for steel-reinforced concrete members [El-Nemr et al., 2013].

[ACI 440.1R-15] has adopted, in **Equation 5.19**, an indirect procedure proposed by [Ospina and Bakis, 2007] that uses the maximum spacing of the FRP reinforcement bars.

$$S_{\max} = 1.15\frac{E_f w}{f_{fs} k_b} - 2.5c_c \le 0.92\frac{E_f w}{f_{fs} k_b} \tag{5.19}$$

where $S_{\max}$ is the maximum allowable center-to-center bar spacing (mm); w is the crack width (mm); f_{fs} is the FRP stress level at service load (MPa); E_f is the FRP design/guaranteed modulus of elasticity (MPa); c_c is the clear cover; and k_b is coefficient for the bond between the FRP and the concrete.

Similar to [ACI 440.1R-15], [AASHTO, 2018] also recommends an indirect procedure that controls flexural-crack widths with the maximum spacing of the GFRP bars using a limit of 0.5 mm for crack width **(Equation 5.20)**.

$$s \le \min\left(1.15\frac{C_b E_f w}{f_{fs}} - 2.5c_c ; 0.92\frac{C_b E_f w}{f_{fs}}\right) \tag{5.20}$$

where w, f_{fs}, E_f, and c_c are the parameters described above, and C_b is a reduction factor that accounts for the degree of bond between the GFRP reinforcing bars and surrounding concrete.

[AASHTO, 2018] states that the bond reduction factor C_b shall be set equal to 0.83 unless otherwise specified by the owner or established through independent physical tests approved by the owner.

Based on the physical model proposed by [Frosch, 1999], [CAN/CSA S6-19] uses **Equation 5.21** to calculate the crack width for members under full-service loads and with FRP strain values in

the tension zone exceeding 0.0015. The code limits the crack width to 0.5 mm and 0.7 mm for members subjected to aggressive environment and nonaggressive environments, respectively.

$$w_{\max} = 2\frac{f_{fs}}{E_f}\frac{h_2}{h_1}k_b\sqrt{d_c^2+\left(\frac{s}{2}\right)^2} \qquad (5.21)$$

where $w_{\max}$ is the maximum permissible crack width at the tension face (mm); h_1 is the distance from the centroid of tension reinforcement to the neutral-axis; h_2 is the distance from the extreme flexural tension surface to the neutral axis; d_c is the clear cover that shall not be taken as greater than 50 mm; and k_b is coefficient for the bond between the FRP and the concrete. [CAN/CSA S6-19] recommends the k_b value of 0.8 and 1.0 for sand-coated and deformed FRP bars.

The predictions with the [ACI 440.1R-15], [CAN/CSA S6-19], and [AASHTO, 2018] provisions were evaluated against the experimentally recorded crack widths of the test segments. **Table 5.4** gives the experimental-to-predicted crack widths $w_{\exp}/w_{pred}$ for all tested segments. **Fig. 5.14** compares the predicted results of the [ACI 440.1R-15], [CAN/CSA S6-19], and [AASHTO, 2018] provisions against the experimental recorded crack widths for all tested segments. As shown in **Fig. 5.14**, the conservative k_b value of 1.4, recommended in [ACI 440.1R-15], resulted in conservative predictions of the crack widths. The $w_{\exp}/w_{pred}$ for the tested segments using the [ACI 440.1R-15] equation ranged between 0.91 and 0.93 at 2,000 με with an average of 0.92 and a corresponding COV of 0.9%. **(Table 5.4)**. In contrast, the recommended small value of k_b (0.8) in [CAN/CSA S6-19] compared to that recommended in [ACI 440.1R-15] contributed to underestimating the crack widths **(Fig. 5.14)**. As shown in **Table 5.4**, the $w_{\exp}/w_{pred}$ for the tested segments using the [CAN/CSA S6-19] provision ranged between 1.21 and 1.26 at 2,000 με with an average of 1.23 and a corresponding COV of 1.9%. Using a bond reduction factor (C_b) of 0.83 as in [AASHTO, 2018] provided accurate predictions for the crack width, as shown in **Fig. 5.14**, with a $w_{\exp}/w_{pred}$ ranging between 1.08 and 1.09 at 2,000 με with an average of 1.08 and a corresponding COV of 0.7% **(Table 5.4)**.

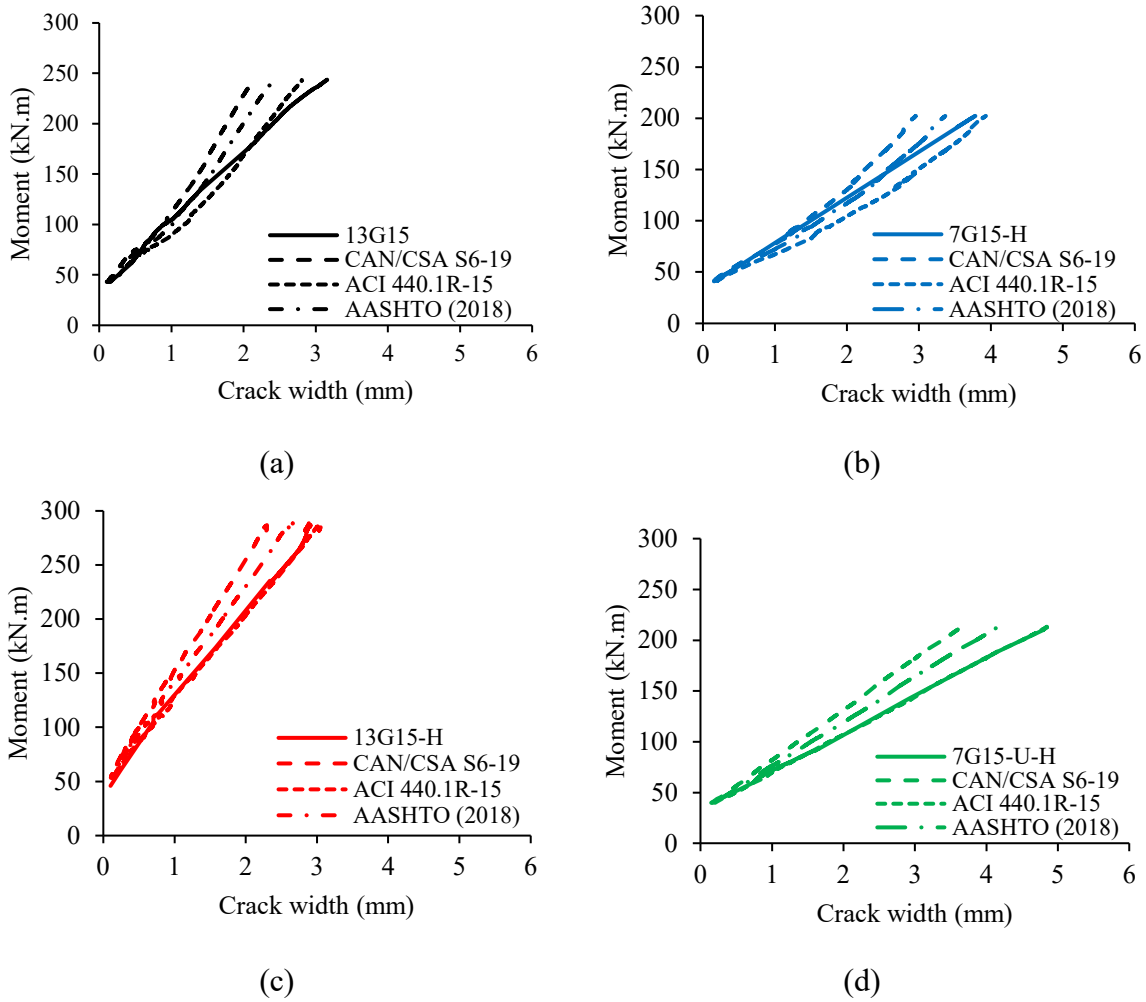

Fig. 5.14 Experimental versus theoretical crack-width for (a) segment 13G15; (b) segment 7G15-H; (c) segment 13G15-H; and (d) segment 7G15-U-H.

5.6 CONCLUSIONS

This study investigated the behavior of precast HSC tunnel lining segments reinforced with GFRP bars under quasi-static cyclic flexural loading experimentally and theoretically. Based on the experimental results and the theoretical study presented herein, the following conclusions can be drawn:

- Using HSC made it possible to take advantage of the higher tensile strength of the GFRP reinforcement bars. Moreover, the hysteretic response of the HSC segments in all of the second excursion loading cycles reflected stable cyclic behavior with no or limited strength degradation until failure.

- Increasing the stiffness of the HSC segments increased segment ultimate strength. Moreover, increasing the reinforcement ratio in HSC segments generally enhanced the cracking behavior at all load levels.
- Although both closed and double U-shaped transverse reinforcement configurations in the HSC resulted the same flexural carrying capacity, the segment with closed ties produced higher cracking moments than the segment with double U-shaped ties. Moreover, the closed tie configurations enhanced the crack distribution in the section of the tested segments.
- The HSC segments had higher ductility indices than their normal-strength counterpart segment. Moreover, increasing the reinforcement ratio did not affect the ductility index in the high-strength concrete segments, if the failure mode was compression controlled.
- The test results indicate that the HSC segments had adequate deformability compared to the [CAN/CSA S6-19] code limit of 4 for rectangular sections, while, compared to the NSC, the deformability of the HSC segments decreased.
- The experimental-to-predicted moment capacity of the HSC segments shows that the [ACI 440.1R-15] and [CAN/CSA S806-12 (R2017)] predictions were unconservative. The rectangular stress block approach proposed by [Ozbakkaloglu and Saatcioglu, 2004] and [Hadhood et al., 2018] showed enhancement in both the [ACI 440.1R-15] and [CAN/CSA S806-12 (R2017)] predictions.
- The conservative k_b value of 1.4, as recommended in [ACI 440.1R-15], resulted in conservative crack-width predictions. In contrast, the small k_b value (0.8) in [CAN/CSA S6-19] compared to that in [ACI 440.1R-15] contributed to underestimating the crack widths. Using a bond reduction factor (C_b) of 0.83 as in [AASHTO, 2018] provided accurate crack-width predictions.
- These experimental results are the first of their kind for GFRP-reinforced precast HSC tunnel lining segments under quasi-static cyclic flexural loading. These experimental results could be considered in the forthcoming provisions of codes related to the efficacy of using HSC for GFRP-reinforced PCTL segments under cyclic conditions.

CHAPTER 6 PERFORMANCE OF PRECAST FRC TUNNEL LINING SEGMENTS REINFORCED WITH GFRP BARS UNDER QUASI-STATIC CYCLIC FLEXURAL LOADING

FOREWORD

Authors and Affiliation:

- **Basil Ibrahim,** Ph.D. candidate, Department of Civil Engineering, Université de Sherbrooke, Sherbrooke, Quebec, Canada, J1K 2R1.
- **Salaheldin Mousa,** Postdoctoral fellow, Department of Civil Engineering, Université de Sherbrooke, Sherbrooke, Quebec, Canada, J1K 2R1.
- **Hamdy M. Mohamed,** Research Associate/Lecturer, Department of Civil Engineering, Université de Sherbrooke, Sherbrooke, Quebec, Canada, J1K 2R1.
- **Brahim Benmokrane,** Professor, Department of Civil Engineering, Université de Sherbrooke, Sherbrooke, Quebec, Canada, J1K 2R1.

Journal Title:

Journal of Composite for Construction

Paper Status:

Submitted on August 07, 2022.

Contribution:

The paper's outcomes are first-of-their-kind for the GFRP-reinforced precast FRC tunnel lining segments under quasi-static cyclic flexural loading. These experimental results could be taken into consideration for the forthcoming design code provisions governing the efficiency of using FRC in GFRP-reinforced PCTL segments under cyclic conditions.

ABSTRACT

Precast fiber-reinforced concrete (FRC) tunnel lining segments are designed using fundamental principles recommended in various international design provisions and guidelines. Current design provisions, however, are not applicable to designing precast concrete tunnel (PCTL) segments reinforced internally with fiber-reinforced polymer (FRP) bars. Moreover, the behavior of PCTL segments reinforced internally with glass-FRP (GFRP) bars under quasi-static cyclic flexural loading is a field in which no experimental research results are available in practice. This paper reports on an investigation of the cyclic behavior of GFRP-reinforced precast FRC tunnel lining segments. Four full-scale GFRP reinforced PCTL segments were fabricated and tested under quasi-static cyclic flexural loading. The segments had a total length, width, and thickness of 3100, 1500, and 250 mm, respectively. The investigated test parameters were the concrete type, the longitudinal reinforcement ratio, and the transverse reinforcement configuration. The hysteresis response, cracking pattern, ductility index, deformability, unloading stiffness degradation, and secant stiffness damage index of the test segments were identified and evaluated. The experimental results from this study show that the hysteretic response of the GFRP-reinforced precast FRC tunnel lining segments exhibited stable cyclic behavior with no or limited strength degradation until failure. Moreover, the test results show that the segments demonstrated adequate ductility index and deformability limits. An analytical model to predict the hysteresis behavior of the test segments was produced and its results compared to the experimental results. The results of this study show the effectiveness of using FRC for GFRP-reinforced PCTL segment applications under quasi-static cyclic flexural conditions.

Keywords: Precast concrete tunnel lining (PCTL) segments; fiber-reinforced concrete (FRC); glass fiber-reinforced polymer (GFRP) bars; quasi-static cyclic load; hysteretic behavior; deformability; energy dissipation.

6.1 INTRODUCTION

Precast concrete tunnel lining (PCTL) segments are designed for a service-life exceeding 100 years. Consequently, tunnel structural performance depends significantly on the durability performance of the PCTL segments. Chloride-ion penetration into conventional steel-reinforced PCTL segments results in reinforcement corrosion, which is the primary threat to the structural durability of PCTL segments and shortens their designed service life. Corrosion of conventional steel reinforcement bars is considered the most prevalent mode of deterioration affecting the serviceability and structural integrity of tunnel structures [Gulikers, 2003]. In fact, many reinforced concrete tunnels worldwide are deteriorating as they age [Zhiqiang and Mansoor, 2013]. Corrosion is the weakening mechanism that is the most costly and problematic in conventionally steel-reinforced concrete structures [ACI 440.1R-15]. The effective solution to this problem is using noncorroding fiber-reinforced polymer (FRP) reinforcing bars instead of conventional steel reinforcement. These lightweight and high-strength FRP bars are characterized by high corrosion resistance, long service life, and reduced maintenance costs [Wang et al., 2017; Solyom and Balázs, 2020; Pan and Yan, 2021; Benmokrane et al., 2021].

Few studies have recently examined the possibility of replacing the conventional steel bars with glass-FRP (GFRP) bars as internal reinforcement in PCTL segments [Caratelli et al., 2017; Spagnuolo et al., 2017; Meda et al., 2019; Hosseini et al., 2022]. All these studies have proved the suitability of using GFRP bars as reinforcement in PCTL segments. Moreover, these studies have revealed no significant differences in the flexural behavior of GFRP-reinforced PCTL segments compared to steel-reinforced ones. Substantively, increasing the strength of the GFRP bars compensated for the lack of ductility compared to the steel-reinforced PCTL segments. Past studies, however, have focused mainly on the static flexural resistance of PCTL segments. During its service life, a tunnel structure can be subjected to permanent loads (dead loads, earth pressure, surcharge loads), live loads (vehicular loads, live-load surcharges, etc.), and transient loads (water loads, earthquakes, superimposed deformations, blasts, fire, construction loads). According to [ACI 544.7R-16], service stage loads are represented by the long-term loads imposed on the lining from the ground, groundwater, surcharges, and other loads from any circumstances such as earthquake, fire, explosion, and breakouts at cross passageways. Essentially, there are no research results in the literature on the cyclic behavior of GFRP-reinforced PCTL segments.

Compared to concrete made with conventional steel reinforcement bars, fiber-reinforced concrete (FRC) results in better crack control characteristics [Tiberti et al., 2014] and improves the member's post-cracking behavior [di Prisco et al., 2009]. In the last century, FRC has been widely used as concrete reinforcement and can be used for PCTL segments using fundamental approaches recommended in the various international design guidelines, codes, and standards [ACI 544.7R-16]. [Abbas, 2014] studied the flexural behavior of steel fiber-reinforced concrete and conventionally steel-reinforced PCTL segments under quasi-static cyclic flexural loading experimentally. He found that both steel fiber-reinforced concrete and conventional steel-reinforced PCTL segments exhibited reasonable ductility and energy dissipation capacities and satisfied the flexural requirement under quasi-static cyclic flexural loading. Basically, the literature contains no research results on the cyclic behavior of GFRP-reinforced PCTL segments. Accordingly, the performance of full-scale GFRP-reinforced precast FRC segments under quasi-static cyclic flexural loading needs to be investigated.

This experimental work is part of an ongoing comprehensive research program carried out in the Department of Civil Engineering at the University of Sherbrooke aiming at improving current practices and developing more efficient design and construction approaches for the use of curvilinear GFRP bars and stirrups in precast concrete tunnel lining segments. This ongoing research investigates the behavior of full-scale GFRP-reinforced PCTL segments under different loading conditions such as static flexural loading [Hosseini et al., 2022]; quasi-static cyclic flexural loading; and punching shear and settlement. So far, this research is the first experimental work providing experimental data using laboratory testing on the performance of GFRP-reinforced precast FRC tunnel lining segments under quasi-static cyclic flexural loading according to [ACI 374.2R-13]. This information can be considered in the forthcoming provisions of codes for the efficiency of using FRC for GFRP-reinforced PCTL segments under quasi-static cyclic flexural conditions.

6.2 RESEARCH SIGNIFICANCE

There are no research results available on the strength and behavior of PCTL segments reinforced with GFRP bars under quasi-static cyclic flexural loading. This study aimed at providing experimental data on the strength and behavior of GFRP-reinforced precast FRC tunnel lining segments under quasi-static cyclic flexural loading. The hysteresis response, ductility index,

deformability, unloading stiffness degradation, and secant stiffness damage index of the test segments were to be identified and evaluated. In addition, an analytical model to predict the hysteresis behavior of the test segments was developed in comparison to experimental results. The experimental and analytical outcomes and conclusions of this work can be implemented in assessing and exploring the feasibility of using GFRP bars as internal reinforcement for PCTL segments under quasi-static cyclic flexural loading. Moreover, this paper illustrates the suitability of using FRC for GFRP-reinforced PCTL segment applications.

6.3 EXPERIMENTAL PROGRAM

6.3.1 Material properties

The mechanical properties of the sand-coated GFRP bars employed in this study were determined according to [ASTM D7205/D7205M-21] and are listed in **Table 6.1**. Number 5 (15 mm) curvilinear GFRP bars and No. 4 (13 mm) GFRP ties were used for the longitudinal and transverse reinforcement, respectively. In addition, No. 5 (15 mm) U-shaped GFRP bars were used as anchorage for the longitudinal reinforcement bars at both ends of each segment. **Fig. 6.1(a)** shows the different GFRP bars used in the experimental program.

Table 6.1 Mechanical properties of the GFRP reinforcement

Reinforcement type	Bar size	Bar diameter (mm)	Cross-sectional area – nominal (mm^2)	Cross-sectional area – immersed (mm^2)	Modulus of elasticity (GPa)	Tensile strength (MPa)	Tensile strain (%)
Curvilinear-GFRP bars	#5	15.0	199	222±1.2	55.1	1115	2.0
U-shaped GFRP bars	#5	15.0	199	222±1.2	53.5	1283	2.4
GFRP ties (closed / U-shaped)	#4	13.0	129	148±1.1	55.6	1248	2.2

Note: Properties calculated based on the nominal cross-sectional area.

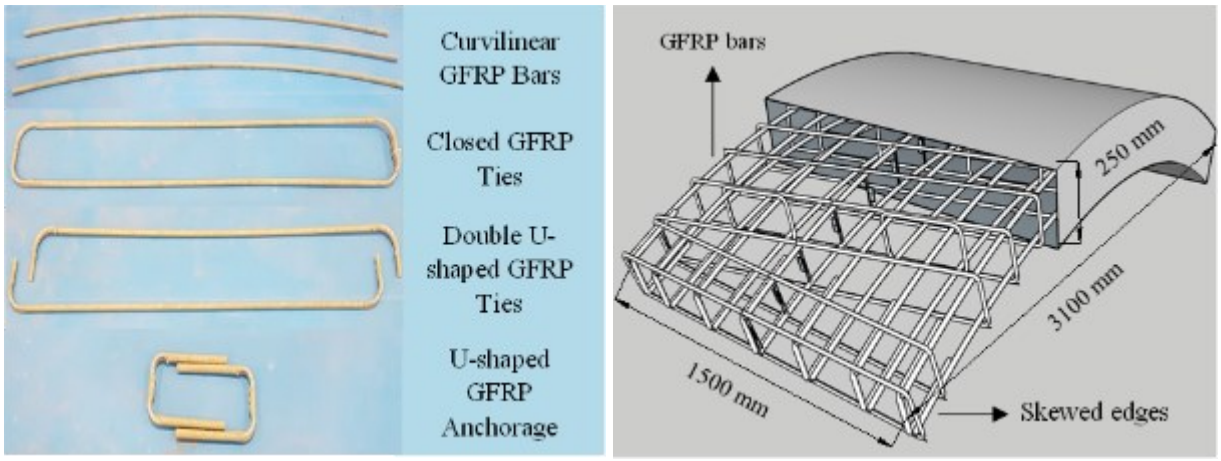

(a) (b)

Fig. 6.1 Overview: (a) GFRP bars used; and (b) schematic of the PCTL segments.

The concrete for all the PCTL segments was designed to be within the range of normal-strength concrete (35 MPa to 45 MPa). Therefore, all the PCTL segments—both the fiber-reinforced concrete (FRC) segments and the normal-strength concrete (NSC) segments—were cast with a targeted compressive strength of 40 MPa. Half-inch (13 mm) micro-synthetic polypropylene fibers were added to the concrete mix for the FRC segments. **Table 6.2** gives the concrete mix designs used for the FRC and NSC segments. **Table 6.3** presents the actual concrete strength based on the average test results of 100 x 200 mm concrete cylinders tested on the first day of segment testing.

Table 6.2 Concrete mix design

Concrete type	Cement (kg/m^3)	Sand (kg/m^3)	Limestone (kg/m^3)	Superplasticizer (mL/m^3)	Air entrainment (mL/m^3)	Water (L/m^3)	Fiber (kg/m^3)
FRC	450	615	1015	4500	140	170	3.51
NSC	450	615	1015	4500	140	170	-

Moreover, the average tested results of the 100 x 100 x 500 mm concrete prism samples, taken from each precast FRC tunnel lining segment, were used to determine the tension behavior of the FRC. The prism samples were tested under four-point bending load in accordance with [ASTM C1609/C1609M-19a]. **Table 6.3** lists the peak load (P_P), the residual load at the net deflection of L/600 (P^D_{600}), and the residual load at the net deflection of L/150 (P^D_{150}), for the precast FRC tunnel lining segments. The peak strength (f_P), the residual strength at the net deflection of L/600 (f^D_{600}) and the residual strength at the net deflection of L/150 (f^D_{150}) were determined with **Equation 6.1**, as shown in **Table 6.3**.

$$f = \frac{PL}{bd^2} \tag{6.1}$$

where L is length of the test span of the FRC prism samples; b is the average width of the prism sample; and d is the average depth of the prism sample.

Table 6.3 Concrete properties from the concrete cylinders and concrete prisms testing results

Specimen ID	Concrete type	Concrete compressive strength (MPa)	P_P (kN)	P_{600}^D (kN)	P_{150}^D (kN)	f_P (MPa)	f_{600}^D (MPa)	f_{150}^D (MPa)
7G15	NSC	52	-	-	-	-	-	-
7G15-FRC	FRC	37	12.3	5.4	4.4	3.69	1.62	1.32
13G15-FRC	FRC	37	12.1	5.0	3.9	3.63	1.50	1.17
7G15-U-FRC	FRC	37	12.1	5.2	4.1	3.63	1.56	1.23

6.3.2 Test matrix and parameters

A total of four full-scale GFRP reinforced PCTL segments (consisting of three precast FRC and one NSC tunnel lining segments) were designed, fabricated, and tested under quasi-static cyclic flexural loading. The segments were designed with a total length of 3100 mm, width of 1500 mm, and thickness of 250 mm. The clear cover was kept constant at 40 mm for all the segments. For practicality, the edges of the segments were skewed on both edges, as shown in **Fig. 6.1(b)**. The test parameters investigated in this experimental work were the concrete type (FRC versus NSC), the longitudinal curvilinear GFRP reinforcement ratio, and the configuration of the transverse GFRP ties (closed versus double U-shaped). **Table 6.4** lists the test matrix and the reinforcement details of the test segments. Each segment was identified with an alphanumeric code. The first number represents the number of top/bottom longitudinal reinforcement bars. The letter G indicates GFRP reinforcement. The second number represents the nominal diameter of the top/bottom curvilinear GFRP longitudinal reinforcing bars. The letter U preceded by a hyphen indicates the segments reinforced transversely with double U-shaped ties. Lastly, the expression FRC preceded by a hyphen identifies the segments cast with FRC.

Table 6.4 Test matrix and segment details

Specimen ID	Reinforcement type	Concrete type	Longitudinal reinforcement	Transverse reinforcement	Transverse reinforcement configuration
7G15	GFRP	NSC	7 No. 5 bars	No. 4 bars spaced at 200 mm	Closed ties
7G15-FRC	GFRP	FRC	7 No. 5 bars	No. 4 bars spaced at 200 mm	Closed ties
13G15-FRC	GFRP	FRC	13 No. 5 bars	No. 4 bars spaced at 200 mm	Closed ties
7G15-U-FRC	GFRP	FRC	7 No. 5 bars	No. 4 bars spaced at 200 mm	Double U-shaped ties

To illustrate, segments 7G15-FRC and 13G15-FRC are FRC segments with top and bottom longitudinal reinforcement consisting of 7 curvilinear No. 5 GFRP bars and 13 curvilinear No. 5 GFRP bars, respectively. Both segments were reinforced transversely with closed No. 4 GFRP ties spaced at 200 mm. Segment 7G15-U-FRC is an FRC segment longitudinally reinforced (top and bottom) with 7 curvilinear No. 5 GFRP bars and transversely with No. 4 double U-shaped GFRP ties spaced at 200 mm. The control segment – 7G15 – was cast with NSC and reinforced longitudinally (top and bottom) with 7 curvilinear GFRP bars, and transversely with closed No. 4 GFRP ties spaced at 200 mm. In all the test segments, U-shaped No. 5 GFRP anchorage bars were installed on each side of the segment. **Fig. 6.2** shows the reinforcement details of the test segments.

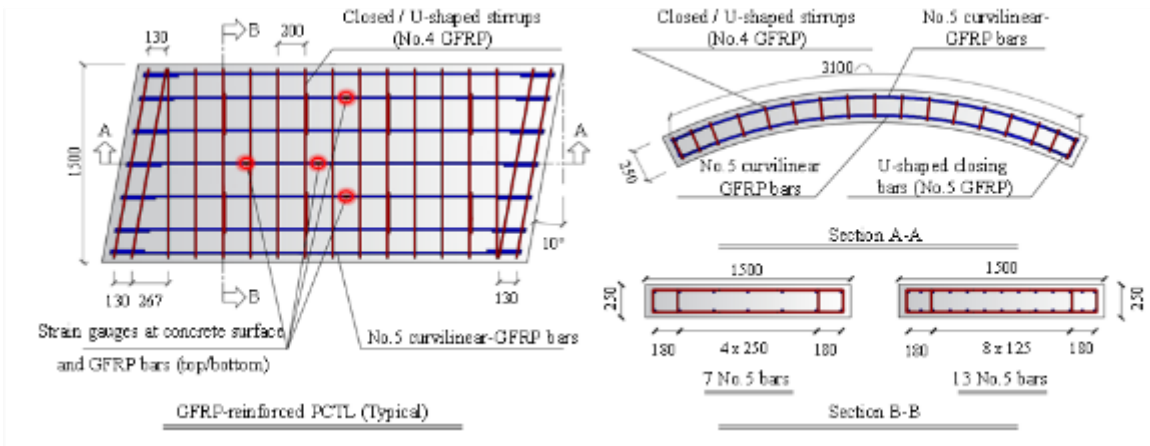

Fig. 6.2 Reinforcement detials for the test segments. (Note: all dimensions in mm)

6.3.3 Test segment fabrication

The GFRP reinforcement cages, for the various details and configurations, were assembled in the University of Sherbrooke laboratory, as shown in **Figs. 6.3(a) and (b)**, and transported to the

SYM-TECH precast concrete (Saint-Hyacinthe, Quebec) for casting. The specimens were cast in very stiff wooden forms prepared at the precast plant, as shown in **Fig. 6.3(c)**. **Figs. 6.3(d), (e), and (f)** show the PCTL segments cast in the precast plant, segment storage, and segment transportation from the precast plant to the laboratory, respectively.

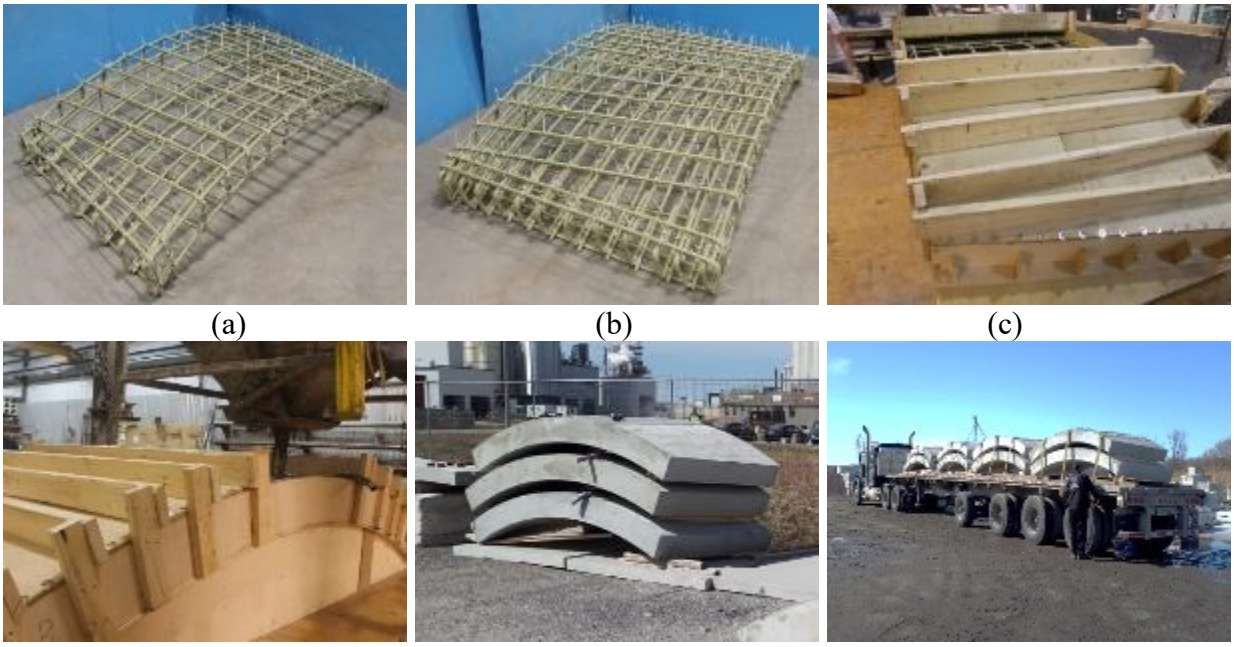

(a) (b) (c)

(d) (e) (f)

Fig. 6.3 Overview: (a) assembled GFRP cages for segments with 7 top/bottom GFRP bars; (b) assembled GFRP cages for segments with 13 top/bottom GFRP bars; (c) wooden formwork; (d) concrete casting; (e) segment storage; and (f) transportation from SYM-TECH to the laboratory.

The segments were designed in accordance with [ACI 440.1R-15] and [CAN/CSA S806-12 (R2017)], taking into account the arch effect, as expressed in **Equations 6.2 – 6.5**.

$$X = R\sin\theta \tag{6.2}$$

$$Y = R\cos\theta \tag{6.3}$$

$$P = 2R\cos\theta \tag{6.4}$$

$$\text{Moment} = \left(\text{R}\cos\theta \times \frac{\text{L}}{2}\right) + \left(\text{R}\Delta\sin\theta\right) = \left(\frac{PL}{4}\right) + \left(\frac{P\Delta\tan\theta}{2}\right) \tag{6.5}$$

where θ is the angle of inclination of the segment's supports from the vertical axis; and Δ is the vertical distance between the segment's centerline at mid-span and the supports' resistance forces, as shown in **Fig. 6.4**.

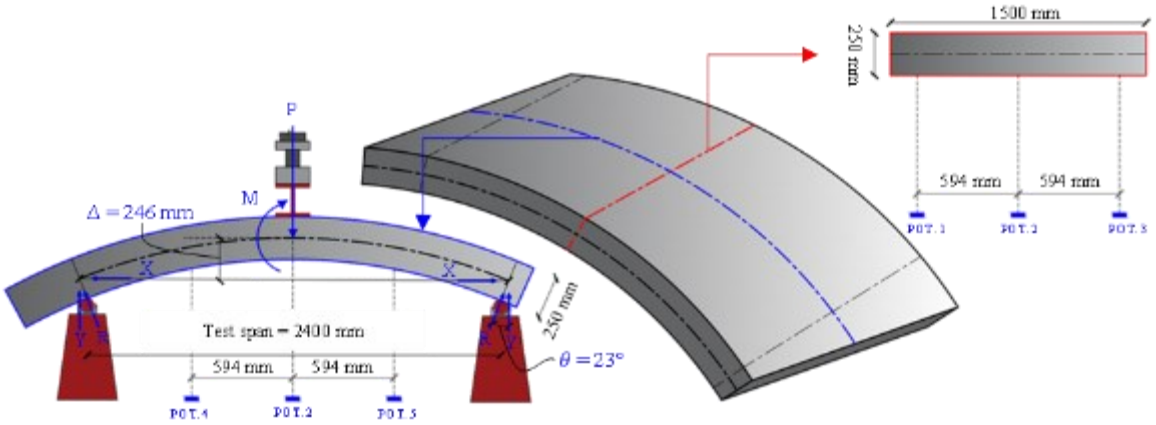

Fig. 6.4 Test setup.

6.3.4 Test setup and instrumentation

The quasi-static cyclic flexural loading was applied in three-point bending mode at a displacement-controlled rate of 0.8 mm/min in the University of Sherbrooke's CFI structural laboratory on a 11,000 kN MTS universal testing machine attached to a spreader beam, as shown in **Fig. 6.4**. The test span for the segments was 2400 mm. Five linear potentiometers (LPOTs) were placed to measure deflection at the segments' mid- and quarter-spans, as shown in **Fig. 6.4**. In addition, 10 mm and 60 mm electrical resistance strain gauges were installed on the reinforcing bars and attached to the concrete surfaces, respectively, to measure the strain at mid-and quarter-span of the PCTL segments **(Fig. 6.2)**.

6.3.5 Quasi-static cyclic flexural loading procedure

The cyclic loads acting on the PCTL segments was simulated in accordance with the tests of structural components under slowly applied quasi-static loading as in [ACI 374.2R-13]. Quasi-static cyclic flexural loading was applied in terms of percentage of the maximum displacement obtained from the static testing results [Hosseini et al., 2022]. Two cycles of loading and unloading were conducted for 1.25%, 2.5%, 5%, 10%, 25%, 50%, and 75% of the maximum displacement cycles, followed by one cycle up to failure. In all cycles, the unloading phase was stopped at a

minimum load of 5 kN in order to keep the test machine engaged with the segments. **Fig. 6.5** shows the segment loading scheme.

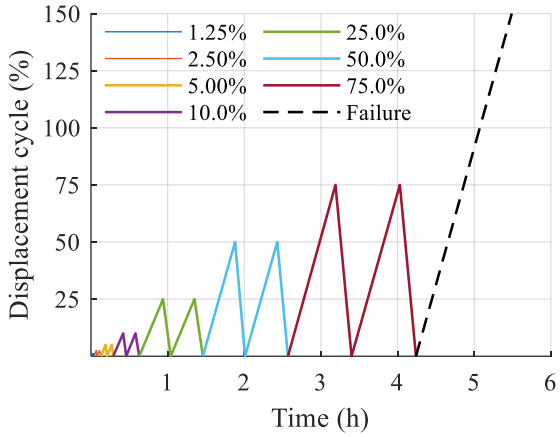

Fig. 6.5 Loading scheme for the test segments.

6.4 TEST RESULTS AND OBSERVATIONS

This section summarizes the experimental results, including the hysteresis response, strain distribution, ductility, and quasi-static cyclic flexural behavior of the test segments. **Table 6.5** summarizes the test results for all the segments tested.

Table 6.5 Summary of results

Segment ID	Cracking moment (kN.m)	Service moment[a] (kN.m)	Failure moment (kN.m)	Type of failure	Deflection at failure (mm)	Ductility index, μ_e	J-factor	Experimental to analytically predicted M_n
7G15	48	62	206	Concrete crushing	57	1.5	5.9	0.96
7G15-FRC	29	64	214	Concrete crushing	73	1.7	11.8	0.95
13G15-FRC	35	73	244[b]	Shear compression	46	1.5	10.9	-*
7G15-U-FRC	34	62	206	Concrete crushing	72	1.6	11.9	0.91

[a] The service moment of the test specimens is estimated at 0.3 of M_n.
[b] The shear load failure = 178 kN.

6.4.1 Hysteresis response

Fig. 6.6 shows the hysteresis behavior for all the segments tested in the form of the moment versus mid-span deflections. The hysteretic response for all the segments tested in all second excursions reflected stable cyclic behavior with no or limited strength degradation until failure. At 1.25% and 2.5% of the maximum displacement cycles, all the segments tested exhibited the same linear moment–deflection behavior, corresponding to the condition of the uncracked section. At 5% of the maximum displacement cycles, the initial flexural cracks in the tension zone started to appear under the loading point for all the segments tested. The cracking moment M_{cr} was 48 kN-m for the NSC segment (7G15) and ranged between 29 kN-m and 35 kN-m for the FRC segments (7G15-FRC, 13G15-FRC, and 7G15-U-FRC). The difference in the cracking moments for the NSC and FRC segments can be attributed to the difference in their concrete compressive strength: 52 and 37 MPa, respectively, as shown in **Table 6.3**. As the cracking moment of the tested segments is directly related to their compressive strength, the relatively high concrete compressive strength in the NSC segment 7G15 resulted in higher cracking moment for the segment compared to the FRC segments (7G15-FRC, 13G15-FRC, and 7G15-U-FRC).

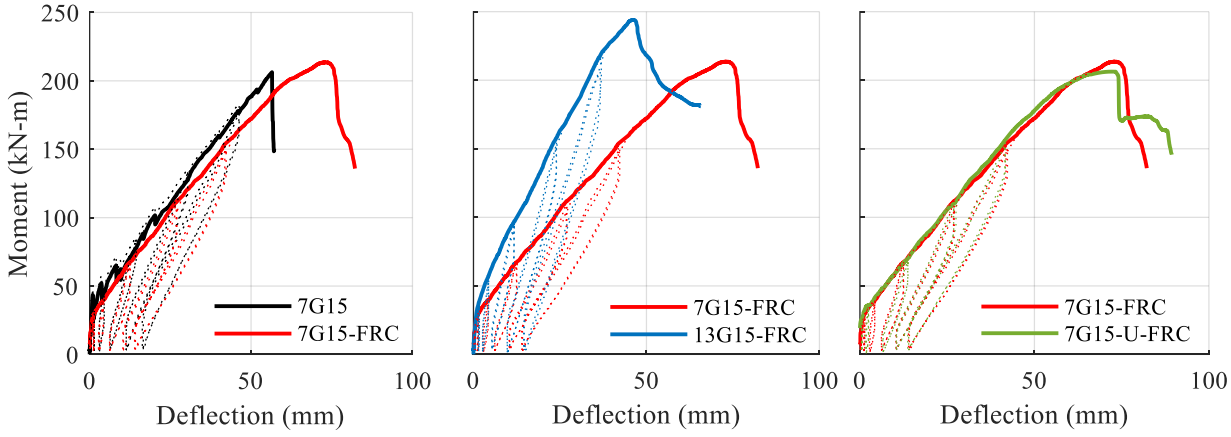

Fig. 6.6 Hysteresis response for (a) segments with different concrete types (FRC or NSC); (b) segments with different longitudinal reinforcement ratios; and (c) segments with different transverse reinforcement configuration (closed or double U-shaped).

All segments exhibited reduced stiffness after cracking with almost linear moment–deflection behavior up to failure. At 10% and 25% of the maximum displacement cycles, further flexural

cracks developed within the shear span of segment 7G15-FRC and its counterpart segment 7G15. **Fig. 6.7(a)** shows the moment–crack-width relationship for all the segments tested. Although the NSC compressive strength was 40% higher than that of the FRC, both segments (7G15-FRC and 7G15) had similar crack widths of around 0.52 mm at service load levels (2000 με), as shown in **Fig. 6.7(a)**. Thereafter, at 75% of the first maximum displacement cycle, the main flexural cracks in both segments 7G15-FRC and 7G15 became wider and propagated towards the loading point. Beyond 75% of the maximum displacement cycles, the cracks along the shear span of both segments 7G15-FRC and 7G15 started to incline towards the loading point in the last loading cycle until failure by concrete crushing occurred. The failure moment M_n for segments 7G15-FRC and 7G15 was 214 kN-m and 206 kN-m, respectively. The crack width at Mn in segments 7G15-FRC and 7G15 was 2.85 mm and 3.76 mm, respectively, as shown in **Fig. 6.7(a)**. This illustrates the contribution of FRC in enhancing the cracking performance of PCTL segments: using FRC in segment 7G15-FRC resulted in crack widths 30% smaller than that in its counterpart segment 7G15 at M_n. In addition, segment 7G15-U-FRC behaved similarly to segment 7G15-FRC and failed due to concrete crushing at an ultimate moment-carrying capacity M_n of 206 kN-m. The crack width in segment 7G15-U-FRC was 0.52 mm and 3.38 mm at 2000 με and M_n, respectively, as shown in **Fig. 6.7(a)**.

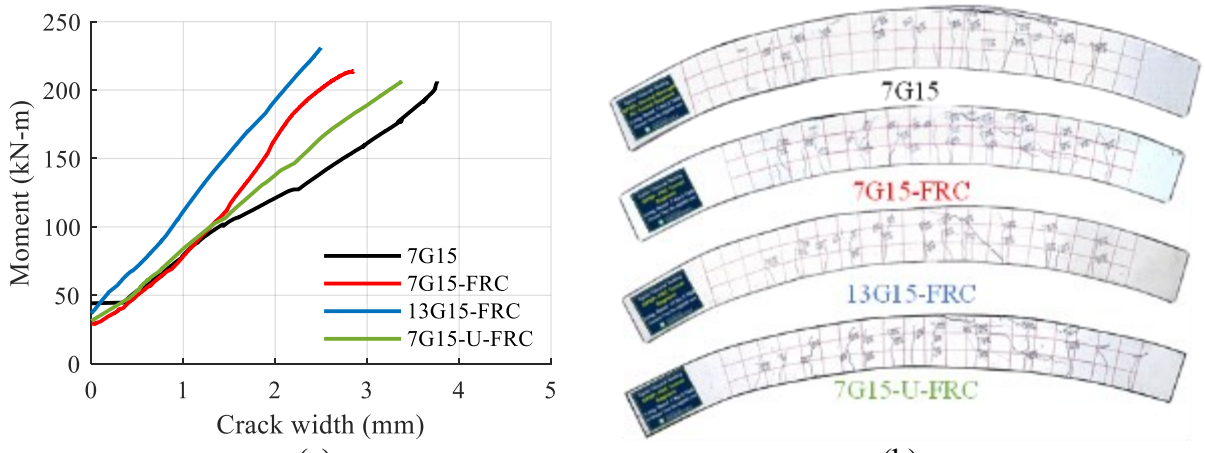

(a) (b)

Fig. 6.7 (a) Experimental moment – crack-width relationship; and (b) cracking pattern at failure for all test segments.

Increasing the reinforcement ratio in segment 13G15-FRC compared to segment 7G15-FRC increased the former's overall stiffness, as shown in **Fig. 6.6(b)**. Beyond 75% of the maximum displacement cycle, however, a main shear crack in segment 13G15-FRC started to develop and propagated until shear–compression failure occurred at a shear load V_n of 178 kN. The crack width in segment 13G15-FRC was 0.53 mm and 2.50 mm at 2000 με and M_n, respectively, as shown in **Fig. 6.7(a)**. **Fig. 6.7(b)** gives the cracking pattern at failure for all the segments tested.

6.4.2 Concrete mid-span strain readings

Fig. 6.8(a) presents the recorded concrete strains in the top location of the mid-span versus the moment for all the segments tested. Prior to segment cracking, the strain readings at the top concrete fibers at 1.25% and 2.5% of the maximum displacement cycles were insignificant (-100 to -250 με) in all the segments tested. Beyond 5% of the maximum displacement cycles, the mid-span concrete strain readings in the top concrete fibers in NSC segment 7G15 increased almost linearly until failure by concrete crushing occurred. Similarly, the mid-span concrete strain readings in segments 7G15-FRC and 7G15-U-FRC increased almost linearly until 75% of the maximum displacement cycles. Beyond that point, the increase in the readings of the mid-span concrete strain gauges readings in segments 7G15-FRC and 7G15-U-FRC gradually decreased until failure by concrete crushing occurred. The maximum recorded mid-span concrete compressive strain in segments 7G15-FRC, 7G15-U-FRC, and 7G15 was -3406, -3186, and -3840 με, respectively.

Similar to the case of segment 7G15-FRC, the mid-span strain readings in the top concrete fibers of segment 13G15-FRC increased almost linearly, with some deviations beyond 75% of the maximum displacement cycles, up to the initiation of shear failure. Beyond this stage, the shear crack propagated towards the loading point in segment 13G15-FRC, resulting in shear–compression failure at a concrete strain of -3433 με. For all the segments tested, the maximum recorded concrete strain readings at failure exceeded the specified ultimate concrete strain of -3000 με in [ACI 440.1R-15] and were consistent with the specified ultimate usable concrete strain in [CAN/CSA S806-12 (R2017)] (-3500 με).

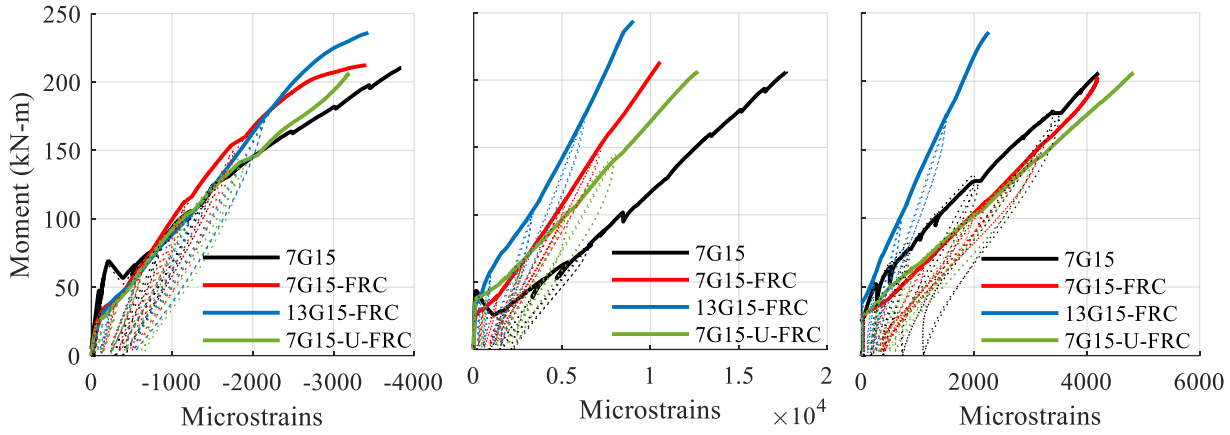

Fig. 6.8 Moment – strain relationship at mid-span (a) at concrete surface; (b) in bottom reinforcement bars; and (c) in top reinforcement bars.

6.4.3 Mid-span strain readings for the longitudinal GFRP bars

Figs. 6.8(b) and (c) show the moment versus the recorded mid-span strains in the bottom and top longitudinal GFRP bars. None of the tested segments had significant strain readings in the bottom and top reinforcement bars before 5% of the maximum displacement cycles. The bottom GFRP bars in all the segments tested exhibited a gradual strain increase until failure with strain readings of 15066, 9042, 12702, and 17695 με (75%, 45%, 64%, and 88% of the GFRP bars' ultimate tensile strain) for segments 7G15-FRC, 13G15-FRC, 7G15-U-FRC, and 7G15, respectively, as shown in **Fig. 6.8(b)**. The strain readings show that the top longitudinal GFRP reinforcement bars in all the segments tested were under tension. The mid-span strains recorded in the top longitudinal GFRP reinforcement bars of segments 7G15-FRC, 13G15-FRC, 7G15-U-FRC, and 7G15 at failure were 4184, 2261, 4828, and 4208 με, respectively, as shown in **Fig. 6.8(c)**.

6.4.4 Ductility

The ductility of reinforced concrete members is defined as the adequacy of withstanding inelastic deformation without a reduction in the member's carrying capacity. The ductility of concrete members reinforced with steel bars is expressed directly as the ratio of the ultimate deformation to the deformation at yield. In contrast, concrete members reinforced with FRP bars have no yield point. Subsequently, the ductility of FRP-reinforced concrete members is computed indirectly in terms of an energy-based ductility index or deformability [Grace et al., 1998]. Using the energy

absorption approach proposed by [Naaman and Jeong, 1995], the ductility index μ_e for all the segments tested under quasi-static cyclic flexural loading was computed with **Equation 6.6**.

$$\mu_e = 0.5\left(\left(E_{tot}/E_{el}\right)+1\right) \tag{6.6}$$

where E_{tot} is the segment's overall energy and E_{el} is the released elastic energy at failure. The total energy E_{tot} and the elastic energy E_{el} are calculated as the area under the segment's envelope load–deflection curve and the area of the triangle formed at the failure load using the weighted average slopes of the two initial stiffnesses of the envelope load–deflection curve, respectively. As shown in **Table 6.5**, the ductility index μ_e for segments 7G15-FRC, 13G15-FRC, 7G15-U-FRC, and 7G15 was 1.7, 1.5, 1.6, and 1.5, respectively.

The deformability of FRP-reinforced concrete members is determined using the J-factor approach of [Jaeger et al., 1997], which has been adopted in the *Canadian Highway Bridge Design Code* [CAN/CSA S6-19]. In this approach, the moment-carrying capacity and the curvature at both the service and ultimate conditions of the FRP-reinforced concrete member are considered, as shown in **Fig. 6.6**. All through the loading history – from service loading state to ultimate state – the J-factor illustrates the deflection and cracking of the FRP-reinforced concrete member. The J-factor was computed with **Equation 6.7** [CAN/CSA S6-19].

$$J = \frac{M_{ultimate}}{M_s} \times \frac{\psi_{ultimate}}{\psi_s} \tag{6.7}$$

where ψ_s is the curvature at service condition (strain at the top concrete surface is 1000 με); ψ_u is the curvature at ultimate load; M_s is the moment at service condition; and M_u is the ultimate moment. **Table 6.5** shows that all the GFRP-reinforced segments demonstrated adequate deformability under quasi-static cyclic flexural loading when compared to the [CAN/CSA S6-19] code limit of 4 for rectangular sections. The deformability J-factors for segments 7G15-FRC, 13G15-FRC, 7G15-U-FRC, and 7G15 were 11.8, 10.9, 11.9, and 5.89, respectively.

6.4.5 Quasi-static cyclic flexural behavior

Reinforced concrete members subjected to large cyclic loading exhibit levels of stiffness degradation caused by cracking, loss of bond, or integration with high shear or axial stress [Al-Saadi et al., 2019]. The level of stiffness degradation depends on the characteristics of the reinforced concrete members and the loading history [Xiao and Mo, 2018]. The quasi-static cyclic flexural behavior of all the segments tested is defined herein in terms of unloading stiffness and secant stiffness damage index.

Initially, unloading stiffness is an important parameter in determining the value of the residual deformation and the recoverability of a structure [Fahmy et al., 2009]. Unloading stiffness degradation is considered advantageous in improving the structural reparability under cyclic loading conditions, as the residual structural deformation is directly related to unloading stiffness. Under cyclic loading conditions, lower unloading stiffness reduces residual structural deformation [Ding et al., 2013]. To study the relationship between the unloading stiffness degradation and the residual deformation at the end of each cycle for the tested segment, the unloading stiffness degradation was characterized by the ratio $K_{unloading} / K_0$, where $K_{unloading}$ is the unloading stiffness at each cycle and K_0 is the segment's initial stiffness at the first 1.25% of the maximum displacement cycle. Moreover, the residual deformation at the end of each cycle for all the segments tested is presented by the ratio $\delta_{residual} / \delta_{\max\_i}$, where $\delta_{residual}$ is the residual deformation at each cycle and $\delta_{\max\_i}$ is the maximum deformation reached at the end of each loading cycle. **Fig. 6.9(a)** shows the unloading stiffness ratio $K_{unloading} / K_0$ and the residual deformation ratio $\delta_{residual} / \delta_{\max\_i}$ of all the segments tested at each loading cycle. Initially, at the 1.25% and 2.5% maximum displacement cycles, $K_{unloading} / K_0$ was relatively high in all the segments tested. Beyond the 5% maximum displacement cycles, $K_{unloading} / K_0$ dropped rapidly for all the segments tested. **Fig. 6.9(a)** indicates that the residual deformation for all the segments tested $\delta_{residual} / \delta_{\max\_i}$ was smaller at the 50% and 75% maximum displacement cycles than in the preceding loading cycles. **Fig. 6.9(b)** shows the cumulative residual deformation at each loading cycle for all the segments tested. The cumulative residual deformation at 75% of the maximum

displacement cycle was 14.2, 14.7, 15.9, and 16.6 mm, respectively, for segments 7G15-FRC, 13G15-FRC, 7G15-U-FRC and 7G15.

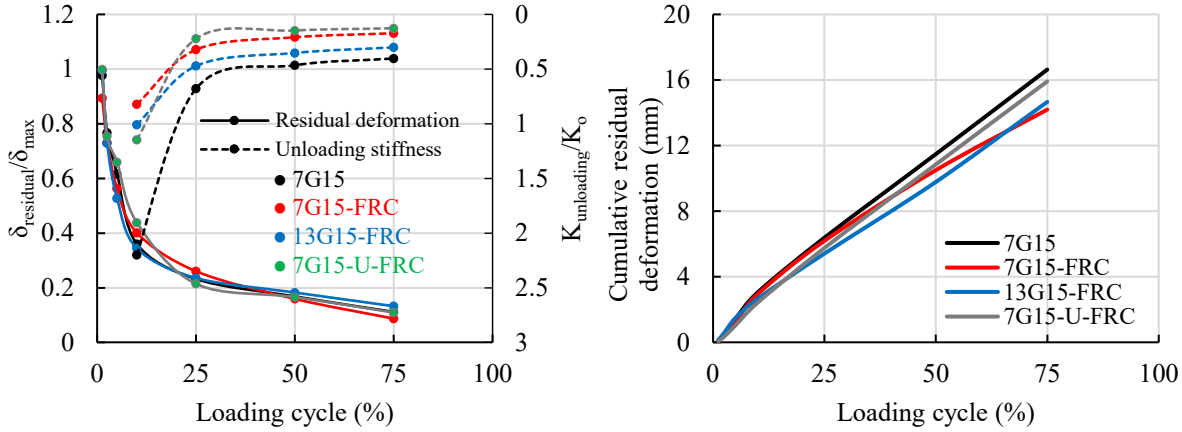

Fig. 6.9 (a) Unloading stiffness degradation ratio ($K_{unloading} / K_0$) versus residual deformation ratio ($\delta_{residual} / \delta_{\max\_i}$); and (b) cumulative residual deformation for all the tested segments.

The damage caused to the reinforced concrete structures under cyclic loading conditions can be established using the damage index. Several approaches are currently available to determine the damage index based on a wide range of parameters, such as deformation [Cosenza et al., 1993], stiffness [Meyer et al., 1983; Ghobarah et al., 1999; Kim et al., 2005], and energy absorption [Fardis et al., 1993]. The approach of [Mayer et al., 1981] – which computes the damage index as the ratio of the initial stiffness to the reduced secant stiffness at the maximum displacement of each cycle – was used to determine the secant stiffness damage index (KI) in loading and unloading for all the segments tested. The KI is described as the cycle's secant stiffness, $K_{\sec\_i}$, to the post-cracking stiffness ratio. **Fig. 6.10** shows the secant stiffness damage index at each loading cycle for all the segments tested. At 1.25% of the maximum displacement cycles, the KI for segments 7G15-FRC, 13G15-FRC, 7G15-U-FRC, and 7G15 was 39.3, 11.2, 23.1, and 37.5 respectively. Beyond that, the KI decreased for all the segments tested. The rate of KI degradation was not confirmed for all the segments tested, where the rate of KI decreased in the segment reinforced with the high longitudinal reinforcement ratio (13G15-FRC) was less than that in segments 7G15-FRC, 7G15-U-FRC and 7G15. Therefore, the last loading cycle's residual stiffness for all the segments tested was comparable to a KI of 1.4, 1.6, 1.4, and 1.7 for segments 7G15-FRC, 13G15-FRC, 7G15-U-FRC, and 7G15, respectively, as shown in **Fig. 6.10**.

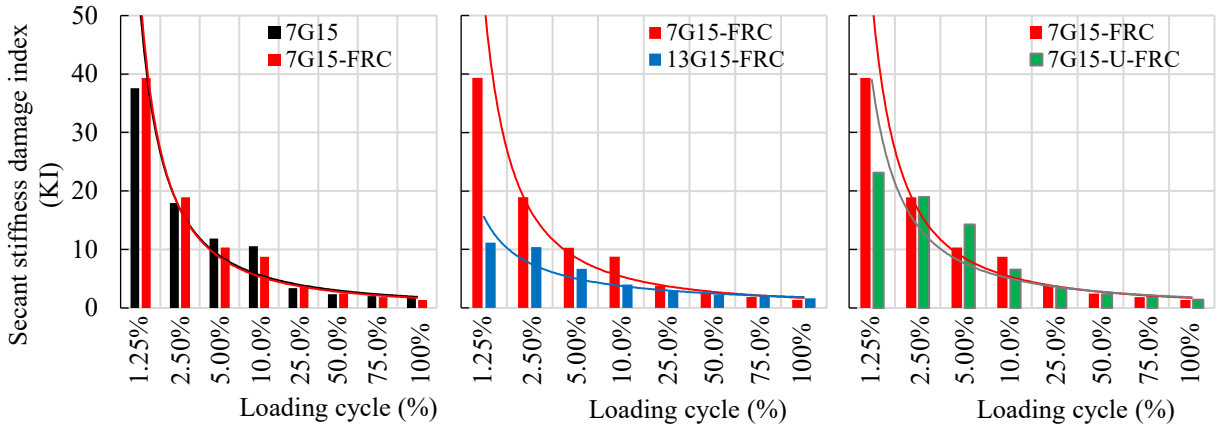

(a) (b) (c)

Fig. 6.10 Secant stiffness damage index at each load cycle for (a) segments with different concrete types (FRC or NSC); (b) segments with different longitudinal reinforcement ratios; and (c) segments with different transverse reinforcement configuration (closed or double U-shaped).

6.5 DISCUSSION

This section discusses the experimental observations and presents the effect of each test parameter on the behavior of the tested segments, including the influence of concrete type (FRC or NSC), the longitudinal reinforcement ratio (0.50% or 0.90%), and the transverse reinforcement configuration (closed or double U-shaped ties).

6.5.1 Influence of concrete type

Segments 7G15-FRC and 7G15 had a longitudinal reinforcement ratio of 0.50% but different concrete types (FRC or NSC). The use of FRC for the segments with the same longitudinal reinforcement ratio enhanced the segment's overall crack distribution under quasi-static cyclic flexural loading. Using FRC in segment 7G15-FRC resulted in narrower crack width with reduced crack spacing, as shown in **Fig. 6.7**. Although NSC segment 7G15 had a compressive strength 40% higher than FRC segment 7G15-FRC, they had similar crack widths at service loads limits. The crack width for both segments 7G15-FRC and 7G15 was 0.52 mm at 2000 με. Beyond the service load levels and at 50% and 75% of the maximum displacement cycles, however, the cracks in control segment 7G15 were much wider than those in FRC segment 7G15-FRC. At the ultimate load level, the crack width in segment 75G15 was about 32% wider than that in segment 7G15-FRC at M_n, as shown in **Fig. 6.7**. Moreover, using FRC for segments with the same longitudinal

reinforcement ratio increased segment ductility under the quasi-static cyclic flexural loading. FRC segment 7G15-FRC had a ductility index μ_e 13% higher than its counterpart control segment 7G15, as shown in **Table 6.5**. In addition, the computed deformability J-factor of the FRC segment 7G15-FRC was about twice the computed deformability of the control segment 7G15, as shown in **Table 6.5**. **Fig. 6.9(a)** shows that the unloading stiffness ratio $K_{unloading} / K_0$ of FRC segment 7G15-FRC was slightly higher in each cycle than that of control segment 7G15, resulting in segment 7G15-FRC having a smaller residual deformation ratio $\delta_{residual} / \delta_{\max\_i}$ than its counterpart segment 7G15. The cumulative residual deformation in control segment 7G15 at 75% of the maximum displacement cycle was about 17% higher than that of FRC segment 7G15-FRC, as shown in **Fig. 6.9(b)**. Indeed, although NSC segment 7G15 had a compressive strength 40% higher than FRC segment 7G15-FRC, both segments had identical secant stiffness damage indices (KIs) at each loading cycle, as shown in **Fig. 6.10(a)**.

6.5.2 Influence of longitudinal reinforcement ratio

FRC segments 7G15-FRC and 13G15-FRC had longitudinal reinforcement ratios of 0.50% and 0.90%, respectively. Increasing the stiffness of segment 13G15-FRC generally increased the segment's ultimate carrying capacity under quasi-static cyclic flexural loading. It is worth mentioning, however, that segment 13G15-FRC did not reach its full flexural load-carrying capacity due to the segment's shear failure. Segment 13G15-FRC's load-carrying capacity was 14% higher than that of segment 7G15-FRC, as shown in **Fig. 6.6(b)**. Moreover, increasing the longitudinal reinforcement ratio from 0.50% in segment 7G15-FRC to 0.90% in segment 13G15-FRC generally enhanced the cracking at ultimate load levels under quasi-static cyclic flexural loading, as shown in **Fig. 6.7**. Although segments 7G15-FRC and 13G15-FRC both had similar crack widths of 0.52 mm and 0.53 mm, respectively, at 2000 με, segment 7G15-FRC had much wider cracks at 50% and 75% of the maximum displacement cycles than segment 13G15-FRC. At the ultimate load level, the crack width in segment 7G15-FRC was about 114% of that in segment 13G15-FRC at M_n, as shown in **Fig. 6.7**. Furthermore, the reduction in the ductility index με due to the increase in longitudinal reinforcement ratio was compensated for by the FRC. The segment with 0.90% longitudinal reinforcement ratio had a ductility index μ_e of 1.5, similar to that of control NSC segment 7G15, as shown in **Table 6.5**. Similarly, the reduction in the deformability

J-factor due to the increase in longitudinal reinforcement ratio was insignificant and compensated for by the FRC. The deformability J-factor for segment 13G15-FRC was about 92% that of segment 7G15-FRC, as shown in **Table 6.5**. **Fig. 6.9(a)** shows segments 7G15-FRC and 13G15-FRC had comparable levels of degradation of the unloading stiffness ratio $K_{unloading} / K_0$ and the residual deformation ratio $\delta_{residual} / \delta_{\max\_i}$. Accordingly, these segments had comparable levels of cumulative residual deformation of 14.2 and 14.7 mm, respectively, as shown in **Fig. 6.9(b)**. **Fig. 6.10(b)** shows that using FRC reduced the rate of decrease in the secant stiffness damage index (KI) by increasing the longitudinal reinforcement ratio, resulting in segments 13G15-FRC and 7G15-FRC having similar levels of residual stiffness in the last loading cycles.

6.5.3 Influence of transverse reinforcement configuration

Segment 7G15-U-FRC was designed similar to segment 7G15-FRC, except for the transverse reinforcement configuration. Segment 7G15-FRC was reinforced transversely with closed ties, while segment 7G15-U-FRC had double U-shaped transverse ties. **Fig. 6.7** reveals that the closed tie configuration in segment 7G15-FRC enhanced the crack distribution in the section, compared to the double U-shaped tie configuration in segment 7G15-U-FRC under quasi-static cyclic flexural loading. Both segments evidenced the same crack width of 0.52 mm at service load levels (2000 με). Beyond the service load levels and at 50% and 75% of the maximum displacement cycles, however, the cracks in segment 7G15-U-FRC were much wider than in segment 7G15-FRC. At the ultimate load level, the crack width in segment 75G15-U-FRC was about 19% greater than that in segment 7G15-FRC at M_n, as shown in **Fig. 6.7**. **Table 6.5** illustrates that the transverse reinforcement configuration had insignificant effect on the segments' ductility. Segments 7G15-FRC and 7G15-U-FRC had a ductility index μ_e of 1.7 and 1.6, respectively. Likewise, segments 7G15-FRC and 7G15-U-FRC had a deformability J-factor of 11.8 and 11.9, respectively. **Fig. 6.9(a)** shows comparable degradation of the unloading stiffness ratio $K_{unloading} / K_0$ and the residual deformation ratio $\delta_{residual} / \delta_{\max\_i}$ for segments 7G15-FRC and 7G15-U-FRC. Accordingly, both segments had comparable levels of cumulative residual deformation of 14.2 mm and 15.9 mm, respectively, as shown in **Fig. 6.9(b)**. Moreover, these two segments had comparable reductions in the secant stiffness damage index (KI), as shown in **Fig. 6.10(c)**.

6.6 ANALYTICAL MODEL

A layer-by-layer iterative approach was applied by idealizing the cross section as series of layers to analytically predict the hysteresis response of the GFRP-reinforced PCTL segments, as presented in the following section. This model was first proposed by [Newmark, 1943] and has been widely implemented for predicting the flexural capacity of reinforced concrete members [Kara et al., 2015; Mousa et al., 2018].

6.6.1 Material relationships

The concrete stress strain model proposed by [Popovics, 1973] was used in the analytical model for segment concrete compressive stress, f_c, corresponding to the strain ε_c, as expressed in **Equation 6.8** and shown in **Fig. 6.11(a)**.

$$f_c = \frac{f_c^{'}\left(\varepsilon_c / \varepsilon_c^{'}\right)\mu}{\mu - 1 + \left(\varepsilon_c / \varepsilon_c^{'}\right)^{\mu}} \tag{6.8}$$

where f_c is the unconfined concrete strength, obtained from the cylinder tests; $\varepsilon_c^{'}$ is corresponding strain; and $\mu = E_{\tan} / \left(E_{\tan} - E_{\sec}\right)$. The tangent and secant modulus $E_{\tan}$ and $E_{\sec}$ are determined as $E_{\tan} = 4500\sqrt{f_c^{'}}$ (MPa), as recommended in [CAN/CSA S806-12 (R2017)], and $E_{\sec} = f_c^{'} / \varepsilon_c^{'}$, respectively.

According to [ACI 544.4R-18], the tensile strength of plain concrete is insignificant and therefore it was not taken into account for the NSC segment (7G15). Nevertheless, the effective tensile strength of the FRC was considered for the predictions of the FRC segments. Hence, the model proposed in [RILEM TC 162-TDF, 2003] for the tensile strength of FRC members was employed for the concrete tensile strength of the FRC segments, as shown in **Fig. 6.11(a)**.

The concrete cracking moments for the segments were defined in the analytical model, as expressed in **Equation 6.9**.

$$M_{cr} + M_{eq} = \left(\frac{f_r I_g}{y_t}\right) \tag{6.9}$$

where M_{eq} is the equivalent moment due to self-weight of the segment; I_g is the concrete gross section moment of inertia about the centroid axis; and y_t is the distance from the centroid axis of gross section to the tension face.

The concrete modulus of rupture f_r is determined as $f_r = 0.6\lambda\sqrt{f_c'}$ (MPa), as recommended in [CAN/CSA S6-19]. The analytically predicted cracking moments were evaluated against the experimental cracking moments of the test segments, as shown in **Table 6.5**. The analytical model produced accurate predictions for the cracking moments of NSC segment 7G15. The experimental to the analytically predicted cracking moment for NSC segment 7G15 ratio was 1.00 **(Table 6.5)**. In contrast, the FRC segments cracked at slightly smaller moments compared to the analytically predicted cracking moments. The experimental to the analytically predicted cracking moment ratio for the FRC segments (7G15-FRC, 13G15-FRC, and 7G15-U-FRC) ranged between 0.81 and 0.95 with an average and coefficient of variance of 0.89 and 8.2, respectively **(Table 6.5)**.

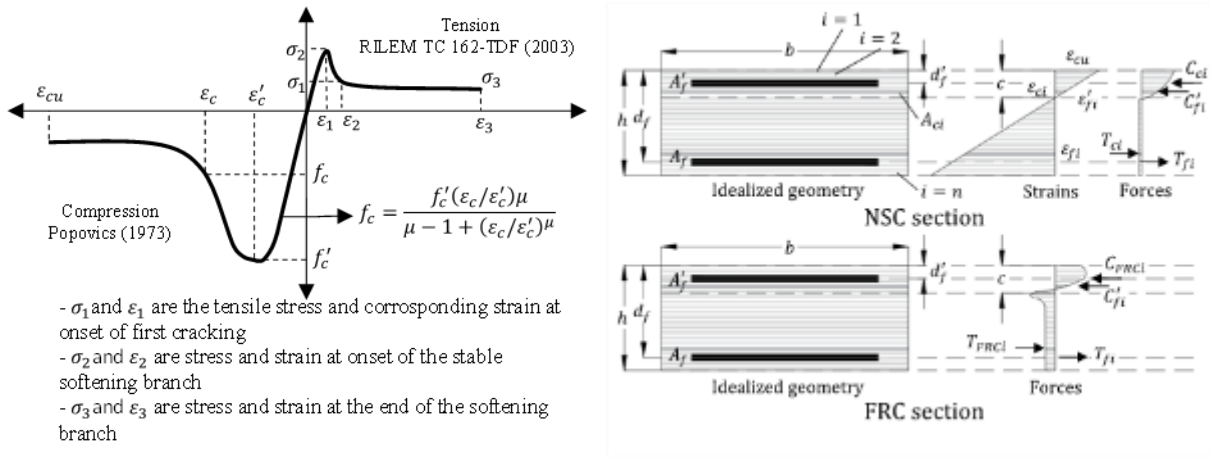

(a) (b)

Fig. 6.11 (a) Schematic of the stress – strain diagram in the analytical model; and (b) idealized cross section and stress – strain distribution in the analytical model.

6.6.2 Flexural capacity

Based on force equilibrium and strain compatibility, the hysteresis response of the tested segments was computed using the layer-by-layer approach in integrating the stresses over the cross-sectional areas of the concrete and the longitudinal GFRP reinforcement bars. The idealized geometry of the GFRP-reinforced PCTL segments is illustrated in **Fig. 6.11(b)**. The depth of the section h is

divided into number of layers n of equal thickness. The centroid of each layer is located at its mid-thickness, and the layer's depth is computed as the distance from the top concrete fibers to the layer's centroid. Strains are linearly distributed along the depth of the section. The stress in the concrete and FRP bars is based on material relationships, as shown in **Fig. 6.11(a)**. The stresses at the centroid of a strip are assumed to be constant throughout its thickness. Moreover, **Fig. 6.11(b)** illustrates the linear strain distribution across the depth, as the top and bottom strains are ε_{Top} and ε_{Bottom}, respectively. The depth of the compression zone from the top of the section is the neutral-axis depth c. The analytical model was implemented in a computer program capable of constructing the moment–curvature curve for the given GFRP-reinforced PCTL segment. **Fig. 6.12** provides a flowchart describing the numerical procedure used by the computer program.

For the FRC segments, the hybrid reinforcement was designed according to [ACI 544.4R-18]. The general form of the nominal moment capacity of a member with hybrid reinforcement as defined in [ACI 544.4R-18] is shown in **Equation 6.10**. The moment capacity of the hybrid FRC segments was introduced in the analytical model to take into account the contribution of the GFRP bars and fibers, as shown in a general form in **Fig. 6.11(b)**. The compressive stress is carried by the concrete, while the tensile stresses/forces are carried by the hybrid action of the GFRP bars and fibers.

$$M_{n-HFRC} = M_{n-RC} + M_{n-FRC} \tag{6.10}$$

where M_{n-RC} is the moment capacity of the plain concrete section; and M_{n-FRC} is moment capacity of the FRC section computed in accordance with the simplified method in the [ACI 544.4R-18], as expressed in **Equation 6.11**.

$$M_{n-FRC} = f_{150}^{D} \times \left(bh^2/6\right) \tag{6.11}$$

6.6.3 Flexural deformations, rotation, and displacement

The radius of curvature R in the analytical model is measured to the neutral axis. The radius of curvature R, neutral-axis depth kd, concrete strain in the extreme compression fiber ε_c varies along the member because the concrete carries some of the tension between the cracks. Considering only a small element of length dx of the segment, the rotation between the ends of the element is given by **Equations 6.12 and 6.13**.

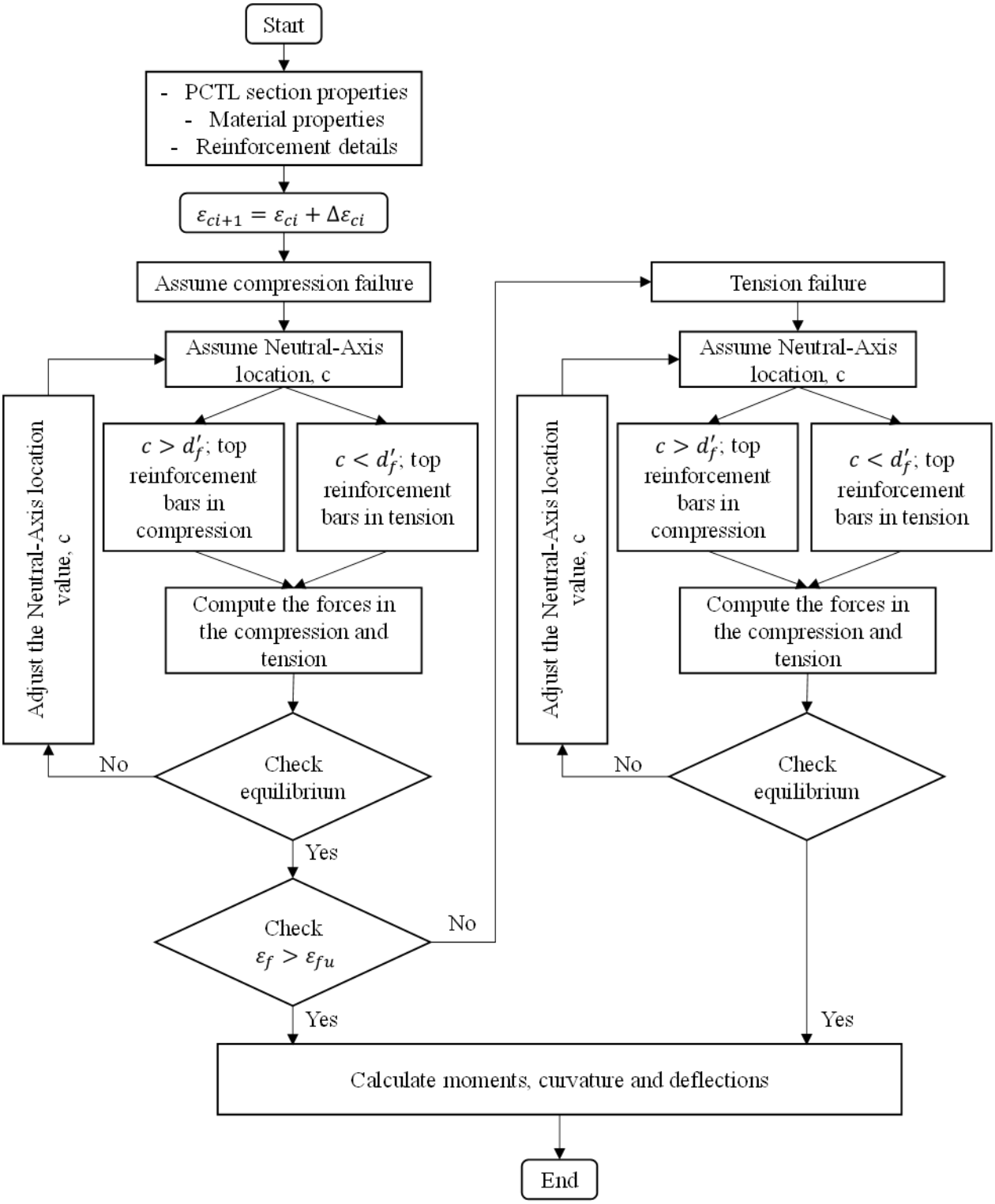

Fig. 6.12 Flowchart of the computer program.

$$\frac{dx}{R} = \frac{\varepsilon_c dx}{kd} = \frac{\varepsilon_f dx}{d\left(1-k\right)} \tag{6.12}$$

$$\frac{1}{R} = \frac{\varepsilon_c}{kd} = \frac{\varepsilon_f}{d(1-k)} \tag{6.13}$$

The curvature ϕ is computed as the rotation per unit length of the segment $\left(\phi = 1/R\right)$, as expressed in **Equation 6.14**.

$$\phi = \frac{\varepsilon_c}{kd} = \frac{\varepsilon_f}{d\left(1-k\right)} = \frac{\varepsilon_c + \varepsilon_f}{d} \tag{6.14}$$

The curvature varies along the length of the segment because of fluctuations in the neutral-axis depth and the strains between the cracks.

The theoretical moment–curvature curves for the GFRP-reinforced PCTL segment under flexural and axial loading is derived based on assumptions similar to those used to determine flexural strength. It is assumed that sections plane before bending remain plane after bending and that the stress–strain curves for the concrete and GFRP are known. The curvatures associated with a range of bending moments and axial loads is determined using these assumptions and from the requirements of strain compatibility and equilibrium of forces. The rotation of the test segments is computed as the area under the curvature diagram, and the displacement represents the moment of the area under the curvature diagram. **Fig. 6.13** compares the analytically predicted hysteresis response with the experimental response of the test segments. **Table 6.5** presents the experimental-to-predicted ratios for the flexural-moment capacities of the test segments. The table indicates good predictions with experimental-to-predicted ratios ranging between 0.95 and 0.96.

6.6.4 Dissipated energy

Structural ductility considerations aside, the dissipated energy is an effective index, as the energy from the cyclic loading gets injected into the structure and must be dissipated. The role of the reinforcement in dissipating the energy of the cyclic loading acting on the structure can be determined by distinguishing the dissipative mechanisms, as shown in **Equation 6.15** [Daniel and Loukili, 2002].

$$E_T - E_S = E_e + E_a \tag{6.15}$$

where E_T is the principle energy injected to the structure; E_S is the energy dissipated into the soil; and E_e and E_a are the energy used by the structure over the elastic and inelastic domains, respectively.

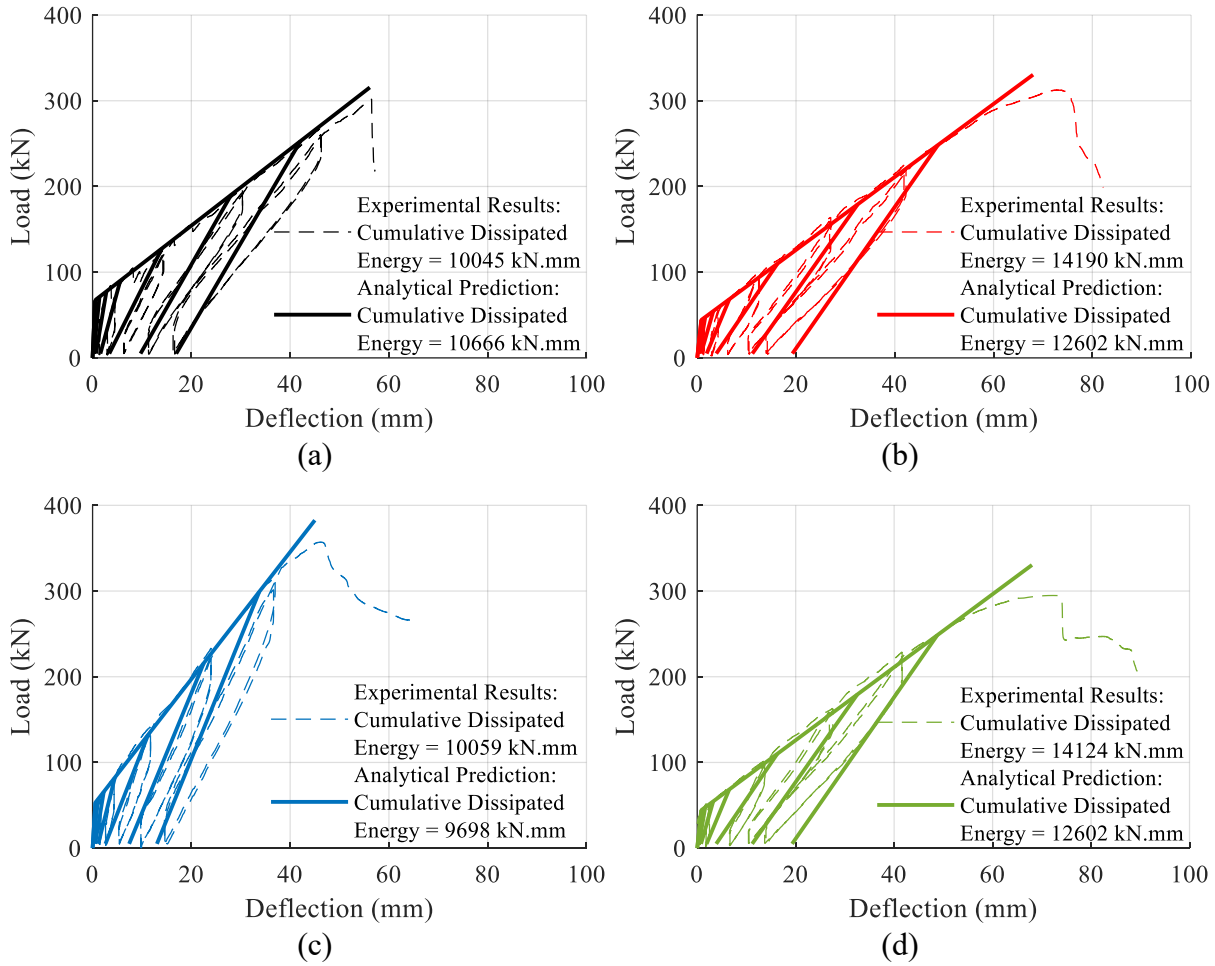

Fig. 6.13 Experimental versus analytically predicted hysteresis behavior for (a) segment 7G15; (b) segment 7G15-FRC; (c) segment 13G15-FRC; and (d) segment 7G15-U-FRC.

Therefore, increasing the energy storage capacity in both the elastic and inelastic domains is essential to avoid structural collapse. The primary dissipated energy computations for the test segments were carried out by determining the hysteretic area of each cycle up to failure. **Fig. 6.13** shows that the cumulative dissipated energy for segments 7G15-FRC, 13G15-FRC, 7G15-U-FRC, and 7G15 were 14190, 10059, 14124, and 10045 kN-mm, respectively. Segment 7G15-FRC

achieved overall dissipated energy 41.3% higher than its counterpart NSC segment 7G15 **(Fig. 6.13)**. Moreover, increasing the reinforcement ratio allowed segment 13G15-FRC to record overall dissipated energy similar to the control segment (7G15). Therefore, using the FRC compensated for the overall loss of dissipated energy with the higher longitudinal reinforcement ratio. This means that the longitudinal reinforcement ratio could be increased without affecting the total energy storage in the inelastic domain **(Fig. 6.13)**. **Fig. 6.13** indicates, moreover, good predictions for the analytical model with experimental-to-predicted cumulative dissipated energy ratios of 1.13, 1.04, 1.06, and 1.12 for segments 7G15-FRC, 13G15-FRC, 7G15-U-FRC, and 7G15, respectively.

6.7 CONCLUSIONS

The behavior of precast FRC tunnel lining segments reinforced with GFRP bars under quasi-static cyclic flexural loading was investigated experimentally and analytically. Based on the experimental results and the analytical study presented in this paper, the following conclusions can be drawn:

- The hysteretic response of the FRC segments in all second excursions reflected stable cyclic behavior with no or limited strength degradation up until failure. Moreover, the unloading stiffness degradation in all the segments tested was advantageous in improving the structural reparability and reducing the residual deformation at the end of each cycle under cyclic loading conditions.
- The use of FRC instead of NSC for the segments with the same longitudinal reinforcement ratio enhanced segment overall cracking distribution under quasi-static cyclic flexural loading. Moreover, using FRC for segments with the same longitudinal reinforcement ratio increased segment ductility and deformability under quasi-static cyclic flexural loading.
- Increasing the longitudinal reinforcement ratio in the FRC segments increased the segments' ultimate carrying capacity under quasi-static cyclic flexural loading. It is worth mentioning, however, that segment 13G15-FRC did not reach its full flexural load-carrying capacity due to its shear failure. In addition, increasing the longitudinal reinforcement ratio in the FRC segments reduced the crack width and crack spacing in the section of the segment at ultimate load levels.

- The reduction in the ductility index μ_e due to the increased longitudinal reinforcement ratio was compensated for with the use of FRC where the segment with 0.90% longitudinal reinforcement ratio had a ductility index comparable to that of the NSC segment with 0.50% longitudinal reinforcement ratio.
- The use of the closed tie configuration in FRC segments enhanced the crack distribution in the section at ultimate load levels compared to the double U-shaped tie configuration. Nevertheless, the double U-shaped tie configuration in the FRC segments slightly increased segment ductility under quasi-static cyclic flexural loading.
- The damage caused to the GFRP-reinforced PCTL segments under cyclic loading conditions was established using the secant stiffness damage index (KI). The rate of KI degradation during the loading cycles was not confirmed for all the segments tested. The decrease in KI rate in the segment reinforced with the higher longitudinal reinforcement ratio was less than that in segments reinforced with the lower longitudinal reinforcement ratio. Therefore, the residual stiffness in the last loading cycle was comparable for all the segments tested.
- Using the layer-by-layer iterative approach, the analytical model presented in this study was capable of predicting the hysteresis response of the GFRP-reinforced PCTL segments under quasi-static cyclic flexural loading. The model provided good predictions with experimental-to-predicted ratios ranging between 0.95 and 0.96 for all the segments tested. In addition, the analytical model yielded good predictions for the cumulative dissipated energy, with experimental-to-predicted cumulative dissipated energy ratios ranging between 0.94 and 1.13, for all the segments tested.
- First-of-their-kind experimental results were presented for the GFRP-reinforced precast FRC tunnel lining segments under quasi-static cyclic flexural loading. These experimental results could be taken into consideration for the forthcoming design code provisions governing the efficiency of using FRC in GFRP-reinforced PCTL segments under cyclic conditions.

CHAPTER 7 STIFFNESS AND HYSTERESIS RESPONSE PREDICTIONS OF CURVILINEAR-GFRP REINFORCED PRECAST CONCRETE TUNNEL SEGMENTS UNDER QUASI-STATIC CYCLIC LOAD

FOREWORD

Authors and Affiliation:

- **Basil Ibrahim,** Ph.D. candidate, Department of Civil Engineering, Université de Sherbrooke, Sherbrooke, Quebec, Canada, J1K 2R1.
- **Salaheldin Mousa,** Postdoctoral fellow, Department of Civil Engineering, Université de Sherbrooke, Sherbrooke, Quebec, Canada, J1K 2R1.
- **Hamdy M. Mohamed,** Research Associate/Lecturer, Department of Civil Engineering, Université de Sherbrooke, Sherbrooke, Quebec, Canada, J1K 2R1.
- **Brahim Benmokrane,** Professor, Department of Civil Engineering, Université de Sherbrooke, Sherbrooke, Quebec, Canada, J1K 2R1.

Journal Title:

ACI Structural Journal

Paper Status:

Submitted on January 19, 2023.

Contribution:

The chapter's outcomes are first-of-their-kind for the hysteresis behavior of the curvilinear-GFRP reinforced PCTL under quasi-static cyclic flexural loading. The analytical predictions could be taken into consideration for the forthcoming design code provisions governing the efficiency of using curvilinear-GFRP reinforcement for the PCTL segments application under cyclic conditions.

ABSTRACT

The hysteresis response of precast concrete tunnel lining (PCTL) segments reinforced internally with fiber-reinforced polymer (FRP) bars under quasi-static cyclic flexural loading is a field in which no experimental research results are available. This paper investigates the hysteresis behavior of PCTL segments reinforced internally with glass-FRP (GFRP) bars. Full-scale curvilinear-GFRP reinforced PCTL segments were designed, fabricated and tested under quasi-static cyclic flexural loading. The segments have a total length, width and thickness of 3100 mm (122 in.), 1500 mm (59 in.) and 250 mm (9.8 in.), respectively. The test parameters included in this study are the longitudinal reinforcement ratio, the transverse reinforcement configuration, and the concrete compressive strength. The hysteresis response, cracking pattern, and ductility of the PCTL segments were identified and experimentally evaluated. The experimental results of the current study demonstrate that the hysteresis response of the curvilinear-GFRP reinforced PCTL segments revealed stable cyclic behavior with no or limited strength degradation until failure. In addition, an analytical prediction for the load carrying capacity, deflection, loading and unloading stiffness of the test segments was carried out. The segments' analytically predicted responses were validated and compared to the experimental results. The segments' analytically predicted models for the post-cracking loading tangent stiffness and the unloading stiffness for the curvilinear-GFRP reinforced PCTL segments was proposed in this paper. The analytically predicted hysteresis response shows accurate predictions with comparable loading stiffness, unloading stiffness and residual deformation at the end of each loading cycle.

Keywords: Precast concrete tunnel lining (PCTL) segments; glass fiber reinforced polymer (GFRP) bars; normal strength concrete (NSC); high strength concrete (HSC); quasi-static cyclic flexural loading; hysteresis behavior; deformability.

7.1 INTRODUCTION

Reinforcement corrosion in the conventionally steel reinforced precast concrete tunnel (PCTL) segments causes premature degradation and thus requires expensive maintenance and repair. Many conventionally steel reinforced concrete tunnels are deteriorating as they age [Zhiqiang and Mansoor, 2013]. Since concrete is not perfectly impermeable, chlorinated groundwater saturating the conventionally steel reinforced concrete in tunnels applications causes concrete cover permeating and initiates electrolytic reaction with the reinforcement, which results in accelerating the reinforcement corrosion and loss of structural integrity [Rancourt, 2016]. According to the [ACI 440.1R-15], corrosion is the most problematic deterioration and expensive issue in concrete structures reinforced with conventional steel reinforcement. The reinforcement corrosion in the conventionally steel reinforced concrete structures costs the United States' economy about 1% of the country's gross domestic product [Whitmore and Ball, 2004]. Likewise, corrosion damage repair for the conventionally steel reinforced concrete structures costs Canada more than $10 billion annually [Davis, 2000]. As they are characterized by corrosion resistance, long lifespan, and reduced maintenance costs, the noncorrosive lightweight and high-strength fiber-reinforced polymer (FRP) reinforcement is one effective alternative for the conventional steel reinforcement in solving this corrosion issues [Wang et al., 2017; Solyom and Balázs, 2020; Pan and Yan, 2021; Benmokrane et al., 2021].

The flexural behavior of PCTL segments reinforced with the noncorrosive curvilinear-glass-FRP (curvilinear-GFRP) reinforcement bars as an alternative for the conventional steel reinforcement has been narrowly investigated in the literature [Caratelli et al., 2016; 2017; Spagnuolo et al., 2017; Hosseini et al., 2022]. Compared to the flexural behavior of the streel reinforced PCTL segments, it has been demonstrated that the curvilinear-GFRP reinforcement can be an effective alternative to the conventional steel reinforcement [Caratelli et al., 2017; Hosseini et al., 2022]. Moreover, it has been illustrated that the flexural behavior of both curvilinear-GFRP reinforced and conventionally steel reinforced PCTL segments are comparable. Despite the brittleness of the curvilinear-GFRP reinforcement, it has been moreover demonstrated that the curvilinear-GFRP reinforced PCTL segments exhibited adequate ductility compared to the conventionally steel reinforced PCTL segments [Caratelli et al., 2016]. In addition, the failure warning in the

curvilinear-GFRP reinforced PCTL segments is ensured by the wide cracking generated by the high strain that the curvilinear-GFRP bars exhibited before failure [Spagnuolo et al., 2017].

According to [ACI 544.7R-16], the loads acting on the PCTL segments from casting up to erection within the tunnel boring machine (TBM) shield fall into three stages. these three stages are the production and transient stage, the construction stage, and the service stage. The final service stages are represented by the long-term loads acting on the lining from the ground, groundwater, surcharges, and other loads from any circumstances such as earthquake, fire, explosion, and breakouts at cross passageways. Essentially, there are no research results in the literature on the hysteresis response of the curvilinear-GFRP reinforced PCTL segments under cyclic loads. The flexural cyclic behavior of steel-fiber reinforced concrete (SFRC) and conventionally steel reinforced PCTL segments under quasi-static cyclic flexural loading has been experimentally studies by [Abbas, 2014]. It was revealed that both SFRC and conventionally steel reinforced PCTL segments exhibited reasonable ductility and energy dissipation capacities and stratified the flexural requirements.

Principally, the hysteresis behavior of the reinforced concrete structures subjected to large cyclic loading exhibit level of stiffness degradation, which is cause by cracking, loss of bond or integration with high shear or axial stress [Al-Saadi et al., 2019]. The level of stiffness degradation depends on the loading history and the characteristics of the reinforced concrete members [Xiao et al., 2018]. The unloading stiffness is an essential constrain in determining the recoverability and the residual deformation of the reinforced concrete members under cyclic loading conditions [Fahmy et al., 2009]. Where the unloading stiffness degradation is considered advantageous in improving the structural reparability under cyclic loading conditions, as the structural residual deformation is directly associated to the unloading stiffness of the reinforced concrete members [Ding et al., 2013]. In terms of loading and unloading stiffness, there are no available experimental results on the hysteresis behavior of curvilinear-GFRP reinforced PCTL segments. Accordingly, this paper studies the hysteresis behavior of the curvilinear-GFRP reinforced PCTL segments under quasi-static cyclic flexural loading.

This work is part of current comprehensive research program carried out in the Department of Civil and Building Engineering at University of Sherbrooke, aiming at improving the exciting practices and developing more competent design and construction approaches for the use of

curvilinear-GFRP bars in precast concrete tunnel lining segments applications. This ongoing research investigates the behavior of full-scale curvilinear-GFRP reinforced PCTL segments under different loading conditions – Static flexural loading [Hosseini et al., 2022]; Quasi-static cyclic flexural loading; Punching shear and Settlement. So far, this research is the first experimental work that provides experimental data using laboratory testing on the curvilinear-GFRP reinforced PCTL segments performance under quasi-static cyclic flexural loading, according to the [ACI 374.2R-13]. Which can be considered in the forthcoming provisions of codes for the efficiency of replacing the conventional steel reinforcement with noncorrosive curvilinear-GFRP reinforcement for the cyclic behavior of the PCTL segments.

7.2 RESEARCH SIGNIFICANCE AND OBJECTIVES

The hysteresis behavior, in terms of loading and unloading stiffness, of the curvilinear-GFRP reinforced PCTL segments is one field in which no experimental research results are available. This study aims at investigating the loading and unloading stiffness of the curvilinear-GFRP reinforced PCTL segments under quasi-static cyclic flexural loading. An experimental program to evaluate the hysteresis response has been carried out. In addition, the hysteresis behavior of the PCTL segments, in terms of loading and unloading stiffness, is analytically investigated and compared to the experimental results. Furthermore, in order to experimentally and analytically examine the recoverability of the curvilinear-GFRP reinforced PCTL segments, in this study, a damage index for the PCTL segments is defined and evaluated in accordance with the residual deformation. All the experimental and analytical outcomes and conclusions of this work are implemented to assess and explore the feasibility of the use of the curvilinear-GFRP bars as internal reinforcement for the PCTL segments application under cyclic loading conditions. Moreover, the outcomes of this study will be useful for design engineers and represent a significant contribution to North American technical committees engaged in developing standards and design provisions for PCTL segments reinforced with GFRP bars.

7.3 EXPERIMENTAL PROGRAM

7.3.1 Materials

The mechanical properties of the different sand coated GFRP bars employed in this study were determined in accordance with the [ASTM D7205/D7205M-21] as listed in **Table 7.1**. Number 6

(20 mm) and number 5 (15 mm) curvilinear-GFRP bars were used for the PCTL segments' longitudinal reinforcement. In addition, number 6 (20 mm) and number 5 (15 mm) U-shaped GFRP bars were used as anchorage for the longitudinal reinforcement, at both ends of each segment. For the transverse reinforcement, number 4 (13 mm) closed and double U-shaped ties were used for the PCTL segments. All the PCTL segments were cast at the SYM-TECH precast concrete facility in Saint-Hyacinthe, Quebec, Canada. The targeted concrete compressive strength was 40 MPa (5.8 ksi) and 80 MPa (11.6 ksi) for the normal strength concrete (NSC) and the high strength concrete (HSC) segments, respectively. **Table 7.2** lists the average actual concrete compressive strength based on the average tested results of 100 x 200 mm (3.94 x 7.89 in.) concrete cylinders tested on the first day of the start of testing the segments.

Table 7.1 Mechanical properties of the reinforcement bars

Reinforcement type	Bar size	Bar diameter (mm)	Nominal cross-sectional area (mm^2)	Modulus of elasticity (GPa)	Tensile strength (MPa)	Tensile strain (%)
Curvilinear-GFRP bars	#5	15.0	199	55.1	1115	2.0
	#6	20.0	284	52.9	1068	2.0
U-shaped GFRP bars	#5	15.0	199	53.5	1283	2.4
	#6	20.0	284	53.2	1131	2.1
Closed GFRP ties	#4	13.0	129	55.6	1248	2.2

Note: 1 mm = 0.0394 in; 1 MPa = 145.04 psi; 1 GPa = 145.04 ksi.

7.3.2 Test segment

The experimental program was designed to provide data on the cyclic behavior of curvilinear-GFRP reinforced PCTL segments. Four full-scale curvilinear-GFRP reinforced PCTL segments were designed, fabricated, and tested under quasi-static cyclic flexural loading. The PCTL segments were kept skewed at both ends, and the clear cover was kept constant at 40 mm (1.57 in.) for all test segments. The segments were designed in accordance with the [ACI 440.1R-15] and [CAN/CSA S806-12 (R2017)]. The test parameters in this experimental program included the longitudinal reinforcement ratio, the transverse reinforcement configuration (closed versus double U-shaped ties), and the concrete compressive strength. **Table 7.2** shows the reinforcement details and the test matrix for the PCTL segments.

Table 7.2 Test matrix and segment details

Specimen ID	Reinforcement type	Concrete type	Concrete compressive strength (MPa)	Longitudinal reinforcement		Transverse reinforcement
				Number of bars	ρ_f (%)	
7G15	GFRP	NSC	52	7 bars No. 5	0.50	No. 4 closed GFRP ties spaced at 200 mm
7G20	GFRP	NSC	47	7 bars No. 6	0.70	No. 4 closed GFRP ties spaced at 200 mm
7G15-U	GFRP	NSC	50	7 bars No. 5	0.50	No. 4 double U-shaped GFRP ties spaced at 200 mm
7G15-U-H	GFRP	HSC	81	7 bars No. 5	0.50	No. 4 double U-shaped GFRP ties spaced at 200 mm

Each segment is identified with an alphanumeric code. The first number of the code represents the number of the top/bottom longitudinal reinforcement bars. The letter G refers to the GFRP reinforcement used for the PCLT segments. The second number represents the curvilinear-GFRP nominal diameter of the top/bottom longitudinal reinforcing bars. To differentiate between the segments with different transverse reinforcement configuration, the letter U is added to the segments reinforced transversely with double U-shaped ties. In addition, the letter H is added to the segment cast with HSC. Segment 7G15 and 7G20 are NSC segments with top and bottom longitudinal reinforcement consisting of 7 No. 5 curvilinear-GFRP bars and 7 No. 6 curvilinear-GFRP bars with longitudinal reinforcement ratio of 0.50% and 0.70%, respectively. Both segments were reinforced transversely with closed number 4 GFPR ties spaced at 200 mm (7.87 in.). Seven No. 5 and No. 6 U-shaped GFRP anchorage bars were installed on each side of segments 7G15 and 7G20, respectively. Segment 7G15-U is also NSC segment reinforced longitudinally (top and bottom) with 7 curvilinear-GFRP bars No. 5. The segment 7G15-U, however, is reinforced transversely with double U-shaped number 4 GFRP ties spaced at 200 mm (7.87 in.). Similarly, the HSC segment 7G15-U-H is reinforced longitudinally (top and bottom) with 7 curvilinear-GFRP bars No. 5 and reinforced transversely with double U-shaped No. 4 GFRP ties spaced at 200 mm (7.87 in.). Moreover, No. 5 U-shaped GFRP anchorage were installed at each side of the two segments 7G15-U and 7G15-U-H. **Fig. 7.1** illustrates the reinforcement details for the test segments.

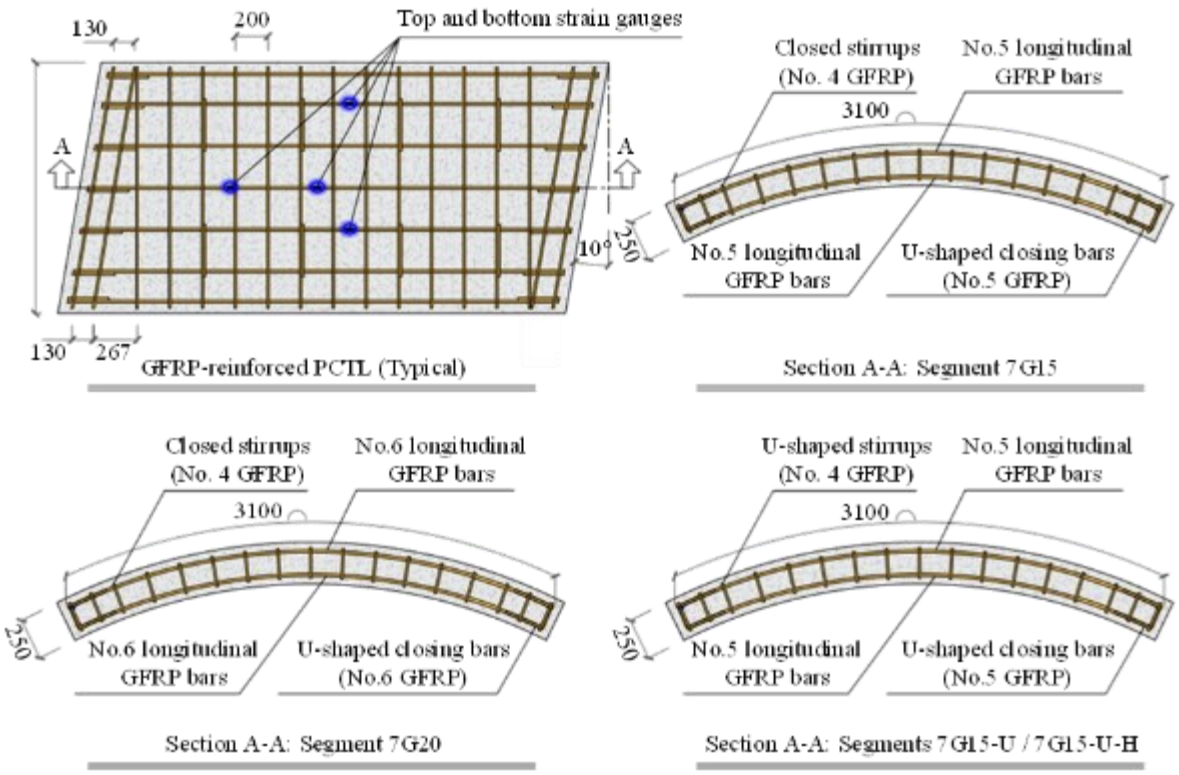

Fig. 7.1 Reinforcement detials for the test segments. (Note: all dimensions in mm; 1 mm = 0.0394 in.)

7.3.3 Test setup and instrumentation

The test setup was designed and fabricated at the University of Sherbrooke's CFI structural laboratory, using 11,000 kN (247.3 kips) capacity MTS universal testing machine attached to a spreader beam, as shown in **Fig. 7.2**. The load was applied in three-point bending load, at a displacement-controlled rate of 0.8 mm/min. The test span for the PCTL segments was 2400 mm (94.5 in.). Five different linear potentiometers (LPOTs) were placed to measure the segments' mid- and quarter-span deflections **(Fig. 7.2)**. In addition, to measure the strain at mid- and quarter-span of the PCTL segments, 10-mm (0.39 in.) and 60-mm (2.36 in.) electrical resistance strain gauges were installed on the reinforcing bars and attached to the concrete surface, respectively **(Fig. 7.1)**. The load was moreover applied in accordance with the tests of structural components under slowly applied quasi-static loading of the [ACI 374.2R-13]. The quasi-static cyclic flexural loading has been applied in terms of percentage of the maximum displacement obtained from the static testing results [Hosseini et al., 2022]. Two cycles of loading and unloading are conducted for 1.25%, 2.5%, 5%, 10%, 25%, 50% and 75% of the maximum displacement, followed by one

cycle up to failure. In all cycles, the unloading phase was stopped at a minimum load of 5 kN (1.12 kips) to keep the test machine engaged to the segments.

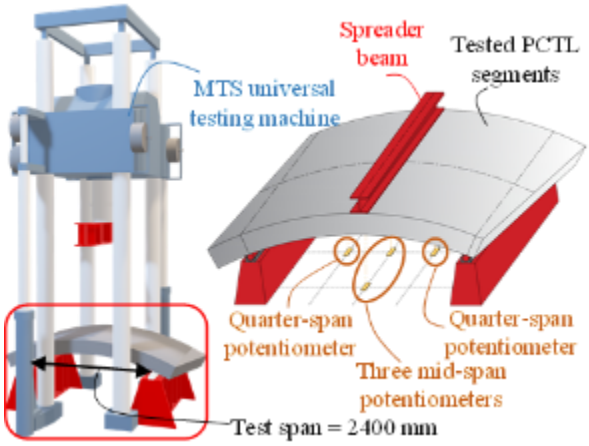

Fig. 7.2 Test setup. (Note: 1 mm = 0.0394 in.)

7.4 TEST RESULTS AND DISCUSSION

This section discusses the experimental hysteresis behavior of the PCTL segments. In addition, ductility index, crack width, and deformability of the PCTL segment were defined, estimated, and evaluated in this section. **Table 7.3** summarizes the experimental test results.

Table 7.3 Summary of results

Specimen ID	Cracking load (kN)	Service Load[a] (kN)	Failure load (kN)	Type of failure	Deflection at failure (mm)	Ductility Index	J-factor	P_{exp}/P_{pred} at P_n
7G15	70	91	302	Concrete crushing	56.5	1.49	5.9	0.93
7G20	62	89	295	Concrete crushing	46.5	1.43	4.7	0.93
7G15-U	59	81	271	Concrete crushing	52.8	1.51	5.9	0.95
7G15-U-H	60	94	312	Concrete crushing	59.5	1.78	4.3	0.88
Average								0.92
Standard deviation								0.03
Coefficient of variance (COV) - %								3.24

[a] The service load of the test specimens is estimated at 0.3 of P_n.
Note: 1 mm = 0.0394 in; 1 kN = 0.2248 kips.

7.4.1 Hysteresis response

Fig. 7.3 shows the hysteresis behavior of the tested segments, in form of load versus mid-span deflections. At 1.25% and 2.5% of the maximum displacement cycles, all segments exhibited the same linear hysteresis response, corresponding to the condition of uncracked section of the segments. Beyond these loading cycles, the first flexural cracks at the tension zone of the tested segments, started to initiate under the loading point, in the 5% of the maximum displacement cycles. The cracking load, P_{cr}, ranged between 59 kN (13.26 kips) to 70kN (15.74 kips), for all tested segments. The stiffness of all tested segments has reduced after cracking, with almost linear hysteresis response up to the failure initiation.

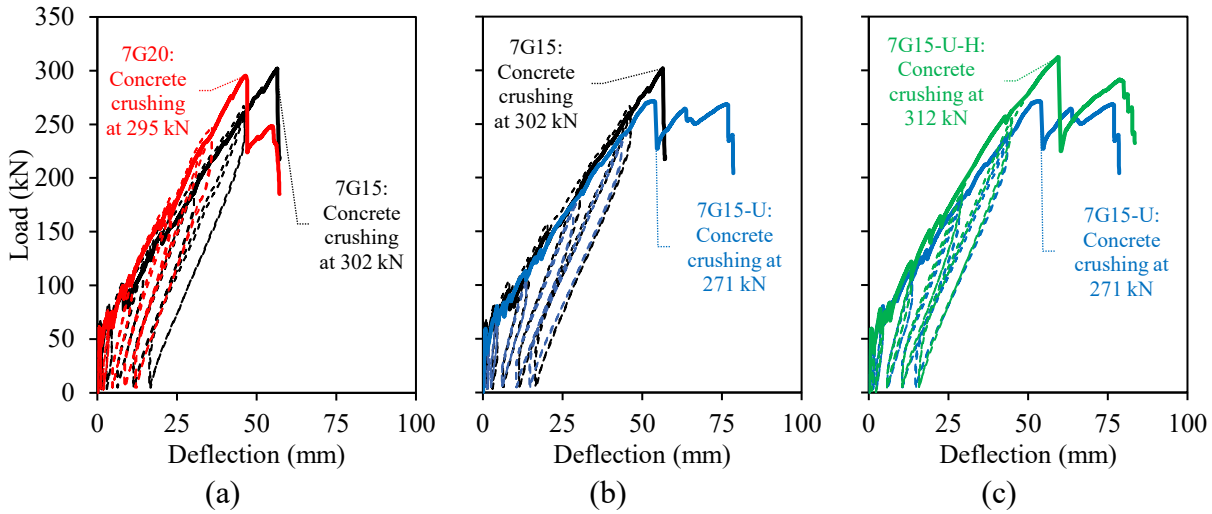

Fig. 7.3 Hysteresis response for (a) segments with different reinforcement ratio; (b) segments with different transverse reinforcement configuration; and (c) segments with different concrete compressive strength.

At 10% and 25% of the maximum displacement cycles, further flexural cracks started to initiate within the shear-span of the tested segments. Thereafter, in the 75% of the maximum displacement cycles, the main flexural cracks became wider and propagated towards the loading point until the failure occurred. All the curvilinear-GFRP reinforced PCTL segments failed by concrete crushing in the compression zone of the segments' mid-span at a load carrying capacity, P_n, of 302 kN (67.89 kips), 295 kN (66.32 kips), 271 kN (60.92 kips), and 312 kN (70.14 kips) for segments 7G15, 7G20, 7G15-U, and 7G15-U-H, respectively, as illustrated in **Fig. 7.4**. Moreover, at 1.25% and

2.5% of the maximum displacement cycles, the unloading stiffness was relatively high in all tested segments. Looking at **Fig. 7.3** reveals that beyond the 5% of the maximum displacement cycles, the unloading stiffness for the segments have reduced rapidly. This unloading stiffness degradation, through the loading cycles, contributed to improving the segments' reparability. As in good agreement with the work of [Ding et al., 2013], the unloading stiffness degradation, resulted in decreasing the segments' residual deformation. The residual deformation for the tested segments, was therefore smaller in the 50% and 75% of the maximum displacement cycles than that in the preceding loading cycles. Furthermore, in all second excursion loading cycles, the hysteresis response for the GFRP reinforced PCTL segments reflected stable cyclic behavior with no or limited strength degradation until failure.

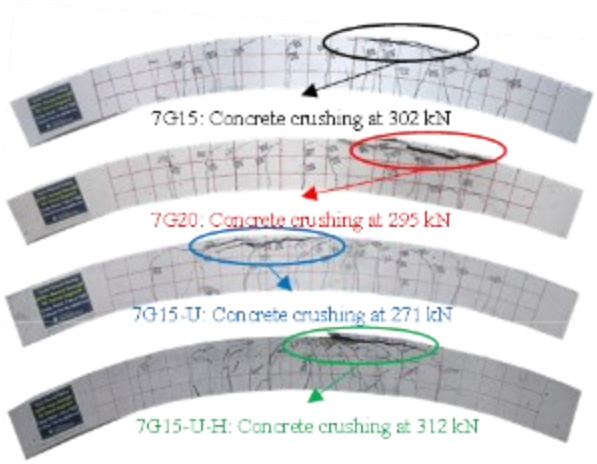

Fig. 7.4 The mode of failure for all test segments.

7.4.2 Strain readings

Fig. 7.5 shows the load-strain relationships for the tested segments, at mid-span. Prior to cracking, at 1.25% and 2.5% of the maximum displacement cycles, the strain readings at the top concrete fibers in all segments were insignificant (-80 με to -200 με), as shown in **Fig. 7.5(a)**. Beyond the 5% of the maximum displacement cycles, the mid-span concrete strain readings at the top concrete fibers of the tested segments, increased almost linearly until the failure initiation. The maximum recorded mid-span concrete compressive strain readings in segments 7G15, 7G20, 7G15-U, and 7G15-U-H were -3840 με, -2683 με, -2640 με, and -2950 με, respectively, as shown in **Fig. 7.5(a)**. In addition, **Figs. 7.5(b) and (c)** shows that before the 5% of the maximum displacement cycles, there were no significant strain readings neither in the bottom nor the top reinforcement bars. The

bottom and top GFRP bars exhibited a gradual strain increase until the failure occurred. **Fig. 7.5(b)** shows that the maximum recorded mid-span strain for the bottom bars in segments 7G15, 7G20, 7G15-U, and 7G15-U-H was 17965 με, 11637 με, 14326 με and 17890 με, respectively. The mid-span strains in the bottom longitudinal reinforcement bars demonstrate that the increase of the longitudinal reinforcement ratio in segment 7G20 resulted in reducing the tensile strains in the longitudinal reinforcement bars compared to its counterpart segment 7G15. The maximum recorded mid-span strains in the bottom longitudinal reinforcement bars in segments 7G15 and 7G20 represents 88% and 58% of the curvilinear-GFRP bars' ultimate tensile strain, respectively. Moreover, in agreement with the work of [Faza and GangaRao, 1993], the use of high strength concrete in segment 7G15-U-H resulted in exploiting higher tensile strain of the reinforcement bars. The maximum recorded mid-span strains in the bottom longitudinal reinforcement bars in segments 7G15-U and 7G15-U-H represents 72% and 89% of the curvilinear-GFRP bars' ultimate tensile strain, respectively. Furthermore, the strain gauge readings illustrated that, at failure, the top reinforcement bars, for all tested segments, were under tension, with maximum recorded mid-span strains of 4210 με, 3444 με, 4787 με, and 7380 με for segments 7G15, 7G20, 7G15-U, and 7G15-U-H, respectively **(Fig. 7.5(c))**.

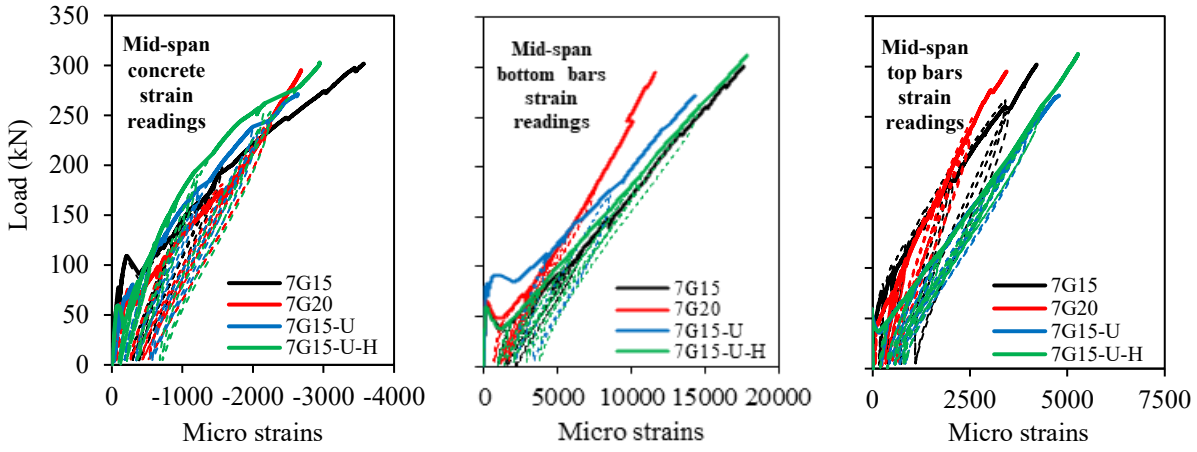

(a) (b) (c)

Fig. 7.5 Load strain relationship at mid-span at (a) concrete surface; (b) bottom reinforcement bars; and (c) top reinforcement bars.

The test results indicate that the strains in the top concrete fibers, the bottom reinforcement bars and the top reinforcement bars at quarter-span of all segments was less than that at mid-span. The maximum recorded concrete compressive strains at the quarter-span in segments 7G15, 7G20,

7G15-U, and 7G15-U-H were -1162 με, -1285 με, -995 με and -617 με, respectively. Similarly, the maximum recorded quarter-span strains in the bottom longitudinal reinforcement bars in segments 7G15, 7G20, 7G15-U, and 7G15-U-H were 8197 με, 6676 με, 7760 με, and 7380 με, respectively. While the maximum recorded quarter-span strains in the top longitudinal reinforcement bars in segments 7G15, 7G20, 7G15-U, and 7G15-U-H were 1168 με, 783 με, 1819 με and 2105 με, respectively.

7.4.3 Crack-width

Fig. 7.6 shows the cracking pattern of the tested segments. Concrete fractures under cyclic loading are characterized by large cracks and stains than concrete fractures under static loading [Xiao et al., 2018]. However, the linear behavior of the curvilinear-GFRP reinforced PCTL segments reduced the cyclic effects on the crack-width and eliminated the residual cracks at the end of each unloading cycle. The LVDTs' readings at the end of each unloading cycle, indicated that the crack widths were insignificant.

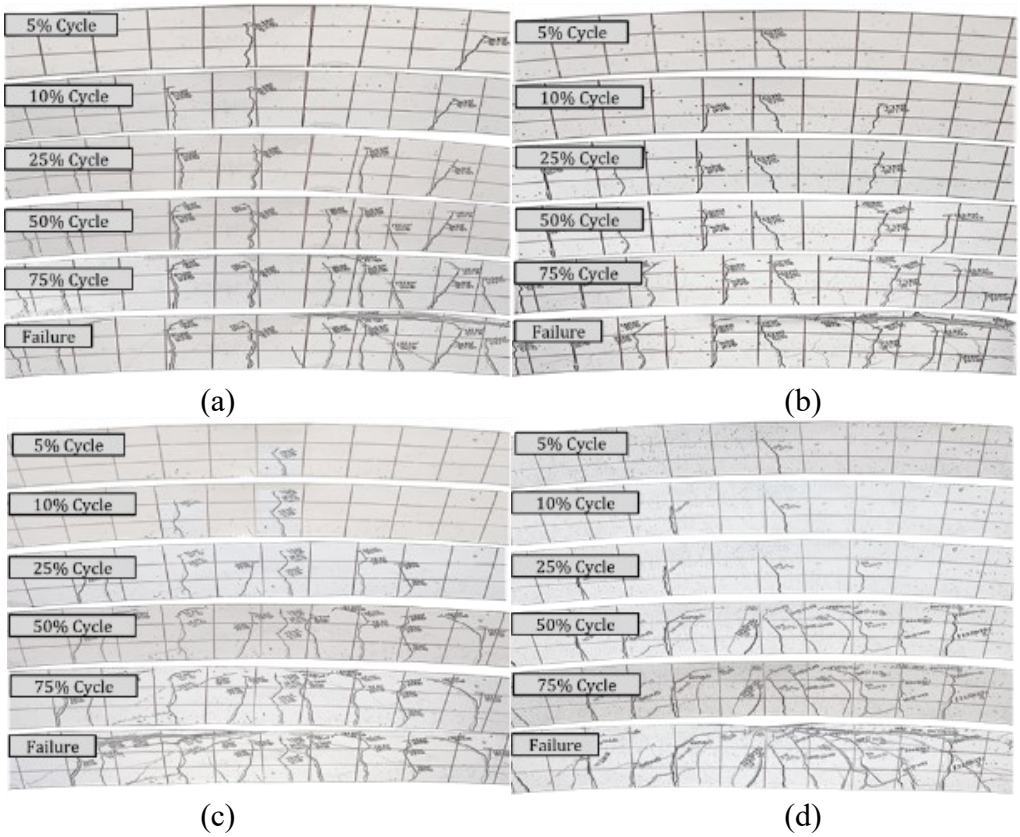

Fig. 7.6 Cracking pattern in (a) segment 7G15; (b) segment 7G20; (c) segment 7G15-U; and (d) segment 7G15-U-H.

Moreover, as seen in **Fig. 7.6**, increasing the longitudinal reinforcement ratio from 0.50% in 7G15 to 0.70% in 7G20 generally enhanced the cracking behavior, where increasing the reinforcement ratio resulted in having narrower cracks with closed cracking spacing, in all loading cycles. As the crack width is mainly controlled by the reinforcing bar spacing, and both 7G15 and 7G20 have the same reinforcing bars' spacing, both segments had almost the same crack width of 0.52 mm (0.02 in.) at the service load levels (2000 με). However, the crack width in 7G15 was about 29% greater than that in segment 7G20 at ultimate load levels (P_n), as shown in **Fig. 7.7**. Similarly, looking at **Fig. 7.6** reveals that the closed tie's configuration in 7G15 slightly enhanced the crack width, compared to the double U-shaped ties' configuration in 7G15-U. At both the service and ultimate load levels, the crack width in 7G15-U was about 5% more than that in 7G15, as shown in **Fig. 7.7**. Moreover, **Fig. 7.6** expresses the concrete compressive strength's effect on cracking behavior of the curvilinear-GFRP reinforced PCTL segments. Increasing the concrete compressive strength resulted in narrower cracks with closer cracking spacing. The crack width in segment 7G15-U was about twicer wider than that in the HSC segment 7G15-U-H at 2000 με.

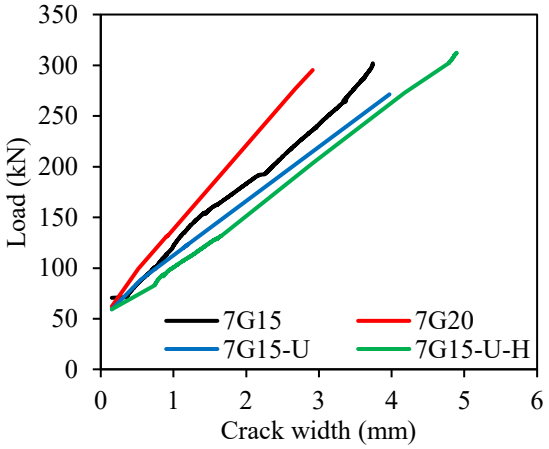

Fig. 7.7 The load versus crack-width for all test segments.

7.4.4 Ductility

The adequacy of withstanding inelastic deformation without reduction in the member's carrying capacity is defined as the member's ductility. Unlike concrete members reinforced with conventional steel reinforcement, where ductility is directly expressed by the ultimate deformation to the deformation at yield ratio, there is no yield point in the FRP reinforced concrete members. Subsequently, the ductility of the concrete members reinforced with FRP reinforcement is

indirectly computed in terms of energy deformation or energy-based ductility index [Grace et al., 1998].

To determine the deformability of the FRP reinforced concrete members, the *Canadian Highway Bridge Design Code* [CAN/CSA S6-19] implements the J-factor approach of [Jaeger et al., 1997]. In this approach, the moment carrying capacity and the curvature of the FRP reinforced concrete members, at both service and ultimate conditions, are considered, as expressed in **Equation 7.1**.

$$J = \left(M_{ultimate} / M_s\right) \times \left(\psi_{ultimate} / \psi_s\right) \tag{7.1}$$

where ψ_s is the curvature at service condition (strain at top concrete surface = 1000 με); ψ_u is ultimate curvature exhibited at failure; M_s is the moment at service condition; and M_u is the ultimate moment.

In addition to the deformability J-factor approach in examining the ductility of the curvilinear-GFRP reinforced PCTL segments, the ductility index, μ_e, had been computed based on the energy absorption approach by [Naaman and Jeong, 1995], as expressed in **Equation 7.2**.

$$\mu_e = 0.5\left[\left(E_{tot} / E_{el}\right) + 1\right] \tag{7.2}$$

where E_{tot} is the segment's overall energy; and E_{el} is the released elastic energy at failure. The total energy, E_{tot}, and the elastic energy, E_{el}, are calculated as the area under the segment's envelope load-deflection curve and the area of the triangle shaped at failure load using the weighted average slopes of the two initial stiffnesses of the envelope load-deflection curve, respectively.

Table 7.3 exposes that when compared to the [CAN/CSA S6-19] code J-factor limit of 4 for the rectangular GFRP reinforced concrete sections, all curvilinear-GFRP reinforced PCTL segments demonstrated adequate deformability. The deformability J-factor for the segments 7G15, 7G20, 7G15-U, and 7G15-U-H were 5.9, 4.7, 5.9, and 4.3, respectively. Moreover, **Table 7.3** indicates that increasing the reinforcement ratio from 0.50% in segment 7G15 to 0.70% in segment 7G20 insignificantly reduced the ductility index of the curvilinear-GFRP reinforced PCTL segments. Both 7G15 and 7G20 segments exhibited a comparable computed μ_e of 1.49 and 1.43,

respectively. Likewise, using different transverse reinforcement has inconsequential effect on the segments' ductility index. As listed in **Table 7.3**, segment 7G15-U exhibited a computed μ_e of 1.51.

7.5 ANALYTICAL STUDY

In this section, the hysteresis response of the curvilinear-GFRP reinforced PCTL segments under quasi-static cyclic flexural loading has been analytically investigated. In addition, both the loading and unloading stiffness for the curvilinear-GFRP reinforced PCTL segments were predicted, evaluated, and compered to the experimental results.

7.5.1 Flexural load-deflection

Based on the strain compatibility and force equilibrium principles, the flexural capacity of the curvilinear-GFRP reinforced PCTL segments was first computed in the analytical analysis. According to Bernoulli's hypothesis, the concrete and the curvilinear-GFRP strains, moreover, are assumed in the analytical analysis to be proportional to the distance from the neutral axis. Furthermore, with accordance to the [ACI 440.11-22], the concrete crushing failure is assumed to occur at the concrete compressive strain of 0.003. In addition, the curvilinear-GFRP bars' tensile behavior is assumed to be linearly elastic in all loading states until failure, and the bond between the concrete and the curvilinear-GFRP bars is assumed to be perfect.

The parameter α_1 and β_1, presented in the equivalent rectangular stress block in **Fig. 7.8(a)**, are used to describe the concrete compressive strength distribution according to the [ACI 440.11-22], as expressed in **Equations 7.3 and 7.4**.

$$\alpha_1 = 0.85 \tag{7.3}$$

$$\beta_1 = 0.85 - \frac{0.05\left(f_c^{'} - 28\right)}{7} \geq 0.65 \tag{7.4}$$

In order to calculate the static load carrying capacity of the curvilinear-GFRP reinforced PCTL segments, the PCTL section properties and material properties were first defined. The neutral axis

depth, c, was then initially assumed. Thereafter, the concrete compression force, C_c, was calculated using **Equation 7.5**.

$$C_c = \alpha_1 f_c^{'} A_c \tag{7.5}$$

where $f_c^{'}$ is the concrete compressive strength of the PCTL segments; and A_c is the cross-sectional area of the PCTL segment.

Subsequently, the strain in the bottom and top curvilinear-GFRP bars, ε_f and $\varepsilon_f^{'}$, was computed using the strain compatibility principle with reference to the ultimate usable concrete strain of 0.003 stated by the [ACI 440.11-22]. The tensile forces in the curvilinear-GFRP bars were then calculated using **Equation 7.6**.

$$T = \varepsilon_f E_f A_f + \varepsilon_f^{'} E_f^{'} A_f^{'} \tag{7.6}$$

where T is the tensile force in the curvilinear-GFRP bars; E_f and $E_f^{'}$ are the modulus of elasticity of the bottom and top curvilinear-GFRP bars; and A_f and $A_f^{'}$ are the area of the bottom and top curvilinear-GFRP bars.

After having both the concrete and reinforcement forces, the section equilibrium was checked, and the process was repeated with the new assumed neutral axis depth, c, until equilibrium is attained. The curvilinear-GFRP reinforced PCTL section's moment carrying capacity was obtained by taking the moment of the forces around the centroid of the PCTL section. The curvilinear-GFRP reinforced PCTL segments' arch effect was also considered in calculating the load carrying capacity from the sections' ultimate moment capacity, using **Equations 7.7 – 7.10**.

$$X = R\sin\theta \tag{7.7}$$

$$Y = R\cos\theta \tag{7.8}$$

$$P = 2R\cos\theta \tag{7.9}$$

$$\text{Moment} = \text{R}\cos\theta \times \frac{\text{L}}{2} + \text{R}\Delta\sin\theta \tag{.10}$$

where θ is the angle of inclination of the segment's supports from the vertical axis; and Δ is the vertical distance between the segment's centerline at mid-span and the supports' resistance forces, as shown in **Fig. 7.8(b)**.

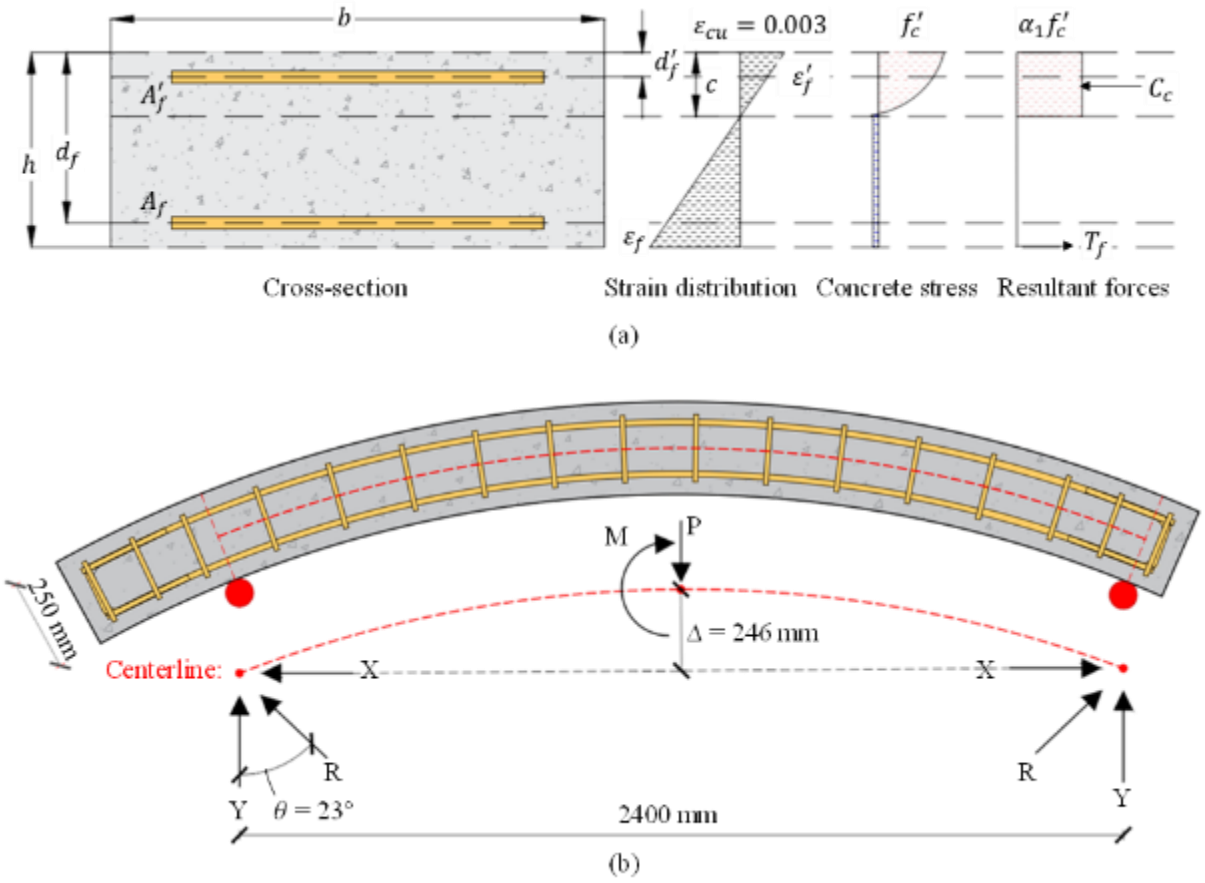

Fig. 7.8 (a) Idealized cross-section and stress-strain distribution; and (b) arch effect on the section's load carrying capacity. (Note: 1 mm = 0.0394 in.)

For the curvature predictions, the radius of curvature, R, to the neutral axis was first calculated. The radius of curvature, R, the neutral axis depth, kd, and the concrete strain in the extreme compression fibers, ε_c, varies along the member, as between the cracks the concrete in fact carries some tension. Considering only a small element of length, dx, of the segment, the rotation between the ends of the element is calculated using **Equations 7.11 and 7.12**.

$$\frac{dx}{R} = \frac{\varepsilon_c dx}{kd} = \frac{\varepsilon_f dx}{d(1-k)} \tag{7.11}$$

$$\frac{1}{R}=\frac{\varepsilon_c}{kd}=\frac{\varepsilon_f}{d(1-k)} \tag{7.12}$$

The curvature of the curvilinear-GFRP reinforced PCTL segments, ϕ, was computed as the rotation per unit length of the segment $\left(\phi=1/R\right)$, as expressed in **Equation 7.13**, where the curvature varies along the length of the segment because of the fluctuation of the neutral axis depth and the strains between the cracks.

$$\phi=\frac{\varepsilon_c}{kd}=\frac{\varepsilon_f}{d\left(1-k\right)}=\frac{\varepsilon_c+\varepsilon_f}{d} \tag{7.13}$$

7.5.2 Hysteresis response

The tensile behavior of the concrete structures reinforced internally with GFRP bars is almost linearly elastic and there is no yielding point in the GFRP reinforced concrete members. Therefore, the loading stiffness of the GFRP reinforced concrete members can be derived into pre-cracking and post-cracking stages.

7.5.2.1 Pre-cracking stiffness

In the pre-cracking stage, where the cracks are not initiated in the concrete section yet, the effective moment of inertia is corresponding to the gross moment of inertial of the transformed uncracked section, thus; the curvilinear-GFRP reinforced PCTL tangent stiffness in this stage is calculated using the simplified formula, as expressed **Equation 7.14** [Dong et al., 2016].

$$K_1=E_cI_g \tag{7.14}$$

where E_c is the PCTL segments' initial modulus of elasticity; and I_g is the uncracked PCLT sections' moment of inertia.

7.5.2.2 Post-cracking stiffness

In the post-cracking stage, cracks start to initiate and keep propagating in the concrete until failure. Therefore, the effective moment of inertia in this stage reduces until reaching the fully cracked section's moment of inertia at failure. The post-cracking tangent stiffness of the curvilinear-GFRP

reinforced PCTL segments is obtained using **Equations 7.15 and 7.16**, or by load-deflection curves regression using the simplified proposed **Equation 7.17**, as demonstrated in **Fig. 7.9(a)**.

$$K_{2\_i} = E_c I_e \tag{7.15}$$

$$I_e = \frac{PL^3}{48 E_c \delta} \tag{7.16}$$

$$K_{2\_i} = a \cdot \delta^{-0.5} \tag{7.17}$$

where K_{2_i} is the post-cracking tangent stiffness at each i cycle; P is the experimentally obtained applied load from the laboratory measures added to the equivalent load due to self-weight of the PCTL segment; E_c is the initial elastic modulus of concrete; L is the segments span length; δ is the experimentally measured mid-span deflection; and f_c' is the concrete compressive strength in MPa.

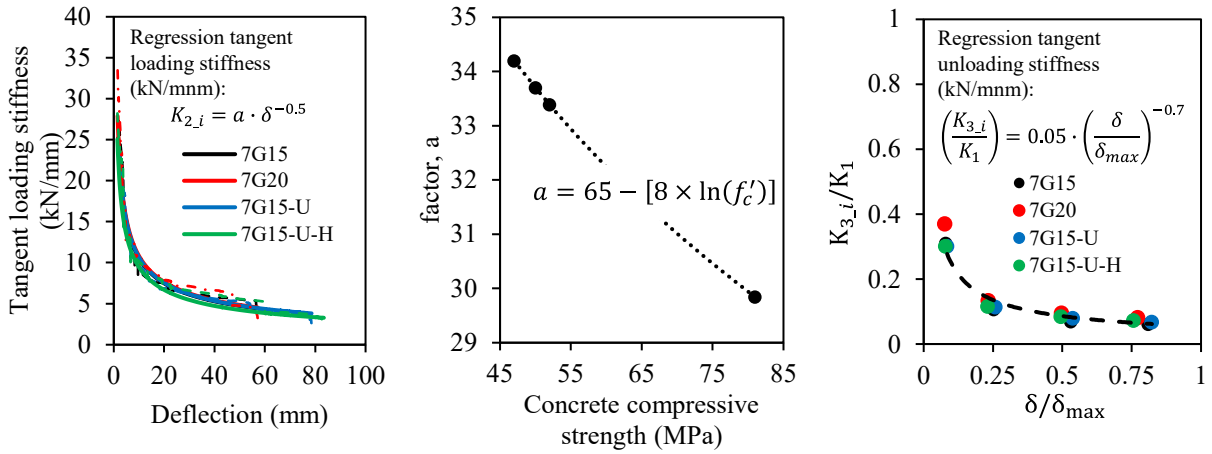

(a) (b) (c)

Fig. 7.9 (a) Regression of post-cracking loading tangent stiffness; (b) the factor, a, used for the post-cracking loading tangent stiffness prediction; and (c) regression of post-cracking unloading tangent stiffness for all tested segments.

As shown in **Fig. 7.9(b)**, the a factor depends on the compressive strength of the test segments and can be obtained using **Equation 7.18**.

$$a = 65 - \left[8 \times \ln\left(f_c'\right)\right] \tag{7.18}$$

7.5.2.3 Unloading stiffness

The unloading stiffness is also an important parameter in determining the value of the residual deformation and recoverability of the structure [Fahmy et al., 2009]. Where the unloading stiffness degradation is considered advantageous in improving the structural reparability under the cyclic loading conditions, as the structural residual deformation is directly related to the unloading stiffness. Under cyclic loading conditions, smaller unloading stiffness results in decreasing the structural residual deformation [Ding et al., 2013]. At the end of each loading cycle of the curvilinear-GFRP reinforced PCTL segments, the unloading stiffness degradation have been characterized by the ratio K_{3_i}/K_1, where K_{3_i} is the unloading stiffness at each i cycle; and K_1 is the segment's initial stiffness of the uncracked section at the first 1.25% of the maximum displacement cycle. Using the experimental K_{3_i}/K_1 of the tested segments, the unloading tangent stiffness, K_{3_i}, is obtained by regression analysis from the load-deflection curves, as shown in **Fig. 7.9(c)**, and can be calculated by **Equation 7.19**.

$$K_{3\_i} = (0.05K_1) \times \left(\frac{\delta}{\delta_{\max}}\right)^{-0.7} \tag{7.19}$$

where δ is the experimentally obtained mid-span deflection; and $\delta_{\max}$ is the experimentally obtained maximum mid-span deflection recorded for the segment at failure.

7.5.2.4 Residual deformation

The relationship between unloading stiffness ratio, K_{3_i}/K_1, degradation and the residual deformation ratio, $\delta_{residual}/\delta_i$, is illustrated in Figure 10, where $\delta_{residual}$ is the analytically predicted residual deformation; and δ_i is the analytically predicted maximum deformation reached at the end of each i cycle. At first, in the 1.25% and 2.5% of the maximum displacement cycles, K_{3_i}/K_1 was relatively high in all tested segments. Beyond the 5% of the maximum displacement cycles, K_{3_i}/K_1 have reduced rapidly. **Fig. 7.10** demonstrates that the residual deformation ratio, $\delta_{residual}/\delta_i$, for all tested segments, was therefore smaller in the 50% and 75% of the maximum displacement cycles than that in the preceding loading cycles. Moreover, **Fig. 7.10** indicates that

the degradation of the unloading stiffness ratio, K_{3_i} / K_1, and the residual deformation ratio, $\delta_{residual} / \delta_i$, for all tested segments was comparable, and therefore all tested segments had comparable cumulative residual deformation at the end of the 75% of the maximum displacement cycles, before failure.

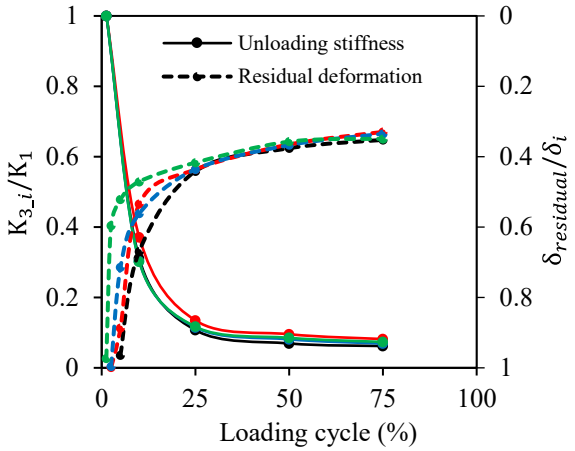

Fig. 7.10 Unloading stiffness degredation versus residual deformation ratio.

7.5.3 Experimental-to-predicted flexural capacities

Table 7.3 lists the experimental-to-predicted ratio for the flexural carrying capacities, P_{exp}/P_{pred}, for all tested segments. The analytical analysis showed accurate predictions for the ultimate load carrying capacity. The average P_{exp}/P_{pred} ratio for all tested segments was 0.92, with standard deviation of 0.03 and coefficient of variance (COV) of 3.24%. In addition, the hysteresis behavior of the curvilinear-GFRP reinforced PCTL segments was compared to the analytically predicted response according to the loading and unloading stiffness predictions, as shown in **Fig. 7.11**. The analytically predicted hysteresis response, shows accurate predictions with comparable loading stiffness, unloading stiffness and residual deformations at the end of each loading cycle.

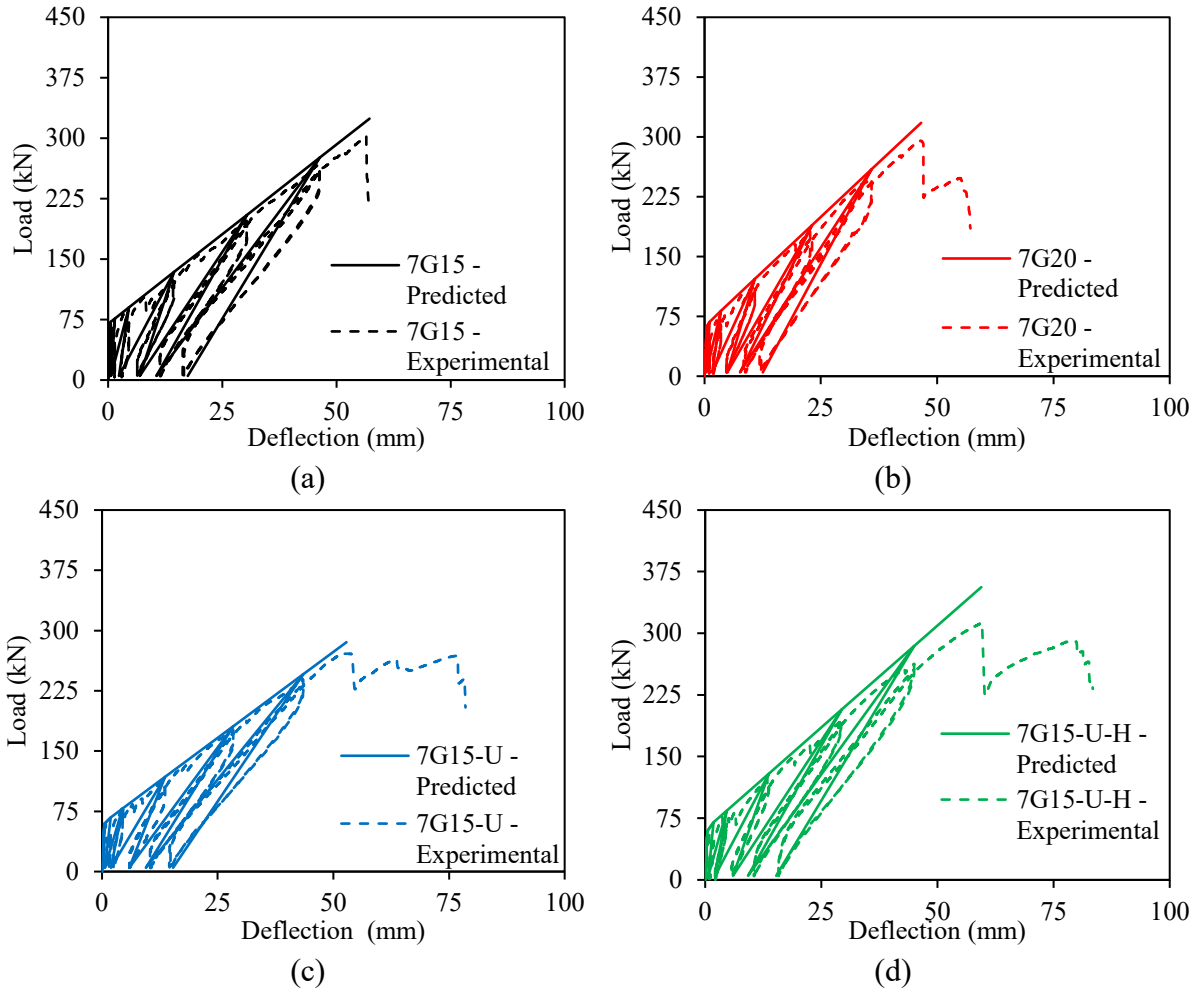

Fig. 7.11 Experimental versus analytically predicted hysteresis behavior for (a) segment 7G15; (b) segment 7G20; (c) segment 7G15-U; and (d) segment 7G15-U-H.

7.6 CONCLUSIONS

The hysteresis behavior of the curvilinear-GFRP reinforced PCTL segments under quasi-static cyclic flexural loading has been experimentally and analytically investigated in this paper. Based on the experimental results and the analytical study presented in this paper, the following conclusions can be drawn:

- In all second excursion loading cycles, the hysteresis response of all tested segments reflected stable cyclic behavior, with no or limited strength degradation until failure. Moreover, the unloading stiffness degradation under the quasi-static cyclic flexural loading was advantageous in improving the structural reparability and reducing the residual deformation at the end of each cycle.

- Although concrete fracture under cyclic loading is characterized by large cracks and strains than concrete fractures under static loading, the linear behavior of the curvilinear-GFRP reinforced PCTL segments reduced the cyclic effects on the crack width and eliminated the residual cracks at the end of each unloading cycle.
- All the curvilinear-GFRP reinforced PCLT segments demonstrated adequate deformability under the quasi-static cyclic flexural loading when compared to the [CAN/CSA S6-19] code limit of 4 for rectangular GFRP reinforced concrete sections.
- The analytical analysis showed accurate predictions for the ultimate load carrying capacity. The average P_{exp}/P_{pred} ratio for all tested segments was 0.92, with standard deviation of 0.03 and coefficient of variance (COV) of 3.24%.
- Analytical models for the post-cracking loading tangent stiffness and the unloading stiffness for the curvilinear-GFRP reinforced PCTL segments were proposed. The analytically predicted hysteresis response showed accurate predictions with comparable loading stiffness, unloading stiffness and residual deformation at the end of each loading cycle.
- First-of-their-kind experimental results and analytical predictions were presented for the hysteresis behavior of the curvilinear-GFRP reinforced PCTL under quasi-static cyclic flexural loading. These experimental results and analytical predictions could be taken into consideration for the forthcoming design code provisions governing the efficiency of using curvilinear-GFRP reinforcement for the PCTL segments application under cyclic conditions.

CHAPTER 8 SUMMARY, CONCLUSIONS AND RECOMMENDATIONS

8.1 SUMMARY

This research investigated the cyclic behavior of GFRP-reinforced PCTL segments, both experimentally and theoretically. A total of twelve full-scale PCTL segments with a total length, width, and thickness of 3100 mm, 1500 mm, and 250 mm, respectively, were constructed and tested under quasi-static cyclic flexural loading. Two cycles of loading and unloading were applied at 1.25%, 2.5%, 5%, 10%, 25%, 50%, and 75% of the estimated maximum displacement, followed by a single cycle up to failure. The test parameters included reinforcement flexural stiffness (GFRP versus steel), GFRP longitudinal reinforcement ratio, the concrete compressive strength (high-strength concrete (HSC) versus normal-strength concrete (NSC)), the concrete type (fiber-reinforced concrete (FRC) versus NSC), and the transverse reinforcement configuration (closed versus double U-shaped ties). The hysteresis response, cracking pattern, residual deformation, dissipated energy, ductility index, deformability, and secant stiffness damage index of the tested specimens were defined, estimated, and evaluated. A theoretical study was conducted to calculate the flexural and shear capacities of PCTL segments reinforced with GFRP bars according to the various current design provisions [ACI 440.1R-15; CAN/CSA S806-12 (R2017); fib TG-9.3, 2007; CNR-DT 203, 2006; AFGC, 2021]. In addition, a theoretical prediction according to the North American codes and design guidelines [ACI 440.1R-15; CAN/CSA S6-19; AASHTO, 2018], including cracking moment and crack width, was made and the results compared to the experimental results. Furthermore, using the layer-by-layer iterative approach, an analytical model was presented for the hysteresis response of the GFRP-reinforced PCTL segments under quasi-static cyclic flexural loading. In addition, analytical models for the post-cracking loading tangent stiffness and the unloading stiffness for the curvilinear-GFRP reinforced PCTL segments were proposed. So far, this research is the first experimental work aimed at providing experimental data involving the laboratory testing of the performance of PCTL segments reinforced with GFRP reinforcement under quasi-static cyclic flexural loading.

8.2 CONCLUSIONS

Based on the experimental, theoretical, and analytical results obtained in this research considering the previous parameters associated with the research program, the following conclusions are drawn:

8.2.1 Main outcomes

- The experimental results were the first of their kind on the applicability of using GFRP as internal reinforcement for PCTLs under quasi-static cyclic flexural loading. These experimental results can be considered in the forthcoming provisions of ACI codes for the use of GFRP as internal reinforcement for PCTL applications.
- This research illustrates the advantages of using HSC for PCTL segments internally reinforced with GFRP bars under quasi-static cyclic flexural conditions. In which using higher strength concrete (HSC) made it possible to take advantage of higher tensile strength in the GFRP reinforcement bars.
- Using FRC for GFRP-reinforced precast concrete tunnel lining segments with the same longitudinal reinforcement ratio increased segment ductility and deformability under quasi-static cyclic flexural loading.
- Analytical predictions were presented for the hysteresis behavior of curvilinear GFRP-reinforced PCTL under quasi-static cyclic flexural loading. These analytical predictions could be taken into consideration in the forthcoming design code provisions governing the efficiency of using curvilinear GFRP reinforcement for PCTL segment applications under cyclic conditions.

8.2.2 Hysteresis behavior, general behavior, and failure mode

- The failure of the GFRP-reinforced precast concrete tunnel lining segments with low longitudinal reinforcement ratios (0.50% and 0.70%) occurred by concrete crushing, while the GFRP-reinforced precast concrete tunnel lining segments with higher longitudinal reinforcement ratios (0.90% and 1.20%) failed due to shear compression and diagonal shear.
- The conventionally steel reinforced precast concrete tunnel lining segment failed due to steel yielding, followed by concrete crushing.

- The hysteresis cycles of the GFRP-reinforced precast normal-strength concrete (NSC) tunnel lining segments, under quasi-static cyclic flexural loading, reflected stable cyclic behavior with no or limited strength degradation that was less than that experienced by the steel-reinforced specimen.
- The unloading stiffness for the GFRP-reinforced precast normal-strength concrete (NSC) tunnel lining segments in all cycles was nearly equal to the reloading stiffness. The yielding of the steel bars in the conventionally steel reinforced precast concrete tunnel lining segment resulted in degradation of the specimen's unloading stiffness.
- The residual deformation of the GFRP-reinforced precast normal-strength concrete (NSC) tunnel lining segments during unloading at 50% and 75% of the maximum displacement cycles was less than in the conventionally steel reinforced precast concrete tunnel lining segment due to the steel bars yielding.
- The experimental results indicate that the hysteresis cycles of the GFRP-reinforced precast normal-strength concrete tunnel (NSC) lining segments had stable cyclic behavior with no or limited strength degradation.
- The hysteretic response of the GFRP-reinforced precast high-strength concrete (HSC) tunnel lining segments in all second excursion loading cycles reflected stable cyclic behavior with no or limited strength degradation until failure.
- Increasing the stiffness of the GFRP-reinforced precast high-strength concrete (HSC) tunnel lining segments increased segment ultimate strength, under quasi-static cyclic flexural loading.
- The hysteretic response of the GFRP-reinforced precast fiber-reinforced concrete (FRC) tunnel lining segments in all second excursions reflected stable cyclic behavior with no or limited strength degradation up until failure.
- The unloading stiffness degradation in all GFRP-reinforced precast fiber-reinforced concrete (FRC) tunnel lining segments was advantageous in improving the structural reparability and reducing the residual deformation at the end of each cycle under cyclic loading conditions.
- Increasing the longitudinal reinforcement ratio in the GFRP-reinforced precast fiber-reinforced concrete (FRC) tunnel lining segments increased the segments' ultimate carrying capacity under quasi-static cyclic flexural loading.

8.2.3 Ductility and deformability

- The GFRP-reinforced precast normal-strength concrete (NSC) tunnel lining segments' ductility index was 78% of the conventionally streel reinforced precast concrete tunnel lining segment's ductility at a similar reinforcement ratio. This difference in ductility was compensated for by the high strength reserve of the GFRP-reinforced segments.
- The test results show that all the GFRP-reinforced precast normal-strength concrete (NSC) tunnel lining segments demonstrated adequate deformability, under quasi-static cyclic flexural loading, when compared to the [CAN/CSA S6-19] code limit of 4 for rectangular sections.
- The test results show that all the GFRP-reinforced precast high-strength concrete (HSC) tunnel lining segments demonstrated adequate deformability, under quasi-static cyclic flexural loading, when compared to the [CAN/CSA S6-19] code limit of 4 for rectangular sections.
- Increasing the reinforcement ratio did not affect the ductility index in the GFRP-reinforced high-strength concrete (HSC) tunnel lining segments, under quasi-static cyclic flexural loading.
- The test results show that all the GFRP-reinforced precast fiber-reinforced concrete (FRC) tunnel lining segments demonstrated adequate deformability, under quasi-static cyclic flexural loading, when compared to the [CAN/CSA S6-19] code limit of 4 for rectangular sections.
- Using FRC for GFRP-reinforced precast concrete tunnel lining segments with the same longitudinal reinforcement ratio increased segment ductility and deformability under quasi-static cyclic flexural loading.
- The reduction in the ductility index due to the increased longitudinal reinforcement ratio was compensated for with the use of FRC where the segment with 0.90% longitudinal reinforcement ratio had a ductility index comparable to that of the NSC segment with 0.50% longitudinal reinforcement ratio.

8.2.4 Secant stiffness damage index

- The damage caused to the GFRP-reinforced precast concrete tunnel lining segments under cyclic loading conditions was established using the secant stiffness damage index (KI). The

rate of KI degradation during the loading cycles was not confirmed for all the segments tested. The decrease in KI rate in the segment reinforced with the higher longitudinal reinforcement ratio was less than that in segments reinforced with the lower longitudinal reinforcement ratio. Therefore, the residual stiffness in the last loading cycle was comparable for all the segments tested.

8.2.5 Cracking and crack-width

- The use of the closed tie configuration in all GFRP-reinforced precast concrete tunnel lining segments enhanced the crack distribution in the section at ultimate load levels compared to the double U-shaped tie configuration.
- Although both closed and double U-shaped transverse reinforcement configurations resulted the same flexural carrying capacity, the segment with closed ties produced higher cracking moments than the segment with double U-shaped ties.
- The closed tie configurations enhanced the crack distribution in the section of the GFRP-reinforced precast concrete tunnel lining segments.
- The higher concrete compressive strength for the GFRP-reinforced precast high-strength concrete (HSC) tunnel lining segments produced higher cracking moments than in the counterpart GFRP-reinforced precast normal-strength concrete (NSC) tunnel lining segments.
- Increasing the reinforcement ratio in GFRP-reinforced precast high-strength concrete (HSC) tunnel lining segments generally enhanced the cracking behavior at all load levels.
- The use of FRC instead of normal-strength concrete (NSC) for the GFRP-reinforced precast concrete tunnel lining segments with the same longitudinal reinforcement ratio enhanced segment overall cracking distribution under quasi-static cyclic flexural loading.
- Increasing the longitudinal reinforcement ratio in the GFRP-reinforced precast fiber-reinforced concrete (FRC) tunnel lining segments reduced the crack width and crack spacing in the section of the segment at ultimate load levels.
- The conservative k_b value of 1.4, as recommended in [ACI 440.1R-15], resulted in conservative crack-width predictions. In contrast, the small k_b value (0.8) in [CAN/CSA S6-19] compared to that in [ACI 440.1R-15] contributed to underestimating

the crack widths. Using a bond reduction factor (C_b) of 0.83 as in [AASHTO, 2018] provided accurate crack-width predictions.

8.2.6 Flexural and Shear capacities

- The experimental-to-predicted ratio of the flexural-moment capacity of GFRP-reinforced precast normal-strength concrete (NSC) tunnel lining segments indicates good predictions for [ACI 440.1R-15], *fib* [TG-9.3, 2007], and [AFGC, 2021], while [CAN/CSA S806-12 (R2017)] overestimated its flexural-moment capacity. On the other hand, [CNR-DT 203, 2006] yielded conservative predictions of its flexural-moment capacity.
- [ACI 440.1R-15] produced conservative shear-load predictions for the GFRP-reinforced precast normal-strength concrete (NSC) tunnel lining segments. Conversely, [CNR-DT 203, 2006] overestimated the shear–load capacities for the GFRP-reinforced precast normal-strength concrete (NSC) tunnel lining segments. The ACI shear modification model proposed in *fib* [TG-9.3, 2007], [AFGC, 2021], and [CAN/CSA S806-12 (R2017)] yielded accurate predictions of the shear–load capacities for the GFRP-reinforced precast normal-strength concrete (NSC) tunnel lining segments.
- The experimental-to-predicted moment capacity of the GFRP-reinforced precast high-strength concrete (HSC) tunnel lining segments shows that the [ACI 440.1R-15] and [CAN/CSA S806-12 (R2017)] predictions were unconservative. The rectangular stress block approach proposed by [Ozbakkaloglu and Saatcioglu, 2004] and [Hadhood et al., 2018] showed enhancement in both the [ACI 440.1R-15] and [CAN/CSA S806-12 (R2017)] predictions.

8.2.7 Analytical predictions

- Using the layer-by-layer iterative approach, the analytical model presented was capable of predicting the hysteresis response of the GFRP-reinforced PCTL segments under quasi-static cyclic flexural loading. The model provided good predictions with experimental-to-predicted ratios ranging between 0.95 and 0.96 for all the segments tested. In addition, the analytical model yielded good predictions for the cumulative dissipated energy, with experimental-to-predicted cumulative dissipated energy ratios ranging between 0.94 and 1.13, for all the segments tested.

- Analytical models for the post-cracking loading tangent stiffness and the unloading stiffness for the curvilinear-GFRP reinforced PCTL segments were proposed. The analytically predicted hysteresis response showed accurate predictions with comparable loading stiffness, unloading stiffness and residual deformation at the end of each loading cycle.

8.3 RECOMMENDATION FOR FUTURE WORK

First-of-their-kind experimental results and analytical predictions were presented for the hysteresis behavior of the curvilinear-GFRP reinforced PCTL under quasi-static cyclic flexural loading. These experimental results and analytical predictions could be taken into consideration for the forthcoming design code provisions governing the efficiency of using curvilinear-GFRP reinforcement for the PCTL segments application under cyclic conditions. The design of the PCTL segments reinforced with FRP bars is not defined or discussed in the current design provisions such as in [ACI 440.1R-15; ACI 544.7R-16; ACI PRC-533.5-20]. Additional research is recommended based on the findings of the current study are recommended to:

- Develop design recommendations for the different international design standards for the use of composite reinforcing bars for the precast concrete tunnel lining (PCTL) segments.
- To optimize the FRP reinforcement details and concrete dimensions of precast concrete tunnel lining (PCTL) segments under different loading conditions.
- Investigate the behavior of the GFRP reinforced precast concrete tunnel lining (PCTL) segments under multidirectional quasi-static cyclic loads.
- Investigate the behavior of the GFRP reinforced precast concrete tunnel lining (PCTL) segments under unidirectional and multidirectional pseudo-dynamic cyclic loads
- Propose analytical models for predicting the hysteresis response of GFRP reinforced precast concrete tunnel lining (PCTL) segments.

French version of this chapter is presented below:

8.4 RÉSUMÉ

Cette recherche a étudié le comportement cyclique des voussoirs RTBP renforcés avec des barres en PRFV, expérimentalement et théoriquement. Un total de douze voussoirs RTBP à échelle réelle avec une longueur, une largeur et une épaisseur totales de 3100 mm, 1500 mm et 250 mm, respectivement, ont été construits et testés sous des charges de flexion cycliques quasi-statiques. Deux cycles de chargement et de déchargement ont été appliqués à 1,25%, 2,5%, 5%, 10%, 25%, 50% et 75% du déplacement maximal estimé, suivis d'un seul cycle jusqu'à la rupture. Les paramètres de l'essai de l'essai comprenaient la rigidité à la flexion de l'armature (PRFV par rapport à l'acier), le taux de renforcement longitudinal du PRFV, la résistance à la compression du béton (béton à haute résistance (BHR) par rapport au béton à résistance normale (BRN)), le type de béton (béton renforcé de fibres (BRF) par rapport au BRN), et la configuration de l'armature transversale (cadres fermés par rapport aux cadres doubles en forme de U). La réponse d'hystérésis, le modèle de fissuration, la déformation résiduelle, l'énergie dissipée, l'indice de ductilité, la déformabilité et l'indice de dommage de la rigidité sécante des spécimens testés ont été définis, estimés et évalués. Une étude théorique a été menée pour calculer les capacités de flexion et de cisaillement des voussoirs RTBP renforcés avec des barres en PRFV selon les différentes dispositions de conception actuelles [ACI 440.1R-15 ; CAN/CSA S806-12 (R2017) ; fib TG-9.3, 2007 ; CNR-DT 203, 2006 ; AFGC, 2021]. En outre, une prédiction théorique selon les codes et les directives de conception nord-américaine [ACI 440.1R-15 ; CAN/CSA S6-19 ; AASHTO, 2018], y compris le moment de fissuration et la largeur des fissures, a été réalisée et les résultats ont été comparés aux résultats expérimentaux. De plus, en utilisant l'approche itérative couche par couche, un modèle analytique a été présenté pour la réponse d'hystérésis des voussoirs RTBP renforcés par des barres en PRFV sous des charges de flexion cycliques quasi-statiques. En outre, des modèles analytiques pour la rigidité tangente de chargement après fissuration et la rigidité de déchargement pour les voussoirs RTBP curvilignes renforcés par des barres PRFV ont été proposés. Jusqu'à présent, cette recherche est le premier travail expérimental visant à fournir des données expérimentales impliquant l'essai en laboratoire de la performance des voussoirs RTBP renforcés avec des barres en PRFV sous des charges de flexion cycliques quasi-statiques.

8.5 CONCLUSIONS

À partir des résultats expérimentaux, théoriques et analytiques obtenus dans cette recherche en considérant les paramètres précédents associés au programme de recherche, les conclusions suivantes sont tirées :

8.5.1 Comportement d'hystérésis, comportement général et mode de défaillance

- La rupture des segments de revêtement de tunnel préfabriqués en béton renforcé de PRFV avec de faibles ratios d'armature longitudinale (0,50 % et 0,70 %) s'est produite par écrasement du béton, tandis que les segments de revêtement de tunnel en béton préfabriqué renforcé de PRFV avec des ratios d'armature longitudinale plus élevés (0,90 % et 1,20 %) se sont rompus en raison de la compression-cisaillement et du cisaillement diagonal.
- Le voussoir du revêtement du tunnel préfabriqués en béton renforcé par de l'acier conventionnel s'est rompu en raison de la déformation de l'acier, suivie d'un écrasement du béton.
- Les cycles d'hystérésis des voussoirs de revêtement de tunnel préfabriqués en béton à résistance normale (BRN) renforcés par des PRFV, sous une charge de flexion cyclique quasi-statique, ont reflété un comportement cyclique stable avec une dégradation de la résistance nulle ou limitée, inférieure à celle de l'échantillon renforcé par de l'acier.
- La rigidité au déchargement des voussoirs de revêtement de tunnel préfabriqués en béton à résistance normale (BRN) renforcés par des PRFV dans tous les cycles était presque égale à la rigidité au rechargement. L'élasticité des barres d'acier dans le voussoir de revêtement de tunnel en béton préfabriqué renforcé par de l'acier conventionnel a entraîné une dégradation de la rigidité à la décharge de l'éprouvette.
- La déformation résiduelle des voussoirs de revêtement de tunnel préfabriqués en béton à résistance normale (BRN) renforcé par des PRFV pendant le déchargement à 50 % et 75 % des cycles de déplacement maximum était inférieure à celle du voussoir de revêtement de tunnel en béton préfabriqué renforcé par de l'acier conventionnel en raison de la déformation des barres d'acier.
- Les résultats expérimentaux indiquent que les cycles d'hystérésis des voussoirs de revêtement de tunnel préfabriqués en béton à résistance normale (BRN) renforcés par des

PRFV avaient un comportement cyclique stable avec une dégradation de la résistance nulle ou limitée.

- La réponse hystérétique des segments de revêtement de tunnel préfabriqués en béton à haute résistance (BHR) renforcés par des PRFV dans tous les cycles de chargement de la deuxième excursion a reflété un comportement cyclique stable avec une dégradation de la résistance nulle ou limitée jusqu'à la rupture.
- L'utilisation d'un béton à haute résistance (BHR) a permis de profiter de la résistance à la traction plus élevée des barres de renforcement en PRFV.
- L'augmentation de la rigidité des voussoirs de revêtement de tunnel préfabriqués en béton à haute résistance (BHR) renforcés par des PRFV a permis d'augmenter la résistance ultime des voussoirs, sous une charge de flexion cyclique quasi-statique.
- La réponse hystérétique des voussoirs de revêtement de tunnel préfabriqués en béton renforcé de fibres (BRF) renforcés par des PRFV dans toute la deuxième excursion a reflété un comportement cyclique stable avec une dégradation de la résistance nulle ou limitée jusqu'à la rupture.
- La dégradation de la rigidité au déchargement dans tous les voussoirs de revêtement de tunnel préfabriqués en béton renforcé de fibres (BRF) renforcés par des PRFV a permis d'améliorer la réparabilité structurelle et de réduire la déformation résiduelle à la fin de chaque cycle dans des conditions de chargement cyclique.
- L'augmentation du taux de renforcement longitudinal dans les voussoirs de revêtement de tunnel préfabriqués en béton renforcé de fibres (BRF) renforcés par des PRFV a permis d'accroître la capacité de charge ultime des voussoirs sous une charge de flexion cyclique quasi-statique.

8.5.2 Ductilité et déformabilité

- L'indice de ductilité des voussoirs de revêtement de tunnel préfabriqués en béton à résistance normale (BRN) renforcés par des PRFV était de 78 % de celui des voussoirs de revêtement de tunnel préfabriqués en béton à armature conventionnelle, pour un taux de renforcement similaire. Cette différence de ductilité a été compensée par la réserve de résistance élevée des voussoirs renforcés par des PRFV.

- Les résultats des essais montrent que tous les voussoirs de revêtement de tunnel préfabriqués en béton à résistance normale (BRN) renforcé par des PRFV ont démontré une déformabilité adéquate, sous une charge de flexion cyclique quasi-statique, par rapport à la limite de 4 du code [CAN/CSA S6-19] pour les sections rectangulaires.
- Les résultats des essais montrent que tous les voussoirs de revêtement de tunnel préfabriqués en béton à haute résistance (BHR) renforcés par des PRFV ont démontré une déformabilité adéquate, sous une charge de flexion cyclique quasi-statique, par rapport à la limite de 4 du code [CAN/CSA S6-19] pour les sections rectangulaires.
- L'augmentation du taux de renforcement n'a pas affecté l'indice de ductilité des voussoirs de revêtement de tunnel en béton à haute résistance (BHR) renforcé par des PRFV, sous une charge de flexion cyclique quasi-statique.
- Les résultats des essais montrent que tous les voussoirs de revêtement de tunnel préfabriqués en béton renforcé de fibres (BRF) renforcés par des PRFV ont démontré une déformabilité adéquate, sous une charge de flexion cyclique quasi-statique, par rapport à la limite de 4 du code [CAN/CSA S6-19] pour les sections rectangulaires.
- L'utilisation de BRF pour des voussoirs de revêtement de tunnel préfabriqués renforcés par des PRFV avec le même taux de renforcement longitudinal a augmenté la ductilité et la déformabilité des voussoirs sous une charge de flexion cyclique quasi-statique.
- La réduction de l'indice de ductilité due à l'augmentation du taux de renforcement longitudinal a été compensée par l'utilisation de BRF, le voussoir avec un taux de renforcement longitudinal de 0,90% ayant un indice de ductilité comparable à celui du voussoir en BRN avec un taux de renforcement longitudinal de 0,50%.

8.5.3 Indice d'endommagement de la rigidité sécante

- Les dommages causés aux voussoirs de revêtement de tunnel préfabriqués en béton renforcés par des PRFV dans des conditions de chargement cyclique ont été établis en utilisant l'indice de dommage de la rigidité sécante (KI). Le taux de dégradation du KI pendant les cycles de chargement n'a pas été confirmé pour tous les voussoirs testés. La diminution du taux de KI dans le voussoir renforcé avec le taux de renforcement longitudinal le plus élevé était inférieure à celle des voussoirs renforcés avec le taux de

renforcement longitudinal le plus faible. Par conséquent, la rigidité résiduelle dans le dernier cycle de chargement était comparable pour tous les voussoirs testés.

8.5.4 Fissuration et largeur de fissure

- L'utilisation d'une configuration d'ancrage fermée dans tous les voussoirs de revêtement de tunnel préfabriqué en béton renforcés par des PRFV a permis d'améliorer la distribution des fissures dans la section au niveau de charge ultime, par rapport à la configuration d'ancrage en double U.
- Bien que les deux configurations d'armature transversale, fermée et en double U, aient donné lieu à la même capacité de charge en flexion, le voussoir avec des cadres fermées a produit des moments de fissuration plus élevés que le voussoir avec des cadres en double U.
- Les configurations de cadres fermés ont amélioré la distribution des fissures dans la section des voussoirs de revêtement de tunnel préfabriqués en béton renforcé par des PRFV.
- La résistance à la compression du béton plus élevée pour les voussoirs de revêtement de tunnel préfabriqués en béton à haute résistance (BHR) renforcée par des PRFV a produit des moments de fissuration plus élevés que dans les voussoirs de revêtement de tunnel préfabriqués en béton à résistance normale (BRN) renforcée par des PRFV.
- L'augmentation du taux de renforcement dans les voussoirs de revêtement de tunnel préfabriqués en béton à haute résistance (BHR) renforcées par des PRFV a généralement amélioré le comportement de fissuration à tous les niveaux de charge.
- L'utilisation de BRF au lieu de béton à résistance normale (BRN) pour les voussoirs de revêtement de tunnel préfabriqués en béton renforcés par des PRFV avec le même taux de renforcement longitudinal a amélioré la distribution globale des fissures des voussoirs sous une charge de flexion cyclique quasi-statique.
- L'augmentation du taux de renforcement longitudinal dans les voussoirs de revêtement de tunnel préfabriqués en béton renforcé de fibres (BRF) renforcé par des PRFV a réduit la largeur et l'espacement des fissures dans la section du voussoir au niveau de charge ultime.
- La valeur prudente de k_b de 1,4, recommandée dans la norme [ACI 440.1R-15], a donné lieu à des prévisions prudentes de la largeur des fissures. En revanche, la faible valeur de k_b (0,8) dans la norme [CAN/CSA S6-19] par rapport à celle de la norme [ACI 440.1R-15]

a contribué à sous-estimer la largeur des fissures. L'utilisation d'un facteur de réduction de la liaison (C_b) de 0,83, comme dans [AASHTO, 2018], a permis d'obtenir des prédictions précises de la largeur des fissures.

8.5.5 Capacités de flexion et de cisaillement

- Le rapport entre les résultats expérimentaux et les prévisions de la capacité de flexion des voussoirs de revêtement de tunnel préfabriqués en béton à résistance normale (BRN) renforcés par des PRFV indique de bonnes prévisions pour [ACI 440.1R-15], [TG-9.3, 2007] et [AFGC, 2021], tandis que [CAN/CSA S806-12 (R2017)] a surestimé sa capacité de flexion. D'autre part, [CNR-DT 203, 2006] a donné des prédictions conservatrices de sa capacité de flexion-moment.
- La norme [ACI 440.1R-15] a produit des prédictions de charge de cisaillement conservatrices pour les voussoirs de revêtement de tunnel préfabriqués en béton à résistance normale (BRN) renforcés par des PRFV. Inversement, [CNR-DT 203, 2006] a surestimé les capacités de charge de cisaillement pour les voussoirs de revêtement de tunnel préfabriqués en béton à résistance normale (BRN) renforcés par des PRFV. Le modèle de modification du cisaillement de l'ACI proposé dans les fibres [TG-9.3, 2007], [AFGC, 2021] et [CAN/CSA S806-12 (R2017)] a donné des prédictions précises des capacités de charge de cisaillement pour les voussoirs de revêtement de tunnel préfabriqués en béton à résistance normale (BRN) renforcés par des PRFV.
- La capacité de moment expérimentale par rapport aux prévisions des voussoirs de revêtement de tunnel préfabriqués en béton à haute résistance (BHR) renforcés par des PRFV montre que les prévisions des normes [ACI 440.1R-15] et [CAN/CSA S806-12 (R2017)] n'étaient pas prudentes. L'approche par blocs de contraintes rectangulaires proposée par [Ozbakkaloglu et Saatcioglu, 2004] et [Hadhood et al., 2018] a montré une amélioration des prédictions de [ACI 440.1R-15] et [CAN/CSA S806-12 (R2017)].

8.5.6 Prédictions analytiques

- En utilisant l'approche itérative couche par couche, le modèle analytique présenté était capable de prédire la réponse d'hystérésis des voussoirs RTBP renforcés par des PRFV sous une charge de flexion cyclique quasi-statique. Le modèle a fourni de bonnes prédictions avec des rapports expérimental/prévu compris entre 0,95 et 0,96 pour tous les

voussoirs testés. En outre, le modèle analytique a fourni de bonnes prédictions pour l'énergie dissipée cumulative, avec des rapports entre l'expérience et la prédiction de l'énergie dissipée cumulative compris entre 0,94 et 1,13, pour tous les voussoirs testés.

- Des modèles analytiques pour la rigidité tangente de chargement après fissuration et la rigidité de déchargement pour les voussoirs RTBP renforcés par des PRFV curvilignes ont été proposés. La réponse d'hystérésis prédite analytiquement a montré des prédictions précises avec une rigidité de chargement, une rigidité de déchargement et une déformation résiduelle comparables à la fin de chaque cycle de chargement.

8.6 RECOMMANDATIONS POUR LES TRAVAUX FUTURS

Des résultats expérimentaux et des prédictions analytiques, les premiers du genre, ont été présentés pour le comportement d'hystérésis du RTBP renforcé par des PRFV curvilignes sous une charge de flexion cyclique quasi-statique. Ces résultats expérimentaux et ces prédictions analytiques pourraient être pris en considération pour les dispositions du code de conception à venir régissant l'efficacité de l'utilisation du renforcement PRFV curviligne pour l'application des voussoirs RTBP dans des conditions cycliques. La conception des voussoirs RTBP renforcés avec des barres PRF n'est pas définie ou discutée dans les dispositions de conception actuelles telles que dans [ACI 440.1R-15; ACI 544.7R-16; ACI PRC-533.5-20]. Des recherches supplémentaires sont recommandées sur la base des résultats de la présente étude :

- Élaborer des recommandations de conception pour les différentes normes de conception internationales concernant l'utilisation de barres d'armature composites pour les voussoirs de revêtement de tunnel en béton préfabriqué (RTBP).
- Optimiser les détails du renforcement en PRF et les dimensions du béton des voussoirs de revêtement de tunnel en béton préfabriqué (RTBP) dans différentes conditions de chargement.
- Étudier le comportement des voussoirs de revêtement de tunnel en béton préfabriqué renforcé par des PRFV sous des charges cycliques multidirectionnelles quasi-statiques.
- Étudier le comportement des voussoirs de revêtement de tunnel en béton préfabriqué renforcé par des PRFV sous des charges cycliques pseudo-dynamiques unidirectionnelles et multidirectionnelles.

- Proposer des modèles analytiques pour prédire la réponse d'hystérésis des voussoirs de revêtement de tunnel en béton préfabriqué (RTBP) renforcés par des PRFV.

REFERENCES

AASHTO. (2018). “AASHTO LRFD bridge design guide specifications for GFRP–reinforced concrete bridge decks and traffic railings.” Washington, DC: *AASHTO*.

Abbas, S. (2014). “Structural and durability performance of precast segmental tunnel linings.” Doctoral dissertation, Western University, Ontario, Canada.

Al-Saadi, N. T. K., Mohammed, A., Al-Mahaidi, R., and Sanjayan, J. (2019). “A state-of-the-art review: Near-surface mounted FRP composites for reinforced concrete structures.” *Construction and Building Materials*, 209, 748-769.

American Concrete Institute (ACI). (2013). “Guide for Testing Reinforced Concrete Structural Elements under Slowly Applied Simulated Seismic Loads.” *ACI 374.2R-13*, Farmington Hills, MI.

American Concrete Institute (ACI). (2015). “Guide for the Design and Construction of Structural Concrete Reinforced with Fiber-Reinforced Polymer (FRP) Bars.” *ACI 440.1R-15*, Farmington Hills, MI.

American Concrete Institute (ACI). (2022). “Building Code Requirements for Structural Concrete Reinforced with Glass Fiber-Reinforced Polymer (GFRP) Bars – Code and Commentary.” *ACI 440.11-22*, Farmington Hills, MI.

American Concrete Institute (ACI) (2020). "Guide for Precast Concrete Tunnel Segments.", *ACI 533.5R-20*, Farmington Hills, MI.

American Concrete Institute (ACI) (2018). "Guide to Design with Fiber-Reinforced Concrete.", *ACI 544.4R-18*, Farmington Hills, MI.

American Concrete Institute (ACI). (2016). "Report on Design and Construction of Fiber-Reinforced Precast Concrete Tunnel Segments.", *ACI 544.7R-16*, Farmington Hills, MI.

American Concrete Institute (ACI) (2015). "Report on Indirect Method to Obtain a Stress-Strain Diagram for Strain Softening Fiber-Reinforced Concrete (FRCs).", *ACI 544.8R-15*, Farmington Hills, MI.

American Concrete Institute (ACI). (2020). "Guide for Precast Concrete Tunnel Segments.", *ACI PRC-533.5-20*, Farmington Hills, MI.

AFGC (2021). "Réparation et renforcement des structures en béton au moyen des matériaux composites." Technical report, *Bulletin scientifique et technique de l'Association Française de Génie Civil* (AFGC), (In French).

ASTM. (2020). "Standard Test Method for Flexural Performance of Fiber-Reinforced Concrete (Using Beam with Third-Point Loading)." *ASTM C1069/C1069M-19a*, West Conshohocken, PA.

ASTM. (2020). "Standard Test Method for Flexural Toughness of Fiber Reinforced Concrete (Using Centrally Loaded Round Panel)" *ASTM 1550-20*, West Conshohocken, PA.

ASTM. (2021). "Standard Test Method for Tensile Properties of Fiber Reinforced Polymer Matrix Composite Bars." *ASTM D7205/D7205M-21*, West Conshohocken, PA.

Bakis, C. E. (1993). "FRP composites: Materials and manufacturing." *In fibre reinforced plastic (FRP) reinforcement for concrete structures: Properties and applications*. Developments in civil engineering, ed. A. Nanni, 42, 13-58.

Bank, L. C. (1993). "Properties of FRP reinforcements for concrete." *In Fiber-Reinforced-Plastic (FRP) Reinforcement for Concrete Structures.* 59-86.

Barwart, C., Romualdi, P., and Barioffi, A. (2013). "Headrace tunnel of the El Alto hydropower project in Panama/Druckstollen des Wasserkraftprojekts El Alto in Panama." *Geomechanics and Tunnelling*, 6(4), 301-311.

Bellakehal, H., Zaidi, A., Masmoudi, R., and Bouhicha, M. (2013). "Combined effect of sustained load and freeze–thaw cycles on one-way concrete slabs reinforced with glass fibre–reinforced polymer." *Canadian Journal of Civil Engineering*, 40(11), 1060-1067.

Benmokrane, B., Ahmed, E., Dulude, C., and Boucher, E. (2012). "Design, construction, and monitoring of the first worldwide two-way flat slab parking garage reinforced with GFRP bars." *In Proc., 6th Int. Conf. on FRP Composites in Civil Engineering*.

Benmokrane, B., and Ali, A. H. (2018). "Durability and Long-Term Performance of Fiber-Reinforced Polymer as a New Civil Engineering Material." *In International Congress on Polymers in Concrete* (pp. 49-59). Springer, Cham.

Benmokrane, B., El-Salakawy, E., Desgagne, G., and Lackey, T. (2004). "FRP bars for bridges." *Concrete international*, 26(8), 84-90.

Benmokrane, B., El-Salakawy, E., El-Gamal, S., and Goulet, S. (2007). "Construction and testing of an innovative concrete bridge deck totally reinforced with glass FRP bars: Val-Alain Bridge on Highway 20 East." *Journal of Bridge Engineering*, 12(5), 632-645.

Benmokrane, B., and Masmoudi, R. (1996). "Flexural response of concrete beams reinforced with FRP reinforcing bars." *Structural Journal*, 93(1), 46-55.

Benmokrane, B., and Mohamed, H. M. (2014). "Extending the service life of water treatment structures." *Concrete international*, 36(2), 40-45.

Benmokrane, B., Mousa, S., Mohamed, K., and Sayed-Ahmed, M. (2021). "Physical, mechanical, and durability characteristics of newly developed thermoplastic GFRP bars for reinforcing concrete structures." *Construction and Building Materials*, 276, 122200.

Brown, V. L., and Bartholomew, C. L. (1996, January). “Long-term deflections of GFRP-reinforced concrete beams.” *In First International Conference on Composites in Infrastructure National Science Foundation National Science Foundation*.

BS EN 14651:2005+A1:2007. “Test Method for Metallic Fibre Concrete.” Measuring the Flexural Tensile Strength (Limit of Proportionality (LOP), residual).

Canadian Standards Association (CSA). (2019). “Canadian highway bridge design code.” *CAN/CSA-S6-19*, Mississauga, Ontario, Canada.

Canadian Standards Association (CSA). (2012). “Design and construction of building components with fiber-reinforced polymers.” *CAN/CSA-S806-12*, Mississauga, ON, Canada – Reapproved 2017.

Caratelli, A., Meda, A., Rinaldi, Z., and Romualdi, P. (2011). “Structural behaviour of precast tunnel segments in fiber reinforced concrete.” *Tunnelling and Underground Space Technology*, 26(2), 284-291.

Caratelli, A., Meda, A., and Rinaldi, Z. (2012). “Design according to MC2010 of a fibre-reinforced concrete tunnel in Monte Lirio, Panama.” *Structural Concrete*, 13(3), 166-173.

Caratelli, A., Meda, A., Rinaldi, Z., and Spagnuolo, S. (2016). “Precast tunnel segments with GFRP reinforcement.” *Tunnelling and Underground Space Technology*, 60, 10-20.

Caratelli, A., Meda, A., Rinaldi, Z., Spagnuolo, S., and Maddaluno, G. (2017). “Optimization of GFRP reinforcement in precast segments for metro tunnel lining.” *Composite Structures*, 181, 336-346.

Chen, J. (2004). “Effect of reinforcement corrosion on the serviceability of reinforced concrete structures” Doctoral dissertation, University of Dundee.

Cheong, Y. W., Kwan, H. P. and Hariyanto, A. D. (2005). "Quality control in precast production, a case study on Tunnel Segment Manufacture." *Journal of Architecture and Built Environment*, 33(2).

CNR-DT 203 (2006). "Guide for the design and construction of concrete structures reinforced with fiber-reinforced polymer bars." *National Research Council*, Rome, Italy.

Cosenza, E., Manfredi, G., and Ramasco, R. (1993). "The use of damage functionals in earthquake engineering: a comparison between different methods." *Earthquake engineering & structural dynamics*, 22(10), 855-868.

Daniel, L., and Loukili, A. (2002). "Behavior of high strength fiber-reinforced concrete beams under cyclic loading." *Structural Journal*, 99(3), 248-256.

Davis, J. R. (Ed.). (2000). "Corrosion: Understanding the basics." *ASM International*, The Materials Information Society, Materials Park, Ohio, USA, 571.

De Rivaz, B., Meda, A., Perruzza, P., Rinaldi, Z., and Romualdi, P. (2012). "Full scale tests on precast tunnel segment made in concrete reinforced with high strengths steel fibers." In WTC 2012.

De Waal, R. G. A. (1999). "Steel fiber reinforced tunnel segments." Doctoral dissertation, Ph. D Dissertation, Delft University of Technology, The Netherlands.

Di Prisco, M., and Felicetti, R. (2004). "On fatigue of plain and fibre-reinforced concrete ground slabs." *In BEFIB 04*, 1195-1206.

Di Prisco, M., Plizzari, G., and Vandewalle, L. (2009). "Fibre reinforced concrete: new design perspectives." *Materials and structures*, 42(9), 1261-1281.

Ding, L., Wu, G., Yang, S., and Wu, Z. (2013). “Performance advancement of RC columns by applying basalt FRP composites with NSM and confinement system.” *Journal of Earthquake and Tsunami*, 7(02), 1350007.

Dong, Z., Zhang, P., Zhu, H., Wu, G., and Wu, Z. (2016). “Study on stiffness and recoverability of Fiber Reinforced Polymers-Reinforced Concrete (FRP-RC) composite T-beams with prefabricated Basalt fiber-reinforced polymers shell.” *Journal of Reinforced Plastics and Composites*, 35(6), 516-529.

Drouin, B., Latour, G., and Mohamed, H. (2011). “More than 10 Years Successful Field Applications of FRP Bars in Canada, CDCC 2011.” *In The Fourth International Conference on Durability & Sustainability of Fiber Reinforced Polymer (FRP) Composites for Construction and Rehabilitation*, proceedings on CD-Rom, Quebec City, Quebec, Canada. 20.

Ehsani, M. R. (1993). “Glass-fiber reinforcing bars.” *Alternative Materials for the Reinforcement and Prestressing of Concrete*, JL Clarke, Blackie Academic & Professional, London, England, 35-54.

El Naggar, H., and Hinchberger, S. D. (2008). “An analytical solution for jointed tunnel linings in elastic soil or rock.” *Canadian Geotechnical Journal*, 45(11), 1572-1593.

El-Nemr, A., Ahmed, E. A., and Benmokrane, B. (2013). “Flexural Behavior and Serviceability of Normal-and High-Strength Concrete Beams Reinforced with Glass Fiber-Reinforced Polymer Bars.” *ACI structural journal*, 110(6).

El-Salakawy, E., and Benmokrane, B. (2003). “Design and testing of a highway concrete bridge deck reinforced with glass and carbon FRP bars.” *Special Publication*, 215, 37-54.

El-Salakawy, E., Benmokrane, B., and Desgagné, G. (2003). "Fibre-reinforced polymer composite bars for the concrete deck slab of Wotton Bridge." *Canadian Journal of Civil Engineering*, 30(5), 861-870.

El-Salakawy, E., Benmokrane, B., El-Ragaby, A., and Nadeau, D. (2005). "Field investigation on the first bridge deck slab reinforced with glass FRP bars constructed in Canada." *Journal of composites for construction*, 9(6), 470-479.

European Federation of Producers and Applicators of Specialist Products for Structures. (1999). "European Specification for Sprayed Concrete — Guidelines for Specifiers and Contractors," Surrey, UK, 35.

European Committee for Standardization (CEN). (2004). "Design of concrete structures—Part 1-1: General rules and rules for buildings." *Eurocode 2*, Brussels, Belgium.

Fahmy M, Wu ZS and Wu G. (2009) "Seismic performance assessment of damage-controlled FRP-retrofitted RC bridge columns using residual deformations." Journal of Composite Construction, 13, 498–513.

Fardis, M. N., Economu, S. N., Antoniou, A. N., Komodromos, P. J., and Sfakianakis, M. G. (1993). "Damage measures and failure criteria-Part I." *Contribution of University of Patras Final Report of Cooperative research on the seismic response of reinforced concrete structures-2nd Phase*.

Faza, S., and GangaRao, H. (1993). "Glass FRP reinforcing bars for concrete. Fiber reinforced (FRP) reinforcement for concrete structures: properties and applications." *In: Developments in civil engineering*, 42, 167-188.

Fédération Internationale de Béton (FIB). (2007) "FRP Reinforcement in RC Structures." *Task Group 9.3*, Lausanne, Switzerland, 157.

Fédération Internationale de Béton (FIB). (2017) “State-of-the-art report, Precast Tunnel segments in Fiber-Reinforced Concrete.” *Bulletin 83*, 162.

Frosch, R. J. (1999). “Another look at cracking and crack control in reinforced concrete.” *ACI Structural Journal*, 96(3), 437-442.

Gentry, T. R., and Husain, M. (1999). “Thermal compatibility of concrete and composite reinforcements.” *Journal of Composites for Construction*, 3(2), 82-86.

Ghobarah, A., Abou-Elfath, H., and Biddah, A. (1999). “Response-based damage assessment of structures.” *Earthquake engineering & structural dynamics*, 28(1), 79-104.

Goldston, M. W., Remennikov, A., and Sheikh, M. N. (2017). “Flexural behaviour of GFRP reinforced high strength and ultra-high strength concrete beams.” *Construction and Building Materials*, 131, 606-617.

Gulikers, J. (2003). “Problems encountered in the detection of reinforcement corrosion in concrete tunnel linings–theoretical considerations.” *Materials and Corrosion*, 54(6), 454-459.

Grace, N. F., Soliman, A. K., Abdel-Sayed, G., and Saleh, K. R. (1998). “Behavior and ductility of simple and continuous FRP reinforced beams.” *Journal of composites for construction*, 2(4), 186-194.

Hadhood, A., Mohamed, H. M., and Benmokrane, B. (2018). “Assessing stress-block parameters in designing circular high-strength concrete members reinforced with FRP bars.” *Journal of Structural Engineering*, 144(10), 04018182.

Hameed, R., Duprat, F., Turatsinze, A., and Sellier, A. (2009). “Mechanical properties of reinforced fibrous concrete beams under reverse cyclic loading.” *In Proc. of 1st International Conference on Sustainable Built Environment Infrastructures in Developing Countries*, SBEIDCO, ENSET Oran (Algeria), 271-278.

Hassanli, R., Manalo, A., Vafaei, D., Yekrangnia, M., Elchalakani, M., and Noël, M. (2023). "Cyclic behavior of GFRP-reinforced concrete one-way slabs with synthetic fibers." *Journal of Building Engineering*, 65, 105741.

Hilar, M., and Beno, J. (2012). "Steel fibre reinforced segmental tunnel linings." *Tunnel*, 21(3), 31-37.

Hillerborg, A., Modéer, M., and Petersson, P. E. (1976). "Analysis of crack formation and crack growth in concrete by means of fracture mechanics and finite elements." *Cement and concrete research*, 6(6), 773-781.

Holschemacher, K., and Muller, T. (2007, December). "Influence of fiber type and concrete composition on properties of steel fiber reinforced concrete." *In Proceedings of International conference on Advances in cement-based materials and applications in civil infrastructure (ACBMACI)*. Lahore-Pakistan, 633-642.

Hosseini, S.M., Mousa, S., Mohamed, H.M., and Benmokrane, B. (2022) "Structural Behavior of Precast RC Tunnel Segments with GFRP Bars and Ties Under Bending Load" *ACI Structural Journal*, Vol. 119, No. 1, 1-13.

Hung, J. C., Monsees, J., Munfah, N., and Wisniewski, J. (2009). "Technical manual for design and construction of road tunnels-civil elements." *Prepared for the US Department of Transportation*.

Jaeger, L. G., Mufti, A. A., and Tadros, G. (1997). "The concept of the overall performance factor in rectangular-section reinforced concrete members." *Proc., 3rd Int. Symp. on Non-Metallic (FRP) Reinforcement for Concrete Structures, FRPRCS-3, V. 2*, Japan Concrete Institute, Tokyo, 551–559.

Kalpana, V. G., and Subramanian, K. (2011). “Behavior of concrete beams reinforced with GFRP BARS.” *Journal of reinforced plastics and composites*, 30(23), 1915-1922.

Kara, I. F., Ashour, A. F., and Köroglu, M. A. (2015). “Flexural behavior of hybrid FRP/steel reinforced concrete beams.” *Composite Structures*, 129, 111–121.

Karsan, I. D., and Jirsa, J. O. (1969). “Behavior of concrete under compressive loadings.” *Journal of the Structural Division*, 95(12), 2543-2564.

Kesner, K. E., Billington, S. L., and Douglas, K. S. (2003). “Cyclic response of highly ductile fiber-reinforced cement-based composites.” *Materials Journal*, 100(5), 381-390.

Kim, T.-H., Lee, K.-M., Chung, Y.-S., and Shin, H.M. (2005). “Seismic damage assessment of reinforced concrete bridge columns.” *Engineering Structures*, 27(4), 576–592.

Koch, G., Varney, J., Thompson, N., Moghissi, O., Gould, M., and Payer, J. (2016). “International measures of prevention, application, and economics of corrosion technologies study.” *NACE international*, 216, 2-3.

Li, J., Li, P., Guo, D., Li, X., and Chen, Z. (2021). “Advanced prediction of tunnel boring machine performance based on big data.” *Geoscience Frontiers*, 12(1), 331-338.

Li, V. C., and Leung, C. K. (1992). “Steady-state and multiple cracking of short random fiber composites.” *Journal of engineering mechanics*, 118(11), 2246-2264.

Mallick, P. K. (2007). “Fiber-reinforced composites: materials, manufacturing, and design.” *CRC press*.

Manalo, A., Maranan, G., Benmokrane, B., Cousin, P., Alajarmeh, O., Ferdous, W., and Hota, G. (2020). “Comparative durability of GFRP composite reinforcing bars in concrete and in simulated concrete environments.” *Cement and Concrete Composites*, 109, 103564.

Mashimo, H., Isago, N., Yoshinaga, S., Shiroma, H., and Baba, K. (2002). "Experimental investigation on load-carrying capacity of concrete tunnel lining." *In Proceedings of twenty-eighth ITA general assembly and world tunnel congress*,1-10.

Masmoudi, R., Zaidi, A., and Gérard, P. (2005). "Transverse thermal expansion of FRP bars embedded in concrete." *Journal of Composites for Construction*, 9(5), 377-387.

Meda, A., Rinaldi, Z., Spagnuolo, S., De Rivaz, B., and Giamundo, N. (2019). "Hybrid precast tunnel segments in fiber reinforced concrete with glass fiber reinforced bars." *Tunnelling and Underground Space Technology*, 86, 100-112.

Meier, U. (1992). "Carbon fiber-reinforced polymers: modern materials in bridge engineering." *Structural engineering international*, 2(1), 7-12.

Meyer, C., Roufaiel, M. S., and Arzoumanidis, S. G. (1983). "Analysis of damaged concrete frames for cyclic loads." *Earthquake Engineering & Structural Dynamics*, 11(2), 207-228.

Michaud, M. C. B., GAGNÉ, R., and RACINE, P. (2014). "Conception, construction et monitorage d'une dalle de grande dimension en béton armé de polymères renforcés de fibres (PRF)."

Minelli, F., Tiberti, G., and Plizzari, G. (2011). "Crack control in RC elements with fiber reinforcement." *Special Publication*, 280, 1-18.

Moccichino, M., Romualdi, P., Perruzza, P., Meda, A., and Rinaldi, Z. (2010). "Experimental tests on tunnel precast segmental lining with fiber reinforced concrete." *In World Tunnel Congress (WTC)*. Vancouver, Canada.

Mohamed, H. M., and Benmokrane, B. (2015). "Torsion Behavior of Concrete Beams Reinforced with Glass Fiber-Reinforced Polymer Bars and Stirrups." *ACI Structural Journal*, 112(5).

Mohamed, H. M., and Benmokrane, B. (2016). “Reinforced concrete beams with and without FRP web reinforcement under pure torsion.” *Journal of Bridge Engineering*, 21(3), 04015070.

Mohamed, H. M., Ali, A. H., and Benmokrane, B. (2017). “Behavior of circular concrete members reinforced with carbon-FRP bars and spirals under shear.” *Journal of Composites for Construction*, 21(2), 04016090.

Mohamed, H. M., Ali, A. H., and Benmokrane, B. (2019). “Mechanism of distributed composite GFRP bars in circular concrete members with and without spirals under shear.” *Composites Part B: Engineering*, 162, 62-72.

Mohamed, H. M., Ali, A. H., Hadhood, A., Mousa, S., Abdelazim, W., and Benmokrane, B. (2020). “Testing, design, and field implementation of GFRP RC soft-eyes for tunnel construction.” *Tunnelling and Underground Space Technology*, 106, 103626.

Mousa, S., Mohamed, H. M., and Benmokrane, B. (2018). “Flexural strength and design analysis of circular reinforced concrete members with glass fiber-reinforced polymer bars and spirals.” *ACI Structural Journal*, 115(5), 1353-7.

Mousa, S., Mohamed, H. M., and Benmokrane, B. (2019). “Strength and deformability aspects of circular concrete members reinforced with hybrid carbon-FRP and glass-FRP under flexure.” *Journal of Composites for Construction*, 23(2), 04019005.

Mousa, S., Mohamed, H. M., and Benmokrane, B. (2019). “Deflection prediction methodology for circular concrete members reinforced with fiber-reinforced polymer bars.” *ACI Structural Journal*, 116(2), 279-293.

Mousa, S., Mohamed, H. M., Benmokrane, B., & Nanni, A. (2020). Flexural behavior of long-span square reinforced concrete members with uniformly distributed fiber-reinforced polymer bars. *ACI Structural Journal*.

Mufti, A. A., Newhook, J., Benmokrane, B., Tadros, G., and Vogel, H. M. (2011). "Durability of GFRP rods in field demonstration projects across Canada." *In Proc., 4th Int. Conf. on Durability & Sustainability of Fibre Reinforced Polymer (FRP) Composites for Construction and Rehabilitation of Structures (CDCC2011).* 27-35, Quebec City.

Mufti, A. A., Onofrei, M. B. N. M. J. B. G., Benmokrane, B., Banthia, N., Boulfiza, M., Newhook, J. P., ... and Brett, P. (2007). "Field study of glass-fibre-reinforced polymer durability in concrete." *Canadian Journal of Civil Engineering*, 34(3), 355-366.

Naaman, A. E., and Jeong, S. M. (1995). "Structural ductility of concrete beams prestressed with FRP tendons." *Proc., 2nd Int. RILEM Symp. on Non-Metallic (FRP) Reinforcement for Concrete Structures*, RILEM, Bagneux, France, 379–386.

Nanni, A. (1993). "Flexural behavior and design of RC members using FRP reinforcement." *Journal of structural engineering*, 119(11), 3344-3359.

National Highway Institute (US), Parsons, Brinckerhoff, and Quade and Douglas. (2010). "Technical manual for design and construction of road tunnels – civil elements." AASHTO.

Nedderman, H. (1973). "Flexural stress distribution in very high strength concrete." Doctoral dissertation, Dept. of Civil Engineering, Univ. of Texas.

Newmark N. M. (1943). "Numerical procedure for computing deflections, moments, and buckling loads". *ASCE Trans.*, 108(1),1161–1188.

Ospina, C. E., and Bakis, C. E. (2007). "Indirect flexural crack control of concrete beams and one-way slabs reinforced with FRP bars." *Proceedings of FRPRCS*, 8.

Ozbakkaloglu, T., and Saatcioglu, M. (2004). "Rectangular stress block for high-strength concrete." *ACI Structural Journal*, 101(4), 475-483.

Pan, Y., and Yan, D. (2021). “Study on the durability of GFRP bars and carbon/glass hybrid fiber reinforced polymer (HFRP) bars aged in alkaline solution.” *Composite Structures*, 261, 113285.

Pearson, M., Donchev, T., and Limbachiya, M. (2011). “An investigation into the sustainability of FRP reinforcement bars.” *In CDCC-11 4th International Conference on Durability and Sustainability of Fibre Composites for Construction and Rehabilitation*, Quebec City, Canada, 71-80.

Poh, J., Tan, K. H., Peterson, G. L., and Wen, D. (2009). “Structural testing of steel fibre reinforced concrete (SFRC) tunnel lining segments in Singapore.” *Land Transport Authority*, Singapore.

Popovics, S. (1973). “A numerical approach to the complete stress-strain curve of concrete.” *Cement and Concrete Research*, 3(5), 583–599.

Rancourt, A. (2016). “Analysis of the costs of a tunnel drilled between Beauport and Lévis.” Report, Géosys, 35.

Ranjbaran, F., Rezayfar, O., and Mirzababai, R. (2018). “Experimental investigation of steel fiber-reinforced concrete beams under cyclic loading.” *International Journal of Advanced Structural Engineering*, 10(1), 49-60.

Ruan, X., Lu, C., Xu, K., Xuan, G., and Ni, M. (2020). “Flexural behavior and serviceability of concrete beams hybrid-reinforced with GFRP bars and steel bars.” *Composite structures*, 235, 111772.

Schnütgen, B. (2003). “Design of precast steel fibre reinforced garages.” *Test and Design Methods for Steel Fibre Reinforced Concrete-Background and Experiences*, S, 153-159.

Solyom, S., and Balázs, G. L. (2020). “Bond of FRP bars with different surface characteristics.” *Construction and Building Materials*, 264, 119839.

Spagnuolo, S., Meda, A., Rinaldi, Z., and Nanni, A. (2017). "Precast concrete tunnel segments with GFRP reinforcement." *Journal of Composites for Construction*, 21(5), 04017020.

Spagnuolo, S., Meda, A., Rinaldi, Z., and Nanni, A. (2018). "Curvilinear GFRP bars for tunnel segments applications." *Composites Part B: Engineering*, 141, 137-147.

Taerwe, L. (1997). "FRP activities in Europe: survey of research and applications." *In Proceedings of the Third International Symposium on Non-Metallic (FRP) Reinforcement for Concrete Structures (FRPRCS-3)*, Sapporo (Japan), 14-16 oktober Volume 1.

Thireiuat, M., and Benmokrane, B. (1998). "Effects of FRP reinforcement ratio and concrete strength on flexural behavior of concrete beams." *Journal of composites for construction*, 2(1), 7-16.

Tiberti, G., Minelli, F., Plizzari, G. A., and Vecchio, F. J. (2014). « Influence of concrete strength on crack development in SFRC members." *Cement and Concrete composites*, 45, 176-185.

Uomoto, T. (1997). "Recommendation for design and construction of concrete structures using continuous fiber reinforcing materials." *A. Machida (Ed.)*. Tokyo, Japan: Japan Soc. of Civil Engineers.

Vafaei, D., Ma, X., Hassanli, R., Duan, J., and Zhuge, Y. (2023). "Experimental study on cyclic flexural behaviour of GFRP-reinforced seawater sea-sand concrete slabs with synthetic fibres." *Ocean Engineering*, 273, 114014.

Vandewalle, L., Nemegeer, D., Balazs, L., Barr, B., Barros, J., Bartos, P., ... and Walraven, J. (2003). "RILEM TC 162-TDF: Test and design methods for steel fibre reinforced concrete'-sigma-epsilon-design method-Final Recommendation." *Materials and Structures*, 36(262), 560-567.

Wang, Z., Zhao, X. L., Xian, G., Wu, G., Raman, R. S., Al-Saadi, S., and Haque, A. (2017). "Long-term durability of basalt-and glass-fibre reinforced polymer (BFRP/GFRP) bars in seawater and sea sand concrete environment." *Construction and Building Materials*, 139, 467-489.

Whitmore, D. W., and Ball, J. C. (2004). "Corrosion management." *ACI Concrete international*, 26(12), 82-85.

Wu, W. P. (1990). "Thermomechanical Properties of Fiber Reinforced Plastic (FRP) Bars." PhD Thesis. West Virginia University, Morgantown, West Virginia, USA.

Ye, L. P., Feng, P., Zhang, K., Lin, L., Hong, W. H., Yue, Q. R., ... and Yang, T. (2003). "FRP in civil engineering in China: research and applications." *In Fibre-Reinforced Polymer Reinforcement for Concrete Structures*. 2, 1401-1412.

Yost, J. R., and Gross, S. P. (2002). "Flexural design methodology for concrete beams reinforced with fiber-reinforced polymers." *Structural Journal*, 99(3), 308-316.

Xiao, S., Li, J., and Mo, Y. L. (2018). "Effect of loading rate on cyclic behavior of reinforced concrete beams." *Advances in Structural Engineering*, 21(7), 990-1001.

Xue, W., Li, L., Cheng, B., and Li, J. (2008). "The reversed cyclic load tests of normal and pre-stressed concrete beams." *Engineering structures*, 30(4), 1014-1023.

Zaidi, A., and Masmoudi, R. (2008). "Thermal effect on fiber reinforced polymer reinforced concrete slabs." *Canadian Journal of Civil Engineering*, 35(3), 312-320.

Zhiqiang, Z., and Mansoor, Y. A. (2013). "Evaluating the strength of corroded tunnel lining under limiting corrosion conditions." *Tunnelling and underground space technology*, 38, 464-475.